https://doi.org/10.15388/vu.thesis.706
https://orcid.org/0000-0002-0632-8758

VILNIUS UNIVERSITY
CENTER FOR PHYSICAL SCIENCES AND TECHNOLOGY

Edgaras Kolomiecas

Chemical Evolution of Galactic Globular Cluster 47 Tucanae

DOCTORAL DISSERTATION

Natural Sciences,
Physics (N 002)

VILNIUS 2025

This dissertation was prepared between 2016 and 2023 at Vilnius University, Institute of Theoretical Physics and Astronomy.

Academic supervisor:
Prof. Dr. Arūnas Kučinskas (Vilnius University, Natural Sciences, Physics – N 002)

Dissertation Defense Panel:

Chairman – Prof. Dr. Vladas Vansevičius (Center for Physical Sciences and Technology, Natural Sciences, Physics – N 002)

Members:
Dr. Mindaugas Karčiauskas (Center for Physical Sciences and Technology, Natural Sciences, Physics – N 002)
Dr. Romualdas Kisielius (Vilnius University, Natural Sciences, Physics – N 002)
Habil. Dr. Tamara Mishenina (I. I. Mechnikov Odessa National University, Natural sciences, Physics – N 002)
Dr. Kastytis Zubovas (Center for Physical Sciences and Technology, Natural Sciences, Physics – N 002)

The dissertation shall be defended at a public meeting of the Dissertation Defense Panel at 14:00 on 19th December 2024 in Room B128 at National Centre of Physical and Technological Sciences.
Address: Saulėtekio av. 3, LT–10257, Vilnius, Lithuania.
Tel. +370 5 2234637; e-mail: tfai@tfai.vu.lt.

The text of this dissertation can be accessed at the libraries of Vilnius University and Center for Physical Sciences and Technology, as well as on the website of Vilnius University:
https://www.vu.lt/naujienos/ivykiu-kalendorius.

https://doi.org/10.15388/vu.thesis.706
https://orcid.org/0000-0002-0632-8758

VILNIAUS UNIVERSITETAS
FIZINIŲ IR TECHNOLOGIJOS MOKSLŲ CENTRAS

Edgaras Kolomiecas

Galaktikos kamuolinio žvaigždžių spiečiaus 47 Tukano cheminė raida

DAKTARO DISERTACIJA

Gamtos mokslai,
Fizika (N 002)

VILNIUS 2025

Disertacija rengta 2016–2023 metais Vilniaus universitete, Teorinės fizikos ir astronomijos institute.

Mokslinis vadovas:
prof. dr. Arūnas Kučinskas (Vilniaus universitetas, gamtos mokslai, fizika, N 002)

Gynimo taryba:

Pirmininkas – prof. dr. Vladas Vansevičius (Fizinių ir technologijos mokslų centras, gamtos mokslai, fizika, N 002)

Nariai:
dr. Mindaugas Karčiauskas (Fizinių ir technologijos mokslų centras, gamtos mokslai, fizika, N 002)
dr. Romualdas Kisielius (Vilniaus universitetas, gamtos mokslai, fizika, N 002)
habil. dr. Tamara Mishenina (I. I. Mechnikov Odessa National University, gamtos mokslai, fizika – N 002)
dr. Kastytis Zubovas (Fizinių ir technologijos mokslų centras, gamtos mokslai, fizika, N 002)

Disertacija ginama viešame Gynimo tarybos posėdyje 2024 m. gruodžio mėn. 19 d. 14:00 val. Nacionalinio Fizinių ir technologijos mokslų centro B128 kabinete.
Adresas: Saulėtekio al. 3, LT-10257, Vilnius, Lietuva.
Tel. +370 5 2234637.

Disertaciją galima peržiūrėti Vilniaus universiteto bei Fizinių ir technologijos mokslų centro bibliotekose ir VU interneto svetainėje adresu: https://www.vu.lt/naujienos/ivykiu-kalendorius.

CONTENTS

LIST OF ABBREVIATIONS

1D	one-dimensional
3D	three-dimensional
1P	Galactic globular clusters first population stars
2P	Galactic globular clusters second population stars
47 Tuc	Galactic globular cluster 47 Tucanae (NGC 104)
AGB	asymptotic giant branch
CMD	color-magnitude diagram
EW	equivalent width
FRMS	fast-rotating massive stars
GGC	Galactic globular cluster
HB	horizontal branch
hs	heavy s-process elements
ls	light s-process elements
LTE	local thermodynamic equilibrium
MPs	multiple stellar populations
MS	main sequence
NLTE	non-local thermodynamic equilibrium
RGB	red giant branch
RHB	red horizontal branch
SGB	subgiant branch

INTRODUCTION

Galactic globular clusters (GGCs) are massive (10^4–10^6 $M_\odot$), compact objects with a typical half-light radius of approximately 4 pc, and are ancient, generally with ages exceeding 10 Gyr. Predominantly situated in the Galactic halo and thick disk, they span a range of metallicities ($-2.5 <$ [Fe/H] < 0.0), with the majority of them being metal-poor.

Historically, GGCs were believed to be homogeneous objects, consisting of stars uniform in age and chemical composition. However, research conducted over the past two decades has shown that GGCs are actually conglomerates of stars that do not share identical chemical compositions and likely originated from distinct star formation episodes (e.g., Bastian & Lardo 2018).

The evidence for the existence of multiple stellar populations (MPs) within GGCs can be found by studying chemical abundances of light elements such as C, N, O, Na, and Mg in GGC stars. More than half of GGC stars belong to a second population, characterized by a peculiar chemical composition unique to GGC stars and not found in the Galactic halo. The remaining stars have chemical composition that is typical of the halo stars of similar metallicity (Gratton et al. 2019). Further compelling evidence of MPs is derived from precise photometry, which uncovers complex color-magnitude diagrams (CMDs). Furthermore, using photometric bands that cover CH, CN, NH absorption features in stellar spectra, evolutionary sequences in CMD can be seen to split into multiple separate sequences. Later it was shown that stars in one sequence are enriched in the abundances of light chemical elements (e.g. He, Na, Al) when compared with the other sequence (Milone et al. 2012).

The detection of chemical abundance inhomogeneities in GGC stars dates back approximately 50 years, initially observed as variations in the strengths of CH, CN, and NH absorption features in stellar spectra across stars of the same evolutionary phase (Osborn 1971). These variations result from star-to-star differences in C and N chemical abundances. The results of recent detailed spectroscopic analyses have shown that nearly all GGCs exhibit variation in the abundances of other light chemical elements (e.g. Li, Na, Al), with abundance spreads reaching up to 1 dex (Charbonnel 2016). Notably, these elements display correlations (e.g. C–O, N–Na, Na–Al, Mg–O) and anti-correlations (e.g. N–C, Na–O, Al–Mg). While GGCs generally seem to be homogeneous concerning n-capture chemical elements, exceptions exist in certain GGCs (Type II clusters) where variations in s-process abundances are found along with variations in CNO and p-capture elements. Unlike typical GGCs (Type I), Type II clusters also exhibit a spread in metallicity (Marino et al. 2019).

Additionally, studies carried out during the last decade have revealed differences in the kinematic properties of stars from different populations. Light

chemical elements display radial dependencies, with second-population stars appearing more centrally concentrated. Moreover, possible variations in absolute radial velocities have been observed between the different stellar populations in the GGCs (Richer et al. 2013; Kučinskas et al. 2014).

This observational evidence supports the idea that GGCs may consist of two or more generations of stars. The second generation (2P) is believed to have formed from material enriched by the ejecta of the first-generation stars (1P), possibly consisting of "primordial" stars, so called polluters. The first generation stars exhibit chemical abundances similar to Galactic halo stars at comparable metallicity. Conversely, the second-generation, or enriched stars, are characterized by enhanced N, Na abundances and depleted C, O abundances relative to field stars of the same metallicity.

A number of evolutionary scenarios of the GGCs have been proposed in order to explain the observed chemical and kinematic trends, for example, pollution by massive asymptotic giant branch stars (AGBs). The temperature within these stars is high enough for the production of elements up to Al. Moreover, these stars, through their slow stellar winds, could distribute this processed material within the cluster, enabling the formation of 2P stars (D'Antona et al. 2016).

An alternative scenario proposes fast-rotating massive stars (FRMS) as the polluters, instead of AGB stars (Krause et al. 2013). During their main sequence (MS) phase, these massive stars undergo core hydrogen burning, reaching temperatures sufficient for Na production, thereby contributing to the enriched material necessary for the formation of a second star generation. Rotationally induced mixing brings enriched material to the surface of such star and because of the rapid rotation this material is then released to the intra-cluster space (Krause et al. 2013).

There also other possible GGC evolutionary scenarios proposed, such as enrichment by massive binaries or early disc accretion scenario (de Mink et al. 2009; Bastian et al. 2013).

Unfortunately, none of the proposed scenarios are able to explain all observed chemical and kinematic properties of GGC populations simultaneously. In many cases abundance analysis was done on a relatively small number of stars leading to inconclusive results, moreover, the analysis linking kinematic properties and abundances of different stellar generations is very limited.

In order to determine which polluters were most likely to enrich the intra-cluster medium during the early stages of GGC formation, one may look at the abundances of s-process elements. AGB stars are known to produce s-process elements in quantities differing from those produced by FRMS (see e.g. Prantzos et al. 2018). Hence, analyzing the abundance correlations between various s-process and light elements could help us identify the types of stars that polluted the intra-cluster medium in the early stages of GGC evolution. A study of

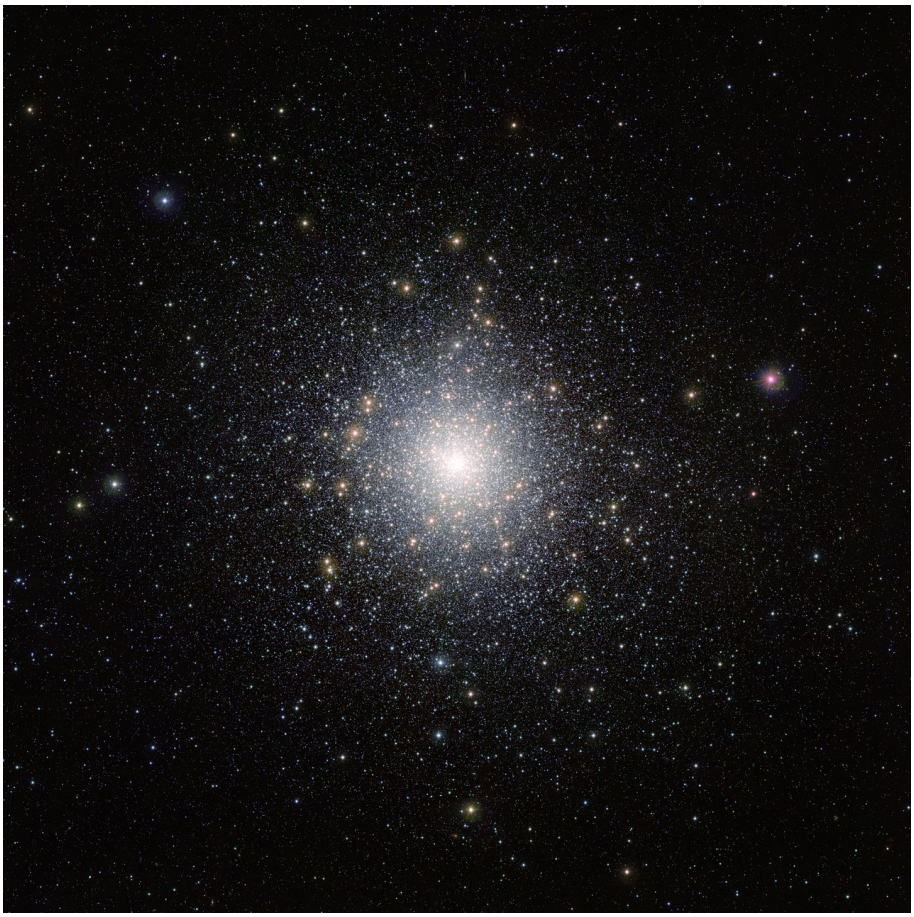

Fig. 1. Galactic globular cluster 47 Tucanae (NGC 104). Credit: ESO/M.-R. Cioni/VISTA Magellanic Cloud survey. Acknowledgment: Cambridge Astronomical Survey Unit.

Gratton et al. (2013) hinted at a possible correlation between the abundances of Na and Ba in the globular cluster 47 Tucanae, which is also known as 47 Tuc or NGC 104 (Fig. 1). To investigate whether similar correlations exist for other s-process elements (such as e.g. Sr, Zr), we determined the abundances of these elements in the atmospheres of RGB stars in 47 Tuc. Additionally, abundances of Na were determined as well. Importantly, studies of Sr and Zr abundances in GGCs have been quite limited to date, making the results inconclusive, not just for 47 Tuc but for other GGCs as well (see e.g. James et al. 2004; Thygesen et al. 2014).

We chose to study 47 Tuc for the following reasons. Over the past two decades, it has been established that this cluster hosts multiple stellar populations that have different light element abundances (e.g. He, O, Na; D'Orazi et al. 2010; Milone et al. 2012). Subsequent research has revealed that both

the SGB and MS split into sequences differing in light element compositions (Anderson et al. 2009; Milone et al. 2012). Studies linking the kinematics and abundances of cluster stars discovered anisotropic proper motions among the bluest MS stars, whereas the reddest stars did not exhibit such anisotropy. Moreover, it was found that 1P stars exhibit higher radial velocity values than their 2P counterparts, and correlations between certain light element abundances (Li, O, Na) and distance from the cluster center were observed (Richer et al. 2013; Kučinskas et al. 2014). These results show that the 47 Tuc is most likely not fully relaxed, stars belonging to different populations may not be well kinematically mixed, which makes it a very good target to study the differences in their chemical and kinematical properties.

The objective of the thesis

The goal of the dissertation is to determine abundances of Na, Sr, Zr, Ba in the atmospheres of the RGB stars in the Galactic globular cluster 47 Tuc and to investigate the possible relations between the chemical and kinematical properties of the stars of this cluster.

The main tasks of the thesis

- Determine abundances of Na, Sr, Zr in the atmospheres of RGB stars in the Galactic globular cluster 47 Tuc using 1D hydrostatic stellar atmosphere models, 1D LTE/NLTE spectral synthesis, and equivalent width abundance determination methodology.
- Compute the 1D NLTE abundance corrections for Na and investigate the influence of NLTE effects on the formation of Na I spectral lines, and determine Na abundances in the samples of investigated RGB stars in 47 Tuc.
- Investigate possible correlations/anti-correlations between the abundances of Na, Sr, Zr, Ba and between chemical and kinematical properties of the 1P and 2P stars in the Galactic globular cluster 47 Tuc.

Results and statements to defend

1. The mean 1D LTE strontium-to-iron and zirconium-to-iron ratios obtained in the atmospheres of RGB stars in Galactic globular cluster 47 Tuc are $\langle[\mathrm{Sr/Fe}]\rangle = 0.18 \pm 0.08$ dex (31 stars), $\langle[\mathrm{Zr/Fe}]\rangle = 0.35 \pm 0.09$ dex (237 stars).
2. 1D NLTE abundances of Na were determined in the atmospheres of 261 RGB stars in the Galactic globular cluster 47 Tuc. The obtained mean abundance ratio is $\langle[\mathrm{Na/Fe}]\rangle = 0.41 \pm 0.16$ dex.
3. The obtained 1D NLTE abundance corrections for the Na I $\lambda = 615.4225$ nm and Na I $\lambda = 616.0747$ nm lines are in the ranges of -0.19 to -0.07 dex, and -0.27 to -0.08 dex, respectively.
4. Using Ba abundance measurements in a sample of 261 RGB stars in 47 Tuc, it was determined that the second population stars in this cluster are not enriched in Ba.
5. There is a statistically significant correlation in the [Zr/Fe]–[Na/Fe] plane. In addition, there is a statistically significant anti-correlation in the [Zr/Fe]–r/r_{h} plane.

Practical and scientific novelty

- Homogeneous analysis of Zr abundance has been performed in a largest sample of stars in any Galactic globular cluster up to date. The analysis led to the detection of a statistically significant correlation between abundances of Zr and Na. The analysis also revealed the existence of anti-correlation between Zr abundance and radial distance from the cluster center.

- For the first time abundance of Sr was determined in the atmospheres of RGB stars in the Galactic globular cluster 47 Tuc. We detected a weak correlation between Sr and Na abundances.

- A correlation between light s-process element Zr and the light element Na, as well as anti-correlation between Zr abundance and distance from the cluster center, was detected for the first time in Galactic globular cluster stars. A correlation between light s-process element Sr and the light element Na was detected for the first time in Galactic globular cluster stars.

Contribution of the author

The author performed the reduction of the observed stellar spectra and computed 1D hydrostatic model atmospheres for all analysed stars in the Galactic globular cluster 47 Tuc and determined microturbulence velocities for half of the analysed star sample. The author measured equivalent widths of Zr spectral lines which were then further used to derive the abundances of Zr in 47 Tuc. The author performed 1D NLTE spectral synthesis and determination of Na abundance in the atmospheres of the analysed RGB stars in 47 Tuc, performed 1D LTE spectral synthesis and determination of Sr abundance in the atmospheres of RGB stars in 47 Tuc; he also performed 1D LTE spectral synthesis and determination of Zr abundance from Zr II spectral lines in the atmospheres of RGB stars in 47 Tuc. The author also determined Fe abundances and obtained radial velocities and full spatial velocities for the analysed stellar sample. The author together with co-authors performed the statistical analysis of the data obtained from the Na, Sr, and Zr study, including an examination of possible relations between abundances of Na, Sr, and Zr chemical elements, and also between abundances of these elements and kinematical properties of 47 Tuc stars. The author performed the analysis and comparison of the abundance ratios of s-process elements in globular cluster 47 Tuc to the predicted nucleosynthesis yields of AGB and massive star models.

1. Methodology of determining chemical element abundances

Analysis of stellar populations in the GGCs that was performed in this Thesis relied on the determination of chemical element abundances in the atmospheres of cluster stars. These abundances were obtained by analysing spectral lines in the observed stellar spectra with the aid of stellar model atmospheres. Therefore, the accuracy and reliability of abundance determinations was directly influenced by the accuracy of physics that was used in stellar model atmospheres.

The two most widely used types of stellar model atmospheres are the classical one-dimensional (1D) hydrostatic models and the state-of-the-art three-dimensional (3D) hydrodynamic models. Classical 1D models are assumed to be hydrostatic and under convective equilibrium, with either plane-parallel or spherically-symmetric geometry. Thermodynamic quantities used to calculate such models are horizontally homogeneous. However, real stellar atmospheres are neither static nor homogeneous. Classical 1D models fail to reproduce dynamic phenomena such as convection or shock waves, nor can they account for horizontal inhomogeneities. It has been confirmed that these limitations may significantly affect the formation of spectral lines, thereby impacting the precision of abundance determinations (see e.g. Caffau & Ludwig 2007; Collet et al. 2007; Dobrovolskas et al. 2013). In this study, we employ classical 1D hydrostatic models: `ATLAS9` (Kurucz 1993), `LHD` (Caffau & Ludwig 2007); as well as 3D hydrodynamic `CO`^{5}`BOLD` models (Freytag et al. 2012).

The next step in abundance analysis after the computation of stellar model atmospheres is the synthesis of synthetic spectra, which are then compared with observed spectra to derive the abundances of the analysed chemical elements. Spectral synthesis contains several steps, including solving the radiative transfer problem, determining the number densities of absorbing chemical species, treatment of line broadening processes, and accounting for line Doppler shifts. For the calculations of spectral synthesis in this work, three different spectral synthesis codes were utilized: `SYNTHE` (Kurucz & Furenlid 1979), which was used for calculating synthetic spectra under the assumption of local thermodynamic equilibrium (LTE) using classical 1D model atmospheres; `MULTI` (Carlsson 1986; Korotin et al. 1999), which was used to synthesize spectral line profiles of a given chemical element under the assumption of non-local thermodynamic equilibrium (NLTE) and using classical 1D model atmospheres; and `Linfor3D` which solves radiation transfer equations in 3Dunder the assumption of LTE.

1.1.1. 1D hydrostatic ATLAS9 stellar model atmosphere code

The ATLAS9 code developed by Robert Kurucz in the early 1970s and continuously updated since, is one of the most widely utilized codes for calculating 1D stellar model atmospheres (Kurucz 1993). These models are computed under the assumption of LTE, implying that the gas properties are influenced solely by the immediate surroundings that are in local thermodynamic equilibrium. Within the model, atomic abundances are pre-defined and remain constant across the atmosphere, with both radiative and convective energy fluxes being constant with depth. The assumptions include plane-parallel geometry, horizontal homogeneity of thermodynamic parameters, and an atmosphere in a static state. The ATLAS9 model atmosphere is defined by three primary parameters (atmospheric parameters): effective temperature, surface gravity, and metallicity (an abundance scaling factor applied to all chemical species).

In the ATLAS9 models, opacity is determined using Opacity Distribution Functions (ODFs), which sample line opacity at 337 wavelength points. The model atmosphere is divided into 72 layers, where the mean Rosseland opacity, $\tau_{\rm Ross}$, ranges from $\tau_{\rm Ross} = -6.875$ in the outermost layer to $\tau_{\rm Ross} = +2.00$ in the innermost layer, with a step of $\Delta \log \tau_{\rm Ross} = 0.125$. To compute a new stellar model atmosphere, the ATLAS9 code requires a starting model from an existing stellar model atmosphere grid. The temperature profile from this starting model serves as a reference: temperatures of the layers are adjusted until the total flux, F, equals the preset value of $F = \sigma T_{\rm eff}^4$, where $T_{\rm eff}$ denotes the effective temperature of the desired model and $\sigma = 5.67 \times 10^{-8} {\rm Wm}^{-2}{\rm K}^{-4}$ is the Stefan-Boltzmann constant. Convergence of the model computation is assumed when the flux error is less than 1% and the flux derivative is less than 10% in every atmospheric layer.

The Mixing-Length Theory (MLT), as proposed by Böhm-Vitense (1958), is used for calculating convective energy transfer. According to this theory, a convective bubble within the stellar atmosphere ascends a distance l before merging with its surroundings and releasing its energy. This distance is defined as $l = \alpha_{\rm MLT} H_{\rm p}$, here $H_{\rm p}$ is the pressure scale height and $\alpha_{\rm MLT}$ the mixing-length parameter.

In this study, we utilized ODFNEW opacity tables from Castelli & Kurucz (2003). The enhancement factor for all α-elements (C, O, Ne, Mg, Si, S, Ar, Ca, Ti) was set to a constant +0.4 dex, and the mixing-length parameter, $\alpha_{\rm MLT}$, was set to 1.25.

1.1.2. 1D hydrostatic LHD stellar model atmosphere code

LHD is another code for calculating 1D hydrostatic stellar model atmospheres,

which is based on a plane-parallel geometry (Caffau & Ludwig 2007). Analogous to ATLAS9, the LHD model atmospheres are characterized by three fundamental parameters: effective temperature, surface gravity, and chemical composition. The convective flux within these models is determined using the MLT, following the formulation proposed by Mihalas (1978). Similar to the ATLAS9 code, the mixing length parameter, α_{MLT}, is a variable that must be defined in advance; for the computation of LHD models in this study, α_{MLT} was set to 1.00.

A key advantage of utilizing LHD model atmospheres over ATLAS9 is that it uses the same input data (equation of state, opacity tables) as the 3D hydrodynamic CO^{5}BOLD model atmospheres (refer to section 1.1.3). This allows a differential comparison between synthetic spectral lines calculated using 3D hydrodynamic models (CO^{5}BOLD) and those calculated with 1D hydrostatic models (LHD). Such comparison allows us to assess the impact of convection on spectral line formation without the results being influenced by discrepancies in the equation of state or opacity tables used. In our study, 1D hydrostatic LHD model atmospheres were employed to investigate the effect of convection on the formation of Sr lines.

1.1.3. 3D hydrodynamic CO^{5}BOLD stellar model atmosphere code

In this Thesis, the dynamic and inherently multidimensional nature of real stellar atmospheres was addressed through the explicit simulation of convection by solving equations of hydrodynamics and radiation transfer in three dimensions. Unlike the classic 1D stellar model atmospheres, 3D hydrodynamical models are computed assuming hydrostatic equilibrium and therefore are time-independent. From observations of the Sun it is evident that the surface of the star constantly changes with time and observed stellar granulation is a clear indication of convection, which significantly influences the formation of spectral lines and the outgoing radiation field by introducing vertical and horizontal inhomogeneities in various dynamic and thermodynamic quantities, thereby affecting determined chemical abundances. If one wants to better understand the connection between convection and spectral line formation, one has to simulate convection explicitly by solving equations of hydrodynamics and radiative transfer in three dimensions.

In our work we used the 3D hydrodynamic atmosphere model computation package CO^{5}BOLD (COnservative COde for the COmputation of COmpressible COnvection in a BOx of L Dimensions, L = 2, 3; Freytag et al. 2012). This code enables the solution of coupled non-linear equations of compressible hydrodynamics in an external gravitational field alongside the radiative transfer equation. The hydrodynamic component comprises equations for mass conservation, momentum conservation, and energy conservation

$$\frac{\partial \rho}{\partial t} + \frac{\partial \rho v_x}{\partial x} + \frac{\partial \rho v_y}{\partial y} + \frac{\partial \rho v_z}{\partial z} = 0,$$

$$\frac{\partial}{\partial t}\rho \begin{pmatrix} v_x \\ v_y \\ v_z \end{pmatrix} + \frac{\partial}{\partial x}\rho \begin{pmatrix} v_x v_x + P \\ v_y v_x \\ v_z v_x \end{pmatrix} + \frac{\partial}{\partial y}\rho \begin{pmatrix} v_x v_y \\ v_y v_y + P \\ v_z v_y \end{pmatrix} + \frac{\partial}{\partial z}\rho \begin{pmatrix} v_x v_z \\ v_y v_z \\ v_z v_z + P \end{pmatrix} = \begin{pmatrix} 0 \\ 0 \\ -\rho g \end{pmatrix},$$

$$\frac{\partial \rho \epsilon_{\mathrm{ik}}}{\partial t} + \frac{\partial \left(\rho \epsilon_{\mathrm{ik}} + P\right) v_x}{\partial x} + \frac{\partial \left(\rho \epsilon_{\mathrm{ik}} + P\right) v_z}{\partial y} + \frac{\partial \left(\rho \epsilon_{\mathrm{ik}} + P\right) v_z}{\partial z} = -\rho g v_z,$$

here x, y, and z denote spatial coordinates, ρ represents density, v_n is the velocity component in direction i, P is pressure, g is gravitational acceleration, and ϵ_{ik} represents the total energy density per unit mass, including both internal and kinetic energy components. A precomputed equation of state is utilized to link internal energy, ρ, and P. The radiative transfer part utilizes monochromatic opacities from the `MARCS` stellar atmosphere package (Gustafsson et al. 2008), divided into six to twelve opacity bins to speed up the computation. This simplification allows the radiative transfer equation to be solved once per opacity bin rather than for millions of wavelength points, a method previously demonstrated to be good enough for calculating realistic 3D hydrodynamic model atmospheres (Nordlund 1982; Ludwig et al. 1994; Vögler et al. 2004).

The `CO`^{5}`BOLD` model atmospheres used in this study are configured using a "box-in-a-star" setup, meaning the modeled stellar atmosphere segment is significantly smaller than the star itself. Cartesian geometry was used, with the box featuring open vertical boundaries (allowing matter and radiation to freely escape vertically) and periodic horizontal boundaries (permitting matter and radiation to re-enter the box from the opposite side upon exiting horizontally).

The structure of 3D model atmosphere (spatial distribution of various thermodynamic and hydrodynamic quantities) is calculated for a single instance of time, which is called a snapshot. When computing 3D model atmospheres with `CO`^{5}`BOLD`, typically, several hundred snapshots are generated. Due to the high computational demands of 3D spectral synthesis, a subset of 20 snapshots were selected for spectral synthesis, chosen to preserve the full ensemble's properties (e.g. average T_{eff}, mean velocity at optical depth unity, mean mass velocity profile, etc.). It has been shown previously that such a sample of snapshots represents the entire sample in terms of spectral line properties sufficiently well (Caffau et al. 2009; Ludwig et al. 2009).

For each selected snapshot, the average <3D> model atmosphere is also calculated, obtained by horizontally and temporally averaging the temperature and gas pressure on surfaces of equal Rosseland optical depth, thus obtaining a

1D model atmosphere that represents the mean properties of the 3D model. By comparing spectral lines and their properties calculated using <3D> model and the full 3D model, we can determine what impact horizontal inhomogeneities have on the process of spectral line formation.

1.2. Spectral synthesis

1.2.1. 1D LTE spectral synthesis package `SYNTHE`

Using the spectral synthesis code `SYNTHE`, one can generate synthetic spectra within a specified wavelength interval (Kurucz & Furenlid 1979). For the computation of synthetic spectra, `SYNTHE` requires an input file that includes a 1D LTE stellar model atmosphere (note that `SYNTHE` is not compatible with 3D model atmospheres), along with an atomic and molecular line list, which includes spectral line parameters such as line wavelengths, oscillator strengths, line excitation potentials, and line broadening parameters. Unless specified otherwise, all spectral line parameters utilized for chemical abundance determinations in this work were taken from the VALD3 (The Vienna Atomic Line Database; Ryabchikova et al. 2015) atomic line database. `SYNTHE` is compatible with various stellar model atmospheres, including `ATLAS9`, `MARCS`, `PHOENIX`.

Several simplifications are implemented in the computation of synthetic spectra using the `SYNTHE` spectral synthesis code. The stellar model atmospheres are assumed to be in local thermodynamic equilibrium, with the radiation field at any given point in the atmosphere characterized by the local temperature, T. The populations of atomic levels are determined by the Boltzmann equation. The fraction of an element in ionization state i relative to state $i+1$ is governed by the Saha equation. Additionally, the velocities of particles are characterized by a Maxwellian distribution.

1.2.2. 1D NLTE spectral synthesis package `MULTI`

When solving the equations of radiation transfer within stellar atmospheres, determining the level populations of an atom during a given transition is essential. Under the LTE approximation, atomic population levels are calculated using the Boltzmann-Saha equation. However, in an actual stellar atmosphere, level populations are influenced not only by the local physical conditions but also by the radiation field coming from distant parts of the atmosphere that are far away from the point at which those level populations were calculated. This describes the assumption of non-local thermodynamic equilibrium or NLTE. Consequently, the physical conditions in regions where spectral lines form may differ from those assumed under LTE. In the NLTE approximation, to calculate the population levels for each atomic level, a statistical equilibrium equation is solved. For an atom with multiple levels, this equation can be written as

$$n_{\rm i} \sum_{\rm j \neq i}^{n_{\rm l}} P_{\rm ij} - \sum_{\rm j \neq i}^{n_{\rm l}} n_{\rm j} P_{\rm ji} = 0, \tag{1.1}$$

here i, j are energy levels, $n_{\rm i}$, $n_{\rm j}$ denote the number density of atoms in those levels, $n_{\rm l}$ is the total number of considered atomic levels, and $P_{\rm ij}$ represents the total rate of atom transition from level i to level j, which consists of a sum of radiative ($R_{\rm ij}$) and collision transition ($C_{\rm ij}$) rates.

Once the level populations are known, it becomes possible to calculate NLTE–LTE departure coefficients for each considered atomic level. The coefficient is defined as $b_{\rm i} = \frac{n_{\rm i}}{n_{\rm i}^*}$, where $n_{\rm i}$ is the NLTE population and $n_{\rm i}^*$ is the LTE population of level i. These departure coefficients can then be utilized together with the radiation transfer equation to compute NLTE spectral line profiles.

In this Thesis, the `MULTI` code (Carlsson 1986), modified by (Korotin et al. 1999), was used to perform NLTE spectral line synthesis by solving the NLTE radiative transfer problem in plane-parallel 1D stellar model atmospheres. `MULTI` requires a model atom for a given chemical species. The model atom includes details about atomic levels, their distribution across different ionization stages, atomic level energies, excitation and ionization probabilities, ionization cross-sections, etc. The modified version of `MULTI` used in this study is capable of computing not only equivalent widths but also synthetic line profiles.

For NLTE sodium spectral line synthesis, the model atom was taken from Dobrovolskas et al. (2014). It consists of the ground level of Na II and 20 energy levels of Na I. To ensure accurate calculations for the doublet transitions at 589 nm, fine splitting of the 3p level was taken into account. In total, 46 bound-bound radiative transitions were accounted for in the level population number computations. Fixed radiative transition rates were used for other weak transitions, and photo-ionization rates were taken from TOPBASE (Cunto et al., 1993). Quantum mechanical collision cross-sections with hydrogen taken from Barklem et al. (2010) were utilized for the lowest 9 atomic levels of Na I, while for other levels, the classical Darwin formula was applied with a correction factor $S_{\rm H} = 1/3$ (Steenbock & Holweger, 1984). Electron collision cross-sections from Igenbergs et al. (2008) were used for transitions between the 8 lowest energy levels of Na I, with the formula of van Regemorter (1962) applied for the remaining allowed transitions and formula of Allen (1973) for forbidden transitions.

1.3. Determination of abundances of chemical elements

Throughout this Thesis, we utilize the conventional notation for astronomical abundances, which are expressed on a logarithmic scale relative to $N_{\rm H} = 10^{12}$ hydrogen atoms. This is defined as $A({\rm X}) = \log_{10}\,(N_{\rm X}/N_{\rm H}) + 12$, where $N_{\rm X}$

and $N_{\rm H}$ represent the number densities of element X and hydrogen, respectively. Furthermore, the element-to-element abundance ratio, [X/Y], is used to describe the ratio of concentrations of two elements relative to the same ratio observed in the Sun

$$[\mathrm{X/Y}] = \log_{10}\left(\frac{N_{\rm X}}{N_{\rm Y}}\right)_{\rm star} - \log_{10}\left(\frac{N_{\rm X}}{N_{\rm Y}}\right)_{\rm sun}. \tag{1.2}$$

In this work, a dual approach is adopted for determining the abundances of chemical elements: the equivalent width method and the spectral synthesis method. The equivalent width method is applied to weaker, unblended spectral lines. The equivalent width (EW) is the main parameter of a spectral line and is defined as

$$EW = \int_{\lambda_1}^{\lambda_2} \left(\frac{F_c - F_\lambda}{F_c}\right) d\lambda, \tag{1.3}$$

here F_c is the continuum flux, F_λ is the flux in the spectral line, and the integration is made over the entire width of the spectral line. The chemical abundance of a selected element is determined by employing curve-of-growth analysis: after measuring the equivalent width of the spectral line, one finds the computed theoretical equivalent width that matches the observed one.

The second method for determining chemical element abundance is the spectral synthesis method. This technique involves fitting a synthetic spectrum to the observed spectrum, adjusting the abundance of the chemical element in the synthetic spectra until the profile of the synthetic spectral line of interest aligns with the profile of the same spectral line in the observed spectrum. This method is preferred for stronger lines or lines that blend with the spectral lines of other chemical elements.

1.4. 3D–1D abundance corrections

3D−1D abundance corrections are used for determining the influence of convection on the formation of spectral lines. The 3D−1D abundance correction is defined as the difference in abundances, A(X), determined using 3D model atmosphere and a classic 1D model atmosphere at a particular equivalent width: $\Delta_{\rm 3D-1D} = A({\rm X})_{\rm 3D} - A({\rm X})_{\rm 1D}$ (Fig. 1.1; see. e.g. Caffau et al. 2011b; Dobrovolskas et al. 2013). The $\Delta_{\rm 3D-1D}$ abundance correction accounts for horizontal temperature inhomogeneities and different temperature stratifications that are caused by the convective motions. It is possible to study these 2 constituents separately: $\Delta_{\rm 3D-<3D>} = A({\rm X})_{\rm 3D} - A({\rm X})_{\rm <3D>}$ is the abundance correction arising from the horizontal temperature inhomogeneities and $\Delta_{\rm <3D>-1D} = A({\rm X})_{\rm <3D>} - A({\rm X})_{\rm 1D}$ is the abundance correction caused by the differences between the temperature profiles of the average <3D> and 1D stel-

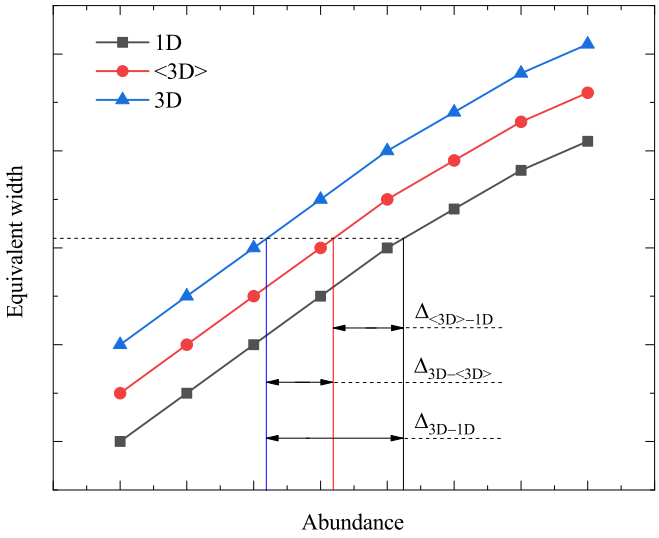

Fig. 1.1. A schematic depiction of 3D−1D abundance corrections. The three lines represent curves-of-growth that were calculated with identical atomic line parameters, but different types of stellar model atmospheres.

lar models. The full 3D−1D abundance correction then is the sum of the two: $\Delta_{\rm 3D-1D} = \Delta_{\rm 3D-<3D>} + \Delta_{\rm <3D>-1D}$.

2. Abundance of Zr in the atmospheres of RGB stars in the globular cluster 47 Tuc

2.1. Observational data

In this chapter, we present an analysis of Zr and Na abundances in 237 RGB stars in the GGC 47 Tuc. This the largest sample of stars for which abundances of Zr were determined in any globular cluster to date.

Galactic globular clusters, GGCs, are characterized by a spread in the abundances of light chemical elements (Carretta et al. 2009b). These abundance patterns show light element abundance correlations or anti-correlations that seem to be related to the cluster mass and metallicity (Bastian & Lardo 2018; Gratton et al. 2019). On the other hand, elements heavier than Fe are much less investigated and, generally, do not display significant variations beyond observational uncertainties.

This said, abundances of the s-process elements may provide additional information about the early chemical evolution of the GGCs. Theoretical models predict that light s-process elements (e.g. Sr, Y, Zr) are produced in high-mass (5–8 $M_{\odot}$) AGB stars and/or in other stars more massive than 9 $M_{\odot}$(e.g. Shingles et al. 2014), whereas heavy s-process elements (e.g. Ba, La) originate from lower mass ($< 5\ M_{\odot}$) AGB stars. Therefore, detecting a correlation between the abundances of light s-process elements (e.g. Zr) and light elements (e.g. Na) could provide insights into the nature of the polluter stars. An earlier study tentatively suggested a correlation between Na and Ba abundances in 47 Tuc (noting that Ba is a heavy s-process element primarily synthesized in low-mass AGB stars during the main s-process, Gratton et al. 2013). However, subsequent investigations of this cluster did not confirm such a correlation, neither for Ba nor for other s-process elements (e.g. Cordero et al. 2014; Thygesen et al. 2014). In general, analyses of s-process elements in 47 Tuc – and in most other GGCs – have been limited to relatively small samples of stars, hindering any robust assessments regarding abundance spreads and correlations and, thus, the identification of potential polluter stars.

In order to fill this gap, we determined the Zr abundance in 237 RGB stars in 47 Tuc. Zr, a light s-process element, is produced during the weak s-process. Importantly, the studies of Zr abundance in the GGCs have been very scarce until now and the results were inconclusive, i.e., not only for this but also for other GGCs.

Stellar spectra utilized for the abundance analysis were obtained using the `GIRAFFE` and `UVES` spectrographs mounted on the VLT UT2 telescope. These spectra were collected across three observational programs: 072.D-0777(A) (PI: François), 073.D-0211(A) (PI: Carretta), and 088.D-0026(A) (PI: McDonald),

Table 2.1. Summary of the spectroscopic data used in this work.

Programme	Date of observation	Setting	$\lambda_{\rm central}$, nm	R	Exposure, s	Stars #
072.D-0777(A)	2003-10-21	HR13	627.3	26400	1500	112
	2003-10-21	HR13	627.3	26400	3600	121
073.D-0211(A)	2004-07-07	HR13	627.3	22500	1600	113
088.D-0026(A)	2011-11-26	HR13	627.3	26400	3×700	113

subsequently retrieved from the ESO Advanced Data Products archive[1]. The signal-to-noise ratio (SNR) of the spectra typically ranged from 70 to 150 at 620 nm. A summary of the spectroscopic data used in this study is shown in Table 2.1. The sky spectrum, median-averaged from all dedicated sky fibers available, was subtracted from each observed stellar spectrum. In cases where multiple exposures of the same star were available, spectra from these exposures were summed to increase the SNR (e.g. several objects from program 088.D-0026(A)). Continuum normalization of all observed stellar spectra was performed using the `IRAF` task `splot`. We identified 14 stars common between the samples of 073.D-0211(A) and 088.D-0026(A), 22 stars between 072.D-0777(A) and 088.D-0026(A), and 22 stars between 072.D-0777(A) and 073.D-0211(A). The three samples have 5 stars in common (Table A.1), which were used to explore potential systematic shifts in the abundances derived from different datasets.

2.2. Radial velocities and proper motions of cluster stars

Radial velocities were determined using the cross-correlation technique with the `IRAF` task `fxcor`. We computed a synthetic spectrum with `SYNTHE`, utilizing the average atmospheric parameters of the observed stars ($T_{\rm eff}$ = 4500 K, $\log g$ = 1.90, [Fe/H] = −0.7, R = 22000) over the wavelength range λ = 612 - 640 nm, which served as a template for cross-correlation. The mean radial velocity obtained is $-17.4\,{\rm km\,s^{-1}}$, with a standard deviation (σ) of $7.9\,{\rm km\,s^{-1}}$and a typical measurement error for an individual star of $\pm 0.1\,{\rm km\,s^{-1}}$. Stars with radial velocities within $\pm 3\sigma$ of the mean cluster radial velocity were identified as cluster members.

Subsequently, we determined the full spatial velocities of the analyzed stars by combining the measured radial velocities with proper motions from the *Gaia* EDR3 catalog (Gaia Collaboration et al. 2021). The coordinates of the observed stars, taken from Bergbusch & Stetson (2009), were matched with the *Gaia* EDR3 catalog within a 1-arcsecond matching radius. The average proper motion of 47 Tuc ($\mu_{\rm RA} = 5.25\,{\rm mas\,yr^{-1}}$ and $\mu_{\rm DEC} = -2.53\,{\rm mas\,yr^{-1}}$)

[1] `http://archive.eso.org/wdb/wdb/adp/phase3_spectral/form`

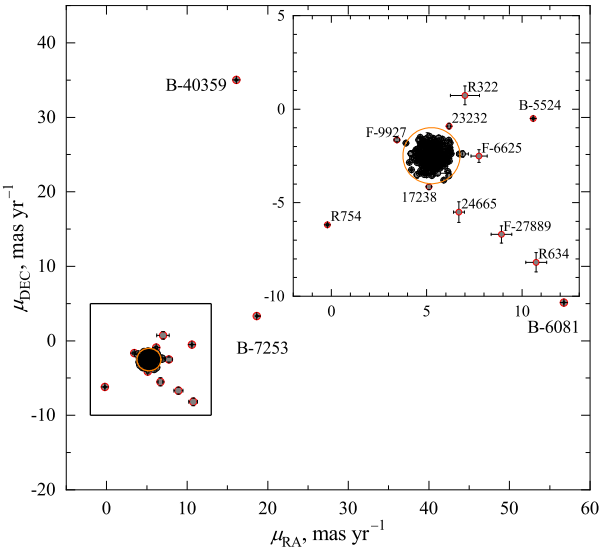

Fig. 2.1. Proper motions of the target RGB stars from the *Gaia* EDR3 catalog (Gaia Collaboration et al. 2021). Identifications of non-member stars are shown next to the symbols. The region that encloses motions falling within 1.5 mas yr^{-1} from the mean cluster proper motion is marked by an orange circle. Stars falling outside this region were rejected from the abundance analysis. Zoomed-in region marked by a square is shown in the top right corner.

was taken from Baumgardt et al. (2019), and the proper motions of individual stars were calculated relative to the cluster's average proper motion (i.e. proper motions were calculated for each star in the analyzed sample individually, but in relation to the average proper motion of 47 Tuc). Following Milone et al. (2018), stars whose proper motions deviated by less than 1.5 mas yr^{-1} from the cluster's average were designated as cluster members. A total of 13 stars were excluded from further analysis (Fig. 2.1).

Finally, we converted proper motions from angular units to km s^{-1}, assuming a distance of 4.5 kpc to the 47 Tuc globular cluster. The full spatial velocities were calculated by summing the radial and tangential (in the plane of the sky) velocities in quadratures.

2.3. Atmospheric parameters

We used a hybrid approach to determine the stellar atmospheric parameters. Effective temperature and surface gravity were derived from photometry, while the microturbulence velocity was obtained from the analysis of neutral Fe lines.

Photometric data from Bergbusch & Stetson (2009), along with the color-effective temperature calibrations by Ramírez & Meléndez (2005), were utilized to determine the effective temperatures of our target stars. Photometric data

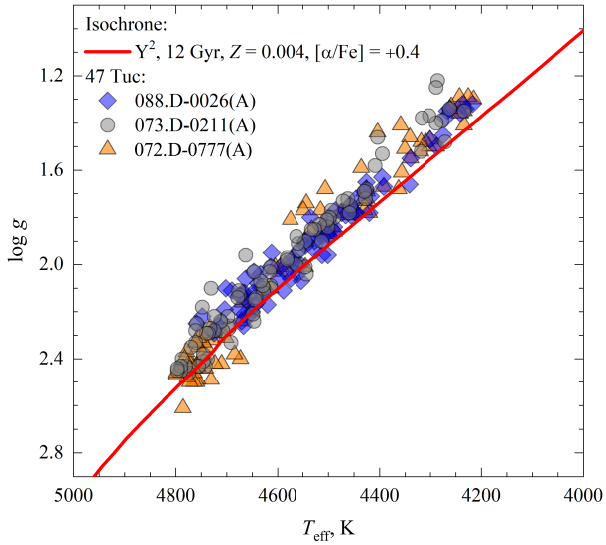

Fig. 2.2. Atmospheric parameters of the target RGB stars used in this work. Stars observed in different programmes are shown in different symbols and colors: orange triangles – 072.D-0777(A), grey circles – 073.D-0211(A), blue diamonds – 088.D-0026(A). The Yonsei-Yale isochrone of 12 Gyr and [M/H] = −0.68, and [α/Fe] = +0.4 is shown for comparison as red solid line (Kim et al. 2002).

was de-reddened using $E\,(B-V) = 0.04$ (Grundahl et al. 2002) and color excess ratio $E(V-I)/E(B-V) = 1.33$ (Bergbusch & Stetson 2009). In order to check the reliability of the obtained effective temperatures, we chose 111 RGB stars from 073.D-0211(A) sample and determined Fe abundances using 23 Fe I spectral lines and effective temperatures from photometry. The comparison yielded an excellent agreement between photometric and spectroscopic effective temperatures, with an average difference of $< 0.03 \pm 0.04$ dex/eV (the error here is 1σ uncertainty). Despite the availability of *Gaia* EDR3 photometry, we opted to use data from Bergbusch & Stetson (2009) to ensure consistency and homogeneity with our previous studies of 47 Tuc (e.g. Dobrovolskas et al. 2014; Černiauskas et al. 2017).

Surface gravities were calculated using the classic formula that relates stellar mass, luminosity, effective temperature, and surface gravity:

$$\log g = 4.44 + 4 \times \log(T_{\rm eff}/T_{\rm eff}^{\odot}) - \log(L/L_{\odot}) + \log(M/M_{\odot}), \qquad (2.1)$$

here $T_{\rm eff}^{\odot} = 5780$ K is the adopted effective temperature of the Sun, M is stellar mass, and L is stellar luminosity. An identical mass of 0.89 $M_{\odot}$ was assumed

for all target stars, based on the Yonsei-Yale isochrone[2] of 12 Gyr and a total metallicity of [M/H] = −0.68. The relation between bolometric correction, effective temperature, and metallicity from Alonso et al. (1999) was employed to calculate stellar luminosity. Although there were 4 Fe II lines in the wavelength range of the observed spectra, it was not possible to use spectroscopic gravities, because it was only possible to reliably determine equivalent widths for ∼2 Fe II lines, which is not enough for reliable surface gravity estimation. Nonetheless, the agreement within 0.01 dex between Fe abundances derived from Fe I and Fe II lines, and the maximum discrepancy of 0.01 dex in any specific star, confirms that the surface gravities determined from photometry and ionization balance condition agree well. The effective temperatures and surface gravities for all 237 target stars are shown in Fig. 2.2.

Microturbulence velocities, $\xi_{\rm micro}$, were determined iteratively for each star by ensuring a zero trend between Fe abundance and equivalent width, using the `splot` task in `IRAF` for all Fe lines. Only unblended lines were considered, and strong lines (EW > 150 mÅ) were excluded due to their reduced sensitivity to microturbulence velocity changes. The determined $\xi_{\rm micro}$ values for the target stars are shown in Fig. 2.3.

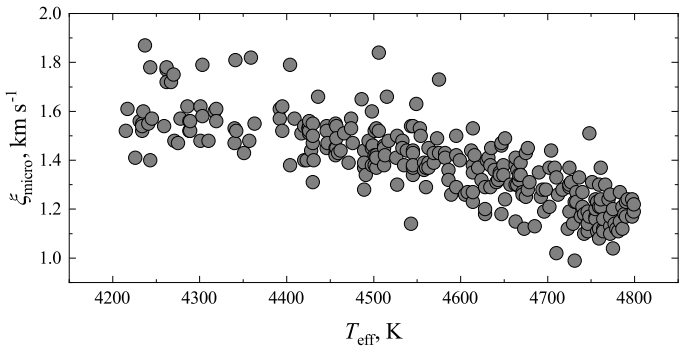

Fig. 2.3. Microturbulence velocity of the target stars, $\xi_{\rm micro}$, plotted versus their effective temperature, $T_{\rm eff}$.

2.4. The complete sample of RGB stars for the abundance analysis

In the 072.D-0777(A) sample, we excluded 36 HB and AGB stars after a visual inspection of the $T_{\rm eff} - \log g$ diagram. For the 073.D-0211(A) and 088.D-0026(A) samples, we excluded 1 HB and 4 HB stars, respectively. The identification of common stars across all programs was achieved through a cross-match of the equatorial coordinates of all observed stars. Based on kinematic analysis, 12 stars were rejected from further investigation (Sect. 2.2). After eliminating

[2]Version 2 from http://www.astro.yale.edu/demarque/yyiso.html

likely non-members based on kinematic criteria, we further narrowed our target sample to stars within the effective temperature range of $4200 \leq T_{\rm eff} \leq 4800\,{\rm K}$ (see Sect. 2.5 below). This restriction was done in order to minimize the impact of uncertainties on the abundances determined at the extremities of the $T_{\rm eff}$ range. Consequently, the final sample for Zr and Na abundance analysis consisted of 237 RGB stars.

2.5. Abundance analysis

Elemental abundances were determined using 1D hydrostatic `ATLAS9` model atmospheres, with an enhancement in the α-element abundances (O, Ne, Mg, Si, S, Ar, Ca, Ti) by $\alpha/{\rm Fe} = +0.4$. In cases when spectra of target stars were taken from multiple observing programs, abundances of Fe, Na, and Zr were determined from each individual spectrum, and averaged abundances were utilized for further analysis. The equivalent width method was used to determine abundances of Fe and Zr, whereas Na abundances were obtained through spectral line synthesis. The atomic parameters of the spectral lines were taken from the VALD3 database (Ryabchikova et al. 2015).

The selection of stars for the abundance analysis was constrained to those with effective temperatures within the range $4200 \leq T_{\rm eff} \leq 4800\,{\rm K}$. This criterion was established because: (a) uncertainties in determining the continuum and potential influences of molecular blends are amplified at lower temperatures, leading to increased errors in Zr abundance estimations; (b) at higher temperatures, uncertainties in Zr abundances grow significantly due to the diminishing strength of Zr I lines; and (c) at higher $T_{\rm eff}$, Zr I lines become too weak to detect in stars with the lowest Zr abundance.

2.5.1. Reference abundances in the Sun and Arcturus

The original Kurucz software package (`ATLAS9`, `WIDTH9`, `SYNTHE`) uses an outdated value for the ionization energy of Zr, set at 6.84 eV. We changed it to 6.634 eV (Hackett et al. 1986), and all further analysis was done with this revised value. This adjustment resulted in a systematic increase in Zr abundance of +0.25 to +0.29 dex for 47 Tuc stars, varying slightly with effective temperature. Specifically, at an effective temperature of 4200 K, the abundance adjustment was +0.29 dex, while at 4800 K, it was +0.25 dex.

Reference abundances for the Sun and Arcturus were determined using the Kitt Peak Solar Flux Atlas (Kurucz et al. 1984) and the Visible and Near Infrared Atlas of the Arcturus Spectrum, 3727-9300 Å (Hinkle et al. 2000), respectively. Fe abundances were determined using the equivalent width method. For the Sun, equivalent widths were measured using a Voigt function, while for Arcturus, Gaussian function was employed to fit the line profiles. The Fe I

line list utilized for abundance determinations is listed in Table B.1. Oscillator strength data for these lines were taken from the VALD3 database.

The model atmosphere for Arcturus was calculated using the `ATLAS9` model atmosphere package, with $T_{\rm eff} = 4286\,{\rm K}$ and $\log g = 1.66$ from Ramírez & Allende Prieto (2011), taking the solar-scaled chemical composition from Asplund et al. (2005) and an α-element enhancement of $+0.4\,{\rm dex}$.

For the Sun, the microturbulence velocity, $\xi_{\rm micro} = 0.93\,{\rm km\,s^{-1}}$, was determined iteratively in order to ensure that no trend of Fe abundance with line strength arises, which agrees well with values found in other studies (0.9–$1.0\,{\rm km\,s^{-1}}$, e.g. Doyle et al. 2014). The average solar Fe abundance obtained using our determined microturbulence velocity is $A({\rm Fe})_{\odot} = 7.55{\pm}0.01$ ($\sigma = 0.06$), calculated from 29 lines with EW$< 105\,{\rm m\AA}$, which agrees well with the value of 7.52 ($\sigma = 0.06$) from Caffau et al. (2011b).

For Arcturus, we determined a microturbulence velocity of $\xi_{\rm micro} = 1.78\,{\rm km\,s^{-1}}$and an Fe abundance of $A({\rm Fe}) = 7.03 \pm 0.02$ ($\sigma = 0.09$) ([Fe/H] $= -0.52$), using 27 Fe I lines with $W < 160\,{\rm m\AA}$. These results are consistent with results from other studies (Ramírez & Allende Prieto 2011, Sheminova 2015).

The solar Na abundance, determined using the same methodology as for RGB stars, is $A({\rm Na})_{\odot} = 6.17$, which agrees well with $A({\rm Na})_{\odot} = 6.21 \pm 0.04$ from Scott et al. (2015). For Arcturus, Na abundance was determined in NLTE using the same lines and methodology as for the analysis of RGB stars in 47 Tuc, yielding identical Na abundances from both Na I lines, $A({\rm Na}) = 5.71$ or [Na/Fe] $= 0.06$. This is reasonably close to the NLTE estimate of $A({\rm Na}) = 5.80$ determined using a set of 14 Na I lines by Osorio et al. (2020). In LTE, we obtained A(Na) $= 5.85$, which agrees well with $A({\rm Na}) = 5.83{\pm}0.03$ determined by Ramírez & Allende Prieto (2011) using two Na I lines employed in our study (we note that, the LTE value from Osorio et al. 2020, $A({\rm Na}) = 5.91$, is higher than both our determination and that of Ramírez & Allende Prieto 2011).

As Zr I lines are too weak in the solar spectrum for reliable reference abundance determination, we used a Zr abundance in the Sun of $A({\rm Zr}) = 2.62$ taken from Caffau et al. (2011a).

Gaussian fits to the profiles of Zr I lines in the Arcturus spectrum yielded equivalent widths of 5.42 pm for the line at 612.7 nm, 4.97 pm for the line at 613.4 nm, and 5.39 pm for the line at 614.3 nm. Using the ATLAS9 model atmosphere computed with atmospheric parameters from Ramírez & Allende Prieto (2011), we obtained Zr abundances of $A({\rm Zr}) = 2.05$, 1.98, and 1.97 for the three lines, respectively. The averaged Zr abundance from the three lines is [Zr/Fe] $= -0.10$ ($\sigma = 0.04$), which is in reasonable agreement with the value obtained by Worley et al. (2009), [Zr/Fe] $= 0.01$ ($\sigma = 0.07$), determined from seven lines of neutral Zr.

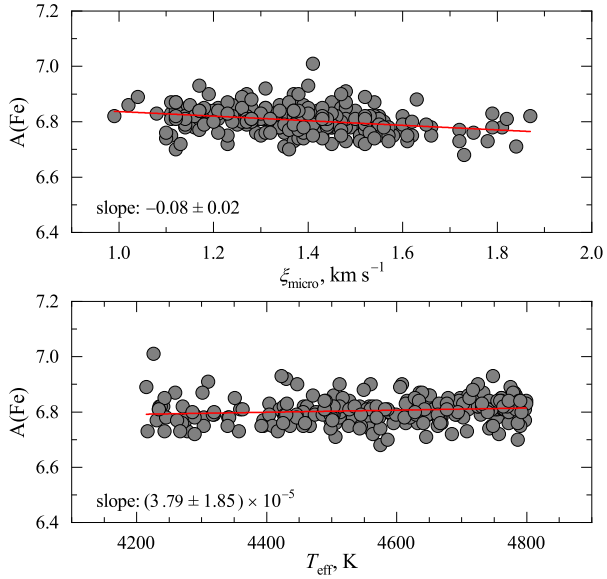

Fig. 2.4. Fe abundance plotted against microturbulence velocity (top panel) and effective temperature (bottom panel) for the investigated RGB stars in 47 Tuc.

2.5.2. Determination of Fe abundance in 47 Tuc

Local thermodynamic equilibrium was assumed in our analysis of Fe abundances, which were determined using the equivalent width method. Fe abundances for the target stars were determined from 17 to 28 Fe I lines situated within the wavelength range of 612.79 − 691.67 nm. The Fe I line list utilized in this analysis is provided in Table B.1. For our sample of 237 RGB stars, we found a mean Fe abundance of $\langle[\mathrm{Fe/H}]\rangle = -0.74 \pm 0.05$, where the error represents the standard deviation due to star-to-star abundance scatter. This value is very similar to those obtained in other studies, for instance, $[\mathrm{Fe/H}] = -0.74 \pm 0.05$ as reported by Carretta et al. (2009b) for 114 RGB stars, and $[\mathrm{Fe/H}] = -0.77 \pm 0.08$ by Wang et al. (2017) for 44 RGB stars.

The determined Fe abundances show minimal dependence on microturbulence velocity (ξ_{micro}) and effective temperature (T_{eff}), as shown in Fig. 2.4. Importantly, however, the discrepancy in average abundance between the most extreme ends of the effective temperature scale is less than 0.05 dex. Furthermore, no statistically significant differences were observed in the Fe abundances determined from spectra acquired during different observing programs (Fig. 2.5).

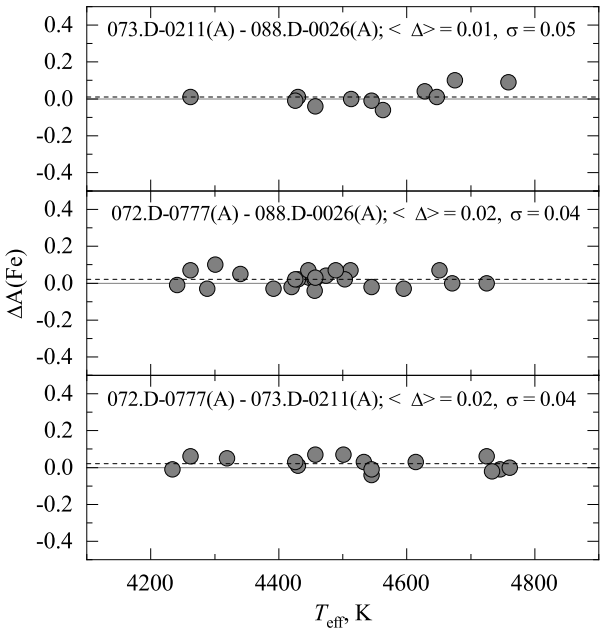

Fig. 2.5. Fe abundances in stars that are common to different observing programs used in this study. In each panel, the $\langle\Delta\rangle$ symbol denotes the mean difference between the average A(Fe) values obtained in different programmes.

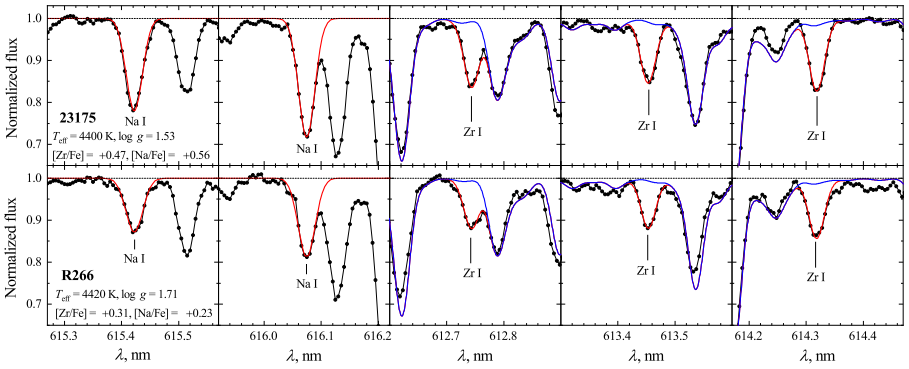

Fig. 2.6. Observed (dots) and best-fitted synthetic profiles of the Na I (NLTE) and Zr I (LTE) lines (red solid lines) in the GIRAFFE spectra of two RGB stars in 47 Tuc: Na-rich (2P, top row) and Na-poor (1P, bottom row). Identification numbers of each star, their atmospheric parameters, the determined Na and Zr abundances are provided in the leftmost panels of each row.

Table 2.2. Parameters of Na I and Zr I lines used in the abundance analysis.

Element	λ, nm	χ, eV	log gf	log γ_{rad}	log $\frac{\gamma_4}{N_e}$	log $\frac{\gamma_6}{N_H}$
Na I	615.4225	2.102	−1.547	7.85	−4.39	−7.28
Na I	616.0747	2.104	−1.246	7.85	−4.39	−7.28
Zr I	612.7475	0.154	−1.060	7.77	−5.69	−7.79
Zr I	613.4585	0.000	−1.277	7.77	−5.70	−7.79
Zr I	614.3252	0.071	−1.097	7.77	−5.69	−7.79

2.5.3. Determination of Na abundance in 47 Tuc

To determine Na abundances in target stars, we adopted a NLTE approach. Two Na I lines, located at 615.4225 and 616.0747 nm, were analyzed. For this analysis, we utilized the spectral synthesis code `MULTI` (Carlsson 1986; Korotin et al. 1999) together with `ATLAS9` model atmospheres. The model atom of Na used in this work was the same as that used in our earlier studies (e.g. Dobrovolskas et al. 2014). Here, we briefly describe the main information: the model atom comprises 20 levels in the neutral state and the ground state of ionized Na, with 46 radiative transitions calculated in detail. Collision rates with electrons and hydrogen were taken from Igenbergs et al. (2008) and Barklem et al. (2010), respectively. Line profiles calculated with `MULTI` were subsequently broadened using a Voigt profile to account for instrumental and macroturbulence broadening effects. Microturbulence velocities were individually determined for all stars in the sample. Abundances were then determined iteratively by varying Na abundance to achieve the best fit to the observed spectra. Several examples of these fits are illustrated in Fig. 2.6.

Discrepancies in Na abundances derived from the two Na I lines are small, typically less than 0.05 dex, as shown in Fig. 2.7. Additionally, we observed no statistically significant differences in Na abundances determined form the spectra taken from different observing programs (Fig. 2.8). There appears to be a slight dependency of Na abundance on $T_{\rm eff}$, although it remains below 0.1 dex. The determined Na abundances are listed in Table F.1, with the relationship between abundance and both microturbulence velocity and effective temperature shownin Fig. 2.9.

2.5.4. Determination of Zr abundance in 47 Tuc using Zr I lines

Equivalent widths of the three Zr I lines, as detailed in Table 2.2, were measured by fitting Gaussian profiles to the observed spectra using the `splot` task in `IRAF`. Several examples of typical best fits are illustrated in Fig. 2.6. The equivalent width for the 612.7475 nm line was determined using the `IRAF` task `deblend` to mitigate the influence of the Fe I 612.7906 nm blend, as shown in Fig. 2.10. The other Zr I lines do not have strong blends except for a weak CN

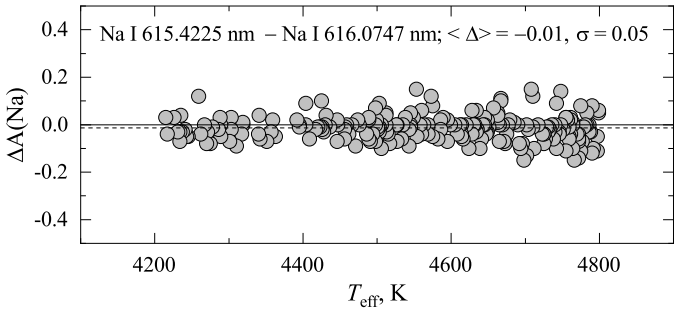

Fig. 2.7. Differences in Na abundances obtained from the two Na I spectral lines used in this work. The $\langle\Delta\rangle$ symbol denotes the mean difference between the A(Na) values obtained using different Na I lines.

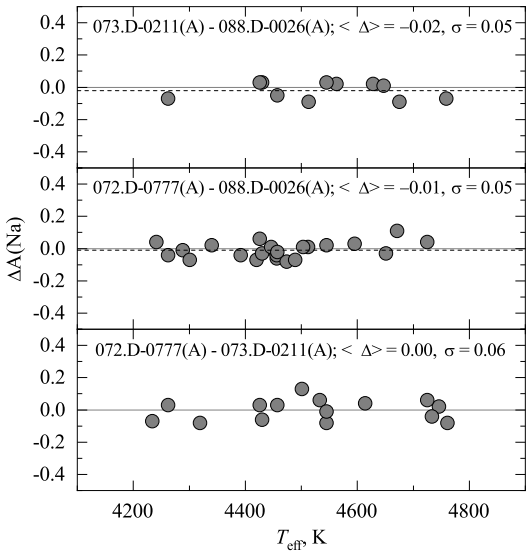

Fig. 2.8. Na abundances in stars that are common to different observing programs used in this study. In each panel, the $\langle\Delta\rangle$ symbol denotes the mean difference between the average A(Na) values obtained in different programs.

influence (detailed in Sect. 2.5.7). Stellar model atmospheres for all analyzed stars were computed with the Linux port of the `ATLAS9` code (more details are provided in Sect. 1.1.1). Zr 1D LTE abundances were determined using the Linux port of the `WIDTH9` package (Kurucz 1993; 2005a), averaging the measurements from all three Zr I lines.

For the abundance determination, we utilized the revised Zr I ionization energy of 6.634 eV (Hackett et al. 1986), as opposed to the default value of 6.840 eV used in the original versions of the Kurucz `ATLAS9`, `WIDTH9`, and `SYNTHE` packages. This adjustment resulted in a systematic shift in Zr abundance of +0.29 dex at $T_{\rm eff} = 4200$ K and +0.25 dex at $T_{\rm eff} = 4800$ K.

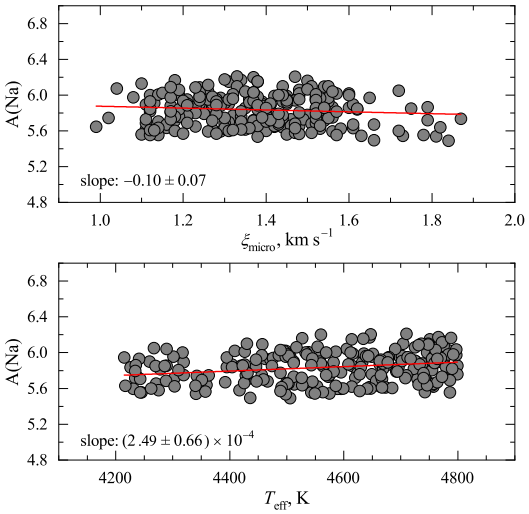

Fig. 2.9. The determined Na abundance, plotted versus microturbulence velocity (top panel) and effective temperature (bottom panel) of the target stars.

Table 2.3. Impact of hyperfine energy level splitting on the determination of Zr abundance from the Zr I lines used in this study.

	HFS		no-HFS		ΔA(Zr)
λ, nm	W, pm	A(Zr)	W, pm	A(Zr)	(HFS-noHFS)
		$T_{\rm eff} = 4320$ K			
612.7475	5.57	2.177	5.46	2.159	+0.018
613.4585	5.61	2.184	5.59	2.181	+0.003
614.3252	6.07	2.174	6.02	2.166	+0.008

The determined Zr abundances for each individual star are presented in Table F.1. The abundances determined from individual Zr I lines agree well, with the typical difference in abundance not exceeding 0.10 dex, as shown in Fig. 2.11. Additionally, we observed no statistically significant differences in Zr abundances when comparing spectra from various observing programs (Fig. 2.12). Furthermore, there are no significant trends between Zr abundance and microturbulence velocity or effective temperature, as shown in Fig. 2.13.

While determining Zr abundances, we did not account for the hyperfine structure splitting (HFS) of Zr I spectral lines. To evaluate its impact, we computed synthetic Zr I spectral lines using the `SYNTHE` package, both with and without HFS taken into account. For this analysis, we employed an `ATLAS9` model atmosphere with $T_{\rm eff} = 4320$ K, $\log g = 1.52$, $\xi_{\rm micro} = 1.56\,{\rm km\,s^{-1}}$, [Fe/H]$= -0.78$, and [$\alpha$/Fe]$= +0.4$. The effective temperature of the model atmosphere closely matches that of the 'coolest' stars in our sample ($T_{\rm eff} \approx$

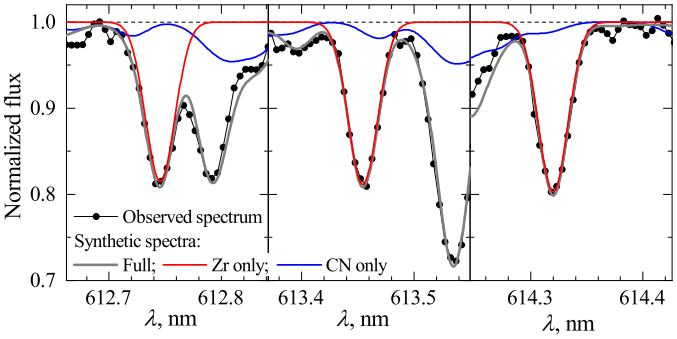

Fig. 2.10. Zr I lines in GIRAFFE spectrum of the target star 23821 (dots) overlaid with the synthetic spectrum (red solid line) computed using $T_{\rm eff}$ = 4404 K, $\log g$ = 1.46, [Fe/H] = −0.76, $\xi_{\rm micro}$ = 1.38 km s^{-1}, $\xi_{\rm macro}$ = 12.5 km s^{-1}. Left panel shows the environment of 612.7 nm Zr I line, middle panel of 613.4 nm line, and right panel of 614.3 nm line. Blue solid line shows synthetic spectrum with CN lines only.

4200 K). Given that Zr I lines are stronger in stars with lower $T_{\rm eff}$, one may anticipate more pronounced HFS-related effects at the lower end of the $T_{\rm eff}$ scale. All synthetic spectra were computed assuming a constant Zr abundance of A(Zr)= 2.16 for both HFS and non-HFS lines.

Line oscillator strengths for individual HFS components were taken from Thygesen et al. (2014), while for the non-HFS line profile computations, these components were added up for each Zr I line (Table 2.3). Upon computing the synthetic spectra, Zr I line equivalent widths were measured by fitting Gaussian profiles to the Zr I profiles in the synthetic spectra. Zr abundances were then determined using the WIDTH9 code with the obtained equivalent widths.

The results of this test, shown in Table 2.3, reveal that the largest abundance discrepancy is only +0.02 dex for the 612.7475 nm line, whereas for lines at 613.4585 and 614.3252 nm it is less than 0.01 dex. At higher $T_{\rm eff}$ values, the discrepancies diminish further due to the weaker Zr I lines. Consequently, we conclude that the Zr abundances determined in our study are unaffected by HFS.

In the 088.D-0026(A) sample, one star – 'R265' or 'Lee 4710' – is strongly enriched in s-process elements (Cordero et al. 2015). For this star, we identified a Zr abundance of [Zr/Fe] = 0.79 ± 0.15 (the error represents the standard deviation due to line-to-line abundance scatter), in a good agreement with the 0.83 ± 0.17 value reported by Cordero et al. (2015). The atmospheric parameters determined in both studies also agree very well: we obtained $T_{\rm eff}$ = 4452 K, $\log g$ = 1.82, $\xi_{\rm micro}$ = 1.55 km s^{-1}, and [Fe/H]= −0.79, while Cordero et al. (2015) reported $T_{\rm eff}$ = 4475 K, $\log g$ = 1.60, $\xi_{\rm micro}$ = 1.65 km s^{-1}, and [Fe/H]= −0.78. Due to its peculiar abundance pattern, Lee 4710 was excluded

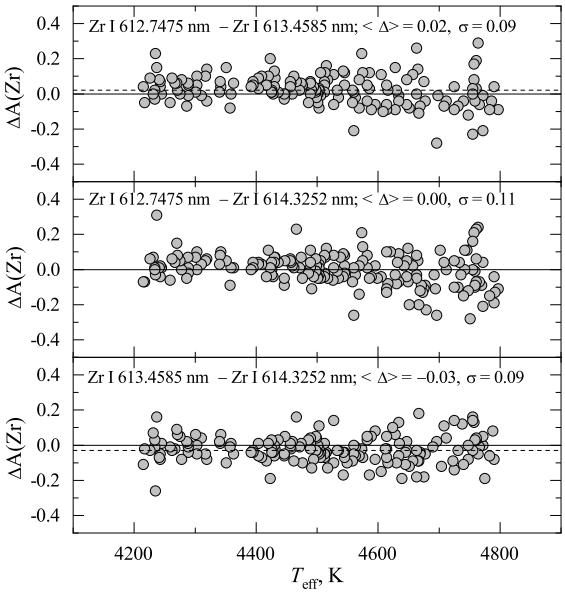

Fig. 2.11. Differences in Zr abundances obtained from different Zr I spectral lines used in this work. In each panel, the $\langle\Delta\rangle$ symbol denotes the mean difference between the A(Zr) values obtained using different Zr I lines.

from further analysis.

2.5.5. Determination of Zr abundance in 47 Tuc using Zr II lines

All three Zr I lines utilized in this study are contaminated by weak CN blends (for details see Sect. 2.5.7). To verify the reliability of abundances determined from these Zr I lines, we compared abundances obtained from Zr I lines with those determined by using Zr II lines. However, no Zr II lines were present within the wavelength range covered by the `VLT/GIRAFFE` spectra used in this work. We therefore used `VLT/UVES` spectra obtained by Thygesen et al. (2014) for 13 RGB stars (spectra were obtained in the 580 nm setting, with a resolving power of $R = 110\,000$). In this sample of stars, there are 3 stars with effective temperatures between $4200 \leq T_{\rm eff} < 4800$ K (our $T_{\rm eff}$ scale) that also appear in our `VLT/GIRAFFE` sample. To our knowledge, these archival `UVES` spectra are the only available spectra of our `GIRAFFE` targets that cover the wavelength range of Zr II lines.

The observed spectra for the three UVES stars were taken from the ESO Advanced Data Products archive[3]. Zr abundances were determined using the same three Zr I lines as in the analysis of `GIRAFFE` spectra (detailed in Sect. 2.5.4). Additionally, we determined the Zr abundance using the Zr I 614.054 nm line, which becomes too weak for reliable measurement in `GIRAFFE` spectra for stars

[3]http://archive.eso.org/wdb/wdb/adp/phase3_spectral/form

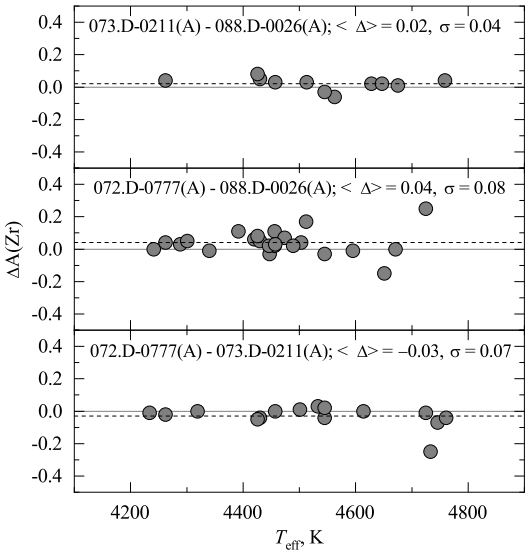

Fig. 2.12. Differences in Zr abundances determined in stars that are common to different observing programs used in this study. In each panel, the $\langle\Delta\rangle$ symbol denotes the mean difference between the average A(Zr) values obtained in different programmes.

Table 2.4. Abundances of Zr in the three stars common to the GIRAFFE (used in this work) and UVES samples (Thygesen et al. 2014), determined from Zr I and Zr II lines in the UVES spectra.

ID	$T_{\rm eff}$ K	$\log g$	$\xi_{\rm micro}$ km s^{-1}	A(Zr)$_{\rm I}$ 612.7475 nm	A(Zr)$_{\rm I}$ 613.4585 nm	A(Zr)$_{\rm I}$ 614.0535 nm	A(Zr)$_{\rm I}$ 614.3252 nm	A(Zr)$_{\rm II}$ 511.2270 nm	A(Zr)$_{\rm II}$ 535.0089 nm	A(Zr)$_{\rm II}$ 535.0350 nm
13396	4245	1.34	1.57	2.24	2.18	2.17*	2.16	2.26	2.14	2.23
20885	4359	1.41	1.82	2.16	2.13*	2.12*	–	2.18	2.16	2.20
29861	4217	1.32	1.61	2.12*	2.18	–	2.18	2.20	2.15	2.22

Note: Atmospheric parameters used in the abundance analysis were those determined in this study. Abundances marked with the asterisks were determined from the weak and/or noisy lines.

with $T_{\rm eff} > 4450$ K. Zr abundances were also determined using Zr II lines at 511.227, 535.009, and 535.035 nm. Abundances from all Zr lines were determined by fitting synthetic spectra to the observed Zr line profiles. This approach was used because all Zr II lines are blended with CN lines. Furthermore, the 535.035 nm line is affected by the blends of the weak V II 535.035 nm and Tl I 535.045 nm lines, and the 511.227 nm Zr II line is influenced by nearby MgH 511.208 nm and Cr I 511.248 nm lines (shown in Fig. 2.14). Additionally, the magnesium abundance impacts the opacity of the stellar model atmosphere, which leads to a slight change in electron density. This, in turn, slightly alters the computed synthetic spectrum and thus the determined Zr abundances. In order to take this effect into account, we utilized Mg abundances determined for the three stars by Thygesen et al. (2014).

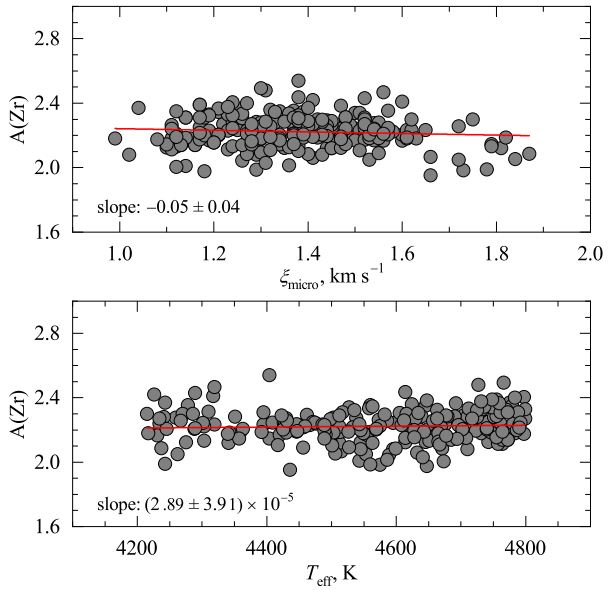

Fig. 2.13. Determined Zr abundance, A(Zr), in the target RGB stars, plotted against the microturbulence velocity (top panel) and effective temperature (bottom panel).

Table 2.5. Mean abundances of Fe, Na, and Zr in the three common stars stars used in our study and that of Thygesen et al. (2014), obtained by us from the GIRAFFE and UVES spectra.

	This study								Thygesen et al. (2014)					
ID	$T_{\rm eff}$ K	log g	$\xi_{\rm micro}$ km s^{-1}	[Fe/H] GIRAFFE	[Na/Fe] GIRAFFE	[Zr I/Fe] GIRAFFE	[Zr I/Fe] UVES	[Zr II/Fe] UVES	$T_{\rm eff}$	log g	$\xi_{\rm micro}$	[Fe/H] UVES	[Na/Fe] UVES	[Zr I/Fe] UVES
13396	4245	1.34	1.57	−0.77	0.16	0.36	0.34	0.36	4190	1.45	1.60	−0.83	0.07	0.25
20885	4359	1.41	1.82	−0.74	0.21	0.31	0.27	0.30	4260	1.35	1.90	−0.84	0.11	0.18
29861	4217	1.32	1.61	−0.82	0.28	0.38	0.36	0.39	4160	1.20	1.50	−0.84	0.10	0.23

Note: Abundances obtained by us from the Zr I 614.0460 nm line were not used in the computation of the mean Zr abundances.

To mitigate the impact of CN blends on the determined Zr abundances, we employed Solar-scaled CN abundances, A(C) = 7.82 and A(N) = 7.22, along with CN line data from Brooke et al. (2014) (further details on the influence of CN blends on Zr abundances are provided in Sect. 2.5.7).

For abundance analysis, we had to modify the oscillator strength of the 535.009 nm line because the abundance determined when using the oscillator strength from VALD3 was higher by ~ 0.28 dex (Fig. 2.15 left) than the reference value of A(Zr) = 2.62 from Caffau et al. (2011a). Consequently, for further analysis we modified oscillator strength of this line so that we would obtain A(Zr) = 2.62 in Kurucz solar spectrum (Fig. 2.15 left). Utilizing the updated oscillator strength value, $\log gf = -0.964$, we determined the Zr abundance from the Zr II 535.009 nm line in Arcturus (shown in Fig. 2.15 right), resulting

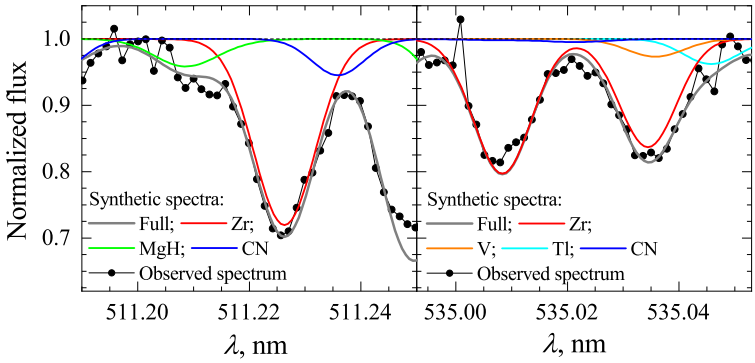

Fig. 2.14. Zr II lines in the UVES spectrum of the target star 20885 (dots) overlaid with the synthetic spectrum (grey solid line) computed using the ATLAS9 model with $T_{\rm eff}$ = 4359 K, $\log g$ = 1.41, [Fe/H] = −0.74, [Zr/Fe] = 0.34, $\xi_{\rm micro}$ = 1.82 km/s, $\xi_{\rm macro}$ = 5.80 km/s and solar-scaled elemental abundances (Grevesse & Sauval 1998). Left panel shows the vicinity of Zr II 511.227 nm line, right panel that of 535.009 nm, and of 535.035 nm Zr II lines. Other solid lines show the influence of various line blends. Left panel: red line − only Zr spectrum, green line – only MgH spectrum, blue line – only CN spectrum. Right panel: red line − only Zr spectrum, orange line – only V spectrum, cyan line – only Tl spectrum, blue line – only CN spectrum.

in A(Zr) = 2.17 ([Zr/Fe] = +0.07, using A(Fe) = −0.52 from Sect. 2.5.1). The latter value agrees well with [Zr/Fe] = +0.01±0.07 determined by Worley et al. (2009) from seven Zr I lines, however, it is slightly higher than the average Zr abundance we determined from Zr I lines: [Zr/Fe] = −0.10 (Sect. 2.5.1).

Abundances determined from individual Zr I and Zr II lines for the three stars common to both GIRAFFE and UVES samples exhibit a discrepancy of ≤ 0.06 dex (Table 2.4; Fig. 2.16). Moreover, the mean difference in abundances determined from Zr I lines in the GIRAFFE and UVES spectra is even smaller, less than 0.03 dex (Table 2.5, Fig. 2.16). We conclude that, even with the small number of stars that was used in this test, the consistency in Zr abundances determined from individual Zr I and Zr II lines suggests that the impact of various factors (line blends, line data, systematic errors in analysis procedures, etc.) on the determined Zr abundances is negligible.

Zr abundances determined from Zr I lines in the UVES spectra are, on average, approximately 0.10 dex higher than those reported by Thygesen et al. (2014) (Table 2.5; Fig. 2.17). Although there are minor discrepancies in effective temperature and gravities between the two studies, these differences cannot account for more than about 0.02 dex of this discrepancy. The microturbulence velocities reported by Thygesen et al. (2014) are, on average, lower by approximately 0.04 km s^{-1} than those determined in this study (Table 2.5). This discrepancy would result in Zr abundances being, on average, ∼0.10 dex

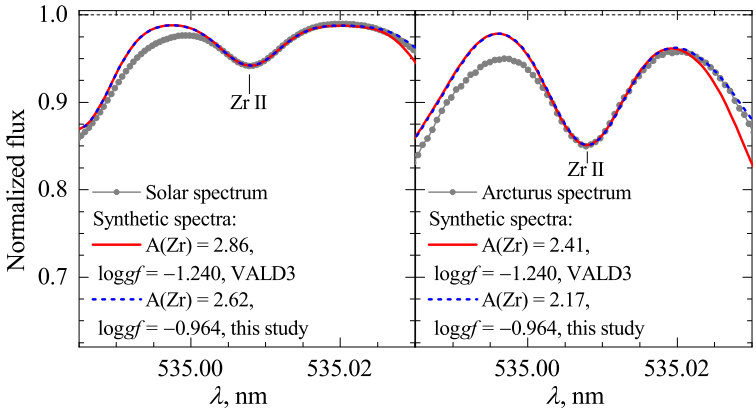

Fig. 2.15. **Left:** fit of synthetic Zr II 535.009 nm line to the observed one in the solar spectrum from Kurucz (2005b). A best fit obtained by using the VALD3 oscillator strength is shown as red solid line, blue dashed line is a fit determined using A(Zr) = 2.62 from Caffau et al. (2011a) and a modified oscillator strength (oscillator strengths and Zr abundances used/determined are indicated in the figure). We used $T_{\rm eff}$= 5777 K and $\log g$= 4.43 for the Sun, with $\xi_{\rm micro}$ = 1.00 km s^{-1}, $\xi_{\rm macro}$ = 3.80 km s^{-1}taken from Doyle et al. (2014). **Right:** fit of synthetic Zr II 535.009 nm line to the one observed in the spectrum of Arcturus from Hinkle et al. (2000). We used $T_{\rm eff}$= 4286 K and $\log g$= 1.66 for Arcturus (Ramírez & Allende Prieto 2011), with $\xi_{\rm micro}$ = 1.70 km s^{-1}, $\xi_{\rm macro}$ = 5.20 km s^{-1}taken from Sheminova (2015).

higher when compared with the abundances determined using $\xi_{\rm micro}$ values derived in this work.

However, a significant factor contributing to the discrepancy is our utilization of the revised ionization potential for Zr I, 6.634 eV, from Hackett et al. (1986), as opposed to the default value used in the older version of the Kurucz package (discussed in Sect. 2.5.1). This adjustment alone results in the Zr abundances determined in our study being higher by ∼0.29 dex. Considering both effects, which influence the determined abundance in opposite directions, it becomes possible to explain the difference in Zr abundances between this work and the results of Thygesen et al. (2014).

2.5.6. Abundance determination errors

To estimate the typical errors in the determined Fe, Na, and Zr abundances, we used the following steps:

- The error in the abundance estimate due to uncertainty in effective temperature ($T_{\rm eff}$) was assessed by adjusting $T_{\rm eff}$ values up and down by an amount corresponding to the uncertainty in the determination of the $V-I$ color. We employed a conservative estimate of $\sigma(V) = \sigma(I) = 0.03$,

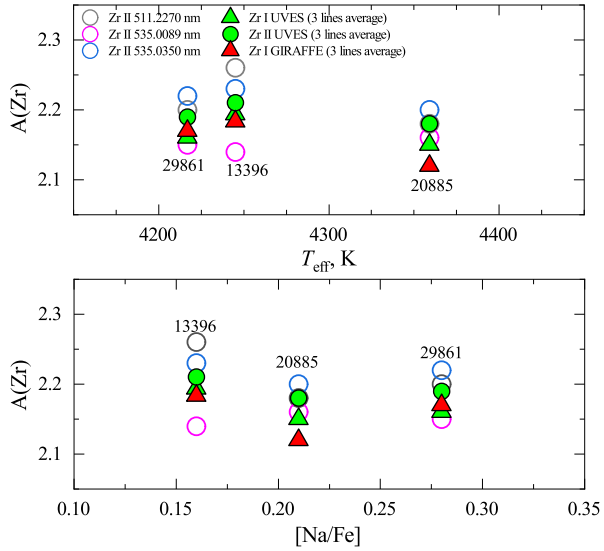

Fig. 2.16. Abundances of Zr in the four RGB stars common to the GIRAFFE (this study) and UVES samples Thygesen et al. (2014), determined by us using different Zr I and Zr II lines in the GIRAFFE and UVES spectra, and plotted versus the effective temperature (**top**) and [Na/Fe] (**bottom**). The mean abundances obtained using Zr I lines in the GIRAFFE and UVES spectra are shown by solid red and green triangles, respectively, while the mean abundances obtained from Zr II lines are plotted as green circles; and abundances determined from individual Zr II lines in the UVES spectra are shown as hollow circles.

leading to an uncertainty of ± 60 K in $T_{\rm eff}$.

- The error in abundance resulting from the uncertainty of $\log g$ determination was evaluated by taking into account errors in effective temperature, luminosity, and stellar mass. The error in $\log g$ is ± 0.2, which has a negligible impact on the abundance error.

- The RMS variation of microturbulence velocity was used as a representative uncertainty in $\xi_{\rm t}$, which is $\pm\ 0.2\,{\rm km\,s^{-1}}$. This value was employed to derive the abundance error due to variation in $\xi_{\rm micro}$.

- The error in continuum determination was estimated by computing the flux dispersion, σ(cont), in the continuum as follows:

$$\sigma({\rm cont}) = \frac{\sigma({\rm flux})}{\sqrt{N}}, \tag{2.2}$$

here N is the total number of wavelength points. This error was then applied to adjust the continuum level upward and downward, followed by re-fitting of the line, and the resulting difference in abundances was

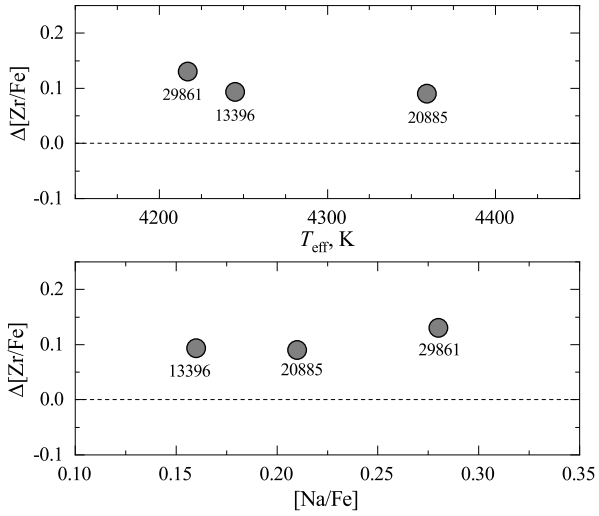

Fig. 2.17. Differences in Zr abundances determined in this study and by Thygesen et al. (2014) using Zr I lines observed in the the UVES spectra, and plotted versus (**top**) effective temperature and (**bottom**) [Na/Fe] ratios of the target RGB stars.

taken as the abundance error due to the uncertainty of continuum determination.

- For estimating the error in line profile fitting, we calculated the RMS deviation between the observed spectra and the Gaussian profile fit. This deviation was then used to adjust the equivalent width of the line, which, in turn, led to a difference in the determined abundance. This difference was then taken as the uncertainty arising from errors in line profile fitting.

A sub-sample of 8 stars with their effective temperatures evenly distributed across the entire $T_{\rm eff}$ range of 237 RGB targets was selected for error estimation of Zr, Na, and Fe abundances. Following the aforementioned method, we determined the typical abundance errors for Zr, Na, and Fe for these stars. In this process, we assumed median equivalent widths of these lines for the given $T_{\rm eff}$, thereby not accounting for variation in line strength. The abundance errors for Zr, Na, and Fe for the remaining target stars were then calculated by interpolating the findings from the sub-sample of 8 stars. The total abundance error, $\sigma_{\rm i}$(total), was derived by summing the individual error components in quadrature. The results are provided in Tables C.1–C.3.

2.5.7. Influence of CN blends on the strength of Zr lines and Zr abundance

Zr lines used in this study are affected by weak CN blends, which could potentially alter the measured equivalent widths of Zr lines and, consequently,

the determined Zr abundances (Fig. 2.6 and 2.10). The abundances of C and N may vary significantly between 1P and 2P stars (e.g. Carretta et al. 2005; Mészáros et al. 2020), and these differences in abundance affect the strength of the CN lines. If the CN lines are blended with the Zr lines, this might lead to a systematically higher determined Zr abundances in 2P stars, because the Zr lines would have a higher apparent equivalent width without taking the influence of CN lines into account (i.e. which was done in this study because abundances of C and N are unknown for the majority of the stars). As the 2P stars have higher Na abundances, the influence of CN blends may lead to systematically overestimated Zr abundances in these stars, which then might create a false correlation between the abundances of Na and Zr. To investigate the potential influence of CN blends, we conducted two tests, the results of which are detailed below.

2.5.7.1. Influence of CN blends

For the first test, we computed synthetic Zr I line profiles for the three Zr I lines analyzed in this study, including CN lines calculated using CNO abundances determined in the `APOGEE-2` (Mészáros et al. 2020, encompassing a total of 82 RGB stars). We selected three sets of CNO abundances corresponding to CN-weak, CN-intermediate, and CN-strong lines. For the nitrogen-depleted composition, we adopted [C/Fe] = +0.20, [N/Fe] = +0.20, [O/Fe] = +0.80 (case-A, "CN-weak"), representing the first (primordial) population of stars (characterized by enhanced O and depleted Na). The chemical composition [C/Fe] = −0.20, [N/Fe] = +1.10, [O/Fe] = +0.60 (case-B, "CN-intermediate") was used for intermediate population stars, and [C/Fe] = −0.80, [N/Fe] = +1.70, [O/Fe] = +0.10 (case-C, "CN-strong") for the second population stars (O depleted and Na enhanced).

Synthetic spectra were computed using `SYNTHE` with the three described CN abundance combinations, a constant Zr abundance $A(\mathrm{Zr}) = 2.16$, and two `ATLAS9` model atmospheres with the parameters: $T_{\mathrm{eff}} = 4320\,\mathrm{K}$, $\log g = 1.52$, [Fe/H]= −0.78, and 4675 K, $\log g = 2.13$, [Fe/H]= −0.67 (both with [α/Fe]= +0.4). The CN line list was taken from Brooke et al. (2014). Equivalent widths of the synthetic Zr lines were measured for the three cases of CN abundance combinations, and the Zr abundance was determined using the same procedure as with the target stars (detailed in Sect. 2.5.4).

We found that variations in C and N abundances within these limits have a small, yet non-negligible effect. However, even in the most extreme scenarios, it did not exceed 0.08 dex (as shown in Table 2.6). The average corrections (for the most extreme cases C–A) were 0.04 dex and 0.07 dex at $T_{\mathrm{eff}} = 4320\,\mathrm{K}$ and 4675 K, respectively. It is important to emphasize that the CNO abundances chosen for cases A and C are extreme, and for the majority of stars, the variation in CNO abundances will be smaller, which means that the abundance correction

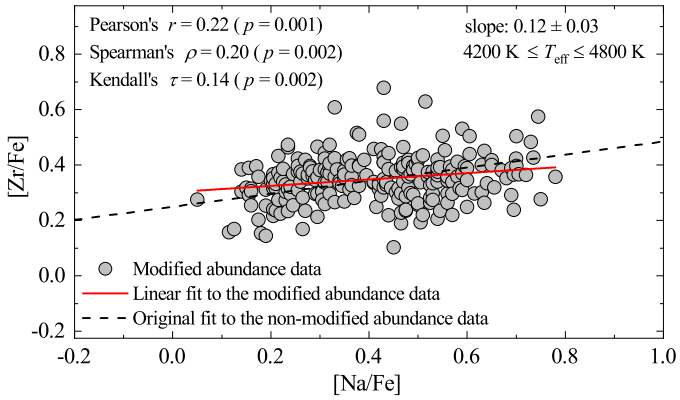

Fig. 2.18. The influence of CN lines on the Zr–Na correlation. The original Zr abundances obtained from Zr I lines in Sect. 2.5.4 were modified by subtracting a correction which changed linearly from zero at [Na/Fe] = 0.10 to 0.08 dex at [Na/Fe] = 0.75 (filled grey circles). Linear fit to the modified data is shown as red solid line, black dashed line is linear fit to the non-modified abundances in the [Zr/Fe] − [Na/Fe] plane.

Table 2.6. Influence of CN line blends on the determination of Zr abundances from Zr I lines at different CNO abundances (see Sect. 2.5.7.1 for details).

	case-A		case-B		case-C		ΔA(Zr)	ΔA(Zr)	ΔA(Zr)
λ, nm	W, pm	A(Zr)	W, pm	A(Zr)	W, pm	A(Zr)	(C–A)	(B–A)	(C–B)
$T_{\mathrm{eff}} = 4320$ K, $\log g = 1.52$, [Fe/H] $= -0.78$									
612.7475	6.09	2.26	6.20	2.28	6.41	2.31	+0.05	+0.02	+0.03
613.4585	5.82	2.22	6.02	2.25	6.19	2.27	+0.05	+0.03	+0.02
614.3252	6.54	2.25	6.68	2.27	6.77	2.28	+0.03	+0.02	+0.01
$T_{\mathrm{eff}} = 4675$ K, $\log g = 2.13$, and [Fe/H] $= -0.67$									
612.7475	2.15	2.26	2.32	2.31	2.43	2.33	+0.07	+0.05	+0.02
613.4585	2.00	2.25	2.18	2.30	2.30	2.33	+0.08	+0.05	+0.03
614.3252	2.53	2.29	2.65	2.32	2.72	2.34	+0.05	+0.03	+0.02

will also be smaller. Nonetheless, to be on the safe side, for subsequent tests, we assumed a moderate change in the slope of the [Zr/Fe]–[Na/Fe] plane due to CN blends of $\approx +0.11$.

To eliminate the impact of CN line blends on the determined Zr abundances, we adjusted the Zr abundances determined from the three Zr I lines (Sect. 2.5.4) by subtracting a correction which changed linearly from +0.04 dex at [Na/Fe]=0.10 to −0.04 dex at [Na/Fe]=0.75. This adjustment corresponds to a slope change of ≈ -0.11 mentioned above. This left us with a residual slope in the [Zr/Fe] − [Na/Fe] plane (equal to $\approx +0.12$) that gives a change in the Zr abundance of +0.07 dex over the range of [Na/Fe] = [+0.10, +0.75]. Using this corrected dataset, we calculated Pearson, Spearman, and Kendall-τ correlation coefficients in the [Zr/Fe] − [Na/Fe] plane. The Student's t-test shows

Table 2.7. The influence of CN lines on the determination of Zr abundances from the selected Zr II lines for the different cases of assumed CNO abundances and the effective temperature of $T_{\rm eff}$= 4320 K.

	case-A		case-C		ΔA(Zr)
λ, nm	W, pm	A(Zr)	W, pm	A(Zr)	(C-A)
$T_{\rm eff}$ = 4320 K					
511.227	3.86	2.23	4.85	2.42	+0.19
535.009	1.56	2.24	1.44	2.20	−0.04
535.035	2.50	2.17	2.46	2.16	−0.01

that the probability of obtaining these values by chance is less than $p = 0.002$ (Fig. 2.18). These results therefore suggest that even if the Zr abundances in this work are influenced by CN line blends, the Zr-Na correlation observed in our data is in fact real.

Given that Zr abundance was determinable using Zr II lines for only three stars, we did not investigate a potential Zr-Na correlation using these lines. Nevertheless, we also estimated the CN effect on Zr abundances determined using Zr II lines following the aforementioned approach, with results presented in Table 2.7. For the 511.227 nm line, the CN line influence is significant, potentially leading to an overestimation of Zr abundance by up to ∼0.19 dex. For the other two Zr II lines, 535.009 nm and 535.035 nm, the impact of CN lines is minimal, up to about 0.04 dex in the worst-case scenario, and these lines can be safely used for Zr abundance determination regardless of CNO abundance variations.

2.5.7.2. Influence of CN blends in the subsample of RGB targets with known C and N abundances

For the second test, we selected a subset of 54 stars from our analyzed sample for which C and N abundances had been determined by Mészáros et al. (2020). Using spectral synthesis methodology, we determined Zr abundances from the same three Zr I lines as outlined in Sect. 2.5.4, in order to remove the influence of CN blends on the Zr lines and therefore the derived Zr abundances. As with the prior test, the CN line list was taken from Brooke et al. (2014), and synthetic spectra were computed using the `SYNTHE` package together with the model atmospheres that were used in the analysis of the target stars in Sect. 2.5.4. The determined Zr abundances are shown in Fig. 2.19.

The results of this test reveal that the slope in the [Zr/Fe] − [Na/Fe] plane is reduced to approximately +0.12 when Zr abundances adjusted for the influence of CN lines are used (Fig. 2.19). This makes the slope about two times smaller than the one obtained by employing the equivalent width method, which is ≈0.23 (Sect. 2.6.1). This discrepancy can be attributed to two factors. Firstly,

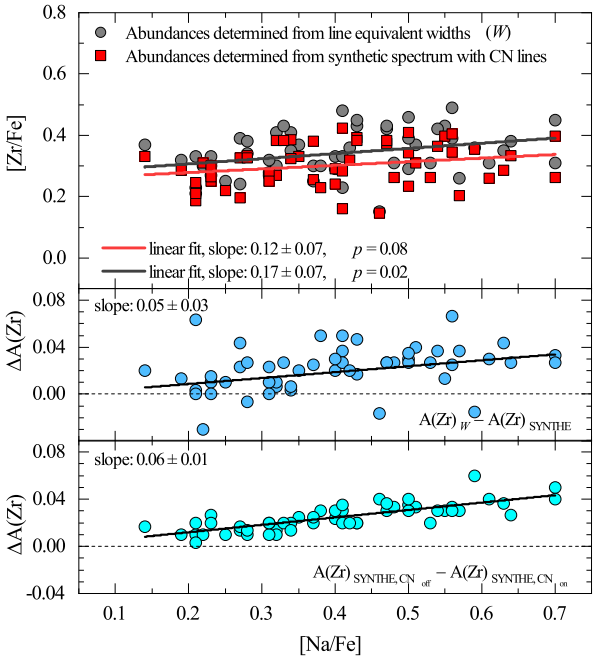

Fig. 2.19. Comparison of Zr abundances obtained in the subsample of 54 RGB stars with and without taking the influence of CN lines into account. **Top**: [Zr/Fe] abundance ratios obtained using the equivalent width method (Sect. 2.5.4, grey circles) and spectral line synthesis (Sect. 2.5.7.2, red squares). **Middle**: Difference between Zr abundances obtained using equivalent width and spectral line synthesis methodologies. **Bottom**: Difference between Zr abundances obtained with the line synthesis methodology when switching the CN lines off and on. In all panels, solid lines are linear best fits to the data.

the slope in the [Zr/Fe] − [Na/Fe] plane for the subset of 54 RGB stars is lower than that determined for the full sample of 237 stars, $\approx +0.17$ vs. $\approx +0.23$. Secondly, the remaining change in the slope, $\Delta = +0.06$, results from the impact of CN lines (Fig. 2.19).

These results confirm that the correlation in the [Zr/Fe] − [Na/Fe] plane remains significant even when using the spectral line synthesis method, which eliminates the influence of CN lines, for Zr abundance determination. In this subset of 54 RGB stars, we obtain a p-value of 0.08. Although this result is statistically insignificant, it is important to keep in mind that the sample size in this test is almost five times smaller than that of the full sample. For this reason alone, the p-value obtained here is increased.

Table 2.8. Minimum, maximum, and mean Fe, Na, and Zr abundance ratios determined in the sample of 237 RGB stars in 47 Tuc.

	$[X/H]_{min}$	$[X/H]_{max}$	$\langle[X/H]\rangle$	$[X/Fe]_{min}$	$[X/Fe]_{max}$	$\langle[X/Fe]\rangle$
Fe I (LTE)	−0.87	−0.54	-0.75 ± 0.05	–	–	–
Na I (NLTE)	−0.70	0.03	-0.34 ± 0.16	0.05	0.78	0.41 ± 0.16
Zr I (LTE)	−0.64	−0.07	-0.40 ± 0.09	0.11	0.68	0.35 ± 0.09

Note: Errors denote the standard deviation due to star-to-star abundance variation.

2.6. Results and discussion

2.6.1. Mean abundances of Fe, Na, and Zr in the target RGB stars in 47 Tuc

The mean iron-to-hydrogen abundance ratio ([Fe/H]) determined in this study for 237 RGB stars in the GGC 47 Tuc, with effective temperatures in the range of $4200 \leq T_{\rm eff} \leq 4800$ K (Sect. 2.5), is [Fe/H] $= -0.75 \pm 0.05$ (error is standard deviation due to star-to-star abundance variation). This result agrees well with those obtained in earlier studies: [Fe/H] $= -0.74 \pm 0.05$ by Carretta et al. (2009b, for 114 RGB stars), and [Fe/H] $= -0.77 \pm 0.08$ by Wang et al. (2017, for 44 RGB stars). The mean Fe abundance determined using Fe II lines in this work is $\langle[Fe/H]_{FeII}\rangle = -0.73 \pm 0.09$[4], which also agrees well with the mean abundance value obtained from Fe I lines.

The mean [Na/Fe] abundance ratio for the 237 RGB stars in this study is $\langle[Na/Fe]\rangle = 0.41 \pm 0.16$, with a significant scatter in Na abundance ranging $0.05 \leq [Na/Fe] \leq 0.78$. These results agree well with the results obtained in other studies: Δ[Na/Fe] $= 0.76$ and $\langle[Na/Fe]\rangle = 0.47 \pm 0.15$ (Carretta et al. 2009b, for 147 RGB stars), Δ[Na/Fe] $= 0.56$ and $\langle[Na/Fe]\rangle = 0.36 \pm 0.18$ (Wang et al. 2017, for 27 RGB stars).

In case of Zr, the mean abundance for the 237 RGB stars in this work is $\langle[Zr/Fe]\rangle = 0.35 \pm 0.09$. The range of star-to-star abundance scatter is large, similar to that of Na: $0.11 \leq [Zr/Fe] \leq 0.68$. The mean Zr abundance obtained by us agrees well with the results from Thygesen et al. (2014): $\langle[Zr/Fe]\rangle = 0.41 \pm 0.19$ (13 RGB stars). A slightly larger difference is obtained when comparing with the results of Wylie et al. (2006, average in 7 RGB/AGB stars): $\langle[Zr/Fe]\rangle = 0.69 \pm 0.15$. The mean abundances for Fe, Na and Zr abundances are provided in Table 2.8.

The abundance analysis of Zr and Na for 237 RGB stars reveals an existence of a weak correlation in the [Zr/Fe] − [Na/Fe] plane (Fig. 2.20, top). In order to estimate the statistical significance of this result, we assumed the null hypothesis that the Pearson's, Spearman's, and Kendall's correlation coefficients (r, ρ, and τ, respectively) are zero in this plane, implying no correlation between the

[4]As mentioned in Sect. 2.5, typically 2-3 Fe II lines could be measured in the average target spectra, which is why stellar gravities were not determined using the assumption of ionization equilibrium.

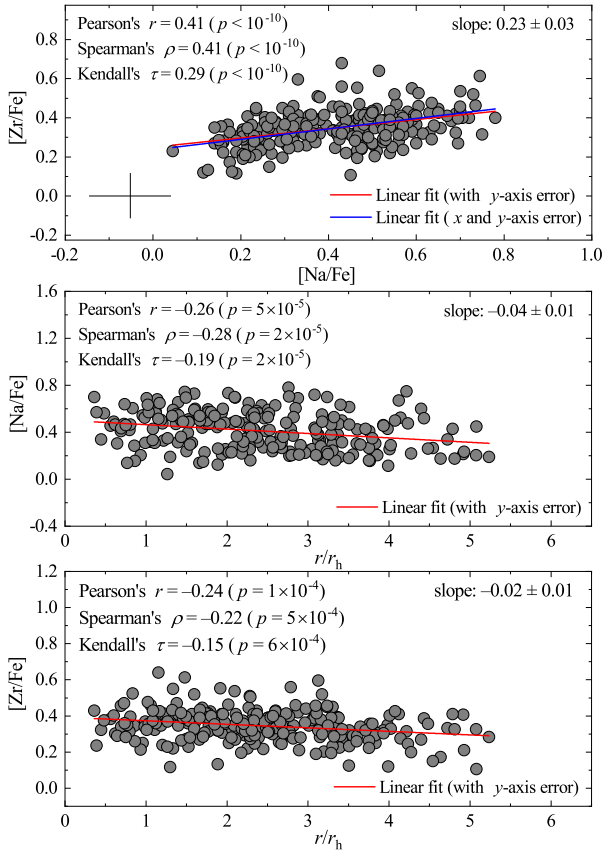

Fig. 2.20. [Zr/Fe] ratios in the sample of 237 RGB stars in 47 Tuc. Top panel: [Zr/Fe] versus [Na/Fe] ratios. Middle and bottom panels, respectively: [Zr/Fe] and [Na/Fe] ratios versus projected distance from the cluster centre, $r/r_{\rm h}$. Linear least-square best fits are shown as solid lines, fit parameters, correlation coefficients, and the p-values are provided in each individual panel. Typical errors of the individual abundance measurements are indicated in the top panel.

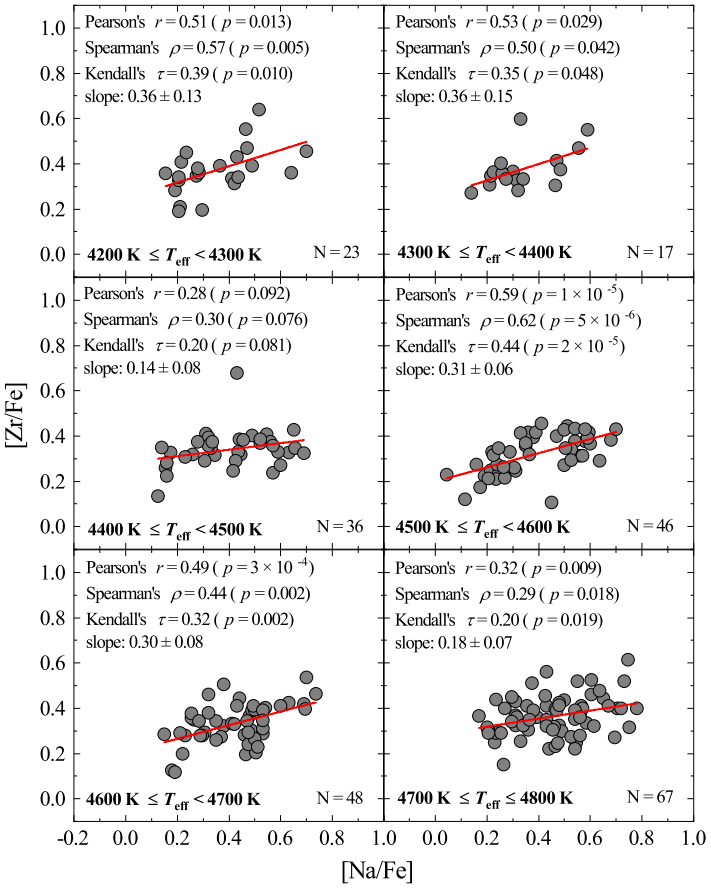

Fig. 2.21. [Zr/Fe]−[Na/Fe] plots for stars divided into bins of $\Delta T_{\rm eff} = 100$ K (N is the number of stars in each bin). Values of different correlation coefficients and the corresponding p-values are provided for each temperature bin.

[Zr/Fe] and [Na/Fe] abundance ratios. We then performed Student's t-test to estimate the two-tailed probability, p, for obtaining such correlation coefficients in the given data set by chance, which are extremely small, as can be seen by the p-values shown in Table 2.9.

Further we divided the entire analyzed star sample into $\Delta T_{\rm eff} = 100$ K bins and constructed new [Zr/Fe]−[Na/Fe] plots for the stars within each bin. In all bins except one ($4400 \leq T_{\rm eff} < 4500$ K), the statistically significant correlation (with p-values < 0.05) between [Zr/Fe] and [Na/Fe] remains intact (Fig. 2.21).

Our data also suggests that there is a weak yet statistically significant anti-correlation between the abundance of Zr and the radial distance from the cluster center, denoted as [Zr/Fe] $- r/r_{\rm h}$ (Fig. 2.20, middle panel), where, r is the projected distance from the center of the cluster to the target star, and $r_{\rm h}$ is the half-light radius of 47 Tuc ($r_{\rm h} = 174''$, Trager et al. 1993). This result

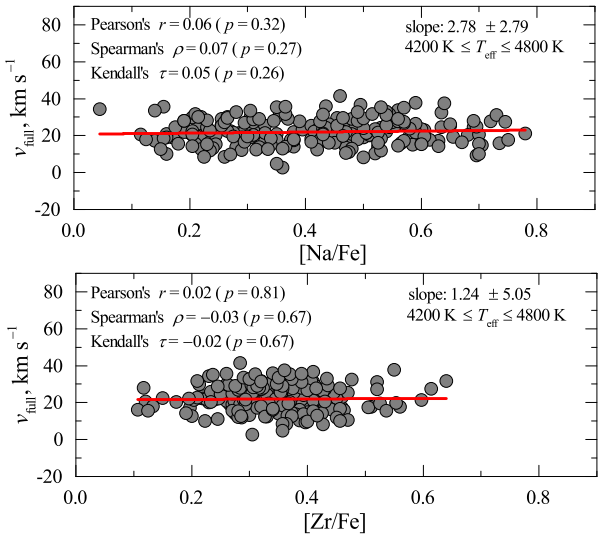

Fig. 2.22. Full spatial velocities of 237 RGB stars in 47 Tuc versus their [Na/Fe] and [Zr/Fe] ratios (top and bottom, respectively).

Table 2.9. Pearson, Spearman and Kendall correlation coefficients and the corresponding p-values in the [Zr/Fe]–[Na/Fe] and abundance–distance planes.

	Pearson		Spearman		Kendall	
	r	p	ρ	p	τ	p
[Zr/Fe] − [Na/Fe]	0.41	$< 10^{-10}$	0.41	$< 10^{-10}$	0.29	$< 10^{-10}$
[Na/Fe] − $r/r_{\rm h}$	−0.26	5×10^{-5}	−0.28	2×10^{-5}	−0.19	2×10^{-5}
[Zr/Fe] − $r/r_{\rm h}$	−0.24	1×10^{-4}	−0.22	5×10^{-4}	−0.15	6×10^{-4}

indicates that stars with the highest [Na/Fe] and [Zr/Fe] abundance rations tend to concentrate more towards the cluster center, which also agrees with the results of the previous studies for Na (e.g. Bastian & Lardo 2018). At the same time, this is first detection of such tendency for Zr. The p-values calculated for the Pearson, Spearman, and Kendall correlation coefficients are provided in Table 2.9.

2.6.2. Statistical significance of possible correlations between the full spatial velocity dispersions and [Na/Fe] and [Zr/Fe] abundance ratios

We tested for the potential correlations in the $v_{\rm full}$ − [Na/Fe] and $v_{\rm full}$ − [Zr/Fe] planes. Similarly to our approach with the abundance–abundance and abundance–radial distance planes, we calculated the p-values using Pearson's, Spearman's, and Kendall's correlation coefficients. In the $v_{\rm full}$ − [Na/Fe] plane, no significant correlation was observed, with the p-value exceeding 0.20. Conversely, in the $\sigma_{v_{\rm full}}$ − [Zr/Fe] plane, $p < 0.04$ was obtained using Spearman's

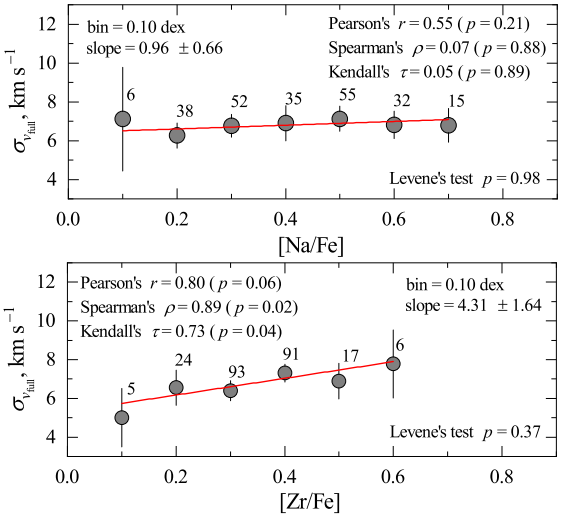

Fig. 2.23. Dispersions of full spatial velocities of the target RGB stars computed in non-overlapping [Zr/Fe] (top panel) and [Na/Fe] (bottom panel) abundance bins of 0.1 dex. Solid lines are linear least-square fits and the number of stars in each abundance bin is indicated next to each data point. Indicated are the p-values that were obtained using different methods (including the Levene's test, see Sect. 2.6.2), and error bars were computed using the bootstrapping technique.

and Kendall's coefficients, suggesting a potential weak correlation. However, Pearson's correlation coefficient yielded a somewhat higher p-value of 0.059. The results of these tests are shown in Fig. 2.22 and Fig. 2.23.

To further explore the potential correlation in the $\sigma_{v_{\rm full}}$ – [Zr/Fe] plane, we conducted Levene's test (Levene 1960; Brown & Forsythe 1974). With this test, we assessed if the differences between the variances of full spatial velocities of individual the stars in the 0.10 dex wide [Zr/Fe] and [Na/Fe] bins are statistically significant (Fig. 2.23). Levene's test was used to evaluate the null hypothesis that the variances of full spatial velocities in the different [Zr/Fe] and [Na/Fe] bins are equal. The test results indicated that the null hypothesis could not be rejected in either the $\sigma(v_{\rm full})$ – [Na/Fe] or the $\sigma(v_{\rm full})$ – [Zr/Fe] planes, with p-values $\geq$ 0.37 in both instances. In summary, the results of this test suggest the absence of statistically significant correlations between the dispersions of full spatial velocities and the [Na/Fe] and [Zr/Fe] ratios in the analyzed target RGB stars.

These results contrast with those reported by Kučinskas et al. (2014), where a weak but statistically significant correlation was identified between the radial velocity dispersion and the [Na/O] and [Li/Na] ratios in an analysis of 101 TO stars in the GGC 47 Tuc. However, the [Na/O] abundance ratio has a much larger variation between 1P and 2P stars ($>$ 1 dex) when compared with the

Table 2.10. Mean [Na/Fe] and [Zr/Fe] abundance ratios in the 1P and 2P stars in 47 Tuc and the corresponding p-values.

	$\langle$[X/Fe]$\rangle_{1P}$	$\langle$[X/Fe]$\rangle_{2P}$	p-value
Zr I (LTE)	0.310 ± 0.008	0.372 ± 0.007	$< 10^{-7}$
Zr I (LTE), CN-adjusted	0.331 ± 0.008	0.361 ± 0.007	0.007

Note: Uncertainties are standard errors of the mean. The last line provides the values obtained with Zr abundances in 237 RGB stars adjusted to account for the influence of CN blends.

variation of [Na/Fe] or [Zr/Fe] ratios, thus the detection of a possible correlation may be much harder in the latter two cases.

2.6.3. Mean values of Na and Zr abundances in the 1P and 2P stars in 47 Tuc

The Zr–Na correlation that we detected in this work is relatively weak, so one can also compare the mean Zr abundances in the 1P and 2P stars in order to check if they are indeed statistically different. To perform this test we followed a prescription in Carretta et al. (2009b) where stars with [Na/Fe] = $[[\mathrm{Na/Fe}]_{\mathrm{min}}, [\mathrm{Na/Fe}]_{\mathrm{min}} + 0.3]$ were classified as 1P stars and those with the higher [Na/Fe] abundance ratios as 2P. Then in each population we calculated the mean [Zr/Fe] ratios and the errors of the mean. The results of this test are provided in Table 2.10.

Further, we performed the two-sample t-test, using the mean 1P and 2P abundances, in order to check if the possible differences between the two populations are statistically significant. The same test was also done with the modified Zr abundances that were determined in Sect. 2.5.7.1. On the other hand, this test was not performed with the 54 RGB stars for which the Zr abundance was determined using the spectral synthesis method (Sect. 2.5.7.2), because the sample size was too small to obtain a reliable comparison of the abundance difference between the two populations.

The results of this test show that for the [Zr/Fe] abundance ratios, p-values do not exceed $p = 0.007$ for both, the unmodified by CN influence abundances (Sect. 2.5.4) as well as abundances adjusted to account for CN blends (Sect. 2.5.7.1).

2.6.4. Implications for nucleosynthesis in the GGCs

The results of the analysis presented in this work suggest that the correlation between the [Zr/Fe] and [Na/Fe] abundance ratios may be statistically significant. Earlier studies of stars in GGCs have not revealed any evidence of a correlation in the [Zr/Fe] − [Na/Fe] plane. However, the sample sizes in those studies were very small ($N < 14$). The results obtained by Thygesen et al. (2014) who analyzed 13 RGB stars in 47 Tuc, showed a potential weak

correlation between the [Zr/Fe] and [Na/Fe] abundance ratios. The authors, however, found it to be statistically insignificant (see their Fig. A.2), which is not surprising given the weakness of the trend and the very small sample size. Furthermore, their data follows the same trend in the [Zr/Fe] − [Na/Fe] plane as it is seen in our data despite a slight difference in the overall mean Zr abundance between the two analyses.

Constraining the nature of potential polluters solely based on Zr abundance analysis is impossible. Theoretical models on s-process element yields have shown that Zr can be synthesized by both AGB stars ($M \approx 1.5 - 5, M_{\odot}$; Cristallo et al. 2015) and massive rotating stars ($M \approx 12 - 25\, M_{\odot}$, $v_{\rm rot} > 150\,{\rm km\,s^{-1}}$; Limongi & Chieffi 2018).

To date, there appear to be no other studies that have detected 1P–2P differences in the s-process element abundances in 47 Tuc. However, there have been indications of such correlations in other Type I GGCs, including Sr–Na and Y–Na relations in M4 (Spite et al. 2016, Villanova & Geisler 2011; see also D'Orazi et al. 2013).

Furthermore, an analysis of 106 RHB stars in 47 Tuc by Gratton et al. (2013) revealed a weak but statistically significant correlation in the [Ba/Fe] − [Na/O] plane. On the other hand, this finding was not corroborated by the results of analysis by Dobrovolskas et al. (2021) who utilized the same RGB stars as in the analysis of Zr abundance, and thus, used the sample size twice as large (see Sect. 3.4 for more details).

In order to determine which of the two enrichment scenarios has operated in 47 Tuc the obtained evidence is not sufficient. Because the abundances of other s-process chemical elements show no evidence of correlations with the abundances of light chemical elements (as is the case with Zr or possibly Ba), it is unclear if these elements were produced by the polluters that have enriched 2P stars with the light chemical elements or if their abundances reflect those of the primordial gas cloud, which has been enriched before the globular cluster formed. Future investigations of differences between the light and heavy s-process elements in the 1P and 2P stars, especially in large samples of GGC stars as this is crucial for a reliable detection of weak correlations between elemental abundances, of this and other GGCs are therefore very desirable.

For example, it would be very useful to check if other s-process elements of the 'first s-process peak' (e.g. Sr, Y, which are produced under similar conditions like Zr), also show similar correlations with light chemical elements, as is the case with Zr. Furthermore, because the s-process elements in different peaks are produced under different conditions and also in different polluter stars, it would also be very useful to check whether there are any differences in the abundances of such heavier s-process elements (e.g. Ba or Pb) in 1P and 2P stars, this would allow to place more stringent constraints on the possible polluters and pollution scenarios.

3. Abundance of Ba in the atmospheres of RGB stars in the globular cluster 47 Tuc

Our analysis presented in Sect. 2 suggests the existence of a weak but statistically significant Na–Zr correlation. The existence of this correlation suggests that light elements and s-process elements should have been produced in the same pollution sources that enriched 2P stars in some light elements and depleted others.

With an aim of shedding more light on the possible 1P–2P differences in s-process element abundances, we investigated the possible 1P–2P differences in Na and Ba abundances in 261 RGB stars in 47 Tuc. In their earlier study of 110 HB stars in 47 Tuc, Gratton et al. (2013) have suggested that there may exist a weak [Ba/Fe] – [Na/O] correlation. Therefore, our main goal was to verify whether a Na–Ba correlation or a 1P–2P Ba abundance difference could be detected in our RGB stellar sample that is more than two times larger than that used in the study of Gratton et al. (2013), and is the largest sample of stars for which Ba abundance was determined in this GGC.

3.1. Observational data

The sample of RGB stars used for Na–Ba abundance analysis largely overlaps with (but is not identical to) the sample that we used to study Zr abundance in 47 Tuc. The starting point was the same set of spectra described in Sect. 2 above, to which we added observations in the HR14A setting that was used for the determination of Ba abundances.

Stars common to multiple programs were identified by cross-matching their coordinates within a 1 arcsec radius. In total, 14 stars were common between the samples 073.D-0211(A) and 088.D-0026(A), 23 stars between 072.D-0777(A) and 088.D-0026(A), 17 stars between 072.D-0777(A) and 073.D-0211(A), and 5 stars were common across all three samples (Table A). The abundances of these stars were computed by averaging the results obtained from the spectra of the individual observing programs.

The determination of radial velocities, proper motions, and cluster membership for the stars in the Ba sample was conducted in the same manner as in the analysis of Zr abundance detailed in Sect. 2.2.

The final target sample consisted of 261 unique RGB stars with Fe, Na, and Ba abundances. This sample is slightly larger than the one used in Sect. 2 because it includes stars with $T_{\rm eff} > 4800$ K, which were excluded from the Zr analysis.

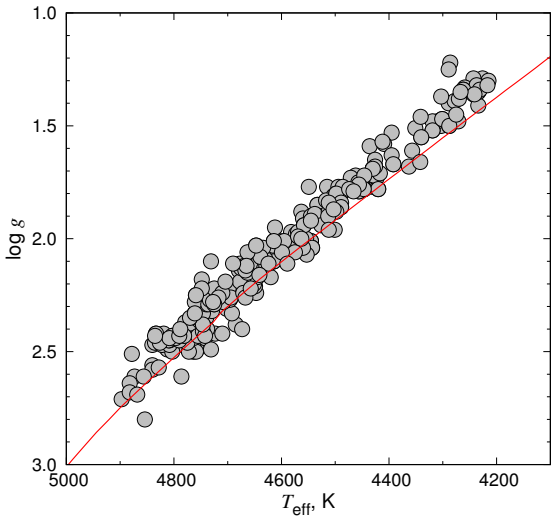

Fig. 3.1. Target RGB stars in the $T_{\rm eff} - \log g$ plane. The red line is Yonsei-Yale (Kim et al. 2002) isochrone (12 Gyr, [M/H] $= -0.68$, [α/Fe] $= +0.4$).

3.2. Atmospheric parameters

For the majority of targets (228 stars in total) in the Ba analysis sample, atmospheric parameters were determined during the Zr abundance analysis (Sect. 2). For the remaining 33 stars, effective temperatures were determined using the photometry from Bergbusch & Stetson (2009) and the color-$T_{\rm eff}$ calibration from by Ramírez & Meléndez (2005). The obtained values were then verified by examining for trends in the Fe abundance-lower excitation potential plane. Typically, the slopes were close to zero, indicating a strong agreement between the photometrically and spectroscopically determined effective temperatures. Surface gravities were determined using the classical equation that relates stellar mass, luminosity, effective temperature, and surface gravity (Eq. 2.1). Microturbulence velocities were determined by ensuring a zero trend in the Fe abundance-equivalent width plane, while keeping photometric effective temperature fixed (see Dobrovolskas et al. 2021 for details). The positions of the target RGB stars used in the Ba abundance analysis are shown in Fig. 3.1. The atmospheric parameters for the individual target stars are provided in Table F.1.

3.3. Abundance analysis

For the majority of targets (228 stars in total) in the Ba star sample, the Na and Fe element abundances were determined during the Zr abundance analysis (Sect. 2). For the remaining 33 RGB stars, which were not included in the Zr

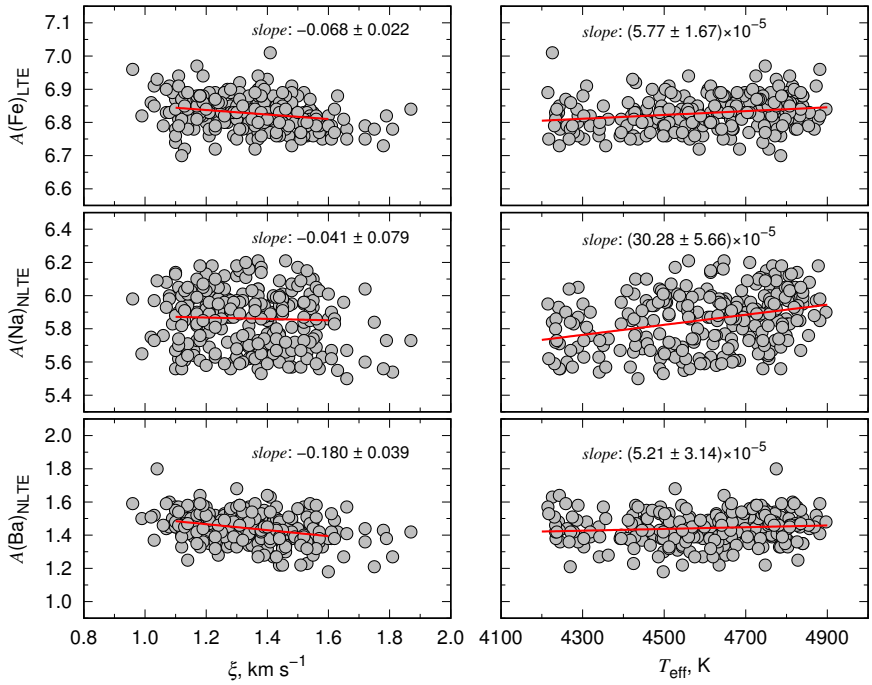

Fig. 3.2. Fe (top row), Na (middle row), and Ba (bottom row) abundances plotted against the microturbulence velocity (left column) and effective temperature (right column). In all panels, the linear fits to the data are shown as the solid red lines.

sample (Sect. 2), the Na and Fe abundances were determined following procedures identical to those previously described. The oscillator strength values for the Ba lines were taken from the VALD3 database (Ryabchikova et al. 2015).

3.3.1. Reference abundances in the Sun

We used Solar abundance of Ba that was determined with the NLTE techniques (Dobrovolskas et al. 2021; see also Sect. 3.3.4). This abundance value, $A(\mathrm{Ba}) = 2.17$, is in a reasonable agreement with $A(\mathrm{Ba})_{\mathrm{1D\ NLTE}} = 2.07$ and $A(\mathrm{Ba})_{\mathrm{3D\ NLTE}} = 2.28$ which were determined by Gallagher et al. (2020) and also matches with the meteoritic value of 2.17 ± 0.02 from Lodders (2003). Solar abundances of Fe and Na were the same as in the analysis of Zr abundance (Sect. 2.5.1).

3.3.2. Determination of Fe abundance

The mean obtained Fe abundance value in the sample of 261 stars was $\langle[\mathrm{Fe/H}]\rangle = -0.75 \pm 0.05$ (the error denotes the standard deviation due to the

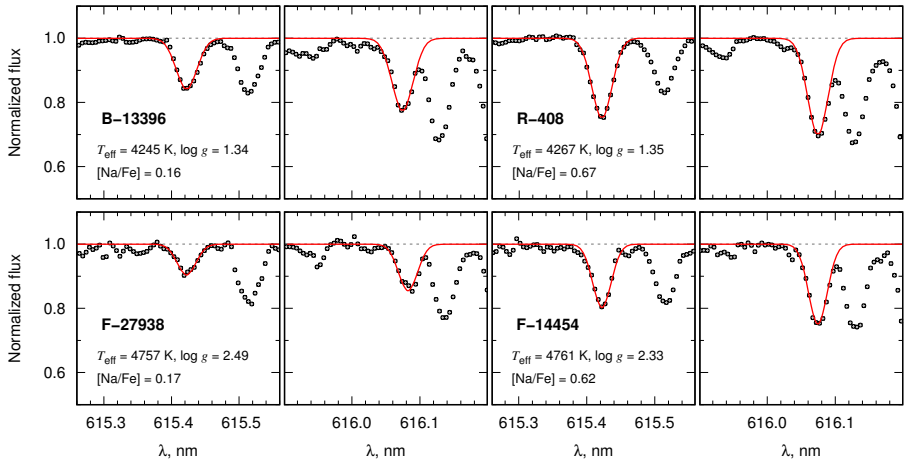

Fig. 3.3. Examples of the observed (black dots) and best-fitted synthetic Na I line profiles (red lines) in the GIRAFFE spectra of the target stars characterised by different Na abundances and effective temperatures ($T_{\rm eff} \approx 4250$ K, top row; $T_{\rm eff} \approx 4750$ K, bottom row). The continuum level is shown as the gray dashed line.

star-to-star abundance scatter), and it agrees well with the values determined in the other studies, e.g. $\langle$[Fe/H]$\rangle = -0.74 \pm 0.05$ from Carretta et al. (2009b), 114 RGB stars. Fe abundances that were determined in all target stars of this sample are shown in the top row of Fig. 3.2.

3.3.3. Determination of Na abundance

Abundances of Na were determined using the same techniques described in Sect. 2.5.3 above. We show the examples of a few of the best-fitted Na I lines in the 1P (Na-poor) and 2P (Na-rich) population stars in Fig. 3.3. Abundances of Na that were determined in all target stars are shown in the middle row of Fig. 3.2. Depending on the effective temperature and strength of the line, the Na NLTE abundance corrections, $\Delta_{\rm 1D\,NLTE-LTE} = A({\rm Na})_{\rm 1D\,NLTE} - A({\rm Na})_{\rm 1D\,LTE}$, were in the range of -0.07 to -0.27 (Table 3.1).

3.3.4. Determination of Ba abundance

The abundance of Ba was determined using a spectral synthesis method under the assumption of NLTE. Whenever possible, the two Ba II lines at 614.17 nm and 649.69 nm were used for the analysis, although in most instances, only the 614.17 nm line was available (Table 3.2). The spectral line profiles of Ba and the level departure coefficients were computed using a version of the `MULTI` code (Carlsson 1986) modified by Korotin et al. (1999). To account for the blending of the 614.17 nm Ba line with the Fe I line, synthetic spectra were calculated

Table 3.1. 1D NLTE abundance corrections for Na and Ba.

Element	λ, nm	W, pm	$\Delta_{\mathrm{1D\,NLTE-LTE}}$
$T_{\mathrm{eff}} = 4250$ K, $\log g = 1.35$			
Na-poor			
Na I	615.42	5.7	−0.08
Na I	616.07	8.7	−0.14
Ba II	614.17	19.0	−0.06
Na-rich			
Na I	615.42	9.6	−0.19
Na I	616.07	11.8	−0.27
$T_{\mathrm{eff}} = 4750$ K, $\log g = 2.40$			
Na-poor			
Na I	615.42	3.6	−0.07
Na I	616.07	5.4	−0.08
Ba II	614.17	14.8	−0.10
Na-rich			
Na I	615.42	6.3	−0.12
Na I	616.07	8.7	−0.15

Table 3.2. Atomic parameters of Na I and Ba II lines used in this study.

Element	λ, nm	χ, eV	$\log gf$	$\log \gamma_{rad}$ [a]	$\log \frac{\gamma_4}{N_e}$ [b]	$\log \frac{\gamma_6}{N_H}$ [c]
Na I	615.4225	2.102	−1.547	7.85	−4.39	−7.28
Na I	616.0747	2.104	−1.246	7.85	−4.39	−7.28
Ba II	614.1730	0.704	−0.076	8.20	−5.48	−7.47
Ba II	649.6910	0.604	−0.377	8.10	−5.48	−7.47

[a] Mashonkina & Bikmaev (1996); [b] Kupka et al. (2000); [c] Korotin et al. (2011)

using the `SynthV` code (Tsymbal 1996). In this process, the NLTE departure coefficients for Ba were computed with the `MULTI` code, while the Fe I line was treated under the assumption of LTE. The model atom for Ba employed in these computations was identical to that used in Andrievsky et al. (2009), consisting of 31 levels of Ba I, 101 levels of Ba II ($n < 50$), and the ground level of Ba III. The model includes 91 bound-bound transitions between the lowest 28 energy levels of Ba II ($n < 12$, $l < 5$). For the $5\mathrm{d}\,^2\mathrm{D}$ and $6\mathrm{p}\,^2\mathrm{P}^0$ levels, the fine structure was incorporated as per the guidelines in Andrievsky et al. (2009). The hyperfine structure of the 649.69 nm Ba line was approximated using three components as suggested by Andrievsky et al. (2009).

For the observational program 088.D-0026(A), Ba abundance was determined using both the 614.17 nm and 649.69 nm spectral lines; for all others, only the 614.17 nm line was available for abundance determination. Where applicable, the final Ba abundance was determined by averaging the abundance estimates from both lines. Unlike the case of Zr (Sect. 2.5.7), the potential

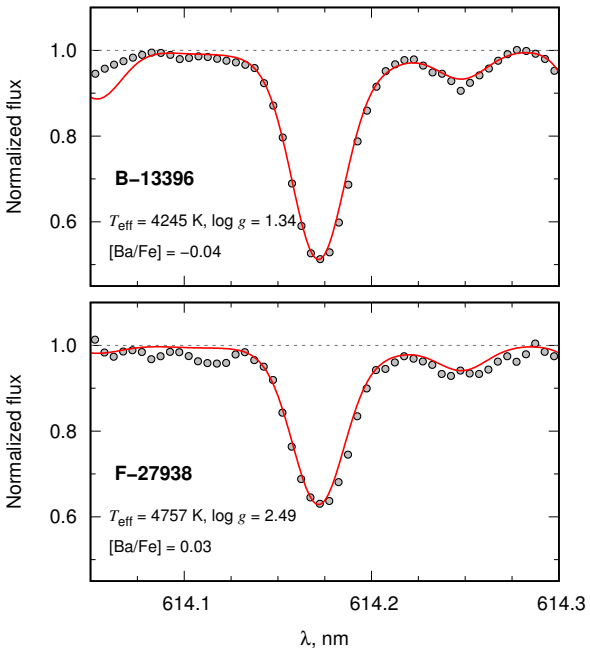

Fig. 3.4. Examples of the observed (black dots) and best-fitted synthetic spectra in the vicinity of Ba II lines (red lines) in the GIRAFFE spectra of the target stars characterised by different effective temperatures ($T_{\rm eff} \approx 4250$ K, top panel; $T_{\rm eff} \approx 4750$ K, bottom panel). The continuum level is shown as the gray dashed line (see Dobrovolskas et al. 2021 for details).

influence of CN on Ba abundance determination was not considered because of the strong Ba II lines, with the estimated effect being less than 0.01 dex. Two typical synthetic spectrum fits of the Ba II 614.17 nm line for stars characterized by different effective temperatures are presented in Fig. 3.4. The Ba abundances are shown in the bottom row of Fig. 3.2 and provided in Table F.1 for each individual star. The $\Delta_{\rm 1D,NLTE-LTE}$ abundance corrections for Ba, as shown in Table 3.1, increase with higher effective temperatures, ranging from 0.06 to −0.10 dex. The average Ba abundance determined from the sample of 261 RGB stars in 47 Tuc is $\langle {\rm [Ba/Fe]}_{\rm 1DNLTE} \rangle = -0.01 \pm 0.06$ dex (the error here is standard deviation due to star-to-star abundance variation).

3.3.5. Errors in the determined Fe, Na, and Ba abundances

The uncertainties in the determined Fe, Na, and Ba abundances were calculated in the same manner as described in Sect. 2.5.6. Briefly, we used two ATLAS9 models, one with $T_{\rm eff} = 4250$ K and $\log g = 1.35$, and the other with $T_{\rm eff} = 4750$ K and $\log g = 2.40$. Abundance errors for temperature, surface gravity, microturbulence velocity, line profile fitting and continuum determina-

Table 3.3. [Ba/Fe] – [Na/Fe] abundance correlation coefficients in the full sample of 261 RGB stars in 47 Tuc and in the sub-samples divided into $\Delta T_{\rm eff}$ = 100 K-wide bins; N is the number of stars in the given (sub-)sample.

Pearson		Spearman		Kendall	
r	p	ρ	p	τ	p
Full sample, N = 261					
−0.18	3×10^{-3}	−0.20	1×10^{-3}	−0.14	7×10^{-4}
$4200 \leq T_{\rm eff} < 4300$, N = 23					
−0.11	0.61	−0.09	0.68	−0.06	0.68
$4300 \leq T_{\rm eff} < 4400$, N = 15					
−0.15	0.60	−0.17	0.54	−0.16	0.42
$4400 \leq T_{\rm eff} < 4500$, N = 35					
−0.38	0.02	−0.34	0.05	−0.24	0.04
$4500 \leq T_{\rm eff} < 4600$, N = 42					
−0.15	0.35	−0.15	0.32	−0.11	0.31
$4600 \leq T_{\rm eff} < 4700$, N = 48					
−0.41	4×10^{-3}	−0.41	3×10^{-3}	−0.28	5×10^{-3}
$4700 \leq T_{\rm eff} < 4800$, N = 66					
−0.11	0.39	−0.16	0.20	−0.12	0.15
$4800 \leq T_{\rm eff} < 4900$, N = 32					
0.15	0.42	0.04	0.83	0.03	0.84

tion were determined, which in case of Ba were 80 K, 0.1 dex, and 0.1 km s^{-1}, respectively. To assess the error due to continuum placement, we calculated the standard deviation of the continuum, $\sigma_{\rm cont}$, adjacent to the analyzed spectral line. We then adjusted the continuum level by $\pm 1\sigma_{\rm cont}$ from the adopted level and redetermined the abundances.

The uncertainty in line profile fitting was estimated by computing the standard deviation of the difference between the observed line profile and the best-fitting synthetic profile. The synthetic spectrum was then altered by $\pm 1\sigma$ and the resultant change in abundance was calculated.

Subsequently, the overall uncertainties for Fe, Na, and Ba abundances were computed by summing the individual errors in quadrature. The typical abundance errors calculated this way are presented in Table E.1.

3.4. Results and discussion

3.4.1. Possible Ba–Na (anti-)correlation in the RGB stars in 47 Tuc?

The determined [Ba/Fe] abundance ratios show a weak but statistically significant anti-correlation with the [Na/Fe] abundance ratios (Fig 3.5). Assuming

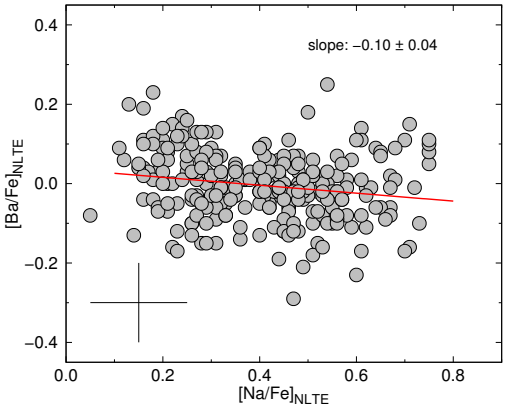

Fig. 3.5. [Ba/Fe] abundance ratios determined in 261 RGB stars in 47 Tuc, plotted versus their [Na/Fe] abundance ratios. Typical abundance error bars are shown in the bottom left corner. The linear fit to the data is shown as the solid red line.

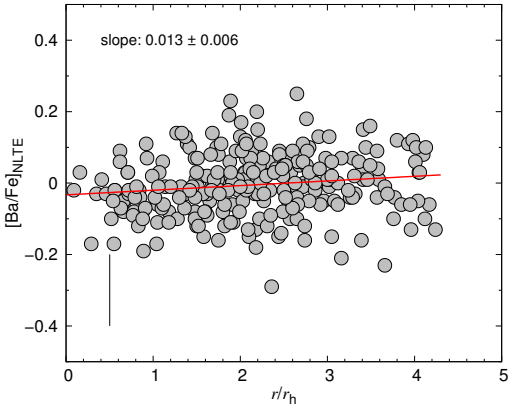

Fig. 3.6. [Ba/Fe] abundance ratios obtained in 261 RGB stars in 47 Tuc, plotted versus relative radial distance from the cluster center. Cluster half-mass radius, $r_{\rm h} = 174$ arcsec, was taken from Trager et al. (1993). Linear fit to the data is marked as the solid red line. Typical abundance error is shown as the vertical bar in the bottom left corner.

the null hypothesis of no correlation between the [Ba/Fe] and [Na/Fe] abundance ratios, the probability of obtaining the observed $r_{\rm P}$ value by chance is $p_{\rm P} = 2.9 \times 10^{-3}$, as determined by using Student's t-test (Table 3.3). For Spearman's and Kendall's rank correlation coefficients, we obtained the following values: $\rho_{\rm S} = -0.20$ with $p_{\rm S} = 1.3 \times 10^{-3}$, and $\tau_K = -0.14$ with $p_{\rm K} = 6.9 \times 10^{-4}$, respectively.

We also investigated the potential correlation between the determined

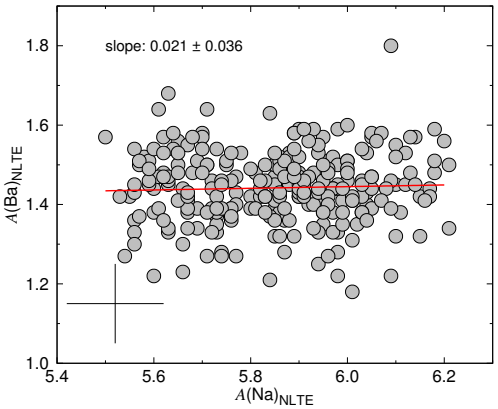

Fig. 3.7. Absolute abundances of Ba and Na in the $A(\mathrm{Ba}) - A(\mathrm{Na})$ plane. Typical abundance error bars are shown in the bottom left corner. The linear fit to the data is shown as the solid red line.

[Ba/Fe] abundances and the radial distance from the center of the cluster. For this purpose, we used the coordinates of the center of 47 Tuc, $\alpha_0(J2000) = 6.023625\,\mathrm{deg}$ and $\delta_0(J2000) = -72.081276\,\mathrm{deg}$, as reported by Baumgardt et al. (2019), along with the half-mass radius of $r_\mathrm{h} = 174\,\mathrm{arcsec}$, taken from Trager et al. (1993). This analysis suggests a weak correlation in the $[\mathrm{Ba/Fe}] - r_\mathrm{h}$ plane, with $r_\mathrm{P} = 0.14$ and $p_\mathrm{P} = 0.019$; Spearman's and Kendall's rank correlation coefficients yielded similar results (Fig. 3.6).

Interestingly, these findings suggest that in the first population of RGB stars in 47 Tuc, characterized by lower Na abundance, Ba appears to be more abundant compared to the second population stars, which exhibit higher Na abundance (Fig. 3.5). Prior studies have shown that second population stars tend to be more centrally concentrated not only in this cluster but also in other GGCs (e.g. Kučinskas et al. 2014). Consequently, we anticipated observing a weak anti-correlation in the $[\mathrm{Ba/Fe}] - r_\mathrm{h}$ plane, which our findings contradict (Fig. 3.6). This result poses a challenge from a nucleosynthesis perspective, given that Ba is predominantly produced in rotating massive stars during the central helium-burning phase or, alternatively, in intermediate-mass AGB stars through the main s-process. The observed correlation in the $[\mathrm{Ba/Fe}] - r_\mathrm{h}$ plane would suggest a mechanism that led to the destruction rather than synthesis of Ba in the second population stars.

However, when plotting Ba and Na abundances in the absolute abundance plane, $A(\mathrm{Ba}) - A(\mathrm{Na})$, the previously detected Ba–Na anti-correlation disappears (Fig. 3.7). We obtain $r_\mathrm{P} = 0.04$ and $p_\mathrm{P} = 0.52$ for the Pearson correlation coefficient, $\rho_S = 0.03$ and $p_\mathrm{S} = 0.63$ for Spearman's, and $\tau_K = 0.03$ and $p_\mathrm{K} = 0.53$ for Kendall's rank correlation coefficients. Additionally, no trend is detected in the $A(\mathrm{Ba}) - r_\mathrm{h}$ plane, where $r_\mathrm{P} = -0.002 \pm 0.006$ and $p_\mathrm{P} = 0.984$.

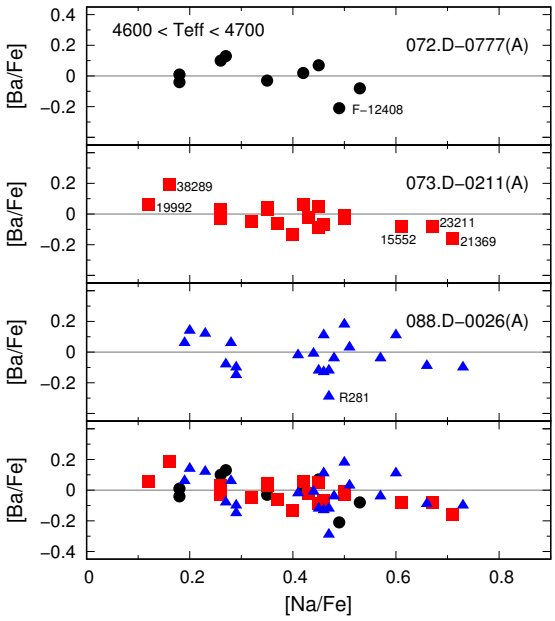

Fig. 3.8. Ba and Na abundances in the effective temperature range $4600 < T_{\rm eff} < 4700$ K. Labels next to the outlying data points show identifications of the stars. Observational program numbers are shown in top right corner of each plot.

Taken together, these results suggest that the observed anti-correlation in the [Ba/Fe] – [Na/Fe] plane and correlation in the [Ba/Fe] – $r_{\rm h}$ plane is caused by the variation in Fe abundance.

In Table 3.3, we present the [Ba/Fe] – [Na/Fe] abundance correlation coefficients for sub-samples divided into $\Delta T_{\rm eff} = 100$ K-wide bins. Here the data shows that the Ba–Na anti-correlation is detectable only in one effective temperature bin, $4600 \leq T_{\rm eff} < 4700$ K, with a potential weaker trend in the $4400 \leq T_{\rm eff} < 4500$ K bin. No statistically significant correlations are detected in any other effective temperature bins. These results suggest that the observed anti-correlation in the full sample of 261 RGB stars is caused by some of the stars in the effective temperature range 4600 and 4700 K, with higher and lower Ba abundance in the lower and higher Na abundance ends. If the three stars, 19992, 38289, and 21369, are removed from the $4600 < T_{\rm eff} < 4700$ K bin, the statistically significant anti-correlation within this temperature range disappears. These outlier stars are illustrated in Fig. 3.8.

All three elements analyzed in this section (Fe, Na, and Ba) exhibit trends with microturbulence velocity (Fig 3.2). The hotter stars ($T_{\rm eff} \geq 4700$ K) are fainter, and the quality of their observed spectra is lower, potentially leading to underestimated microturbulence velocities in this effective temperature

range. When determining microturbulence velocities for these stars, a slight overestimation of the continuum may result in systematically higher abundances derived from weaker Fe I lines compared to stronger lines. As a result, in order to eliminate the trend of Fe abundance with equivalent width, lower microturbulence velocity values would be needed.

The Ba II spectral lines analyzed in this study are the strongest of the three elements examined, resulting in Ba abundances showing the strongest correlation with microturbulence velocities. Therefore, the spurious anti-correlation in the [Ba/Fe] – [Na/Fe] plane could also be created in part by the overestimation of Ba abundances in the stars defined by the lowest microturbulence velocities (those with the highest effective temperatures).

In summary, the anti-correlation in the [Ba/Fe]$-$[Na/Fe] plane and the correlation in the [Ba/Fe] $- r_{\rm h}$ plane are likely caused by systematic deviation in Ba abundances among some stars with the highest and lowest Na abundances within the $4600 \leq T_{\rm eff} < 4700$ K effective temperature bin. This deviation in a single $T_{\rm eff}$ bin can not be explained by e.g. the lower quality of the spectra, because for the hotter and therefore fainter stars there is no such correlation. Furthermore, there is no astrophysical justification for such a correlation to exist within a very narrow range of effective temperatures. Additionally, the lack of detection of such a correlation in the analysis of 110 RGB stars in the same 47 Tuc globular cluster by D'Orazi et al. (2010) indirectly supports our conclusion that the [Ba/Fe] $-$ [Na/Fe] anti-correlation observed in our data is spurious. However, it would be intriguing to investigate whether correlations between heavy s-process and light elements, like Ba–Na or others, can be detected in other globular clusters, especially in light of the Zr–Na correlation that was detected in the analysis done in Sect. 2.

3.4.2. Average Ba abundance in the RGB stars in 47 Tuc

So far, Ba abundance in the stars of the globular cluster 47 Tuc has been analysed by several authors. In one of the earliest studies, James et al. (2004) investigated the Ba abundances of eight SGB and TO stars. The authors reported a [Ba/Fe] abundance ratio of +0.35 for the SGB stars and a lower ratio of +0.22 for the TO stars. These abundance values are higher than those obtained in our study ($\langle [{\rm Ba/Fe}]_{\rm 1D\ NLTE} \rangle = -0.01 \pm 0.06$), especially considering that the average Ba abundance correction is approximately -0.10 dex.

In one of the most comprehensive studies of Ba abundances in globular clusters conducted by D'Orazi et al. (2010), where 1200 stars across 15 GGCs were analyzed, the authors determined a mean value of $\langle [{\rm Ba/Fe}]_{\rm 1D\ LTE} \rangle = 0.15 \pm 0.06$ (the error represents the standard deviation due to natural star-to-star abundance variation) in a sample of 110 RGB stars in 47 Tuc. Adjusted for the NLTE–LTE correction (approximately -0.10 dex), their mean Ba abundance in the 47 Tuc, $\langle [{\rm Ba/Fe}]_{\rm 1D\ LTE} \rangle = 0.05 \pm 0.06$, agrees well with the one obtained

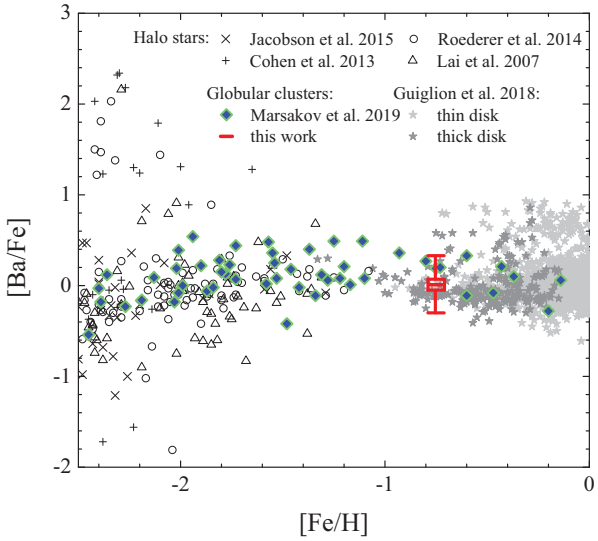

Fig. 3.9. Abundance of Ba in the GGCs (compilation by Marsakov et al. 2019) and Galactic field stars (thin and thick disk stars: Guiglion et al. 2018, halo stars: Lai et al. 2007; Cohen et al. 2013; Roederer et al. 2014; Jacobson et al. 2015). Average [Ba/Fe] ratio obtained in 261 RGB stars in 47 Tuc is marked by the red symbol where the 25th and 75th percentiles and the average values are indicated by the horizontal bars, while the extent of the whiskers correspond to the minimum and the maximum abundance values observed in this cluster.

in our analysis.

In their NLTE abundance analysis of 13 RGB stars in 47 Tuc, Thygesen et al. (2014) found a significantly higher mean abundance, [Ba/Fe] = 0.28±0.07. A possible explanation for this discrepancy could lie in the differences in determined microturbulence velocity and surface gravity values. Among the 6 stars common to our sample of 261 stars and their sample of 13, we found that, on average, our determined surface gravity and microturbulence velocity values were higher by 0.30 dex and 0.33 $\mathrm{km\,s^{-1}}$, respectively. Correcting for these discrepancies, our determined Ba abundances would increase by approximately 0.20 dex, which would make them agree with the mean abundance value reported by Thygesen et al. (2014).

3.4.3. Implications for the chemical evolution scenarios of 47 Tuc

The results of Ba analysis of 261 RGB stars in 47 Tuc suggest that the 2P stars exhibit the same Ba abundance as the 1P stars (Fig. 3.7 and also see Sect. 3.4.1 about the spurious anti-correlation in the [Ba/Fe] − [Na/Fe] plane), indicating no enrichment or depletion occurred in the early stages of 47 Tuc evolution. This result is supported by the analysis of 110 RGB stars in 47 Tuc con-

ducted by D'Orazi et al. (2010), which also suggests a lack of correlations/anti-correlations between Ba and Na abundances. These results contradict those obtained by Gratton et al. (2013), who found a weak but statistically significant Ba–Na correlation in their analyzed sample of 114 RHB stars in the same globular cluster. On the other hand, the observed Ba–Na trend could be partially or entirely explained by the correlation between the [Na/O] abundance ratio and effective temperature along the HB, as demonstrated by Grevesse et al. (2015).

Our determined barium-to-iron abundance ratio in the 261 RGB stars of 47 Tuc, $\langle [\mathrm{Ba/Fe}]_{\mathrm{1D\ NLTE}} \rangle = -0.01 \pm 0.06$, agrees well with abundances obtained at similar metallicities in other GGCs or in Galactic disc and halo stars (Fig. 3.9). This fact taken together with a small spread of Ba abundance, ± 0.06 dex (this can be fully accounted for by the Ba abundance determination error, $\sigma_{\mathrm{A(Ba)}} \approx 0.12$ dex), suggests that the current Ba abundance reflects that of the primordial gas cloud from which 47 Tuc has formed and that this abundance was not changed significantly during the evolution of this GGC.

Considering both the observed Zr–Na correlation (Sect. 2) and the fact that the Ba abundance seems to be constant in both populations of 47 Tuc, it appears that the stars in this GGC were enriched only by some of the s-process elements. This indicates that the polluter stars, which synthesized Zr and altered the abundances of other light chemical elements (e.g., Li, N, O, Mg, and Al, as seen in previous studies such as Bastian & Lardo 2018), did not produce Ba. Theoretical yields from models of low- and intermediate-mass AGB stars suggest that both Zr and Ba should be synthesized in substantial amounts by these stars (Cristallo et al. 2015). A similar conclusion is reached from the explosive nucleosynthesis yields of fast-rotating massive stars, which indicate simultaneous production of both elements (Limongi & Chieffi 2018). Furthermore, in the latter scenario, we should also observe enrichment of Fe-group and r-process elements in the 2P stars, as fast-rotating massive stars are expected to produce these elements. However, such enrichment has not yet been observed in Type I GGCs (e.g., Bastian & Lardo 2018; Gratton et al. 2019). Therefore, it would be highly desirable to investigate whether correlations exist between the other s-process and light chemical elements in 47 Tuc and other Type I GGCs.

4. Abundance of Sr in the atmospheres of RGB stars in the globular cluster 47 Tuc

In Sect. 2, we performed an analysis of 237 RGB stars in the Galactic Globular Cluster 47 Tuc, the results of which showed an existence of a possible correlation between the light s-process element Zr and Na. It would be useful to check whether the abundances of other s-process elements from the 'first s-process peak' (e.g. Rb, Sr, Y), produced under conditions similar to Zr, also correlate with the abundances of light chemical elements as is the case for Zr. Moreover, because different polluters produce different amounts of s-process elements, the ratios of the abundances of these chemical elements, for example [Sr/Zr], could be compared with the model predictions of yields of AGB and FRMS polluter stars and this, in turn, would allow to place more stringent constraints on the possible polluters and pollution scenarios.

To date, the sole investigation of Sr abundance in 47 Tuc involved an analysis of eight SGB and three TO stars (James et al. 2004), which found neither significant Sr abundance spread nor correlations with light element abundances. This outcome could be attributed, at least partially, to the limited sample size, especially considering the subtle spreads and/or weak correlations expected for s-process elements (see e.g. Sect. 2; also Fernández-Trincado et al. 2021; 2022). Consequently, the goal here was twofold: (a) to determine Sr abundances in a larger star sample, and (b) to check whether any 1P–2P abundance differences and/or correlations may exist in case of Sr in this GGC.

4.1. Observational data

The analysis of Fe, Na, and Sr abundances was carried out using archival spectra from four observational programs conducted with the `UVES` spectrograph on the VLT UT2 telescope (programs 072.D-0777(A), PI: Francois; 073.D-0211(A), PI: Carretta; 084.B-0810(A), 086.B-0237(A), PI: Sbordone; 088.D-0026(A), PI: McDonald). To our knowledge, these spectra, accessible through the ESO Advanced Data Products (ADP) archive[1], are the only ones from 47 Tuc in which at least one Sr line could be reliably measured for abundance analysis.

The observation log is provided in Table 4.1. All target spectra were continuum normalized using the `splot` task in the `IRAF` package (Tody 1986). The signal-to-noise ratio typically ranged from $\sim 90 - 160$ at 640 nm. Radial velocities were calculated using the `fxcor` task in `IRAF`, with cross-correlation performed against a template synthetic spectrum, computed using the average atmospheric parameters of the studied stars ($T_{\rm eff} = 4155$ K, $\log g = 1.18$).

[1] `http://archive.eso.org/wdb/wdb/adp/phase3_spectral/form`

Table 4.1. Spectroscopic data used in Sr abundance determinations.

Programme	Date of observation	$\lambda_{\text{interval}}$, nm	R	Exposure, s	Number of targets
072.D-0777(A)	2003-10-20	472 – 683	∼50500	3000–8600	10
073.D-0211(A)	2004-06-26	472 – 683	∼50500	1600–4315	11
084.B-0810(A)	2009-11-16	472 – 683	107200	3600	5
086.B-0237(A)	2010-10-03	472 – 683	107200	3600	8
088.D-0026(A)	2011-11-26	472 – 683	∼48000	4080–8151	4

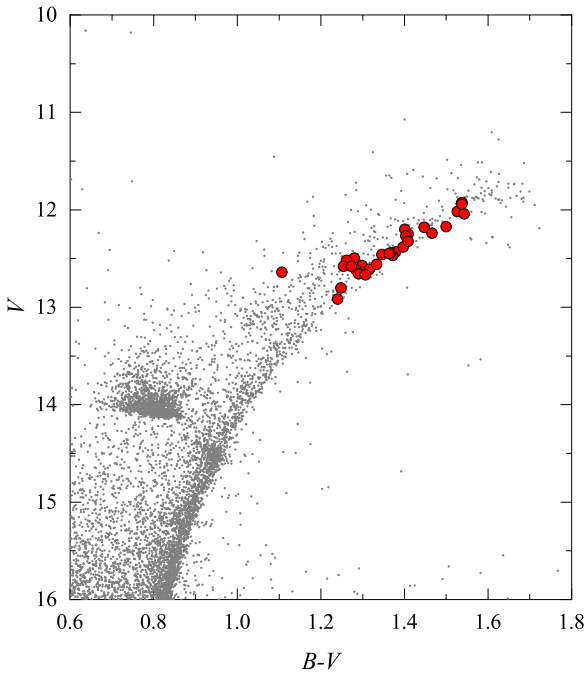

Fig. 4.1. Colour-magnitude diagram of 47 Tuc with the analysed in this work stars marked in red circles. Photometric measurements of cluster stars are taken from Bergbusch & Stetson (2009).

In the 072.D-0777(A) program, we excluded 6 stars due to poor quality of the spectra. These stars also exhibited the highest effective temperatures ($T_{\text{eff}} > 4500$ K) and generally had the weakest Sr I lines. An additional star was excluded due to its very high effective temperature ($T_{\text{eff}} = 6142$ K), the Sr I line was too weak for abundance determination. The final sample consisted of 31 stars, shown on the 47 Tuc colour-magnitude diagram in Fig. 4.1.

Furthermore, we investigated common stars between this `UVES` sample and the `GIRAFFE` sample used for Zr abundance determination in Sect. 2. Cross-correlation of star coordinates showed that there are 17 common stars. Their full spatial velocities (radial velocities plus proper motions from the *Gaia* DR3

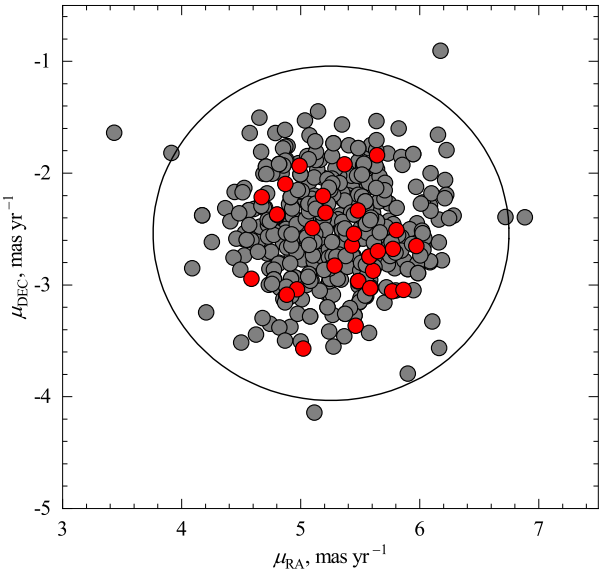

Fig. 4.2. Proper motions of the target RGB stars in 47 Tuc from the *Gaia* DR3 catalog (Gaia Collaboration et al. 2023). The red and gray symbols denote the star samples used in Sr analysis and Zr analysis, respectively. The black circle encompasses the region with a radius of 1.5 mas yr^{-1} from the mean cluster proper motion.

catalog; Gaia Collaboration et al. 2023) confirmed all sample stars as cluster members. For this verification, we compared their individual proper motions (taken from the *Gaia* DR3 catalog, Gaia Collaboration et al. 2023) against the average proper motion of 47 Tuc. Following Milone et al. (2018), a star was considered a cluster member if its proper motion differed by no more than 1.5 mas yr^{-1} from the mean proper motion of 47 Tuc, $\mu_{\rm RA} = 5.25$ mas yr^{-1} and $\mu_{\rm DEC} = -2.53$ mas yr^{-1} (Baumgardt et al. 2019). All selected targets met this criterion (Fig. 4.2).

4.1.1. Atmospheric parameters

The effective temperatures of the target stars were determined using the $T_{\rm eff} - (V - I)$ calibration from Ramírez & Meléndez (2005), along with photometric measurements for 47 Tuc from Bergbusch & Stetson (2009). Despite the availability of *Gaia* DR3 photometry for the target stars, we opted to use the photometry from Bergbusch & Stetson (2009) to maintain consistency with the abundances determined in Sect. 2 and Sect. 3.

Surface gravities were derived using the classic formula that relates effective temperature, stellar mass, luminosity, and surface gravity. We assumed a uniform stellar mass of 0.89 $M_{\odot}$ for all target RGB stars, as determined from the

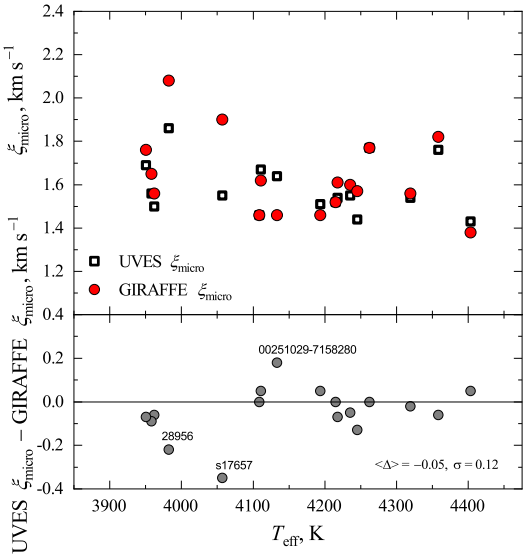

Fig. 4.3. Difference between the microturbulence velocities, $\xi_{\rm micro}$, determined from the Fe I lines in the UVES and GIRAFFE spectra. The mean difference between the two sets of values and their scatter around the mean (measured as standard deviation, σ) are shown in the bottom panel of the figure.

Yonsei-Yale isochrone[2] (12 Gyr, [M/H] = −0.68; Kim et al. 2002). While some systematical differences may be inferred from the comparison of the Yonsei-Yale isochrone and the stellar parameters derived from observations, the differences fall within the scatter between the isochrones computed by different groups ($\pm\,50$ K; e.g. Dotter et al. 2008; Pietrinferni et al. 2021). Additionally, the mean Fe abundance determined for the target stars using Fe I and Fe II lines agrees within 0.01 dex, indicating a good consistency between the $\log g$ values derived from photometry and those obtained through the ionization balance condition.

The microturbulence velocity, $\xi_{\rm micro}$, was individually determined for each target star by ensuring that Fe I lines with different equivalent widths (W) would provide the same Fe abundance. Strong Fe lines with EW > 16 pm were excluded due to their reduced sensitivity to changes in $\xi_{\rm micro}$. The list of Fe I lines used is provided in Table B.1.

Discrepancies between microturbulence velocities determined in this analysis of Sr using UVES spectra and those derived in Zr analysis (see Sect. 2), which utilized GIRAFFE spectra for the 17 common stars, are shown in Fig. 4.3. Microturbulence velocities generally match up to 0.10 km s^{-1}, with exceptions for the three cooler stars. The stronger spectral lines of these stars, combined with the lower resolution of the GIRAFFE spectra resulted in merged line wings,

[2]Version 2 from http://www.astro.yale.edu/demarque/yyiso.html

Table 4.2. Atomic parameters of the spectral lines used in this work.

Element	λ, nm	χ, eV	log gf	log $\gamma_{\rm rad}$	log $\frac{\gamma_4}{N_e}$	log $\frac{\gamma_6}{N_{\rm H}}$
Na I	615.4225	2.102	−1.547	7.85	−4.39	−7.28
Na I	616.0747	2.104	−1.246	7.85	−4.39	−7.28
Sr I	650.3991	2.259	0.320	7.69	−5.73	−7.72
V I	650.4165	1.183	−1.280	7.66	−6.06	−7.76

which made it more difficult to accurately determine the continuum level of the observed spectra. Therefore, microturbulence velocities obtained with the `UVES` spectra are more accurate. The atmospheric parameters for each star analyzed in this work are listed in Table H.1.

4.2. Abundance analysis

The abundances of Sr and Na were determined using the LTE spectral synthesis method. For Na abundances, we additionally applied NLTE abundance corrections that were obtained in Sect. 2.5.3. For the abundance determinations, we used 1D hydrostatic `ATLAS9` stellar model atmospheres with α-element (O, Ne, Mg, Si, S, Ar, Ca, Ti) enhanced chemical composition of $[\alpha/\mathrm{Fe}] = +0.4$ (Kurucz 1993; Sbordone 2005). Atomic line parameters for Fe, Na, Mg, and Sr were taken from the VALD3 database (Table 4.2). In the following sections we describe abundance determination process in more detail.

4.2.1. Determination of the Fe abundances

The 1D LTE Fe abundances were determined using the equivalent width method, where line equivalent widths were measured by fitting Gaussian profiles using the `splot` task in `IRAF`. The measured line equivalent widths, combined with `ATLAS9` stellar model atmospheres, were then used to calculate Fe abundances using the `WIDTH9` code (Sbordone 2005). We used 15–28 Fe I spectral lines, with excitation potentials ranging between 2.18 and 4.61 eV. To minimize the impact of NLTE effects, we excluded lines with excitation potentials lower than 2 eV. A comprehensive list of Fe I lines used in this study is presented in Table B.1. No statistically significant correlations were observed between the determined Fe abundances and the effective temperatures or microturbulence velocities of the stars (Fig. 4.4).

The average Fe abundance for the 31 target RGB stars, $\langle[\mathrm{Fe/H}]\rangle = -0.81 \pm 0.06$ (here the error represents the standard deviation due to star-to-star abundance variation), agrees with results from other studies: $\langle[\mathrm{Fe/H}]\rangle = -0.74 \pm 0.05$ by Carretta et al. (2009b) for 114 RGB stars; $\langle[\mathrm{Fe/H}]\rangle = -0.77 \pm 0.08$ by Wang et al. (2017) for 44 RGB stars. We adopted a Solar Fe abundance of

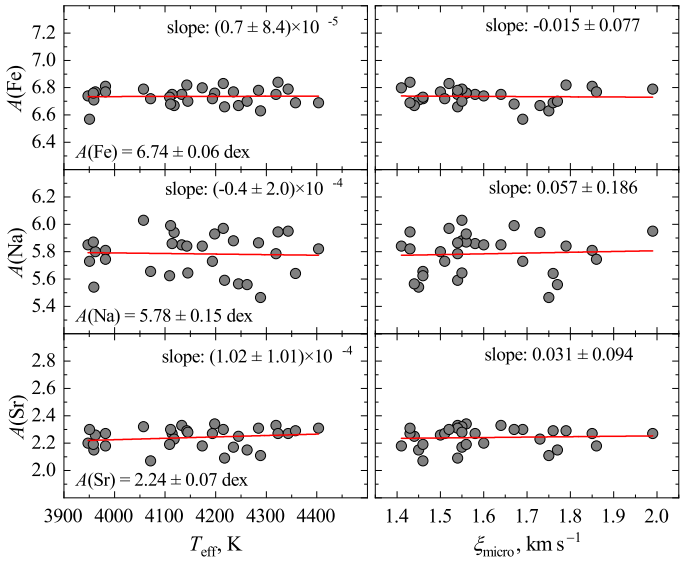

Fig. 4.4. Abundances in the target RGB stars plotted versus the effective temperature and microturbulence velocity, $\xi_{\rm micro}$, in individual stars. The linear fits to the data are shown as red lines.

$A({\rm Fe})_{\odot} = 7.55 \pm 0.06$, as determined in Sect. 2.5.1. The average measurement error for Fe abundance, $\sigma_{\rm i}$, is ∼0.17 dex (refer to Sect. 4.2.5 for further details). Fe abundances for each individual star are provided in Table H.1.

4.2.2. Determination of Na abundances

The 1D LTE Na abundances were determined by applying the spectral synthesis method, using the `SYNTHE` package to compute the synthetic line profiles (Sbordone 2005). Two Na I lines were used for the abundance determinations, with their central wavelengths located at 615.4225 and 616.0747 nm (Table 4.2). The abundances were determined by fitting synthetic Na I line profiles to those observed in the spectra. The obtained 1D LTE Na abundances were then corrected for NLTE effects by applying a uniform NLTE abundance correction of −0.14 dex. This correction was derived from the Na NLTE abundance corrections determined in Sect. 2.5.3, where NLTE Na abundances for a sample of 237 RGB stars were determined, covering the atmospheric parameter range of the target `UVES` stars analyzed here.

The solar Na abundance values, $A({\rm Na})^{\rm LTE}_{\odot} = 6.24$ dex, $A({\rm Na})^{\rm NLTE}_{\odot} = 6.17$ dex, were adopted from Sect. 2.5.1, where the same Na I lines were used. Examples of the synthetic profiles fitted to the Na I lines observed in the target star `UVES` spectra are shown in Fig. 4.5.

No dependence was observed between the Na abundances obtained from the two lines and either $T_{\rm eff}$ or $\xi_{\rm micro}$ of the target stars (Fig. 4.4). The Na

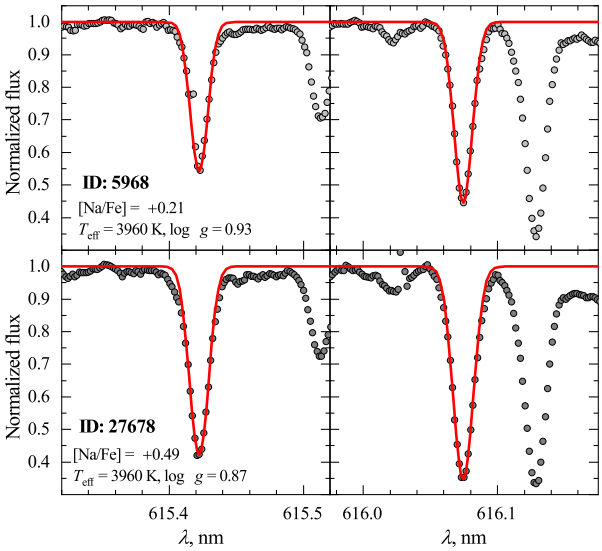

Fig. 4.5. Typical observed (dots) and best-fit synthetic LTE profiles of the Na I 615.4225 and 616.0747 nm lines (solid red lines) in the UVES spectra of two RGB stars in 47 Tuc: Na-poor (5968, 1P, top row) and Na-rich (27678, 2P, bottom row). The identification numbers of each star, their atmospheric parameters, and the determined Na abundances are provided in the leftmost panels of each row.

abundances determined from the two Na I lines also agree well (Fig. 4.6).

The mean [Na/Fe] ratio determined in 31 RGB stars is $\langle$[Na/Fe]$\rangle$ = 0.43 ± 0.12 (error here is the standard deviation due to star-to-star abundance scatter). This result agrees well with the Na abundance obtained using GIRAFFE spectra in Sect. 2.6, $\langle$[Na/Fe]$\rangle = 0.41 \pm 0.16$, and with those obtained in other studies, such as $\langle$[Na/Fe]$\rangle = 0.47 \pm 0.15$ (Carretta et al. 2009b, 147 RGB stars), $\langle$[Na/Fe]$\rangle = 0.36 \pm 0.18$ (Wang et al. 2017, 27 RGB stars). The Na abundances obtained using UVES and GIRAFFE spectra for 17 stars common to both samples are in good agreement as well (Fig. 4.7). The average error in Na abundance determination, $\sigma_{\rm i}$(Na), is $\sim$0.10 dex (see Sect. 4.2.5 for more details).

The range of Na abundances determined for the 31 target UVES stars is slightly smaller than that found using GIRAFFE spectra in Sect. 2.5.3, which is expected given the nearly eight times larger size of the GIRAFFE sample (Fig. 4.8). Nevertheless, the span in Na abundances in the target star can be deemed representative of the full sample. To verify this, we compared the mean Na abundances from the GIRAFFE and UVES spectra using a two-sample t-test to assess the statistical significance of differences between these two samples (under the null hypothesis that the two samples are identical). This analysis confirmed that there is no significant difference between the average Na abundances determined from GIRAFFE and UVES spectra ($p = 0.56$).

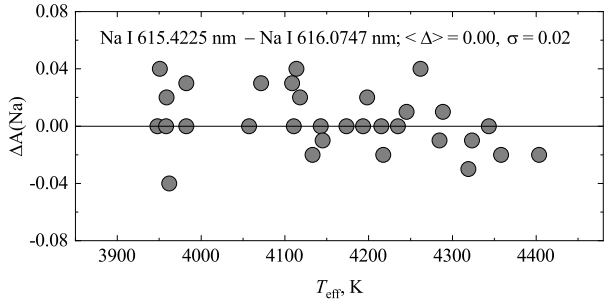

Fig. 4.6. Difference between the Na abundances obtained from the two Na lines plotted against effective temperature.

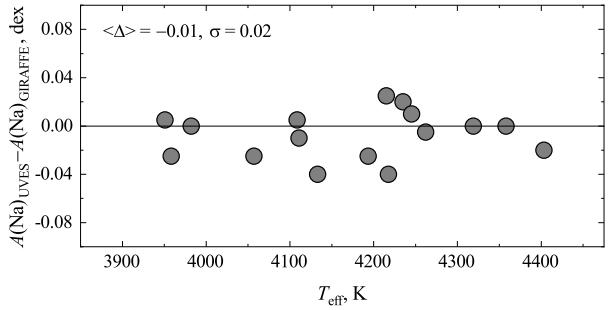

Fig. 4.7. Difference between the Na abundances determined from the `UVES` and `GIRAFFE` spectra (see Sect. 2) for 16 stars in common between the two samples.

Na abundances for each individual star are listed in Table H.1.

4.2.3. Determination of Sr abundances

For all target stars, 1D LTE abundances of Sr were determined using the spectral synthesis method, where synthetic spectra were calculated with the `SYNTHE` package (Sbordone 2005). We used the 650.3991 nm Sr I line for Sr abundance determinations. This was the only line strong enough for reliable Sr abundance determination in the existing `UVES` spectra. This Sr I line is situated on the wing of a much stronger V I (650.4165 nm) line. Consequently, we did our best to estimate the influence of various factors on the determined Sr abundance, especially the impact of V I and CN line blends (Sect. 4.3.2).

Since this line is blended with the V I (650.4165 nm) line (atomic line parameters for this line were obtained from the VALD3 database and are listed in Table 4.2), both V and Sr abundances were iteratively adjusted to achieve the best fit of the synthetic line. An example of the typical Sr line fit is displayed in Fig. 4.9, where we also illustrate how synthetic spectra change when Sr abundances are varied by ±0.20 dex.

Typical fits of the synthetic profiles to the Sr I lines observed in the spectra

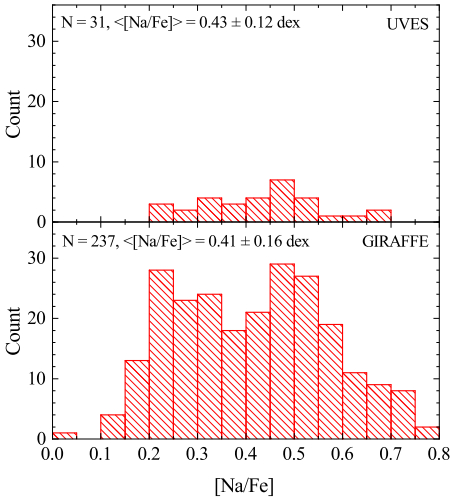

Fig. 4.8. A histogram of [Na/Fe] abundance ratio in the analysed here (Top) and stars studied in Sect. 2 (Bottom). The number of stars in each sample is shown in the top left corner, together with the average [Na/Fe] abundance ratio and standard deviation of the mean.

of 1P and 2P target stars are shown in Fig. 4.10.

The mean V abundance in 47 Tuc determined in this study, $\langle[\mathrm{V/Fe}]\rangle = 0.33 \pm 0.07$, differs from that determined by Thygesen et al. (2014) ($\langle[\mathrm{V/Fe}]\rangle = 0.17 \pm 0.09$) and Ernandes et al. (2018) ($\langle[\mathrm{V/Fe}]\rangle = -0.04 \pm 0.05$), where errors represent the standard deviation due to star-to-star scatter. Our target sample of 31 RGB stars included the 13 stars analyzed by Thygesen et al. (2014). For these 13 stars, we determined a mean V abundance of $\langle[\mathrm{V/Fe}]\rangle = 0.31 \pm 0.07$, but the effective temperatures used by Thygesen et al. (2014) were on average lower by 62 K. When we take into account the difference in T_{eff} and the fact that the V I lines we used yield systematically higher V abundances (by ~ 0.1 dex), our V abundance decreases by about 0.15 dex (see Table 4.3 in Sect. 4.2.4 for more detail), which then agrees well with the [V/Fe] values obtained by Thygesen et al. (2014). A similar case is seen with the [V/Fe] abundance ratios reported by Ernandes et al. (2018), who utilized different $\log gf$ values, solar Fe and V abundances, and individual target star Fe abundances. With these parameters from Ernandes et al. (2018), our V abundances decrease by ~ 0.3 dex, making them comparable to those determined by Ernandes et al. (2018, see Sect. 4.2.4 for additional details).

The determined Sr abundance does not vary with effective temperature or microturbulence velocity (Fig. 4.4). The mean [Sr/Fe] ratio for the 31 RGB stars obtained in this analysis is $\langle[\mathrm{Sr/Fe}]\rangle = 0.18 \pm 0.08$ (error denotes the standard deviation due to star-to-star abundance scatter).

In order to check for any pattern of population distribution along the ef-

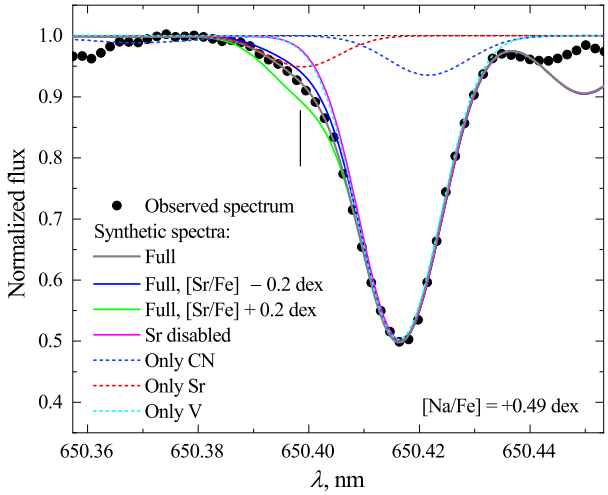

Fig. 4.9. Sr I line in the UVES spectrum of the program star 27678 (dots), overlaid with the synthetic spectrum (solid gray line) that was calculated using the ATLAS9 model with $T_{\rm eff} = 3958\,{\rm K}$, $\log g = 0.87$, [Fe/H] $= -0.79$, $\xi_{\rm micro} = 1.56\,{\rm km\,s^{-1}}$, $\xi_{\rm macro} = 6.20\,{\rm km\,s^{-1}}$, [Sr/Fe] $= 0.02\,{\rm dex}$. The other elemental abundances are solar-scaled (Grevesse & Sauval 1998). The other lines show synthetic spectra with the Sr abundance altered by $\pm 0.2\,{\rm dex}$ (solid blue and green lines, respectively), the full synthetic spectrum without the Sr I 650.3991 nm line (solid magenta line), the CN lines alone (dashed blue line), the Sr I line alone (dashed red line), and the V I 650.4165 nm line alone (dashed cyan line). Location of the Sr I line is indicated by the thin vertical line.

fective temperature range, we plotted the Sr abundances in the A(Sr) vs. $T_{\rm eff}$ plane, as shown in the top panel of Fig. 4.11. It is evident that that both the 1P and 2P stars are uniformly distributed across the entire $T_{\rm eff}$ range. We then categorized the target stars into two populations, adopting the classification from Carretta et al. (2009b), where the 1P stars are defined as those with [Na/Fe] ranging from $[{\rm Na/Fe}]_{\rm min}$ to $[{\rm Na/Fe}]_{\rm min} + 0.3$, and the 2P stars are those with higher Na abundances. The minimum [Na/Fe] value of 0.05 was determined using Na NLTE abundances from the GIRAFFE sample of 237 RGB stars (Sect. 2.5.3). Once more, it is clear that stars from both populations are evenly distributed throughout the entire $T_{\rm eff}$ range, as shown in the bottom panel of Fig. 4.11.

The average Sr abundance measurement error, $\sigma_{\rm i}$, is $\sim$0.11 dex (further details can be found in Sect. 4.2.5). The Sr abundances determined for each individual star are listed in Table H.1.

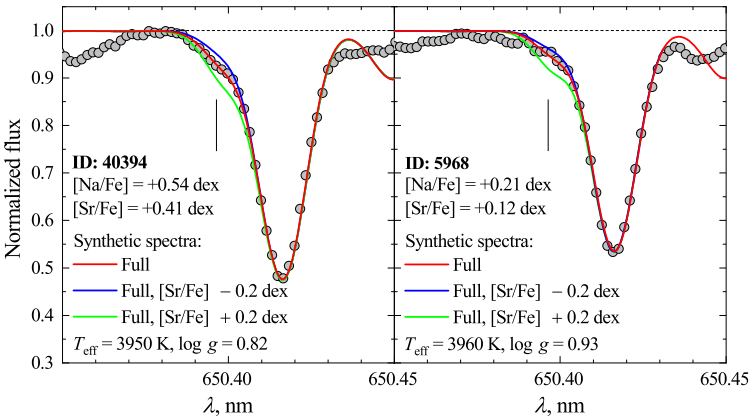

Fig. 4.10. Sr I line in the UVES spectrum of two RGB stars (dots) in 47 Tuc: Na-rich (40394, 2P, left panel) and Na-poor (5968, 1P, right panel) overlaid with the full synthetic spectrum (solid red line). The identification numbers of each star, their atmospheric parameters, and the determined Sr and Na abundances are provided in each panel. The solid blue and green lines show the full synthetic spectrum, with the Sr abundance altered by ±0.2 dex, respectively.

4.2.4. Vanadium abundance

As discussed in the previous section, along with Sr abundances, we also determined V abundances from a single 650.4165 nm V I line. The average V abundance ratio determined from 31 RGB stars using this line is $\langle$[V/Fe]$\rangle$ = 0.33 ± 0.07, here the error is the standard deviation due to star-to-star abundance variation. This value is significantly higher than that obtained by Ernandes et al. (2018) for 5 RGB stars in the same cluster ($\langle$[V/Fe]$\rangle$ = −0.04 ± 0.05), though their analysis used eight different V I lines. Our spectra included these eight lines, therefore, we determined V abundances from them in 3 RGB stars from our sample to assess whether the significant difference in determined V abundances persisted. The results of this test show that, even when using the same eight lines as Ernandes et al. (2018), our [V/Fe] abundance ratios were about 0.30 dex higher (columns 2, 4, and 6 in Table 4.3). Interestingly, these eight lines yielded V abundances up to 0.10 dex lower than the 650.4165 nm V I line initially used for our 31 target stars. In this case, the most likely cause is a blend with a CN line (see Fig. 4.9).

Moreover, Ernandes et al. (2018) calculated [V/Fe] abundance ratios using different loggf values, as well as Fe and V solar abundances (higher by 0.07 dex and lower by 0.05 dex, respectively) and the Fe abundances of individual target stars (higher by an average of 0.13 dex). When we recalculated the abundances using the parameters from their study – also considering that the 650.4165 nm V I line yields a higher abundance by up to 0.10 dex compared to the other eight V I lines, as indicated in Table 4.3 – our determined [V/Fe] abundance

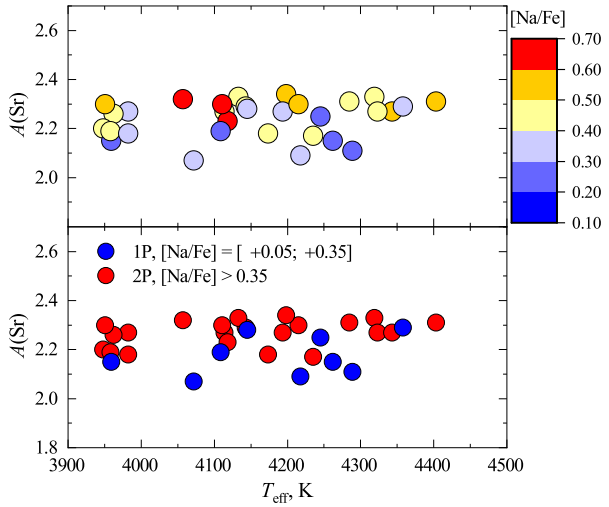

Fig. 4.11. Sr abundance plotted versus effective temperature. Top: the stars are marked in different colours according to their Na abundances, red – highest Na abundance, blue – lowest Na abundance. Bottom: blue – 1P stars ($[\mathrm{Na/Fe}] = [[\mathrm{Na/Fe}]_{\rm min}, [\mathrm{Na/Fe}]_{\rm min} + 0.3]$), red – 2P stars (those with higher Na abundances). The minimum Na value, $[\mathrm{Na/Fe}]_{\rm min}$, is taken from Sect. 2.

ratios decreased by up to 0.30 dex (columns 3, 5, and 7 in Fig 4.3), agreeing well with the average [V/Fe] ratio reported by Ernandes et al. (2018).

4.2.5. Errors in the determined abundances

The errors in the determined Fe, Na, and Sr abundances were obtained in the same way as in the Zr abundance analysis (see. Sect. 2.5.6 for more details). The results are presented in Table G.1.

4.2.6. Non-local thermodynamic equilibrium corrections for Sr

To our knowledge, NLTE corrections for the Sr I 650.3991 nm line are not available in the literature, although such corrections have been determined for other Sr I and Sr II lines. Specifically, NLTE corrections are available for the Sr I 460.7331 nm line and are $\sim +0.2$ dex for stars with metallicity and effective temperatures similar to those of our target stars (Bergemann et al. 2012). The dominating source of NLTE effects for the resonant Sr I 460.7331 nm line is overionization. Given the relatively low excitation energy of the Sr I 650.3991 nm line (> 2 eV), overionization – and thus the role of NLTE effects – is expected to be minimal. Regarding the Sr II lines, NLTE corrections tend to be negligible for stars with $[\mathrm{Fe/H}] > -2$ (see, e.g. Bergemann et al. 2012; Hansen et al. 2013).

NLTE corrections for Sr lines, other than those used in this study, have

Table 4.3. [V/Fe] abundance ratios determined in the sample of three RGB stars from our target sample with the highest [Na/Fe] abundance ratios (columns 2, 4, and 6). The star IDs are given in the first row of the table. The first column shows the central wavelengths of the V I spectral lines. Columns 3, 5, and 7 (marked with an asterisk) show the [V/Fe] abundance ratios that were recalculated with $\log gf$ values, Fe and V solar abundances, and the Fe abundances of individual target stars taken from Ernandes et al. (2018).

	00241344-7211263		s17657		s5270	
λ, nm	[V/Fe]	$[V/Fe]_*$	[V/Fe]	$[V/Fe]_*$	[V/Fe]	$[V/Fe]_*$
570.3560	0.21	−0.06	0.28	0.13	0.27	0.01
608.1440	0.32	0.08	0.32	0.20	0.34	0.11
609.0220	0.22	−0.15	0.31	0.06	0.28	−0.08
611.9520	0.23	−0.16	0.29	0.02	0.28	−0.10
619.9190	0.33	0.04	0.29	0.12	0.35	0.07
624.3100	0.27	0.06	–	–	0.30	0.10
625.1820	0.28	−0.06	0.31	0.09	0.30	−0.03
627.4650	0.29	0.00	0.30	0.13	0.28	0.00
650.4165	0.39	–	0.34	–	0.40	–
Average	0.27 ± 0.04	-0.03 ± 0.09	0.30 ± 0.01	0.11 ± 0.05	0.30 ± 0.03	0.01 ± 0.07

Note: The average values in the last row do not include the 650.4165 nm line in columns 3, 5 and 7 because it was not used by Ernandes et al. (2018). The errors denote the standard deviation due to the star-to-star abundance variation.

been calculated in several prior studies. However, the atmospheric parameters and metallicities of the stars examined in these studies substantially differ from those of our target stars (e.g. Andrievsky et al. 2011, Zhao et al. 2016, Mishenina et al. 2019, Korotin et al. 2020, Lardo et al. 2021, Mashonkina et al. 2022).

Importantly, because our target stars fall into a relatively narrow $T_{\rm eff}$ range (~ 400 K) and are characterized by the same metallicity and very similar Sr abundances, nearly identical Sr NLTE abundance corrections for all target stars would be expected. Consequently, the Sr–Na correlation addressed in Sect. 4.4.1 should not be influenced by NLTE effects.

4.2.7. Uncertainty of microturbulence velocity and its impact on the determined Sr abundances

In order to determine whether the uncertainty in microturbulence velocity influences the determined Sr abundances, we conducted two tests. In the first test, we computed the synthetic profile of the Sr spectral line using the atmospheric parameters and Sr abundance values of star 27678 (unaltered profile). Then, two additional synthetic Sr spectra profiles were computed, with microturbulence velocity values adjusted by ± 0.2 kms^{-1} (using the RMS variation of microturbulence velocity as a representative uncertainty in $\xi_{\rm t}$, which is ± 0.2 kms^{-1}). To match these latter two line profiles with the unaltered profile,

Table 4.4. Atmospheric parameters and $\Delta_{\mathrm{3D-1D\ LTE}}$ abundance corrections for the Sr I line.

T_{eff}, K	$\log g$	[M/H]	ξ_{micro}, km s^{-1}	$\Delta_{\mathrm{3D-1D\ LTE}}$
4040	1.5	−1.0	1.5	+0.05
4485	2.0	−1.0	2.0	+0.01
4492	2.5	−1.0	2.0	0.00

adjustments to the Sr abundance used in their computation would typically be required. However, in practice, the adjustments were found to be negligible (<0.01 dex), leading us to conclude that uncertainty in microturbulence velocity does not impact the determined Sr abundances.

The second test was the same as the first one, with the exception that the synthetic spectra were calculated with all spectral lines enabled, including CN lines. The result of this test was consistent with the results of the initial test, confirming that changes in microturbulence velocity values by ±0.2 km s^{-1} do not alter Sr abundances.

4.2.8. Uncertainty of the Sr abundances due to the effects of convection

To date, the impact of convection on the formation of Sr I lines has not been investigated. Given the low ionization potential of Sr I at 5.695 eV, neutral Sr is a minority species throughout a large extent of the target star atmospheres. This may lead to a pronounced sensitivity of the line formation to convection, as the horizontal temperature fluctuations associated with convection may influence the concentration of Sr I, particularly within the downdrafts situated between the granules. Consequently, this could affect the strength of Sr I lines and the Sr abundances determined using the 1D hydrostatic model atmospheres.

To assess the role of these effects, we computed the Sr I 650.3991 nm line profiles using the 3D hydrodynamical CO^{5}BOLD model atmospheres (Freytag et al. 2012) and 1D hydrostatic LHD model atmospheres (Caffau et al. 2008). The model atmospheres were calculated for three sets of atmospheric parameters that encompass those of the target RGB stars (Table 4.4). Both the 3D and 1D model atmospheres were calculated using the same chemical composition, opacities, and equations of state. Synthetic line profiles were computed using the spectral line parameters from Table 4.2, as well as the average microturbulence velocities and Sr abundances determined in our target stars with analogous atmospheric parameters. Both the 3D and 1D line profiles were computed assuming LTE.

The results demonstrate that the 3D–1D LTE corrections are minor (< 0.05 dex) and exhibit a negligible dependence on atmospheric parameters (e.g. T_{eff}). Moreover, due to the weakness of the observed spectral lines, the choice of microturbulence velocity would not significantly influence the abundance corrections.

Table 4.5. Minimum, maximum, and mean Fe, Na, and Sr abundance ratios determined in the sample of 31 RGB stars in 47 Tuc.

	$[X/H]_{min}$	$[X/H]_{max}$	$\langle[X/H]\rangle$	$[X/Fe]_{min}$	$[X/Fe]_{max}$	$\langle[X/Fe]\rangle$
Fe I (LTE)	−0.98	−0.71	-0.81 ± 0.06	–	–	–
Na I (NLTE)	−0.60	−0.12	-0.29 ± 0.12	0.21	0.69	0.43 ± 0.12
Sr I (LTE)	−0.78	−0.40	-0.63 ± 0.08	0.03	0.41	0.18 ± 0.08

Note: Errors denote the standard deviation due to the star-to-star abundance variation.

It is important to note that the derived 3D–1D LTE abundance corrections should not be directly applied to the measured Sr abundances. In the atmospheres of cool giants, both 3D and NLTE effects can significantly alter line formation. Ideally, both 3D and NLTE effects should be considered in the spectral line synthesis calculations employed for abundance determinations. However, the magnitude of the 3D–1D LTE corrections gives us confidence that the influence of convection on the Sr abundances determined in our target stars is minimal.

4.3. Results

4.3.1. Mean abundance of Sr in the RGB stars of 47 Tuc

The only study of Sr abundance in 47 Tuc prior to ours was conducted by James et al. (2004), who determined Sr abundances in the atmospheres of eight SGB and three TO stars; $\langle[Sr/Fe]\rangle_{SGB} = 0.36 \pm 0.16$ and $\langle[Sr/Fe]\rangle_{TO} = 0.28 \pm 0.14$, respectively. The authors analyzed two Sr II lines at wavelengths of 407.7709 and 421.5519 nm. The average abundances obtained by James et al. (2004) differ significantly from the average Sr abundance we determined in 31 RGB stars, $\langle[Sr/Fe]\rangle = 0.18 \pm 0.08$ dex (Table 4.5; the error is the standard deviation due to star-to-star abundance scatter). This disparity could arise from a range of factors, including those associated with the abundance analysis (e.g. using a larger sample size in our study, variations in the placement of the continuum level, or use of different $\log gf$ values in James et al. 2004). Furthermore, real variations in Sr abundance between the TO/SGB and RGB stars could also explain this observed difference.

The mean Sr abundance in 47 Tuc as determined in our study falls within the observed range of Sr abundance variation in Galactic field stars at the metallicity of 47 Tuc (Fig. 4.12).

4.3.2. CN impact on the derived Sr abundances

One issue of concern is that the spectral lines which were used to derive abundances in this work might be blended with strong CN molecular lines. It has been previously demonstrated that stars in different populations within GGCs

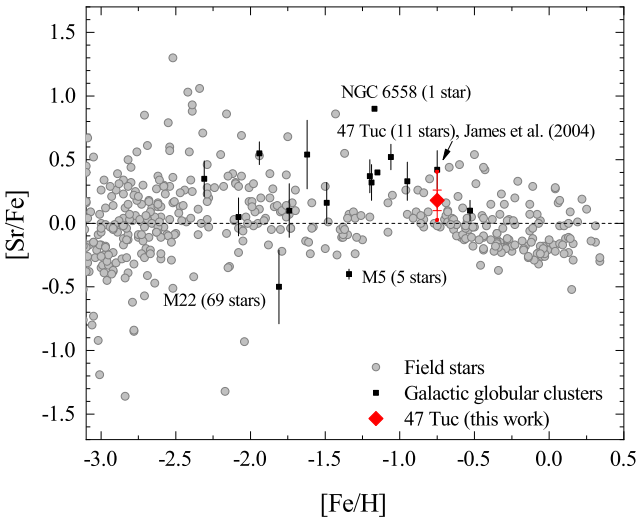

Fig. 4.12. Strontium-to-iron ratios in the GGCs and Galactic field stars. Observational data for field stars: Lai et al. (2008), Ishigaki et al. (2013), Roederer et al. (2014), Battistini & Bensby (2016). Black vertical lines and red vertical line with horizontal lines at the end of its whiskers show standard deviation of the mean due to star-to-star abundance scatter. Vertical red line with dots at the end show minimum and maximum values.

may possess different carbon or nitrogen abundances (Mészáros et al. 2020). Which means that the strengths of the blends with CN lines will be different as well, which may lead to inflated element abundances in 2P stars since CN lines are stronger in these stars. If such is the case with a particular spectral line, a spurious correlation between the abundances of that element and light chemical elements might be observed.

To estimate the influence of CN blends on the determined abundances, we performed a test with two second population stars (IDs: 27678, s23821) having different $T_{\rm eff}$ (4000 K and 4400 K) but identical [Na/Fe] abundances. We determined the abundances of the element in question for both stars using the synthetic spectrum method described in Section 3, with CN line profiles computed using CNO abundances for 47 Tuc determined by Mészáros et al. (2020, 82 stars in total). For CNO abundances, we selected two different sets corresponding to the abundances of first population (1P, "CN-weak") and 2P ("CN-strong") stars:

- [C/Fe] = +0.20, [N/Fe] = +0.20, [O/Fe] = +0.80 (case-A, "CN-weak", 1P);
- [C/Fe] = −0.80, [N/Fe] = +1.70, [O/Fe] = +0.10 (case-B, "CN-strong", 2P).

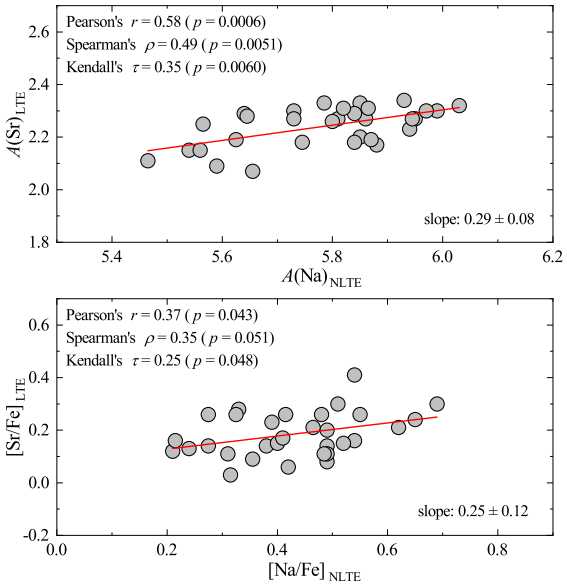

Fig. 4.13. Sr abundance, A(Sr), and [Sr/Fe] ratios determined in the target stars and plotted vs. the Na abundance, A(Na) and [Na/Fe] ratio, respectively.

For both stars, we then calculated the difference in determined element abundances when using the case-B and case-A CNO values.

The 650.3991 nm neutral Sr line used in this study is weakly blended with a nearby CN line (Fig. 4.9). As shown by Mészáros et al. (2020), abundances of CNO can differ very strongly in different stars of the GGCs. This means that one may overestimate the abundances of certain elements of interest when the spectral lines used for the abundance determinations of those elements are blended with CN lines. This could result in higher abundances in 2P stars compared to 1P stars, potentially leading to artificial correlations in abundance-abundance plots.

The results of our CN blend test showed that the difference between Sr abundances determined using case-A and case-B CNO values is always less than 0.01 dex. For the Sr specifically, we also performed a second CN test, because Sr line is located on the wing of another much stronger line. In this test, we computed synthetic spectra with only Sr and CN lines enabled, using the aforementioned stellar and abundance parameters. These synthetic spectra were treated as "real" spectra: we determined the equivalent widths of Sr lines from these spectra, which were then used to calculate Sr abundances with the `WIDTH9` package. The results of this test showed that the difference in Sr abundances between case-B and case-A is no larger than 0.02 dex. Thus, considering the results of both tests, we conclude that CN blends have a negligible impact on the determined Sr abundances in this study.

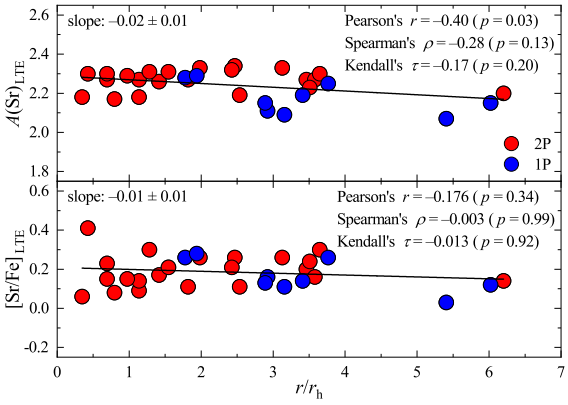

Fig. 4.14. Sr abundance plotted versus relative distance to the cluster centre. The stars are marked in different colours according to their population: blue – first population stars ($[\mathrm{Na/Fe}] = [[\mathrm{Na/Fe}]_{\mathrm{min}}, [\mathrm{Na/Fe}]_{\mathrm{min}} + 0.3]$), red – second population stars (those with higher Na abundances). The minimum sodium-to-iron ratio, $[\mathrm{Na/Fe}]_{\mathrm{min}}$, is taken from Sect. 2.

4.4. Discussion

4.4.1. Possible Sr–Na abundance correlation?

Our data reveal weak correlations between (a) Sr and Na abundances, and (b) the [Sr/Fe] and [Na/Fe] abundance ratios, as illustrated in Fig. 4.13. Under the null hypothesis of no Sr–Na correlation, the Pearson parametric and Spearman and Kendall non-parametric tests indicate that the probability, p, of obtaining the observed correlation coefficients, r, in our dataset is always $p < 0.05$ (Fig. 4.13). This may suggest that the 2P stars in 47 Tuc are slightly enhanced in Sr.

Conversely, statistical tests do not support an Sr–r/r_{h} anti-correlation, here r denotes the projected distance from the cluster center for a given target star, and $r_{\mathrm{h}} = 174''$ represents the half-light radius of 47 Tuc, as reported by Trager et al. (1993) (see Fig. 4.14). An anti-correlation like this would be expected if an Sr–Na correlation existed, as 2P stars (rich in Na and Sr) tend to be more centrally concentrated in 47 Tuc and other GGCs. While the Na–r/r_{h} anti-correlation in 47 Tuc has been confirmed in Sect. 2 and also other studies (see e.g. Bastian & Lardo 2018 and references therein), the data in our analysis do not show this trend (Fig. 4.15). A likely explanation for this discrepancy is that the RGB star sample in our study is too small in size to reliably detect a potentially very weak Sr–r/r_{h} anti-correlation.

On the other hand, our data seem to suggest that Na-rich stars are indeed more concentrated towards the cluster center. This observation is supported by the distribution of Na-rich and Na-poor stars selected in Sect. 4.2.3, both

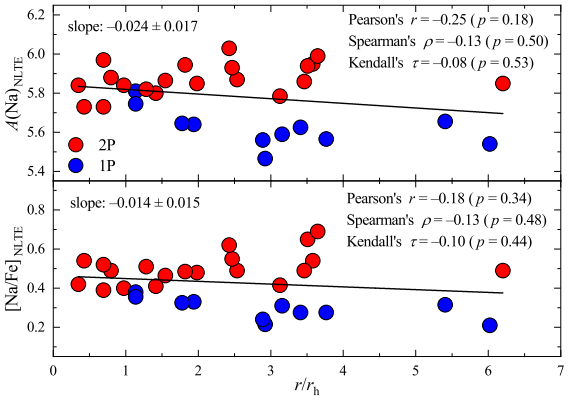

Fig. 4.15. Na abundance plotted versus relative distance to the cluster centre. The stars are marked in different colours according to their population: blue – first population stars ([Na/Fe] = [[Na/Fe]$_{\rm min}$, [Na/Fe]$_{\rm min}$ + 0.3]), red – second population stars (those with higher Na abundances). The minimum sodium-to-iron ratio, [Na/Fe]$_{\rm min}$, is taken from Sect. 2.

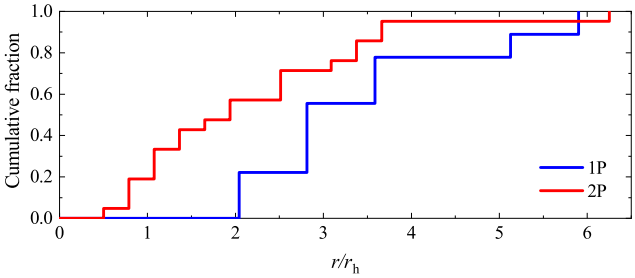

Fig. 4.16. Cumulative number fraction of the stars in the Na-rich (red line) and Na-poor (blue line) populations plotted vs. the relative distance from the cluster center. The results of the K–S test show that the probability of the 1P and 2P groups to be drawn from the same sample is $p = 0.052$.

through visual inspection of their distribution against $r/r_{\rm h}$ (Fig. 4.14) and the Kolmogorov-Smirnov (K-S) test on the cumulative distributions of 1P and 2P stars against $r/r_{\rm h}$ (Fig. 4.16), indicating that the Na-rich population is indeed more clustered towards the center. In particular, the probability that the cumulative distributions of the Na-rich and Na-poor stars are identical is $p \leq 0.05$, as estimated from the K-S test, whereas no statistical evidence for this can be detected in the Na–$r/r_{\rm h}$ plane, most likely because the sample is too small for us to obtain a reliable estimate in this plane.

4.4.2. Production of s-process elements in the 2P polluters?

The results of Sr abundance analysis in 47 Tuc obtained in this work suggest that the polluters responsible for enriching 2P stars with light elements might

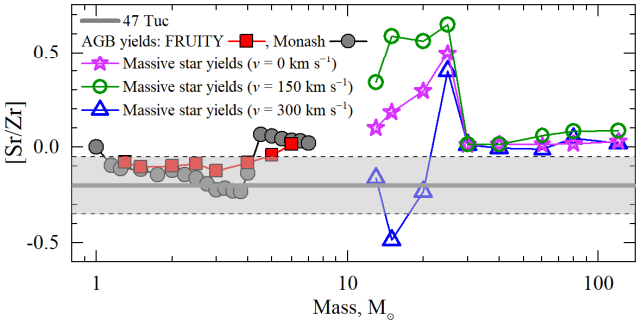

Fig. 4.17. [Sr/Zr] ratio vs. stellar mass. Theoretical AGB yields: FRUITY (Cristallo et al. 2015), and Monash (Karakas et al. 2018). The massive star yields are taken from Limongi & Chieffi (2018). The horizontal solid gray line shows the [Sr/Zr] abundance ratio of 47 Tuc, where the abundances of Sr and Zr were determined in this work. The shaded gray area shows the standard deviation due to the star-to-star Sr and Zr abundance scatter.

also have produced noticeable quantities of s-process elements. This hypothesis is supported by our earlier analysis of Zr in 47 Tuc (Sect. 2), which revealed a small but statistically significant difference in the abundance of Zr, another first s-process peak element, between 2P and 1P stars, as well as a correlation between Zr and Na abundances. Hence, together, the results from both Zr and Sr analysis may indicate that 2P stars in 47 Tuc could have been enriched in first-peak s-process elements. This assertion clearly has to be confirmed by the analysis of Sr abundance in a larger sample of stars, as well as by the analysis of other s-process elements both in this and other GGCs, in particular Y and Rb, which belong to the same (first) s-process peak as Sr and Zr.

The analysis of heavier s-process elements performed by different authors has yielded mixed results. Thygesen et al. (2014), in their study of 13 RGB stars in 47 Tuc, found no correlations between Ba or La abundances with Na. Similarly, no La–Na correlation was observed in 123 RGB stars of this cluster by Cordero et al. (2014). In our study of Ba abundance in 261 RGB stars of 47 Tuc, we also found no correlation between Ba and Na abundances (Sect. 3). Although Ba and La are second s-process peak elements, theoretical predictions from AGB and FRMS suggest Ba and La should be synthesized along with the first s-process peak elements like Sr and Zr (Carretta et al. 2009b; Limongi & Chieffi 2018). Conversely, recent studies by Fernández-Trincado et al. (2021; 2022) on 47 Tuc and several other GGCs proposed the existence of Ce–N and Ce–Al correlations. Reconciling the absence of a 2P–1P difference for Ba and La with a potential Ce–N correlation is challenging since these elements, belonging to the same second s-process peak, are expected to exhibit similar abundance patterns.

Comparing the mean Sr and Zr abundance ratio in 47 Tuc, with theoretical

s-process nucleosynthesis predictions in AGB and massive stars, suggests both elements could have originated from AGB stars or, less conclusively, from high-mass ($M = 10 - 20\ M_{\odot}$) rapidly rotating ($v_{\rm rot} = 200 - 300\,{\rm km\,s^{-1}}$) stars (Fig. 4.17). More data on s-process element abundances are essential to better constrain the likely progenitors in GGCs.

In conclusion, our analysis of Sr abundance in 31 RGB stars in 47 Tuc, alongside a previously observed Zr–Na correlation, suggests that the polluter stars enriching 2P stars with light elements might also have synthesized noticeable amounts of light s-process elements like Sr and Zr. Confirming the Sr–Na correlation with the analysis of a larger star sample and by using other spectral lines of Sr is crucial. Given the lack of 2P–1P abundance differences for the first-peak s-process elements in earlier GGC studies, it would be particularly interesting to explore whether such differences exist for other first-peak s-process elements in this and other GGCs. The results for heavier s-process elements, such as Ba, La, and Ce, are more mixed, with some studies observing possible 2P–1P differences for certain elements but not others. Notably, no studies have yet investigated third-peak s-process elements, making such research highly desirable. Clearly, a further analysis of s-process elements in conjunction with theoretical predictions for different polluters is required to gain more information about the abundance patterns of s-process elements in different clusters and on the nature of the possible polluters. Even if the 2P–1P differences are subtle and the correlations between s-process and light element abundances are not reliably detected, confirming or rejecting the abundance differences in larger samples of 2P and 1P stars will provide valuable insights about the nature of polluters and nucleosynthesis in GGCs at large.

SUMMARY AND CONCLUSIONS

In this Thesis, we explored potential connections between the chemical and kinematic properties of RGB stars in multiple stellar populations of the Galactic globular cluster 47 Tuc. For this, we determined abundances of Na, Sr and Zr in the atmospheres of RGB stars, utilizing high-resolution spectra obtained with the `GIRAFFE` and `UVES` spectrographs mounted on the VLT UT2 telescope at the European Southern Observatory (ESO).

The spectroscopic data were analyzed using 1D `ATLAS9` stellar model atmospheres and 1D LTE/NLTE abundance analysis tools. For Na the 1D NLTE spectral line synthesis was conducted with the `MULTI` package, while the `SYNTHE` code was used for the 1D LTE line synthesis for Sr. Abundances of Zr were determined using equivalent width method, where equivalent widths were measured with the `splot` task in `IRAF` and abundances determined with the `WIDTH9` code. Additionally, we utilized 3D hydrodynamical `CO5BOLD` and 1D hydrostatic `LHD` model atmospheres to compute 3D–1D abundance corrections for Sr in order to assess the influence of convection on the formation of these lines.

The sample-averaged abundances obtained for RGB stars in 47 Tuc were $\langle[\mathrm{Na/Fe}]_{\mathrm{NLTE}}\rangle = 0.41, \pm 0.16$ for 261 stars, $\langle[\mathrm{Zr/Fe}]_{\mathrm{LTE}}\rangle = 0.35 \pm 0.09$ for 237 stars, $\langle[\mathrm{Sr/Fe}]_{\mathrm{LTE}}\rangle = 0.18 \pm 0.08$ for 31 stars, here the errors represent the standard deviation due to natural star-to-star abundance variation.

For Zr, we observed a wide range of star-to-star abundance variation and identified a weak but statistically significant correlation in the $[\mathrm{Zr/Fe}] - [\mathrm{Na/Fe}]$ plane. The data also reveal a small but statistically significant difference between the mean Zr abundances in the 1P and 2P stars, of namely $\Delta[\mathrm{Zr/Fe}]_{\mathrm{2P-1P}} \approx 0.06$ dex. Additionally, our data suggest a statistically significant anti-correlation between Zr abundance and the radial distance from the cluster center, $[\mathrm{Zr/Fe}] - r/r_{\mathrm{h}}$. However, we did not find statistically significant correlations between the dispersions of full spatial velocities and Zr abundances.

We also performed similar analysis for Ba but in this case no statistically significant relationships in the $[\mathrm{Ba/Fe}] - [\mathrm{Na/Fe}]$ or $[\mathrm{Ba/Fe}] - r/r_{\mathrm{h}}$ planes were found. Both the 1P and 2P stars in 47 Tuc appear to share the same Ba abundance, suggesting no enrichment or depletion in the early stages of the evolution of this GGC.

Regarding Sr, results of our analysis indicate weak potential correlations between Sr and Na abundances and between the [Sr/Fe] and [Na/Fe] abundance ratios. We did not detect an anti-correlation in the $[\mathrm{Sr/Fe}] - r/r_{\mathrm{h}}$ plane.

Our results also demonstrate that NLTE effects are significant in the formation of Na I lines in the atmospheres of RGB stars in 47 Tuc, with 1D NLTE abundance corrections for Na I lines ranging from –0.08 dex to –0.27 dex.

We determined that the impact of convection on the formation of the Sr I spectral line used in this work was minimal, as indicated by the small size of 3D–1D LTE abundance corrections, which did not exceed 0.05 dex. The dependence of these corrections on atmospheric parameters, such as $T_{\rm eff}$, was very weak, too.

The results obtained in this study revealed the existence of a Zr–Na and Sr-Na correlation in GGC 47 Tuc. This suggests that the astrophysical processes responsible for enriching (or depleting) 2P stars with light elements may also have synthesized significant quantities of Sr and Zr. Theoretical modelling of s-process element yields indicates that Zr can be synthesized both in the AGB stars ($M \sim 1.5 - 5\,M_{\odot}$; Cristallo et al. 2015) and FRMS ($M \sim 12 - 25\,M_{\odot}$, $v_{\rm rot} > 150\,{\rm km\,s^{-1}}$; Limongi & Chieffi 2018). However, s-process elements are typically produced during the late evolutionary phases of FRMS and are ejected into the intra-cluster medium during the core-collapse supernova explosions. It remains uncertain whether GGCs can retain material expelled by supernova explosions, with the possible exception of the most massive clusters, such as ω Centauri. Moreover, since variations in Fe abundances are not observed in Type I GGCs, and Fe is synthesized during the explosion, evolutionary scenarios involving FRMS as polluters suggest pollution occurs through stellar winds before the supernova explosion. Consequently, FRMS winds are expected to carry variations in proton-capture elements rather than in s-process elements.

In contrast, this study reveals that polluter stars did not synthesize Ba, as both 1P and 2P stars exhibit the same Ba abundance. Assuming that the 2P was enriched in Zr and Sr but not in Ba suggests that only certain s-process elements were produced by the polluters that enriched the 2P stars in Na and modified the abundances of other light elements, such as Li, N or O, as discussed in earlier studies (see e.g. Bastian & Lardo 2018). Theoretical yields from low- and intermediate-mass AGB stars suggest that Zr and Ba can be produced in substantial amounts but should be synthesized simultaneously (Cristallo et al. 2015). Similarly, substantial quantities of Zr and Ba could be produced in massive rotating stars, yet both elements should also be produced simultaneously (Limongi & Chieffi 2018).

Having more information about the abundances of other s-process elements may allow to put further constraints on the potential polluters. Various s-process element ratios, such as [La/Rb], [Pb/Zr], or [Pb/*hs*] (*hs* – heavy s-process elements of the second s-process peak), could be used for such an analysis. Rb is predominantly synthesized in AGB stars within a narrow mass range $\sim 4 - 5\,M_{\odot}$ and is minimally produced in massive stars. Pb, particularly in stars with higher metallicity ($>$ [Fe/H] = –1.5), is mostly synthesized in AGB stars rather than massive stars. Comparing Pb to heavy s-process elements like Ba, La, and Ce can assist in evaluating the neutron exposure and the s-process efficiency within the stellar environment. High [Pb/hs] ratios sug-

gest a significant operation of the s-process, likely indicating AGB stars as the primary contributors. However, the determination of Pb abundance in stars, especially within GGCs, presents observational challenges, as Pb lines can be weak and difficult to detect in stellar spectra.

It would be highly beneficial to determine the abundances of Sr and Zr in a larger number of stars across various GGCs to investigate the presence of Sr–Na or Zr–Na correlations elsewhere, as 47 Tuc may be an exceptional case. Determining Ba abundances in other GGCs, particularly those with distinct parameters (age, mass, or metallicity) and those showing correlations of light elements with Al and Si, could also be useful. The absence of Al, Si, and light element correlations in 47 Tuc suggests that the polluter stars did not reach temperatures high enough to produce these elements. Thus, examining other GGCs where polluters achieved sufficient temperatures to produce Al, Si and then possibly Ba could help determine the temperatures and, consequently, the stellar masses of the polluter stars.

In conclusion, explaining the observed abundance correlations in GGCs using a singular type of polluter appears challenging; it is highly plausible that multiple types of polluters contributed. Extensive abundance analysis including a broad array of chemical elements and a larger sample of stars would greatly aid in trying resolve the long standing question of how multiple populations in GGCs formed. Moreover, advancements in the evolutionary models of stars are crucial, as the accuracy of their elemental yields is very important for predicting and interpreting the abundances of GGC stars.

BIBLIOGRAPHY

Allen, C. W. 1973, Astrophysical quantities (Athlone Press)

Alonso, A., Arribas, S., & Martínez-Roger, C. 1999, A&AS, 140, 261

Anderson, J., Piotto, G., King, I. R., Bedin, L. R., & Guhathakurta, P. 2009, ApJ, 697, L58

Andrievsky, S. M., Spite, F., Korotin, S. A., François, P., Spite, M., Bonifacio, P., Cayrel, R., & Hill, V. 2011, A&A, 530, A105

Andrievsky, S. M., Spite, M., Korotin, S. A., Spite, F., François, P., Bonifacio, P., Cayrel, R., & Hill, V. 2009, A&A, 494, 1083

Asplund, M., Grevesse, N., & Sauval, A. J. 2005, Astronomical Society of the Pacific Conference Series, 336, 25

Barklem, P. S., Belyaev, A. K., Dickinson, A. S., & Gadéa, F. X. 2010, A&A, 519, A20

Bastian, N., Cabrera-Ziri, I., Davies, B., & Larsen, S. S. 2013, MNRAS, 436, 2852

Bastian, N. & Lardo, C. 2018, ARA&A, 56, 83

Battistini, C. & Bensby, T. 2016, A&A, 586, A49

Baumgardt, H., Hilker, M., Sollima, A., & Bellini, A. 2019, MNRAS, 482, 5138

Bergbusch, P. A. & Stetson, P. B. 2009, AJ, 138, 1455

Bergemann, M., Hansen, C. J., Bautista, M., & Ruchti, G. 2012, A&A, 546, A90

Biemont, E., Grevesse, N., Hannaford, P., & Lowe, R. M. 1981, ApJ, 248, 867

Böhm-Vitense, E. 1958, ZAp, 46, 108

Bonifacio, P., Pasquini, L., Molaro, P., Carretta, E., François, P., Gratton, R. G., James, G., Sbordone, L., Spite, F., & Zoccali, M. 2007, A&A, 470, 153

Brooke, J. S. A., Ram, R. S., Western, C. M., Li, G., Schwenke, D. W., & Bernath, P. F. 2014, ApJS, 210, 23

Brown, M. B. & Forsythe, A. B. 1974, J. Am. Stat. Assoc., 69, 364

Caffau, E., Faraggiana, R., Ludwig, H. G., Bonifacio, P., & Steffen, M. 2011a, Astronomische Nachrichten, 332, 128

Caffau, E. & Ludwig, H. G. 2007, A&A, 467, L11

Caffau, E., Ludwig, H. G., Steffen, M., Ayres, T. R., Bonifacio, P., Cayrel, R., Freytag, B., & Plez, B. 2008, A&A, 488, 1031

Caffau, E., Ludwig, H. G., Steffen, M., Freytag, B., & Bonifacio, P. 2011b, Sol. Phys., 268, 255

Caffau, E., Maiorca, E., Bonifacio, P., Faraggiana, R., Steffen, M., Ludwig, H. G., Kamp, I., & Busso, M. 2009, A&A, 498, 877

Carlsson, M. 1986, Uppsala Astronomical Observatory Reports, 33

Carretta, E., Bragaglia, A., Gratton, R., D'Orazi, V., & Lucatello, S. 2009a, A&A, 508, 695

Carretta, E., Bragaglia, A., Gratton, R. G., Lucatello, S., Catanzaro, G., Leone, F., Bellazzini, M., Claudi, R., D'Orazi, V., Momany, Y., Ortolani, S., Pancino, E., Piotto, G., Recio-Blanco, A., & Sabbi, E. 2009b, A&A, 505, 117

Carretta, E., Gratton, R. G., Bragaglia, A., Bonifacio, P., & Pasquini, L. 2004, A&A, 416, 925

Carretta, E., Gratton, R. G., Lucatello, S., Bragaglia, A., & Bonifacio, P. 2005, A&A, 433, 597

Castelli, F. & Kurucz, R. L. 2003, New Grids of ATLAS9 Model Atmospheres, 210, A20

Charbonnel, C. 2016, EAS Publications Series, Vol. 80-81, 177

Cohen, J. G., Christlieb, N., Thompson, I., McWilliam, A., Shectman, S., Reimers, D., Wisotzki, L., & Kirby, E. 2013, ApJ, 778, 56

Collet, R., Asplund, M., & Trampedach, R. 2007, A&A, 469, 687

Cordero, M. J., Hansen, C. J., Johnson, C. I., & Pilachowski, C. A. 2015, ApJ, 808, L10

Cordero, M. J., Pilachowski, C. A., Johnson, C. I., McDonald, I., Zijlstra, A. A., & Simmerer, J. 2014, ApJ, 780, 94

Cristallo, S. 2018, European Physical Journal Web of Conferences, Vol. 184, 01004

Cristallo, S., Straniero, O., Piersanti, L., & Gobrecht, D. 2015, ApJS, 219, 40

Cunto, W., Mendoza, C., Ochsenbein, F., & Zeippen, C. J. 1993, A&A, 275, L5

Černiauskas, A., Kučinskas, A., Klevas, J., Prakapavičius, D., Korotin, S., Bonifacio, P., Ludwig, H. G., Caffau, E., & Steffen, M. 2017, A&A, 604, A35

D'Antona, F., Vesperini, E., D'Ercole, A., Ventura, P., Milone, A. P., Marino, A. F., & Tailo, M. 2016, MNRAS, 458, 2122

de Mink, S. E., Pols, O. R., Langer, N., & Izzard, R. G. 2009, A&A, 507, L1

Dobrovolskas, V., Kolomiecas, E., Kučinskas, A., Klevas, J., & Korotin, S. 2021, A&A, 656, A67

Dobrovolskas, V., Kučinskas, A., Bonifacio, P., Korotin, S. A., Steffen, M., Sbordone, L., Caffau, E., Ludwig, H. G., Royer, F., & Prakapavičius, D. 2014, A&A, 565, A121

Dobrovolskas, V., Kučinskas, A., Steffen, M., Ludwig, H. G., Prakapavičius, D., Klevas, J., Caffau, E., & Bonifacio, P. 2013, A&A, 559, A102

D'Orazi, V., Campbell, S. W., Lugaro, M., Lattanzio, J. C., Pignatari, M., & Carretta, E. 2013, MNRAS, 433, 366

D'Orazi, V., Gratton, R., Lucatello, S., Carretta, E., Bragaglia, A., & Marino, A. F. 2010, ApJ, 719, L213

Dotter, A., Chaboyer, B., Jevremović, D., Kostov, V., Baron, E., & Ferguson, J. W. 2008, ApJS, 178, 89

Doyle, A. P., Davies, G. R., Smalley, B., Chaplin, W. J., & Elsworth, Y. 2014, MNRAS, 444, 3592

Ernandes, H., Barbuy, B., Alves-Brito, A., Friaça, A., Siqueira-Mello, C., & Allen, D. M. 2018, A&A, 616, A18

Fernández-Trincado, J. G., Beers, T. C., Barbuy, B., Mészáros, S., Minniti, D., Smith, V. V., Cunha, K., Villanova, S., Geisler, D., Majewski, S. R., Carigi, L., Tang, B., Moni Bidin, C., & Vieira, K. 2021, ApJ, 918, L9

Fernández-Trincado, J. G., Villanova, S., Geisler, D., Barbuy, B., Minniti, D., Beers, T. C., Mészáros, S., Tang, B., Cohen, R. E., Moni Bidin, C., Garro, E. R., Baeza, I., & Muñoz, C. 2022, A&A, 658, A116

Freytag, B., Steffen, M., Ludwig, H. G., Wedemeyer-Böhm, S., Schaffenberger, W., & Steiner, O. 2012, Journal of Computational Physics, 231, 919

Gaia Collaboration, Brown, A. G. A., Vallenari, A., Prusti, T., de Bruijne, J. H. J., Babusiaux, C., Biermann, M., & et al. 2021, A&A, 649, A1

Gaia Collaboration, Vallenari, A., Brown, A. G. A., Prusti, T., & et al. 2023, A&A, 674, A1

Gallagher, A. J., Bergemann, M., Collet, R., Plez, B., Leenaarts, J., Carlsson, M., Yakovleva, S. A., & Belyaev, A. K. 2020, A&A, 634, A55

Gratton, R., Bragaglia, A., Carretta, E., D'Orazi, V., Lucatello, S., & Sollima, A. 2019, A&A Rev., 27, 8

Gratton, R., Sneden, C., & Carretta, E. 2004, ARA&A, 42, 385

Gratton, R. G., Lucatello, S., Sollima, A., Carretta, E., Bragaglia, A., Momany, Y., D'Orazi, V., Cassisi, S., Pietrinferni, A., & Salaris, M. 2013, A&A, 549, A41

Grevesse, N. & Sauval, A. J. 1998, Space Sci. Rev., 85, 161

Grevesse, N., Scott, P., Asplund, M., & Sauval, A. J. 2015, A&A, 573, A27

Grundahl, F., Stetson, P. B., & Andersen, M. I. 2002, A&A, 395, 481

Guiglion, G., de Laverny, P., Recio-Blanco, A., & Prantzos, N. 2018, A&A, 619, A143

Gustafsson, B., Edvardsson, B., Eriksson, K., Jørgensen, U. G., Nordlund, Å., & Plez, B. 2008, A&A, 486, 951

Hackett, P. A., Humphries, M. R., Mitchell, S. A., & Rayner, D. M. 1986, J. Chem. Phys., 85, 3194

Hansen, C. J., Bergemann, M., Cescutti, G., François, P., Arcones, A., Karakas, A. I., Lind, K., & Chiappini, C. 2013, A&A, 551, A57

Hinkle, K., Wallace, L., Valenti, J., & Harmer, D. 2000, Visible and Near Infrared Atlas of the Arcturus Spectrum 3727-9300 Å, eds. K. Hinkle, L. Wallace, J. Valenti, & D. Harmer (San Francisco: ASP), 200

Igenbergs, K., Schweinzer, J., Bray, I., Bridi, D., & Aumayr, F. 2008, Atomic Data and Nuclear Data Tables, 94, 981

Ishigaki, M. N., Aoki, W., & Chiba, M. 2013, ApJ, 771, 67

Jacobson, H. R., Keller, S., Frebel, A., Casey, A. R., Asplund, M., Bessell, M. S., Da Costa, G. S., Lind, K., Marino, A. F., Norris, J. E., Peña, J. M., Schmidt, B. P., Tisserand, P., Walsh, J. M., Yong, D., & Yu, Q. 2015, ApJ, 807, 171

James, G., François, P., Bonifacio, P., Carretta, E., Gratton, R. G., & Spite, F. 2004, A&A, 427, 825

Karakas, A. I., Lugaro, M., Carlos, M., Cseh, B., Kamath, D., & García-Hernández, D. A. 2018, MNRAS, 477, 421

Kim, Y.-C., Demarque, P., Yi, S. K., & Alexander, D. R. 2002, ApJS, 143, 499

Korotin, S., Mishenina, T., Gorbaneva, T., & Soubiran, C. 2011, MNRAS, 415, 2093

Korotin, S. A., Andrievsky, S. M., Caffau, E., Bonifacio, P., & Oliva, E. 2020, MNRAS, 496, 2462

Korotin, S. A., Andrievsky, S. M., & Luck, R. E. 1999, A&A, 351, 168

Krause, M., Charbonnel, C., Decressin, T., Meynet, G., & Prantzos, N. 2013, A&A, 552, A121

Kupka, F. G., Ryabchikova, T. A., Piskunov, N. E., Stempels, H. C., & Weiss, W. W. 2000, Baltic Astronomy, 9, 590

Kurucz, R. L. 1993, ATLAS9 Stellar Atmosphere Programs and 2 km/s Grid, CD-ROM No.13, Cambridge, Mass

Kurucz, R. L. 2005a, Mem. Soc. Astron. Italiana, 8, 14

Kurucz, R. L. 2005b, Mem. Soc. Astron. Italiana, 8, 189

Kurucz, R. L. & Furenlid, I. 1979, SAO Special Report, 387

Kurucz, R. L., Furenlid, I., Brault, J., & Testerman, L. 1984, Solar flux atlas from 296 to 1300 nm

Kučinskas, A., Dobrovolskas, V., & Bonifacio, P. 2014, A&A, 568, L4

Lai, D. K., Bolte, M., Johnson, J. A., Lucatello, S., Heger, A., & Woosley, S. E. 2008, ApJ, 681, 1524

Lai, D. K., Johnson, J. A., Bolte, M., & Lucatello, S. 2007, ApJ, 667, 1185

Lardo, C., Mashonkina, L., Jablonka, P., Bonifacio, P., Caffau, E., Aguado, D. S., González Hernández, J. I., Sestito, F., Kielty, C. L., Venn, K. A., Hill, V., Starkenburg, E., Martin, N. F., Sitnova, T., Arentsen, A., Carlberg, R. G., Navarro, J. F., & Kordopatis, G. 2021, MNRAS, 508, 3068

Levene, H. 1960, Robust tests for equality of variances, in ed. I. Olkin, Contributions to Probability and Statistics (Palo Alto: Stanford University Press)

Limongi, M. & Chieffi, A. 2018, ApJS, 237, 13

Lodders, K. 2003, ApJ, 591, 1220

Ludwig, H. G., Caffau, E., Steffen, M., Freytag, B., Bonifacio, P., & Kučinskas, A. 2009, Mem. Soc. Astron. Italiana, 80, 711

Ludwig, H. G., Jordan, S., & Steffen, M. 1994, A&A, 284, 105

Marino, A. F., Milone, A. P., Renzini, A., D'Antona, F., Anderson, J., Bedin, L. R., Bellini, A., Cordoni, G., Lagioia, E. P., Piotto, G., & Tailo, M. 2019, MNRAS, 487, 3815

Marks, M. & Kroupa, P. 2010, MNRAS, 406, 2000

Marsakov, V. A., Koval', V. V., & Gozha, M. L. 2019, Astronomy Reports, 63, 274

Mashonkina, L., Pakhomov, Y. V., Sitnova, T., Jablonka, P., Yakovleva, S. A., & Belyaev, A. K. 2022, MNRAS, 509, 3626

Mashonkina, L. I. & Bikmaev, I. F. 1996, Astronomy Reports, 40, 94

Mészáros, S., Masseron, T., García-Hernández, D. A., Allende Prieto, C., Beers, T. C., & et al. 2020, MNRAS, 492, 1641

Mihalas, D. 1978, Stellar Atmospheres, Freeman and Company, p.186

Milone, A. P., Marino, A. F., Mastrobuono-Battisti, A., & Lagioia, E. P. 2018, MNRAS, 479, 5005

Milone, A. P., Piotto, G., Bedin, L. R., King, I. R., Anderson, J., Marino, A. F., Bellini, A., Gratton, R., Renzini, A., Stetson, P. B., Cassisi, S., Aparicio, A., Bragaglia, A., Carretta, E., D'Antona, F., Di Criscienzo, M., Lucatello, S., Monelli, M., & Pietrinferni, A. 2012, ApJ, 744, 58

Mishenina, T., Pignatari, M., Gorbaneva, T., Bisterzo, S., Travaglio, C., Thielemann, F. K., & Soubiran, C. 2019, MNRAS, 484, 3846

Mucciarelli, A., Bellazzini, M., & Massari, D. 2021, A&A, 653, A90

Nordlund, A. 1982, A&A, 107, 1

Norris, J. E. 2004, ApJ, 612, L25

Osborn, W. 1971, The Observatory, 91, 223

Osorio, Y., Allende Prieto, C., Hubeny, I., Mészáros, S., & Shetrone, M. 2020, A&A, 637, A80

Pietrinferni, A., Hidalgo, S., Cassisi, S., Salaris, M., Savino, A., Mucciarelli, A., Verma, K., Silva Aguirre, V., Aparicio, A., & Ferguson, J. W. 2021, ApJ, 908, 102

Prantzos, N., Abia, C., Limongi, M., Chieffi, A., & Cristallo, S. 2018, MNRAS, 476, 3432

Ramírez, I. & Allende Prieto, C. 2011, ApJ, 743, 135

Ramírez, I. & Meléndez, J. 2005, ApJ, 626, 465

Richer, H. B., Heyl, J., Anderson, J., Kalirai, J. S., Shara, M. M., Dotter, A., Fahlman, G. G., & Rich, R. M. 2013, ApJ, 771, L15

Roederer, I. U., Preston, G. W., Thompson, I. B., Shectman, S. A., Sneden, C., Burley, G. S., & Kelson, D. D. 2014, AJ, 147, 136

Ryabchikova, T., Piskunov, N., Kurucz, R. L., Stempels, H. C., Heiter, U., Pakhomov, Y., & Barklem, P. S. 2015, Phys. Scr, 90, 054005

Sbordone, L. 2005, Mem. Soc. Astron. Italiana, 8, 61

Sbordone, L., Bonifacio, P., Castelli, F., & Kurucz, R. L. 2004, Mem. Soc. Astron. Italiana, 5, 93

Scott, P., Grevesse, N., Asplund, M., Sauval, A. J., Lind, K., Takeda, Y., Collet, R., Trampedach, R., & Hayek, W. 2015, A&A, 573, A25

Sheminova, V. A. 2015, Kinematics and Physics of Celestial Bodies, 31, 172

Shingles, L. J., Karakas, A. I., Hirschi, R., Fishlock, C. K., Yong, D., Da Costa, G. S., & Marino, A. F. 2014, ApJ, 795, 34

Spite, M., Spite, F., Gallagher, A. J., Monaco, L., Bonifacio, P., Caffau, E., & Villanova, S. 2016, A&A, 594, A79

Steenbock, W. & Holweger, H. 1984, A&A, 130, 319

Thygesen, A. O., Sbordone, L., Andrievsky, S., Korotin, S., Yong, D., Zaggia, S., Ludwig, H. G., Collet, R., Asplund, M., Ventura, P., D'Antona, F., Meléndez, J., & D'Ercole, A. 2014, A&A, 572, A108

Tody, D. 1986, in Society of Photo-Optical Instrumentation Engineers (SPIE) Conference Series, Vol. 627, Instrumentation in astronomy VI, ed. D. L. Crawford, 733

Trager, S. C., Djorgovski, S., & King, I. R. 1993, Structure and Dynamics of Globular Clusters, 50, 347

Tsymbal, V. 1998, M.A.S.S., Model Atmospheres and Spectrum Synthesis, 108, 198

van Regemorter, H. 1962, ApJ, 136, 906

Ventura, P. & D'Antona, F. 2011, MNRAS, 410, 2760

Villanova, S. & Geisler, D. 2011, A&A, 535, A31

Vögler, A., Bruls, J. H. M. J., & Schüssler, M. 2004, A&A, 421, 741

Wang, Y., Primas, F., Charbonnel, C., Van der Swaelmen, M., Bono, G., Chantereau, W., & Zhao, G. 2017, A&A, 607, A135

Wiese, W. L. & Martin, G. A. 1980, in Wavelengths and transition probabilities for atoms and atomic ions: Part 2, Transition probabilities, NSRDS-NBS, Vol. 68

Worley, C. C., Cottrell, P. L., Freeman, K. C., & Wylie-de Boer, E. C. 2009, MNRAS, 400, 1039

Worley, C. C., Cottrell, P. L., McDonald, I., & van Loon, J. T. 2010, MNRAS, 402, 2060

Wylie, E. C., Cottrell, P. L., Sneden, C. A., & Lattanzio, J. C. 2006, ApJ, 649, 248

Zhao, G., Mashonkina, L., Yan, H. L., Alexeeva, S., Kobayashi, C., Pakhomov, Y., Shi, J. R., Sitnova, T., Tan, K. F., Zhang, H. W., Zhang, J. B., Zhou, Z. M., Bolte, M., Chen, Y. Q., Li, X., Liu, F., & Zhai, M. 2016, ApJ, 833, 225

Appendices

A. List of stars common to different observing programs

Table A.1. List of stars common to different observing programs.

072.D-0777(A)	073.D-0211(A)	088.D-0026(A)
B-1256	–	R287
F-1389	1389	–
B-3449	–	R563
F-3476	–	R317
F-4373	4373	–
–	5172	R259
B-5362	–	R253
F-7711	7711	–
–	7904	R443
B-7993	–	R277
B-9163	–	R800
–	9518	R237
–	9717	R682
B-9997	–	R248
F-10198	–	R756
F-10527	–	R782
F-12408	–	R784
F-13668	13668	–
B-13795	13795	R752
B-13853	–	R246
B-14583	14583	–
F-15451	15451	–
–	15552	R381
B-16667	–	R790
B-17819	–	R245
–	21369	R249
F-24463	24463	–
B-29146	–	R256
–	29490	R231
B-30463	30463	–
B-30949	–	R766
B-32730	32730	–
B-35878	35878	–
B-38976	–	R762
B-41429	–	R392
B-42866	42866	R656
B-42887	–	R760
F-43632	43632	R512
B-43852	43852	R704
B-43889	43889	R450

B. The list of Fe I and Fe II lines used in the abundance analysis

Table B.1. The list of Fe I and Fe II lines used in the abundance analysis.

λ, nm	χ, eV	log gf	Ion. stage
612.79070	4.1400	–1.398	Fe I
615.16180	2.1800	–3.300	Fe I
616.53600	4.1400	–1.460	Fe I
617.33360	2.2200	–2.810	Fe I
618.02040	2.7300	–2.650	Fe I
618.79900	3.9400	–1.580	Fe I
620.03130	2.6100	–2.310	Fe I
621.34300	2.2200	–2.550	Fe I
621.92810	2.2000	–2.410	Fe I
622.92283	2.8450	–2.805	Fe I
623.26410	3.6500	–1.130	Fe I
624.63188	3.6020	–0.733	Fe I
625.25554	2.4040	–1.687	Fe I
626.51340	2.1800	–2.510	Fe I
627.02250	2.8600	–2.570	Fe I
627.12788	3.3320	–2.703	Fe I
630.15012	3.6540	–0.718	Fe I
631.58115	4.0760	–1.710	Fe I
632.26860	2.5900	–2.280	Fe I
633.53308	2.1980	–2.177	Fe I
633.68243	3.6860	–0.856	Fe I
634.41490	2.4300	–2.890	Fe I
638.07430	4.1900	–1.270	Fe I
660.91100	2.5600	–2.610	Fe I
670.35670	2.7600	–3.010	Fe I
672.66660	4.6100	–1.010	Fe I
675.01530	2.4200	–2.580	Fe I
680.68450	2.7300	–3.090	Fe I
681.02630	4.6100	–0.940	Fe I
684.36560	4.5500	–0.780	Fe I
685.51620	4.5600	–0.570	Fe I
685.81500	4.6100	–0.910	Fe I
691.66820	4.1500	–1.260	Fe I
614.92580	3.8900	–2.720	Fe II
623.83920	3.8700	–2.520	Fe II
624.75570	3.8900	–2.320	Fe II
636.94620	2.8910	–4.160	Fe II

C. Typical Fe, Na, Zr abundance measurement errors of RGB stars in 47 Tuc

Table C.1. Typical Fe measurement errors (see Sect. 2.5.6 for details).

$T_{\rm eff}$	Star ID	$\sigma(T_{\rm eff})$ dex	$\sigma(\log g)$ dex	$\sigma(\xi_{\rm t})$ dex	σ(cont) dex	σ(fit) dex	$\sigma_{\rm i}$(total) dex
4195	19042	0.03	0.02	0.12	0.10	0.02	0.16
4317	23335	0.03	0.02	0.12	0.10	0.02	0.16
4395	23175	0.03	0.02	0.12	0.10	0.02	0.16
4459	13047	0.03	0.02	0.12	0.10	0.03	0.16
4560	27381	0.03	0.02	0.11	0.10	0.03	0.16
4645	30297	0.03	0.02	0.11	0.10	0.04	0.16
4712	10496	0.04	0.02	0.11	0.10	0.05	0.16
4797	26403	0.04	0.02	0.11	0.10	0.05	0.16

Table C.2. Typical Na measurement errors (see Sect. 2.5.6 for details).

$T_{\rm eff}$	Star ID	$\sigma(T_{\rm eff})$ dex	$\sigma(\log g)$ dex	$\sigma(\xi_{\rm t})$ dex	σ(cont) dex	σ(fit) dex	$\sigma_{\rm i}$(total) dex
4195	19042	0.06	0.01	0.05	0.03	0.03	0.09
4317	23335	0.06	0.01	0.05	0.03	0.04	0.09
4395	23175	0.06	0.01	0.04	0.03	0.04	0.09
4459	13047	0.06	0.01	0.04	0.03	0.04	0.09
4560	27381	0.06	0.01	0.04	0.03	0.05	0.09
4645	30297	0.06	0.01	0.03	0.03	0.05	0.09
4712	10496	0.06	0.01	0.03	0.03	0.05	0.09
4797	26403	0.06	0.01	0.03	0.03	0.05	0.09

Table C.3. Typical Zr measurement errors (see Sect. 2.5.6 for details).

$T_{\rm eff}$	Star ID	$\sigma(T_{\rm eff})$ dex	$\sigma(\log g)$ dex	$\sigma(\xi_{\rm t})$ dex	σ(cont) dex	σ(fit) dex	$\sigma_{\rm i}$(total) dex
4195	19042	0.11	0.02	0.09	0.03	0.04	0.15
4317	23335	0.11	0.01	0.07	0.03	0.04	0.14
4395	23175	0.11	0.01	0.04	0.03	0.05	0.13
4459	13047	0.11	0.01	0.03	0.03	0.05	0.13
4560	27381	0.11	0.00	0.03	0.03	0.05	0.13
4645	30297	0.11	0.00	0.02	0.03	0.05	0.13
4712	10496	0.11	0.00	0.01	0.03	0.05	0.12
4797	26403	0.11	0.00	0.01	0.03	0.05	0.12

D. Abundances of Fe, Na, and Zr determined in the sample of 237 RGB stars in 47 Tuc

Table D.1. Abundances of Fe, Na, and Zr determined in the sample of 237 stars in 47 Tuc.

GAIA Source ID	$T_{\rm eff}$ K	log g	$\xi_{\rm micro}$ km s^{-1}	A(Fe)	[Fe/H]	A(Na)	[Na/Fe]	A(Zr)	[Zr/Fe]	ID	Obs. programme
4689624698313319040	4746	2.38	1.14	6.81	−0.74	5.63	0.20	2.19	0.31	4373	073.D-0211(A)
			1.14	6.80	−0.75	5.65	0.23	2.12	0.25	F-4373	072.D-0777(A)
4689625144980306432	4675	2.13	1.25	6.88	−0.67	5.81	0.31	2.26	0.31	5172	073.D-0211(A)
			1.43	6.78	−0.77	5.90	0.50	2.25	0.40	R259	088.D-0026(A)
4689613840634674048	4271	1.48	1.48	6.82	−0.73	5.66	0.22	2.30	0.41	5277	073.D-0211(A)
4689614837066802944	4630	2.09	1.40	6.79	−0.76	5.84	0.43	2.27	0.41	6808	073.D-0211(A)
4689624801392182784	4759	2.25	1.21	6.88	−0.67	5.85	0.35	2.38	0.43	7904	073.D-0211(A)
			1.30	6.79	−0.76	5.92	0.51	2.34	0.48	R443	088.D-0026(A)
4689629405598401664	4738	2.40	1.17	6.83	−0.72	5.88	0.43	2.25	0.35	9268	073.D-0211(A)
4689637205260940416	4513	1.90	1.42	6.80	−0.75	5.60	0.18	2.20	0.33	9518	073.D-0211(A)
			1.42	6.80	−0.75	5.69	0.27	2.17	0.30	R237	088.D-0026(A)
4689626210141359616	4628	2.12	1.18	6.87	−0.68	5.77	0.28	2.21	0.27	9717	073.D-0211(A)
			1.29	6.83	−0.72	5.75	0.30	2.19	0.29	R682	088.D-0026(A)
4689623594517841024	4696	2.27	1.19	6.84	−0.71	5.84	0.38	2.23	0.32	10397	073.D-0211(A)
4689626313210555904	4712	2.24	1.26	6.85	−0.70	5.95	0.48	2.33	0.41	10496	073.D-0211(A)
4689629779253913984	4543	2.04	1.14	6.82	−0.73	5.56	0.12	2.01	0.12	10994	073.D-0211(A)
4689632669773515392	4649	2.21	1.34	6.79	−0.76	5.76	0.35	2.21	0.35	11008	073.D-0211(A)
4689626381940026752	4708	2.28	1.37	6.73	−0.82	5.72	0.37	2.15	0.35	11169	073.D-0211(A)
4689626416300118400	4790	2.45	1.17	6.84	−0.71	5.82	0.36	2.22	0.31	11675	073.D-0211(A)
4689637578914081024	4616	2.03	1.42	6.84	−0.71	5.99	0.53	2.30	0.39	11709	073.D-0211(A)
4689625862273037696	4781	2.43	1.11	6.87	−0.68	5.73	0.24	2.24	0.30	11756	073.D-0211(A)
4689627099193944064	4517	1.83	1.48	6.85	−0.70	6.06	0.59	2.31	0.39	11927	073.D-0211(A)
4689637819432237952	4459	1.78	1.43	6.76	−0.79	5.70	0.32	2.22	0.39	13047	073.D-0211(A)
4689638373492020736	4614	2.10	1.27	6.79	−0.76	5.60	0.19	2.16	0.30	13668	073.D-0211(A)
			1.23	6.82	−0.73	5.64	0.20	2.14	0.25	F-13668	072.D-0777(A)
4689627167942570240	4742	2.43	1.18	6.84	−0.71	5.72	0.26	2.20	0.29	13718	073.D-0211(A)
4689625896603074816	4736	2.29	1.33	6.83	−0.72	6.10	0.65	2.35	0.45	13939	073.D-0211(A)
4689627236649879936	4755	2.43	1.17	6.81	−0.74	5.81	0.38	2.39	0.51	14487	073.D-0211(A)
4689625965322548992	4614	2.01	1.38	6.87	−0.68	6.13	0.64	2.43	0.49	15552	073.D-0211(A)
			1.53	6.78	−0.77	6.16	0.76	2.47	0.62	R381	088.D-0026(A)
4689627240923227392	4698	2.22	1.28	6.85	−0.70	5.96	0.49	2.23	0.31	16462	073.D-0211(A)
4689646070074296960	4694	2.26	1.28	6.80	−0.75	5.79	0.37	2.15	0.28	16597	073.D-0211(A)
4689625965322548096	4679	2.14	1.31	6.85	−0.70	5.95	0.48	2.29	0.37	16777	073.D-0211(A)
4689637926807831040	4725	2.22	1.19	6.90	−0.65	6.06	0.54	2.32	0.35	16957	073.D-0211(A)
4689625965322552832	4278	1.39	1.57	6.73	−0.82	5.82	0.47	2.35	0.55	17193	073.D-0211(A)
4689637716353064960	4471	1.73	1.39	6.86	−0.69	5.93	0.45	2.25	0.32	17926	073.D-0211(A)
4689627447091792640	4761	2.28	1.21	6.85	−0.70	5.95	0.48	2.35	0.43	18374	073.D-0211(A)
4689637789368802816	4628	2.10	1.20	6.80	−0.75	5.57	0.15	2.16	0.29	19992	073.D-0211(A)
4689638785808484224	4582	1.97	1.43	6.81	−0.74	5.79	0.36	2.30	0.42	20019	073.D-0211(A)
4689638781505129216	4582	1.98	1.41	6.80	−0.75	5.89	0.47	2.27	0.40	20387	073.D-0211(A)
4689627481441306624	4748	2.18	1.17	6.93	−0.62	6.09	0.54	2.39	0.39	20701	073.D-0211(A)
4689638781505112576	4498	1.80	1.45	6.79	−0.76	5.96	0.55	2.27	0.41	20983	073.D-0211(A)
4689627584520466944	4494	1.77	1.48	6.81	−0.74	6.02	0.59	2.21	0.33	22726	073.D-0211(A)
4689637995535079168	4395	1.53	1.52	6.77	−0.78	5.95	0.56	2.31	0.47	23175	073.D-0211(A)
4689627584530658048	4634	2.07	1.38	6.84	−0.71	6.16	0.70	2.31	0.40	23211	073.D-0211(A)
4689639266835463552	4317	1.38	1.60	6.79	−0.76	6.00	0.59	2.41	0.55	23335	073.D-0211(A)
4689639473003821440	4404	1.46	1.38	6.79	−0.76	5.84	0.43	2.54	0.68	23821	073.D-0211(A)
4689642496660354048	4303	1.37	1.79	6.78	−0.77	5.72	0.32	2.13	0.28	23879	073.D-0211(A)
4689641946904328576	4770	2.35	1.24	6.82	−0.73	5.94	0.50	2.33	0.44	24533	073.D-0211(A)
4689641775105775488	4788	2.40	1.18	6.84	−0.71	6.17	0.71	2.31	0.40	24553	073.D-0211(A)
4689639473003144704	4289	1.25	1.52	6.72	−0.83	5.86	0.52	2.43	0.64	25226	073.D-0211(A)
4689638059950649728	4409	1.58	1.57	6.75	−0.80	6.02	0.65	2.25	0.43	25961	073.D-0211(A)
4689639473007322496	4286	1.22	1.62	6.80	−0.75	5.85	0.43	2.30	0.43	26058	073.D-0211(A)
4689627790688724096	4643	2.14	1.32	6.81	−0.74	5.96	0.53	2.19	0.31	26281	073.D-0211(A)
4689639125125572864	4797	2.45	1.24	6.81	−0.74	6.04	0.61	2.41	0.53	26403	073.D-0211(A)
4689641878184846464	4790	2.43	1.23	6.75	−0.80	5.80	0.43	2.23	0.41	26713	073.D-0211(A)
4689639507362821760	4731	2.10	1.23	6.83	−0.72	6.09	0.64	2.38	0.48	26870	073.D-0211(A)
4689639399980545280	4560	1.91	1.37	6.90	−0.65	6.20	0.68	2.35	0.38	27381	073.D-0211(A)
4689639125102514176	4289	1.40	1.56	6.78	−0.77	6.04	0.64	2.21	0.36	27385	073.D-0211(A)
4689642629818274176	4797	2.44	1.17	6.77	−0.78	5.98	0.59	2.18	0.34	27499	073.D-0211(A)
4689627859408196864	4692	2.33	1.25	6.79	−0.76	5.79	0.38	2.37	0.51	27755	073.D-0211(A)
4689639610432530304	4645	2.15	1.35	6.71	−0.84	5.62	0.29	2.13	0.35	30297	073.D-0211(A)
4689628026902152448	4501	1.84	1.52	6.75	−0.80	5.92	0.55	2.17	0.35	30463	073.D-0211(A)
			1.42	6.82	−0.73	6.05	0.61	2.18	0.29	B-30463	072.D-0777(A)
4689639747880182784	4746	2.41	1.11	6.75	−0.80	5.69	0.32	2.18	0.36	30952	073.D-0211(A)
4689628061260674304	4558	1.94	1.39	6.74	−0.81	5.90	0.54	2.19	0.38	31190	073.D-0211(A)
4689639438642541696	4503	1.81	1.37	6.86	−0.69	5.99	0.51	2.28	0.35	31426	073.D-0211(A)
4689640331996429696	4462	1.72	1.44	6.82	−0.73	5.93	0.49	2.29	0.40	31525	073.D-0211(A)
4689639644800976896	4428	1.72	1.44	6.79	−0.76	5.75	0.34	2.23	0.37	31560	073.D-0211(A)
4689638888887480576	4677	2.11	1.28	6.81	−0.74	5.89	0.46	2.16	0.28	31638	073.D-0211(A)
4689643390013939968	4775	2.44	1.20	6.81	−0.74	5.91	0.48	2.21	0.33	33009	073.D-0211(A)
4689639674858450944	4563	1.88	1.39	6.82	−0.73	5.85	0.41	2.35	0.46	34033	073.D-0211(A)
4689640568211564416	4527	1.85	1.50	6.84	−0.71	6.16	0.70	2.34	0.43	35160	073.D-0211(A)
4689639159462279552	4740	2.29	1.21	6.81	−0.74	5.77	0.34	2.20	0.32	35454	073.D-0211(A)
4689639846657238912	4533	1.85	1.48	6.76	−0.79	5.97	0.59	2.20	0.37	35878	073.D-0211(A)
			1.45	6.79	−0.76	6.03	0.62	2.23	0.37	B-35878	072.D-0777(A)
4689639885318980224	4614	2.09	1.35	6.76	−0.79	5.86	0.48	2.12	0.29	37036	073.D-0211(A)

Continued on next page

Table D.1 – *Continued from previous page*

GAIA Source ID	$T_{\rm eff}$ K	$\log g$	$\xi_{\rm micro}$ km s^{-1}	A(Fe)	[Fe/H]	A(Na)	[Na/Fe]	A(Zr)	[Zr/Fe]	ID	Obs. programme
4689640091468599936	4647	2.24	1.18	6.79	−0.76	5.60	0.19	1.98	0.12	38289	073.D-0211(A)
4689640602571357312	4489	1.80	1.37	6.84	−0.71	6.03	0.57	2.15	0.24	39101	073.D-0211(A)
4689640980528658048	4775	2.46	1.04	6.89	−0.66	6.08	0.57	2.37	0.41	42243	073.D-0211(A)
4689637617577709696	4310	1.48	1.48	6.91	−0.64	5.81	0.28	2.31	0.33	B-12128	072.D-0777(A)
4689624354715978112	4340	1.55	1.47	6.77	−0.78	5.64	0.25	2.17	0.33	B-1256	072.D-0777(A)
			1.53	6.72	−0.83	5.62	0.28	2.18	0.39	R287	088.D-0026(A)
4689614970198135296	4245	1.34	1.57	6.78	−0.77	5.56	0.16	2.21	0.36	B-13396	072.D-0777(A)
4689626652510887168	4262	1.34	1.72	6.81	−0.74	5.60	0.17	2.05	0.17	B-13795	072.D-0777(A)
			1.77	6.75	−0.80	5.57	0.20	2.07	0.25	13795	073.D-0211(A)
			1.78	6.74	−0.81	5.64	0.28	2.03	0.22	R752	088.D-0026(A)
4689637510186504064	4392	1.67	1.61	6.73	−0.82	5.65	0.30	2.24	0.44	B-13853	073.D-0211(A)
			1.57	6.76	−0.79	5.69	0.31	2.13	0.30	R246	088.D-0026(A)
4689633799342000640	4357	1.61	1.48	6.73	−0.82	5.57	0.22	2.15	0.35	B-14013	073.D-0211(A)
4689638403539699584	4319	1.52	1.56	6.82	−0.73	5.71	0.27	2.26	0.37	B-14583	073.D-0211(A)
			1.56	6.77	−0.78	5.79	0.40	2.26	0.42	14583	073.D-0211(A)
4689639919678548736	4259	1.33	1.54	6.87	−0.68	5.90	0.41	2.28	0.34	B-14653	073.D-0211(A)
4689637888151712640	4506	1.68	1.84	6.71	−0.84	5.49	0.16	2.05	0.27	B-15797	073.D-0211(A)
4689645928342350976	4420	1.78	1.54	6.80	−0.75	5.82	0.40	2.18	0.31	B-16667	073.D-0211(A)
			1.40	6.82	−0.73	5.89	0.45	2.12	0.23	R790	088.D-0026(A)
4689638476571141248	4503	1.86	1.42	6.79	−0.76	5.66	0.25	2.21	0.35	B-16865	073.D-0211(A)
4689638648369724288	4425	1.69	1.53	6.76	−0.79	5.66	0.28	2.20	0.37	B-17189	073.D-0211(A)
4689638334822345984	4512	1.84	1.38	6.93	−0.62	5.89	0.34	2.37	0.37	B-17819	073.D-0211(A)
			1.38	6.86	−0.69	5.88	0.40	2.20	0.27	R245	088.D-0026(A)
4689638545290915584	4404	1.44	1.79	6.83	−0.72	5.87	0.42	2.15	0.25	B-18661	073.D-0211(A)
4689626893035580032	4506	1.84	1.52	6.76	−0.79	5.96	0.58	2.26	0.43	B-19269	073.D-0211(A)
4689638918944031616	4359	1.41	1.82	6.81	−0.74	5.64	0.21	2.19	0.31	B-20885	073.D-0211(A)
4689627030474839936	4476	1.78	1.47	6.80	−0.75	5.94	0.52	2.24	0.37	B-23032	073.D-0211(A)
4689627756329297024	4431	1.72	1.40	6.83	−0.72	5.77	0.32	2.26	0.36	B-25554	073.D-0211(A)
4689641976960762240	4549	1.77	1.63	6.88	−0.67	5.55	0.05	2.18	0.23	B-26147	073.D-0211(A)
4689628065566610176	4503	1.87	1.53	6.83	−0.72	5.97	0.52	2.20	0.30	B-30949	073.D-0211(A)
			1.41	6.81	−0.74	5.96	0.53	2.16	0.28	R766	088.D-0026(A)
4689628129980153216	4234	1.35	1.52	6.80	−0.75	5.76	0.34	2.26	0.39	B-32730	073.D-0211(A)
			1.55	6.81	−0.74	5.83	0.40	2.27	0.39	32730	073.D-0211(A)
4689639812297492608	4319	1.48	1.61	6.79	−0.76	5.90	0.49	2.23	0.37	B-33689	073.D-0211(A)
4689628129977913728	4234	1.41	1.54	6.81	−0.74	5.72	0.29	2.24	0.36	B-33886	073.D-0211(A)
4689639713520390144	4491	1.84	1.34	6.84	−0.71	5.62	0.16	2.17	0.26	B-36153	073.D-0211(A)
4689639954038489984	4436	1.59	1.66	6.75	−0.80	5.50	0.13	1.95	0.13	B-36270	073.D-0211(A)
4689640435075431040	4423	1.73	1.40	6.93	−0.62	5.86	0.31	2.29	0.29	B-37056	073.D-0211(A)
4689645245438479360	4515	1.77	1.66	6.78	−0.77	5.67	0.27	2.07	0.22	B-3769	073.D-0211(A)
4689640121528464128	4341	1.46	1.81	6.78	−0.77	5.54	0.14	2.12	0.27	B-38890	073.D-0211(A)
4689639988398164736	4489	1.86	1.44	6.84	−0.71	5.74	0.28	2.20	0.29	B-38976	073.D-0211(A)
			1.39	6.77	−0.78	5.81	0.42	2.18	0.34	R762	088.D-0026(A)
4689644592602980608	4243	1.29	1.78	6.73	−0.82	5.56	0.21	1.99	0.19	B-4047	073.D-0211(A)
4689643660581944192	4301	1.47	1.48	6.92	−0.63	5.92	0.38	2.27	0.28	B-41429	073.D-0211(A)
			1.62	6.82	−0.73	5.99	0.55	2.22	0.33	R392	088.D-0026(A)
4689640774370214528	4235	1.32	1.60	6.82	−0.73	5.86	0.42	2.20	0.31	B-41595	073.D-0211(A)
4689643630522760960	4215	1.30	1.52	6.89	−0.66	5.95	0.44	2.30	0.34	B-41654	073.D-0211(A)
4689643733610139648	4430	1.69	1.55	6.80	−0.75	6.07	0.65	2.19	0.32	B-42866	073.D-0211(A)
			1.47	6.79	−0.76	6.13	0.72	2.23	0.37	42866	073.D-0211(A)
			1.50	6.78	−0.77	6.10	0.70	2.14	0.29	R656	088.D-0026(A)
4689640984830516992	4446	1.78	1.52	6.82	−0.73	5.85	0.41	2.20	0.31	B-42887	073.D-0211(A)
			1.54	6.75	−0.80	5.84	0.47	2.18	0.36	R760	088.D-0026(A)
4689622877246364288	4543	1.74	1.54	6.74	−0.81	5.86	0.50	2.24	0.43	B-4374	073.D-0211(A)
4689643767969828352	4457	1.75	1.54	6.85	−0.70	6.10	0.63	2.25	0.33	B-43852	073.D-0211(A)
			1.49	6.78	−0.77	6.07	0.67	2.25	0.40	43852	073.D-0211(A)
			1.45	6.82	−0.73	6.12	0.68	2.22	0.33	R704	088.D-0026(A)
4689625144989910784	4447	1.78	1.47	6.81	−0.74	5.68	0.25	2.18	0.30	B-5362	073.D-0211(A)
			1.47	6.78	−0.77	5.68	0.28	2.21	0.36	R253	088.D-0026(A)
4689626107062230528	4243	1.36	1.40	6.85	−0.70	5.71	0.24	2.37	0.45	B-7330	073.D-0211(A)
4689625793515738368	4430	1.77	1.31	6.92	−0.63	5.70	0.16	2.27	0.28	B-7391	073.D-0211(A)
4689625759155999232	4226	1.29	1.41	7.01	−0.54	5.84	0.21	2.42	0.34	B-7752	073.D-0211(A)
4689625729105416704	4456	1.76	1.43	6.81	−0.74	5.72	0.29	2.27	0.39	B-7993	073.D-0211(A)
			1.45	6.79	−0.76	5.78	0.37	2.16	0.30	R277	088.D-0026(A)
4689626343279687168	4351	1.51	1.43	6.85	−0.70	5.70	0.23	2.28	0.36	B-8742	073.D-0211(A)
4689623530081721216	4363	1.68	1.55	6.81	−0.74	5.74	0.31	2.21	0.33	B-8871	073.D-0211(A)
4689623770599380864	4575	1.81	1.73	6.68	−0.87	5.55	0.25	1.98	0.23	B-9121	073.D-0211(A)
4689629474317872256	4456	1.79	1.55	6.73	−0.82	5.95	0.60	2.10	0.30	B-9163	073.D-0211(A)
			1.42	6.77	−0.78	5.99	0.60	2.08	0.24	R800	088.D-0026(A)
4689618238680828800	4303	1.50	1.58	6.75	−0.80	5.63	0.26	2.22	0.40	B-9254	073.D-0211(A)
4689637239620659968	4474	1.78	1.53	6.81	−0.74	5.81	0.38	2.28	0.40	B-9997	073.D-0211(A)
			1.57	6.77	−0.78	5.89	0.50	2.21	0.37	R248	088.D-0026(A)
4689625827883561216	4608	2.02	1.27	6.90	−0.65	5.87	0.35	2.23	0.26	F-10396	073.D-0211(A)
4689627069134206080	4742	2.44	1.10	6.74	−0.81	5.56	0.20	2.13	0.32	F-11617	073.D-0211(A)
4689627825048445312	4731	2.49	0.99	6.82	−0.73	5.65	0.21	2.18	0.29	F-11867	073.D-0211(A)
4689830753653279104	4669	2.16	1.34	6.78	−0.77	5.82	0.42	2.18	0.33	F-121	073.D-0211(A)
4689632974708827776	4651	2.20	1.24	6.89	−0.66	5.97	0.46	2.09	0.13	F-12408	073.D-0211(A)
			1.49	6.82	−0.73	6.00	0.56	2.24	0.35	R784	088.D-0026(A)
4689633700565630848	4777	2.48	1.14	6.78	−0.77	6.01	0.61	2.31	0.46	F-12518	073.D-0211(A)
4689633696284068480	4786	2.61	1.12	6.70	−0.85	5.56	0.24	2.21	0.44	F-12919	073.D-0211(A)
4689633082090295808	4673	2.40	1.12	6.81	−0.74	5.61	0.18	2.01	0.13	F-13235	073.D-0211(A)
4689637819439945856	4772	2.42	1.17	6.84	−0.71	5.73	0.27	2.31	0.40	F-13569	073.D-0211(A)
4689626446376048000	4799	2.46	1.19	6.83	−0.72	5.76	0.31	2.33	0.43	F-13631	073.D-0211(A)
4689628099926335232	4723	2.42	1.12	6.87	−0.68	5.82	0.33	2.20	0.26	F-13663	073.D-0211(A)
4689644730042488192	4545	2.01	1.44	6.76	−0.79	5.60	0.22	2.11	0.28	F-1389	073.D-0211(A)
			1.34	6.80	−0.75	5.68	0.26	2.15	0.28	1389	073.D-0211(A)
4689637823736084736	4779	2.37	1.12	6.87	−0.68	5.85	0.36	2.35	0.41	F-13977	073.D-0211(A)
4689634044162968192	4685	2.38	1.13	6.72	−0.83	5.61	0.27	2.14	0.35	F-14223	073.D-0211(A)
4689638442211483136	4761	2.33	1.24	6.85	−0.70	6.09	0.62	2.24	0.32	F-14454	073.D-0211(A)
4689638442211457920	4725	2.28	1.30	6.85	−0.70	5.94	0.47	2.30	0.38	F-15451	073.D-0211(A)
			1.30	6.79	−0.76	5.88	0.47	2.31	0.45	15451	073.D-0211(A)
4689626519378816768	4746	2.33	1.19	6.82	−0.73	6.00	0.56	2.17	0.28	F-16258	073.D-0211(A)
4689638712785607680	4663	2.15	1.30	6.75	−0.80	5.63	0.26	2.18	0.36	F-18549	073.D-0211(A)

Continued on next page

Table D.1 – *Continued from previous page*

GAIA Source ID	$T_{\rm eff}$ K	$\log g$	$\xi_{\rm micro}$ km s^{-1}	A(Fe)	[Fe/H]	A(Na)	[Na/Fe]	A(Zr)	[Zr/Fe]	ID	Obs. programme
4689627683309862784	4772	2.44	1.13	6.85	−0.70	5.91	0.44	2.14	0.22	F-22407	073.D-0211(A)
4689641946904350720	4761	2.33	1.37	6.84	−0.71	5.99	0.53	2.26	0.35	F-24463	073.D-0211(A)
			1.21	6.84	−0.71	6.07	0.61	2.30	0.39	24463	073.D-0211(A)
4689642840257564032	4757	2.49	1.11	6.83	−0.72	5.62	0.17	2.27	0.37	F-27938	073.D-0211(A)
4689831853164838784	4783	2.40	1.27	6.81	−0.74	5.98	0.55	2.40	0.52	F-2861	073.D-0211(A)
4689642737178089472	4764	2.50	1.16	6.82	−0.73	5.67	0.23	2.14	0.25	F-30311	073.D-0211(A)
4689643115127053184	4499	1.86	1.46	6.78	−0.77	5.66	0.26	2.17	0.32	F-31510	073.D-0211(A)
4689642423637641984	4786	2.44	1.21	6.76	−0.79	5.69	0.31	2.20	0.37	F-31519	073.D-0211(A)
4689643145217009792	4799	2.47	1.22	6.84	−0.71	5.86	0.40	2.27	0.36	F-31758	073.D-0211(A)
4689628134286385792	4772	2.41	1.26	6.80	−0.75	6.12	0.70	2.14	0.27	F-33686	073.D-0211(A)
4689639640518059136	4757	2.43	1.23	6.72	−0.83	5.65	0.31	2.11	0.32	F-35206	073.D-0211(A)
4689625041910730112	4755	2.31	1.20	6.84	−0.71	5.94	0.48	2.16	0.25	F-3616	073.D-0211(A)
4689639709218245632	4586	2.00	1.32	6.81	−0.74	6.01	0.58	2.26	0.38	F-37781	073.D-0211(A)
4689640671311342720	4792	2.46	1.24	6.80	−0.75	5.98	0.56	2.25	0.38	F-40001	073.D-0211(A)
4689640538154028672	4783	2.45	1.15	6.86	−0.69	6.03	0.55	2.18	0.25	F-40035	073.D-0211(A)
4689641122269520640	4759	2.43	1.12	6.84	−0.71	6.00	0.54	2.13	0.22	F-42112	073.D-0211(A)
4689642389271520512	4755	2.35	1.24	6.82	−0.73	5.90	0.46	2.29	0.40	F-42188	073.D-0211(A)
4689641190988972288	4766	2.44	1.30	6.81	−0.74	6.18	0.75	2.49	0.61	F-43415	073.D-0211(A)
4689625076270567168	4595	2.03	1.29	6.76	−0.79	5.60	0.22	2.08	0.25	F-4754	073.D-0211(A)
4689624732673041664	4740	2.35	1.27	6.80	−0.75	5.72	0.30	2.21	0.34	F-4974	073.D-0211(A)
4689622533650157056	4759	2.50	1.08	6.83	−0.72	5.98	0.53	2.18	0.28	F-5404	073.D-0211(A)
4689623255203461632	4702	2.31	1.21	6.83	−0.72	5.90	0.45	2.21	0.31	F-5576	073.D-0211(A)
4689628546604996608	4772	2.50	1.10	6.76	−0.79	6.13	0.75	2.15	0.32	F-6363	073.D-0211(A)
4689625484312800640	4729	2.32	1.14	6.79	−0.76	5.71	0.30	2.31	0.45	F-6420	073.D-0211(A)
4689623152124232576	4764	2.46	1.11	6.81	−0.74	5.90	0.47	2.11	0.23	F-7200	073.D-0211(A)
4689625793517924480	4733	2.27	1.23	6.86	−0.69	5.85	0.37	2.16	0.23	F-7711	073.D-0211(A)
			1.27	6.88	−0.67	5.89	0.39	2.41	0.46	7711	073.D-0211(A)
4689625763465150336	4751	2.29	1.31	6.81	−0.74	6.15	0.72	2.28	0.40	F-8025	073.D-0211(A)
4689628684043911040	4710	2.42	1.02	6.86	−0.69	5.75	0.27	2.08	0.15	F-8173	073.D-0211(A)
4689626725536875904	4764	2.44	1.12	6.82	−0.73	5.93	0.49	2.19	0.30	F-9325	073.D-0211(A)
4689625832184604160	4755	2.44	1.16	6.78	−0.77	5.64	0.24	2.14	0.29	F-9733	073.D-0211(A)
4689626313220598400	4605	2.01	1.26	6.89	−0.66	6.04	0.53	2.31	0.35	F-9734	073.D-0211(A)
4689618891515852160	4704	2.19	1.44	6.81	−0.74	6.10	0.67	2.29	0.41	R198	088.D-0026(A)
4689619166393741824	4512	1.96	1.46	6.82	−0.73	5.73	0.29	2.22	0.33	R199	088.D-0026(A)
4689830508836705664	4217	1.32	1.61	6.73	−0.82	5.63	0.28	2.18	0.38	R213	088.D-0026(A)
4689641465868395648	4599	2.06	1.40	6.79	−0.76	5.60	0.19	2.09	0.23	R214	088.D-0026(A)
4689638132973884160	4545	1.92	1.43	6.75	−0.80	5.68	0.31	2.08	0.26	R221	088.D-0026(A)
4689638407851742464	4665	2.12	1.36	6.77	−0.78	5.92	0.53	2.13	0.29	R222	088.D-0026(A)
4689830684933831552	4620	2.17	1.37	6.78	−0.77	5.72	0.32	2.23	0.38	R228	088.D-0026(A)
4689642737171879936	4563	2.00	1.45	6.75	−0.80	5.55	0.18	2.15	0.33	R231	088.D-0026(A)
			1.37	6.69	−0.86	5.57	0.26	2.09	0.33	29490	073.D-0211(A)
4689638300460480640	4690	2.11	1.35	6.79	−0.76	6.04	0.63	2.29	0.43	R234	088.D-0026(A)
4689625316788603648	4569	1.99	1.39	6.78	−0.77	5.75	0.35	2.21	0.36	R238	088.D-0026(A)
4689637514498506240	4727	2.28	1.31	6.85	−0.70	5.90	0.43	2.48	0.56	R239	088.D-0026(A)
4689642286190119680	4395	1.63	1.62	6.75	−0.80	5.84	0.47	2.23	0.41	R247	088.D-0026(A)
4689638609700267264	4647	2.03	1.47	6.84	−0.71	6.20	0.74	2.37	0.46	R249	088.D-0026(A)
			1.46	6.85	−0.70	6.21	0.74	2.39	0.47	21369	073.D-0211(A)
4689642290501499904	4241	1.36	1.55	6.82	−0.73	5.91	0.47	2.28	0.39	R256	088.D-0026(A)
			1.55	6.81	−0.74	5.95	0.52	2.28	0.40	B-29146	073.D-0211(A)
4689637548858307584	4657	2.22	1.30	6.81	−0.74	5.69	0.26	2.26	0.38	R258	088.D-0026(A)
4689831165970072448	4486	1.77	1.65	6.79	−0.76	5.97	0.56	2.23	0.37	R264	088.D-0026(A)
4689643351342005888	4417	1.71	1.51	6.73	−0.82	5.58	0.23	2.11	0.31	R266	088.D-0026(A)
4689625454227561984	4667	2.26	1.34	6.78	−0.77	5.71	0.31	2.14	0.29	R269	088.D-0026(A)
4689638682729411712	4612	1.95	1.44	6.78	−0.77	6.00	0.60	2.26	0.41	R273	088.D-0026(A)
4689637922511631872	4667	2.14	1.32	6.76	−0.79	5.61	0.23	2.11	0.28	R274	088.D-0026(A)
4689642251832561280	4573	1.98	1.49	6.78	−0.77	5.73	0.33	2.26	0.41	R279	088.D-0026(A)
4689643145185459072	4635	2.10	1.45	6.87	−0.68	5.99	0.50	2.21	0.27	R281	088.D-0026(A)
4689831264750937344	4237	1.32	1.87	6.82	−0.73	5.74	0.30	2.09	0.20	R283	088.D-0026(A)
4689637926815132032	4639	2.08	1.36	6.87	−0.68	5.96	0.47	2.29	0.35	R288	088.D-0026(A)
4689643218214134016	4649	2.12	1.38	6.86	−0.69	5.96	0.48	2.17	0.24	R310	088.D-0026(A)
4689624556566726912	4725	2.29	1.37	6.82	−0.73	5.88	0.44	2.08	0.19	R317	088.D-0026(A)
			1.29	6.82	−0.73	5.92	0.48	2.33	0.44	F-3476	073.D-0211(A)
4689639159462267392	4426	1.65	1.56	6.79	−0.76	5.87	0.46	2.24	0.38	R330	088.D-0026(A)
4689637991231168768	4466	1.79	1.51	6.75	−0.80	5.68	0.31	2.23	0.41	R342	088.D-0026(A)
4689638820168905088	4702	2.10	1.37	6.78	−0.77	5.96	0.56	2.21	0.36	R346	088.D-0026(A)
4689638815864893312	4624	2.11	1.32	6.83	−0.72	5.77	0.32	2.36	0.46	R348	088.D-0026(A)
4689624835742003840	4575	2.06	1.43	6.74	−0.81	5.75	0.39	2.23	0.42	R352	088.D-0026(A)
4689625969623521152	4663	2.06	1.41	6.79	−0.76	5.90	0.49	2.27	0.41	R356	088.D-0026(A)
4689637785072541952	4663	2.15	1.38	6.81	−0.74	5.87	0.44	2.33	0.45	R360	088.D-0026(A)
4689637995526918400	4535	1.80	1.38	6.82	−0.73	5.98	0.54	2.32	0.43	R377	088.D-0026(A)
4689832712158218880	4498	1.80	1.60	6.77	−0.78	6.02	0.63	2.17	0.33	R390	088.D-0026(A)
4689624797099838080	4267	1.35	1.72	6.73	−0.82	6.05	0.70	2.26	0.46	R408	088.D-0026(A)
4689643905408840320	4426	1.68	1.52	6.82	−0.73	5.98	0.54	2.21	0.32	R450	088.D-0026(A)
			1.54	6.84	−0.71	6.04	0.58	2.24	0.33	B-43889	073.D-0211(A)
			1.51	6.81	−0.74	6.01	0.58	2.29	0.41	43889	073.D-0211(A)
4689643905408839424	4545	1.90	1.37	6.80	−0.75	5.92	0.50	2.23	0.36	R512	088.D-0026(A)
			1.54	6.78	−0.77	5.94	0.54	2.20	0.35	F-43632	073.D-0211(A)
			1.38	6.79	−0.76	5.95	0.54	2.18	0.32	43632	073.D-0211(A)
4689645107999550720	4288	1.50	1.52	6.80	−0.75	5.70	0.28	2.19	0.32	R563	088.D-0026(A)
			1.56	6.77	−0.78	5.69	0.30	2.22	0.38	B-3449	073.D-0211(A)
4689643729302626688	4489	1.84	1.28	6.81	−0.74	5.57	0.14	2.23	0.35	R613	088.D-0026(A)
4689623049045585280	4717	2.26	1.28	6.88	−0.67	5.93	0.43	2.27	0.32	R615	088.D-0026(A)
4689626072702505856	4558	1.94	1.36	6.82	−0.73	5.95	0.51	2.34	0.45	R617	088.D-0026(A)
4689621880814574592	4498	1.88	1.38	6.74	−0.81	5.54	0.18	2.14	0.33	R640	088.D-0026(A)
4689627481451470208	4748	2.22	1.51	6.75	−0.80	6.10	0.73	2.34	0.52	R643	088.D-0026(A)
4689639674858443136	4270	1.38	1.75	6.76	−0.79	5.85	0.47	2.30	0.47	R650	088.D-0026(A)
4689622739807987328	4641	2.16	1.31	6.76	−0.79	5.60	0.22	2.03	0.20	R664	088.D-0026(A)
4689621709015302400	4560	2.04	1.29	6.81	−0.74	5.88	0.45	1.99	0.11	R677	088.D-0026(A)
4689627515811202176	4669	2.12	1.39	6.76	−0.79	5.88	0.50	2.22	0.39	R680	088.D-0026(A)
4689639331261085824	4526	1.94	1.41	6.75	−0.80	5.72	0.35	2.19	0.37	R683	088.D-0026(A)
4689640744312947072	4527	1.90	1.30	6.81	−0.74	5.64	0.21	2.09	0.21	R689	088.D-0026(A)
4689641190988963456	4632	2.13	1.41	6.76	−0.79	5.89	0.51	2.06	0.23	R717	088.D-0026(A)

Continued on next page

Table D.1 – *Continued from previous page*

GAIA Source ID	$T_{\rm eff}$ K	$\log g$	$\xi_{\rm micro}$ km s^{-1}	A(Fe)	[Fe/H]	A(Na)	[Na/Fe]	A(Zr)	[Zr/Fe]	ID	Obs. programme
4689626240194530560	4710	2.24	1.33	6.81	−0.74	6.21	0.78	2.28	0.40	R730	088.D-0026(A)
4689640843083316480	4677	2.19	1.45	6.83	−0.72	5.94	0.49	2.29	0.39	R735	088.D-0026(A)
4689640057117702272	4665	2.21	1.30	6.83	−0.72	5.75	0.30	2.18	0.28	R738	088.D-0026(A)
4689621846454233216	4589	2.11	1.26	6.80	−0.75	5.60	0.18	2.04	0.17	R740	088.D-0026(A)
4689639850959315072	4634	2.04	1.29	6.81	−0.74	5.97	0.54	2.28	0.40	R744	088.D-0026(A)
4689640946182241792	4538	1.89	1.44	6.79	−0.76	6.01	0.60	2.28	0.42	R745	088.D-0026(A)
4689623560134016256	4595	2.01	1.50	6.79	−0.76	5.76	0.35	2.24	0.38	R756	088.D-0026(A)
			1.42	6.76	−0.79	5.79	0.41	2.23	0.40	F-10198	073.D-0211(A)
4689575185928019840	4275	1.45	1.47	6.77	−0.78	5.58	0.19	2.12	0.28	R761	088.D-0026(A)
4689641019190234496	4569	1.97	1.43	6.82	−0.73	6.00	0.56	2.20	0.31	R767	088.D-0026(A)
4689626755588392192	4645	2.17	1.34	6.86	−0.69	6.17	0.69	2.35	0.42	R769	088.D-0026(A)
4689622288822455168	4342	1.66	1.52	6.78	−0.77	5.74	0.34	2.18	0.33	R770	088.D-0026(A)
4689575289007212416	4231	1.34	1.56	6.77	−0.78	5.60	0.21	2.17	0.33	R772	088.D-0026(A)
4689622361850255488	4446	1.72	1.45	6.78	−0.77	5.92	0.52	2.24	0.39	R774	088.D-0026(A)
4689645795196398208	4586	2.03	1.36	6.70	−0.85	5.63	0.31	2.02	0.25	R777	088.D-0026(A)
4689632669773531520	4671	2.24	1.27	6.82	−0.73	5.85	0.41	2.10	0.21	R782	088.D-0026(A)
			1.26	6.82	−0.73	5.96	0.52	2.10	0.21	F-10527	073.D-0211(A)
4689581263316313856	4553	2.07	1.53	6.77	−0.78	5.63	0.24	2.05	0.21	R786	088.D-0026(A)
4689646001354810368	4554	2.00	1.50	6.81	−0.74	6.07	0.64	2.17	0.29	R788	088.D-0026(A)
4689634181601863296	4512	1.88	1.45	6.78	−0.77	5.90	0.50	2.12	0.27	R789	088.D-0026(A)
4689633941083703424	4501	1.96	1.38	6.77	−0.78	5.66	0.27	2.10	0.26	R793	088.D-0026(A)

Note. In cases where abundances were determined using data from several observing programs, we provide microturbulence velocities and abundances obtained using spectra from each individual program. The IDs of individual stars and IDs of the corresponding observing programs are given in the last two columns, respectively (072.D-0777(A), PI: P. François; 073.D-0211(A), PI: E. Carretta; 088.D-0026(A), PI: I. McDonald).

E. Typical Fe, Na, and Ba abundance measurement errors

Table E.1. Typical Fe, Na, and Ba abundance measurement errors.

Element	$\sigma(T_{\rm eff})$ dex	$\sigma(\log g)$ dex	$\sigma(\xi_{\rm t})$ dex	σ(cont) dex	σ(fit) dex	$\sigma_{A({\rm X})}$(total) dex
			$T_{\rm eff} = 4250\,{\rm K}$, $\log g = 1.35$			
Fe	0.03	0.02	0.12	0.10	0.02	0.16
Na	0.06	0.01	0.05	0.03	0.04	0.09
Ba	0.01	0.04	0.10	0.04	0.03	0.12
			$T_{\rm eff} = 4750\,{\rm K}$, $\log g = 2.40$			
Fe	0.04	0.02	0.11	0.10	0.05	0.16
Na	0.06	0.01	0.03	0.03	0.05	0.09
Ba	0.02	0.02	0.08	0.05	0.06	0.12

F. Abundances of Fe, Na, and Ba determined in the sample of 263 RGB stars in 47 Tuc

Table F.1. Abundances of Fe, Na, and Ba in the sample of 263 stars in 47 Tuc. In cases when abundances were determined using data from several observing programs, microturbulence velocities and abundances obtained using spectra from each individual program are provided. The IDs of individual stars and IDs of the corresponding observing programs are given in the last two columns, respectively (072.D-0777(A), PI: P. François; 073.D-0211(A), PI: E. Carretta; 088.D-0026(A), PI: I. McDonald).

GAIA Source ID	$T_{\rm eff}$ K	$\log g$	$\xi_{\rm micro}$ km s^{-1}	A(Fe)	[Fe/H]	A(Na)	[Na/Fe]	A(Ba)	[Ba/Fe]	ID	Obs. program
4689575185928019840	4275	1.45	1.47	6.77	-0.78	5.58	0.19	1.54	0.15	R761	088.D-0026(A)
4689575289007212416	4231	1.34	1.56	6.77	-0.78	5.60	0.21	1.54	0.15	R772	088.D-0026(A)
4689581263316313856	4553	2.07	1.53	6.77	-0.78	5.63	0.24	1.39	0.00	R786	088.D-0026(A)
4689613840634674048	4271	1.48	1.48	6.82	-0.73	5.66	0.22	1.38	-0.06	5277	073.D-0211(A)
4689614837066802944	4630	2.09	1.40	6.79	-0.76	5.84	0.43	1.28	-0.13	6808	073.D-0211(A)
4689614970198135296	4245	1.34	1.57	6.78	-0.77	5.56	0.16	1.36	-0.04	B-13396	072.D-0777(A)
4689618238680828800	4303	1.50	1.58	6.75	-0.80	5.63	0.26	1.33	-0.04	B-9254	072.D-0777(A)
4689618891515852160	4704	2.19	1.44	6.81	-0.74	6.10	0.67	1.42	-0.01	R198	088.D-0026(A)
4689619166393741824	4512	1.96	1.46	6.82	-0.73	5.73	0.29	1.36	-0.08	R199	088.D-0026(A)
4689621709015302400	4560	2.04	1.29	6.81	-0.74	5.88	0.45	1.42	-0.01	R677	088.D-0026(A)
4689621846454233216	4589	2.11	1.26	6.80	-0.75	5.60	0.18	1.52	0.10	R740	088.D-0026(A)
4689621880814574592	4498	1.88	1.38	6.74	-0.81	5.54	0.18	1.45	0.09	R640	088.D-0026(A)
4689622288822455168	4342	1.66	1.52	6.78	-0.77	5.74	0.34	1.42	0.02	R770	088.D-0026(A)
4689622361850255488	4446	1.72	1.45	6.78	-0.77	5.92	0.52	1.46	0.06	R774	088.D-0026(A)
4689622533650157056	4759	2.50	1.08	6.83	-0.72	5.98	0.53	1.45	0.00	F-5404	072.D-0777(A)
4689622739807987328	4641	2.16	1.31	6.76	-0.79	5.60	0.22	1.49	0.11	R664	088.D-0026(A)
4689623049045585280	4717	2.26	1.28	6.88	-0.67	5.93	0.43	1.59	0.09	R615	088.D-0026(A)
4689623152124232576	4764	2.46	1.11	6.81	-0.74	5.90	0.47	1.47	0.04	F-7200	072.D-0777(A)
4689623220843690112	4828	2.57	1.14	6.81	-0.74	5.94	0.51	1.25	-0.18	F-8766	072.D-0777(A)
4689623255203461632	4702	2.31	1.21	6.83	-0.72	5.90	0.45	1.43	-0.02	F-5576	072.D-0777(A)
4689623530081721216	4363	1.68	1.55	6.81	-0.74	5.74	0.31	1.28	-0.15	B-8871	072.D-0777(A)
4689623560134016256	4595	2.01	1.42	6.76	-0.79	5.79	0.41	1.19	-0.19	F-10198	072.D-0777(A)
			1.50	6.79	-0.76	5.76	0.35	1.37	-0.04	R756	088.D-0026(A)
4689623594517841024	4696	2.27	1.19	6.84	-0.71	5.84	0.38	1.49	0.03	10397	073.D-0211(A)
4689624354715978112	4340	1.55	1.47	6.77	-0.78	5.64	0.25	1.48	0.09	B-1256	072.D-0777(A)
			1.53	6.72	-0.83	5.62	0.28	1.45	0.11	R287	088.D-0026(A)
4689624556566726912	4725	2.29	1.29	6.82	-0.73	5.92	0.48	1.46	0.02	F-3476	072.D-0777(A)
			1.37	6.82	-0.73	5.88	0.44	1.44	0.00	R317	088.D-0026(A)
4689624698313319040	4746	2.38	1.14	6.81	-0.74	5.63	0.20	1.52	0.09	4373	073.D-0211(A)
			1.14	6.80	-0.75	5.65	0.23	1.56	0.14	F-4373	072.D-0777(A)
4689624732673041664	4740	2.35	1.27	6.80	-0.75	5.72	0.30	1.44	0.02	F-4974	072.D-0777(A)
4689624799099838080	4267	1.35	1.72	6.73	-0.82	6.05	0.70	1.39	0.04	R408	088.D-0026(A)
4689624801392182784	4759	2.25	1.21	6.88	-0.67	5.85	0.35	1.39	-0.11	7904	073.D-0211(A)
			1.30	6.79	-0.76	5.92	0.51	1.54	0.13	R443	088.D-0026(A)
4689624835742003840	4575	2.06	1.43	6.74	-0.81	5.75	0.39	1.30	-0.06	R352	088.D-0026(A)
4689625041910730112	4755	2.31	1.20	6.84	-0.71	5.94	0.48	1.53	0.07	F-3616	072.D-0777(A)
4689625076270567168	4595	2.03	1.29	6.76	-0.79	5.60	0.22	1.38	0.00	F-4754	072.D-0777(A)
4689625144980306432	4675	2.13	1.25	6.88	-0.67	5.81	0.31	1.41	-0.09	5172	073.D-0211(A)
			1.43	6.78	-0.77	5.90	0.50	1.42	0.02	R259	088.D-0026(A)
4689625144989910784	4447	1.78	1.47	6.81	-0.74	5.68	0.25	1.50	0.07	B-5362	072.D-0777(A)
			1.47	6.78	-0.77	5.68	0.28	1.49	0.09	R253	088.D-0026(A)
4689625316788603648	4569	1.99	1.39	6.78	-0.77	5.75	0.35	1.48	0.08	R238	088.D-0026(A)
4689625346839144960	4826	2.45	1.10	6.87	-0.68	6.14	0.65	1.57	0.08	F-6178	072.D-0777(A)
4689625454227561984	4667	2.26	1.34	6.78	-0.77	5.71	0.31	1.51	0.11	R269	088.D-0026(A)
4689625484312800640	4729	2.32	1.14	6.79	-0.76	5.71	0.30	1.50	0.09	F-6420	072.D-0777(A)
4689625729105416704	4456	1.76	1.43	6.81	-0.74	5.72	0.29	1.50	0.07	B-7993	072.D-0777(A)
			1.45	6.79	-0.76	5.78	0.37	1.52	0.11	R277	088.D-0026(A)
4689625759155999232	4226	1.29	1.41	7.01	-0.54	5.84	0.21	1.63	0.00	B-7752	072.D-0777(A)
4689625763465150336	4751	2.29	1.31	6.81	-0.74	6.15	0.72	1.42	-0.01	F-8025	072.D-0777(A)
4689625793515738368	4430	1.77	1.31	6.92	-0.63	5.70	0.16	1.58	0.04	B-7391	072.D-0777(A)
4689625793517924480	4733	2.27	1.27	6.88	-0.67	5.89	0.39	1.51	0.01	7711	073.D-0211(A)
			1.23	6.86	-0.69	5.85	0.37	1.49	0.01	F-7711	072.D-0777(A)
4689625827883561216	4608	2.02	1.27	6.90	-0.65	5.87	0.35	1.49	-0.03	F-10396	072.D-0777(A)
4689625832184604160	4755	2.44	1.16	6.78	-0.77	5.64	0.24	1.54	0.14	F-9733	072.D-0777(A)
4689625862273037696	4781	2.43	1.11	6.87	-0.68	5.73	0.24	1.42	-0.07	11756	073.D-0211(A)
4689625866544538880	4803	2.50	1.03	6.85	-0.70	5.73	0.26	1.37	-0.10	F-9927	072.D-0777(A)
4689625896603074816	4736	2.29	1.33	6.83	-0.72	6.10	0.65	1.34	-0.11	13939	073.D-0211(A)
4689625965322548992	4614	2.01	1.38	6.87	-0.68	6.13	0.64	1.41	-0.08	15552	073.D-0211(A)
			1.53	6.78	-0.77	6.16	0.76	1.35	-0.05	R381	088.D-0026(A)
4689625965322548096	4679	2.14	1.31	6.85	-0.70	5.95	0.48	1.38	-0.09	16777	073.D-0211(A)
4689625965322552832	4278	1.39	1.57	6.73	-0.82	5.82	0.47	1.38	0.03	17193	073.D-0211(A)
4689625969623521152	4663	2.06	1.41	6.79	-0.76	5.90	0.49	1.57	0.16	R356	088.D-0026(A)
4689626072702505856	4558	1.94	1.36	6.82	-0.73	5.95	0.51	1.47	0.03	R617	088.D-0026(A)
4689626107062230528	4243	1.36	1.40	6.85	-0.70	5.71	0.24	1.64	0.17	B-7330	072.D-0777(A)
4689626210141359616	4628	2.12	1.18	6.87	-0.68	5.77	0.28	1.50	0.01	9717	073.D-0211(A)
			1.29	6.83	-0.72	5.75	0.30	1.54	0.09	R682	088.D-0026(A)
4689626240194530560	4710	2.24	1.33	6.81	-0.74	6.21	0.78	1.59	0.16	R730	088.D-0026(A)

Continued on next page

Table F.1 – *Continued from previous page*

GAIA EDR3 ID	$T_{\rm eff}$ K	$\log g$	$\xi_{\rm micro}$ km s^{-1}	A(Fe)	[Fe/H]	A(Na)	[Na/Fe]	A(Ba)	[Ba/Fe]	ID	Obs. program
4689626313210555904	4712	2.24	1.26	6.85	-0.70	5.95	0.48	1.35	-0.12	10496	073.D-0211(A)
4689626313220598400	4605	2.01	1.26	6.89	-0.66	6.04	0.53	1.43	-0.08	F-9734	072.D-0777(A)
4689626343279687168	4351	1.51	1.43	6.85	-0.70	5.70	0.23	1.57	0.10	B-8742	072.D-0777(A)
4689626381940026752	4708	2.28	1.37	6.73	-0.82	5.72	0.37	1.31	-0.04	11169	073.D-0211(A)
4689626416300118400	4790	2.45	1.17	6.84	-0.71	5.82	0.36	1.38	-0.08	11675	073.D-0211(A)
4689626446376048000	4799	2.46	1.19	6.83	-0.72	5.76	0.31	1.36	-0.09	F-13631	072.D-0777(A)
4689626519378816768	4746	2.33	1.19	6.82	-0.73	6.00	0.56	1.51	0.07	F-16258	072.D-0777(A)
4689626652510887168	4262	1.34	1.77	6.75	-0.80	5.57	0.20	1.47	0.10	13795	073.D-0211(A)
			1.72	6.81	-0.74	5.60	0.17	1.46	0.03	B-13795	072.D-0777(A)
			1.78	6.74	-0.81	5.64	0.28	1.37	0.01	R752	088.D-0026(A)
4689626725536875904	4764	2.44	1.12	6.82	-0.73	5.93	0.49	1.40	-0.04	F-9325	072.D-0777(A)
4689626755588392192	4645	2.17	1.34	6.86	-0.69	6.17	0.69	1.44	-0.04	R769	088.D-0026(A)
4689626893035580032	4506	1.84	1.52	6.76	-0.79	5.96	0.58	1.39	0.01	B-19269	072.D-0777(A)
4689627030474839936	4476	1.78	1.47	6.80	-0.75	5.94	0.52	1.40	-0.02	B-23032	072.D-0777(A)
4689627069134206080	4742	2.44	1.10	6.74	-0.81	5.56	0.20	1.45	0.09	F-11617	072.D-0777(A)
4689627099193944064	4517	1.83	1.48	6.85	-0.70	6.06	0.59	1.37	-0.10	11927	073.D-0211(A)
4689627167942570240	4742	2.43	1.18	6.84	-0.71	5.72	0.26	1.29	-0.17	13718	073.D-0211(A)
4689627206563533056	4819	2.42	1.07	6.86	-0.69	5.92	0.44	1.55	0.07	16089	073.D-0211(A)
4689627206573600640	4803	2.43	1.19	6.82	-0.73	6.04	0.60	1.40	-0.04	17526	073.D-0211(A)
4689627236649879936	4755	2.43	1.17	6.81	-0.74	5.81	0.38	1.42	-0.01	14487	073.D-0211(A)
4689627240923227392	4698	2.22	1.28	6.85	-0.70	5.96	0.49	1.40	-0.07	16462	073.D-0211(A)
4689627408431607936	4810	2.45	1.20	6.82	-0.73	6.02	0.58	1.42	-0.02	18896	073.D-0211(A)
4689627447091792640	4761	2.28	1.21	6.85	-0.70	5.95	0.48	1.45	-0.02	18374	073.D-0211(A)
4689627481441306624	4748	2.18	1.17	6.93	-0.62	6.09	0.54	1.48	-0.07	20701	073.D-0211(A)
4689627481451470208	4748	2.22	1.51	6.75	-0.80	6.10	0.73	1.25	-0.12	R643	088.D-0026(A)
4689627515811202176	4669	2.12	1.39	6.76	-0.79	5.88	0.50	1.31	-0.07	R680	088.D-0026(A)
4689627584520466944	4494	1.77	1.48	6.81	-0.74	6.02	0.59	1.34	-0.09	22726	073.D-0211(A)
4689627584530658048	4634	2.07	1.38	6.84	-0.71	6.16	0.70	1.38	-0.08	23211	073.D-0211(A)
4689627683309862784	4772	2.44	1.13	6.85	-0.70	5.91	0.44	1.45	-0.02	F-22407	072.D-0777(A)
4689627687609838976	4833	2.42	1.28	6.74	-0.81	5.81	0.45	1.26	-0.10	23236	073.D-0211(A)
			1.18	6.86	-0.69	5.88	0.40	1.60	0.12	F-23236	072.D-0777(A)
4689627756329297024	4431	1.72	1.40	6.83	-0.72	5.77	0.32	1.47	0.02	B-25554	072.D-0777(A)
4689627790688724096	4643	2.14	1.32	6.81	-0.74	5.96	0.53	1.40	-0.03	26281	073.D-0211(A)
4689627825048445312	4731	2.49	0.99	6.82	-0.73	5.65	0.21	1.50	0.06	F-11867	072.D-0777(A)
4689627859408196864	4692	2.33	1.25	6.79	-0.76	5.79	0.38	1.45	0.04	27755	073.D-0211(A)
4689628026902152448	4501	1.84	1.52	6.75	-0.80	5.92	0.55	1.30	-0.07	30463	073.D-0211(A)
			1.42	6.82	-0.73	6.05	0.61	1.48	0.04	B-30463	072.D-0777(A)
4689628061260674304	4558	1.94	1.39	6.74	-0.81	5.90	0.54	1.38	0.02	31190	073.D-0211(A)
4689628065566610176	4503	1.87	1.53	6.83	-0.72	5.97	0.52	1.49	0.04	B-30949	072.D-0777(A)
			1.41	6.81	-0.74	5.96	0.53	1.55	0.12	R766	088.D-0026(A)
4689628099926335232	4723	2.42	1.12	6.87	-0.68	5.82	0.33	1.44	-0.05	F-13663	072.D-0777(A)
4689628129977913728	4234	1.41	1.54	6.81	-0.74	5.72	0.29	1.46	0.03	B-33886	072.D-0777(A)
4689628129980153216	4234	1.35	1.55	6.81	-0.74	5.83	0.40	1.37	-0.06	32730	073.D-0211(A)
			1.52	6.80	-0.75	5.76	0.34	1.43	0.01	B-32730	072.D-0777(A)
4689628134286385792	4772	2.41	1.26	6.80	-0.75	6.12	0.70	1.53	0.11	F-33686	072.D-0777(A)
4689628168645809792	4854	2.80	1.06	6.79	-0.76	5.76	0.35	1.46	0.05	F-14106	072.D-0777(A)
4689628546604996608	4772	2.50	1.10	6.76	-0.79	6.13	0.75	1.48	0.10	F-6363	072.D-0777(A)
4689628684043911040	4710	2.42	1.02	6.86	-0.69	5.75	0.27	1.51	0.03	F-8173	072.D-0777(A)
4689629405598401664	4738	2.40	1.17	6.83	-0.72	5.88	0.43	1.54	0.09	9268	073.D-0211(A)
4689629474317872256	4456	1.79	1.55	6.73	-0.82	5.95	0.60	1.45	0.10	B-9163	072.D-0777(A)
			1.42	6.77	-0.78	5.99	0.60	1.45	0.06	R800	088.D-0026(A)
4689629779253913984	4543	2.04	1.14	6.82	-0.73	5.56	0.12	1.40	-0.04	10994	073.D-0211(A)
			1.36	6.80	-0.75	5.72	0.30	1.75	0.33	R795	088.D-0026(A)
4689632669773515392	4649	2.21	1.34	6.79	-0.76	5.76	0.35	1.36	-0.05	11008	073.D-0211(A)
4689632669773531520	4671	2.24	1.26	6.82	-0.73	5.96	0.52	1.47	0.03	F-10527	072.D-0777(A)
			1.27	6.82	-0.73	5.85	0.41	1.59	0.15	R782	088.D-0026(A)
4689632974708827776	4651	2.20	1.24	6.89	-0.66	5.97	0.46	1.45	-0.06	F-12408	072.D-0777(A)
			1.49	6.82	-0.73	6.00	0.56	1.14	-0.30	R784	088.D-0026(A)
4689633082090295808	4673	2.40	1.12	6.81	-0.74	5.61	0.18	1.39	-0.04	F-13235	072.D-0777(A)
4689633696284068480	4786	2.61	1.12	6.70	-0.85	5.56	0.24	1.33	0.01	F-12919	072.D-0777(A)
4689633700565630848	4777	2.48	1.14	6.78	-0.77	6.01	0.61	1.41	0.01	F-12518	072.D-0777(A)
4689633799342000640	4357	1.61	1.48	6.73	-0.82	5.57	0.22	1.50	0.15	B-14013	072.D-0777(A)
4689633941083703424	4501	1.96	1.38	6.77	-0.78	5.66	0.27	1.56	0.17	R793	088.D-0026(A)
4689634044162968192	4685	2.38	1.13	6.72	-0.83	5.61	0.27	1.47	0.13	F-14223	072.D-0777(A)
4689634181601863296	4512	1.88	1.45	6.78	-0.77	5.90	0.50	1.35	-0.05	R789	088.D-0026(A)
4689637067822049024	4873	2.61	1.03	6.91	-0.64	5.97	0.44	1.52	-0.01	F-5007	072.D-0777(A)
4689637205260940416	4513	1.90	1.42	6.80	-0.75	5.60	0.18	1.44	0.02	9518	073.D-0211(A)
			1.42	6.80	-0.75	5.69	0.27	1.51	0.09	R237	088.D-0026(A)
4689637239620659968	4474	1.78	1.53	6.81	-0.74	5.81	0.38	1.42	-0.01	B-9997	072.D-0777(A)
			1.57	6.77	-0.78	5.89	0.50	1.38	-0.01	R248	088.D-0026(A)
4689637239620674688	4815	2.48	1.08	6.91	-0.64	6.00	0.47	1.60	0.07	F-9326	072.D-0777(A)
4689637510186504064	4392	1.67	1.61	6.73	-0.82	5.65	0.30	1.32	-0.03	B-13853	072.D-0777(A)
			1.57	6.76	-0.79	5.69	0.31	1.46	0.08	R246	088.D-0026(A)
4689637514498506240	4727	2.28	1.31	6.85	-0.70	5.90	0.43	1.61	0.14	R239	088.D-0026(A)
4689637544562238464	4840	2.56	1.14	6.88	-0.67	5.99	0.49	1.50	0.00	F-11073	072.D-0777(A)
4689637548858307584	4657	2.22	1.30	6.81	-0.74	5.69	0.26	1.60	0.17	R258	088.D-0026(A)
4689637578914081024	4616	2.03	1.42	6.84	-0.71	5.99	0.53	1.45	-0.01	11709	073.D-0211(A)
4689637617577709696	4310	1.48	1.48	6.91	-0.64	5.81	0.28	1.48	-0.05	B-12128	072.D-0777(A)
4689637716353064960	4471	1.73	1.39	6.86	-0.69	5.93	0.45	1.51	0.03	17926	073.D-0211(A)
4689637720649454464	4835	2.43	1.14	6.85	-0.70	6.04	0.57	1.43	-0.04	17238	073.D-0211(A)
4689637785072541952	4663	2.15	1.38	6.81	-0.74	5.87	0.44	1.46	0.03	R360	088.D-0026(A)
4689637789368802816	4628	2.10	1.20	6.80	-0.75	5.57	0.15	1.48	0.06	19992	073.D-0211(A)
4689637819432237952	4459	1.78	1.43	6.76	-0.79	5.70	0.32	1.46	0.08	13047	073.D-0211(A)
4689637819439945856	4772	2.42	1.17	6.84	-0.71	5.73	0.27	1.54	0.08	F-13569	072.D-0777(A)
4689637823736084736	4779	2.37	1.12	6.87	-0.68	5.85	0.36	1.50	0.01	F-13977	072.D-0777(A)
4689637892455512576	4840	2.47	1.28	6.85	-0.70	5.95	0.48	1.35	-0.12	F-15916	072.D-0777(A)
4689637922511631872	4667	2.14	1.32	6.76	-0.79	5.61	0.23	1.57	0.19	R274	088.D-0026(A)
4689637926807831040	4725	2.22	1.19	6.90	-0.65	6.06	0.54	1.54	0.02	16957	073.D-0211(A)
4689637926815132032	4639	2.08	1.36	6.87	-0.68	5.96	0.47	1.53	0.04	R288	088.D-0026(A)
4689637991231168768	4466	1.79	1.51	6.75	-0.80	5.68	0.31	1.37	0.00	R342	088.D-0026(A)
4689637995535079168	4395	1.53	1.52	6.77	-0.78	5.95	0.56	1.36	-0.03	23175	073.D-0211(A)
4689638059950649728	4409	1.58	1.57	6.75	-0.80	6.02	0.65	1.34	-0.03	25961	073.D-0211(A)

Continued on next page

Table F.1 – *Continued from previous page*

GAIA EDR3 ID	$T_{\rm eff}$ K	$\log g$	$\xi_{\rm micro}$ km s^{-1}	A(Fe)	[Fe/H]	A(Na)	[Na/Fe]	A(Ba)	[Ba/Fe]	ID	Obs. program
4689638132973884160	4545	1.92	1.43	6.75	-0.80	5.68	0.31	1.46	0.09	R221	088.D-0026(A)
4689638300460480640	4690	2.11	1.35	6.79	-0.76	6.04	0.63	1.57	0.16	R234	088.D-0026(A)
4689638334822345984	4512	1.84	1.38	6.93	-0.62	5.89	0.34	1.50	-0.05	B-17819	072.D-0777(A)
			1.38	6.86	-0.69	5.88	0.40	1.58	0.10	R245	088.D-0026(A)
4689638373492020736	4614	2.10	1.27	6.79	-0.76	5.60	0.19	1.48	0.07	13668	073.D-0211(A)
			1.23	6.82	-0.73	5.64	0.20	1.40	-0.04	F-13668	072.D-0777(A)
4689638403539699584	4319	1.52	1.56	6.77	-0.78	5.79	0.40	1.34	-0.05	14583	073.D-0211(A)
			1.56	6.82	-0.73	5.71	0.27	1.39	-0.05	B-14583	072.D-0777(A)
4689638407851742464	4665	2.12	1.36	6.77	-0.78	5.92	0.53	1.62	0.23	R222	088.D-0026(A)
4689638442211457920	4725	2.28	1.30	6.79	-0.76	5.88	0.47	1.30	-0.11	15451	073.D-0211(A)
			1.30	6.85	-0.70	5.94	0.47	1.45	-0.02	F-15451	072.D-0777(A)
4689638442211483136	4761	2.33	1.24	6.85	-0.70	6.09	0.62	1.46	-0.01	F-14454	072.D-0777(A)
4689638476571141248	4503	1.86	1.42	6.79	-0.76	5.66	0.25	1.44	0.03	B-16865	072.D-0777(A)
4689638510930785024	4882	2.64	0.96	6.96	-0.59	5.98	0.40	1.59	0.01	F-18267	072.D-0777(A)
4689638609700267264	4647	2.03	1.46	6.85	-0.70	6.21	0.74	1.24	-0.23	21369	073.D-0211(A)
			1.47	6.84	-0.71	6.20	0.74	1.42	-0.04	R249	088.D-0026(A)
4689638648369724288	4425	1.69	1.53	6.76	-0.79	5.66	0.28	1.23	-0.15	B-17189	072.D-0777(A)
4689638682729411712	4612	1.95	1.44	6.78	-0.77	6.00	0.60	1.41	0.01	R273	088.D-0026(A)
4689638712785607680	4663	2.15	1.30	6.75	-0.80	5.63	0.26	1.47	0.10	F-18549	072.D-0777(A)
4689638781505112576	4498	1.80	1.45	6.79	-0.76	5.96	0.55	1.34	-0.07	20983	073.D-0211(A)
4689638781505129216	4582	1.98	1.41	6.80	-0.75	5.89	0.47	1.40	-0.02	20387	073.D-0211(A)
4689638785808484224	4582	1.97	1.43	6.81	-0.74	5.79	0.36	1.35	-0.08	20019	073.D-0211(A)
4689638815864893312	4624	2.11	1.32	6.83	-0.72	5.77	0.32	1.40	-0.05	R348	088.D-0026(A)
4689638888887480576	4677	2.11	1.28	6.81	-0.74	5.89	0.46	1.41	-0.02	31638	073.D-0211(A)
4689638991966936704	4897	2.71	1.17	6.84	-0.71	5.90	0.44	1.48	0.02	F-21775	072.D-0777(A)
4689639056383040768	4826	2.46	1.23	6.74	-0.81	5.84	0.48	1.32	-0.04	25487	073.D-0211(A)
4689639125102514176	4289	1.40	1.56	6.78	-0.77	6.04	0.64	1.54	0.14	27385	073.D-0211(A)
4689639125125572864	4797	2.45	1.24	6.81	-0.74	6.04	0.61	1.35	-0.08	26403	073.D-0211(A)
4689639159462267392	4426	1.65	1.56	6.79	-0.76	5.87	0.46	1.35	-0.06	R330	088.D-0026(A)
4689639159462279552	4740	2.29	1.21	6.81	-0.74	5.77	0.34	1.49	0.06	35454	073.D-0211(A)
4689639232475550336	4412	1.57	1.44	6.82	-0.73	5.88	0.44	1.45	0.01	24665	073.D-0211(A)
4689639331261085824	4526	1.94	1.41	6.75	-0.80	5.72	0.35	1.41	0.04	R683	088.D-0026(A)
4689639399980545280	4560	1.91	1.37	6.90	-0.65	6.20	0.68	1.46	-0.06	27381	073.D-0211(A)
4689639438642541696	4503	1.81	1.37	6.86	-0.69	5.99	0.51	1.47	-0.01	31426	073.D-0211(A)
4689639473003144704	4289	1.25	1.52	6.72	-0.83	5.86	0.52	1.32	-0.02	25226	073.D-0211(A)
4689639473007322496	4286	1.22	1.62	6.80	-0.75	5.85	0.43	1.45	0.03	26058	073.D-0211(A)
4689639507362821760	4731	2.10	1.23	6.83	-0.72	6.09	0.64	1.28	-0.17	26870	073.D-0211(A)
4689639610432530304	4645	2.15	1.35	6.71	-0.84	5.62	0.29	1.30	-0.03	30297	073.D-0211(A)
4689639640518059136	4757	2.43	1.23	6.72	-0.83	5.65	0.31	1.41	0.07	F-35206	072.D-0777(A)
4689639644800943872	4856	2.61	1.07	6.83	-0.72	6.08	0.63	1.44	-0.01	F-33465	072.D-0777(A)
4689639644800976896	4428	1.72	1.44	6.79	-0.76	5.75	0.34	1.35	-0.06	31560	073.D-0211(A)
4689639674858443136	4270	1.38	1.75	6.76	-0.79	5.85	0.47	1.24	-0.14	R650	088.D-0026(A)
4689639674858450944	4563	1.88	1.39	6.82	-0.73	5.85	0.41	1.47	0.03	34033	073.D-0211(A)
4689639709218245632	4586	2.00	1.32	6.81	-0.74	6.01	0.58	1.42	-0.01	F-37781	072.D-0777(A)
4689639713520390144	4491	1.84	1.34	6.84	-0.71	5.62	0.16	1.57	0.11	B-36153	072.D-0777(A)
4689639747880182784	4746	2.41	1.11	6.75	-0.80	5.69	0.32	1.50	0.13	30952	073.D-0211(A)
4689639812297492608	4319	1.48	1.61	6.79	-0.76	5.90	0.49	1.42	0.01	B-33689	072.D-0777(A)
4689639846657238912	4533	1.85	1.48	6.76	-0.79	5.97	0.59	1.22	-0.16	35878	073.D-0211(A)
			1.45	6.79	-0.76	6.03	0.62	1.36	-0.05	B-35878	072.D-0777(A)
4689639850959315072	4634	2.04	1.29	6.81	-0.74	5.97	0.54	1.51	0.08	R744	088.D-0026(A)
4689639885318980224	4614	2.09	1.35	6.76	-0.79	5.86	0.48	1.43	0.05	37036	073.D-0211(A)
4689639919678548736	4259	1.33	1.54	6.87	-0.68	5.90	0.41	1.59	0.10	B-14653	072.D-0777(A)
4689639954038489984	4436	1.59	1.66	6.75	-0.80	5.50	0.13	1.57	0.20	B-36270	072.D-0777(A)
4689639988398164736	4489	1.86	1.44	6.84	-0.71	5.74	0.28	1.42	-0.04	B-38976	072.D-0777(A)
			1.39	6.77	-0.78	5.81	0.42	1.46	0.07	R762	088.D-0026(A)
4689640052815669632	4826	2.44	1.13	6.85	-0.70	5.90	0.43	1.42	-0.05	37233	073.D-0211(A)
4689640057117702272	4665	2.21	1.30	6.83	-0.72	5.75	0.30	1.42	-0.03	R738	088.D-0026(A)
4689640091468599936	4647	2.24	1.18	6.79	-0.76	5.60	0.19	1.60	0.19	38289	073.D-0211(A)
4689640121528464128	4341	1.46	1.81	6.78	-0.77	5.54	0.14	1.27	-0.13	B-38890	072.D-0777(A)
4689640160196860672	4868	2.69	1.10	6.78	-0.77	5.88	0.48	1.45	0.05	F-39156	072.D-0777(A)
4689640297636711424	4835	2.46	1.10	6.80	-0.75	5.66	0.24	1.51	0.09	31223	073.D-0211(A)
4689640331996429696	4462	1.72	1.44	6.82	-0.73	5.93	0.49	1.39	-0.05	31525	073.D-0211(A)
4689640435075431040	4423	1.73	1.40	6.93	-0.62	5.86	0.31	1.52	-0.03	B-37056	072.D-0777(A)
4689640538154028672	4783	2.45	1.15	6.86	-0.69	6.03	0.55	1.42	-0.06	F-40035	072.D-0777(A)
4689640568211564416	4527	1.85	1.50	6.84	-0.71	6.16	0.70	1.40	-0.06	35160	073.D-0211(A)
4689640602571357312	4489	1.80	1.37	6.84	-0.71	6.03	0.57	1.49	0.03	39101	073.D-0211(A)
4689640671311342720	4792	2.46	1.24	6.80	-0.75	5.98	0.56	1.44	0.02	F-40001	072.D-0777(A)
4689640744312947072	4527	1.90	1.30	6.81	-0.74	5.64	0.21	1.71	0.28	R689	088.D-0026(A)
4689640774370214528	4235	1.32	1.60	6.82	-0.73	5.86	0.42	1.38	-0.06	B-41595	072.D-0777(A)
4689640843083316480	4677	2.19	1.45	6.83	-0.72	5.94	0.49	1.37	-0.08	R735	088.D-0026(A)
4689640916111100800	4812	2.49	1.20	6.80	-0.75	6.13	0.71	1.57	0.15	F-41372	072.D-0777(A)
4689640946182241792	4538	1.89	1.44	6.79	-0.76	6.01	0.60	1.51	0.10	R745	088.D-0026(A)
4689640980528658048	4775	2.46	1.04	6.89	-0.66	6.08	0.57	1.76	0.25	42243	073.D-0211(A)
4689640984830516992	4446	1.78	1.52	6.82	-0.73	5.85	0.41	1.37	-0.07	B-42887	072.D-0777(A)
			1.54	6.75	-0.80	5.84	0.47	1.40	0.03	R760	088.D-0026(A)
4689641019190234496	4569	1.97	1.43	6.82	-0.73	6.00	0.56	1.47	0.03	R767	088.D-0026(A)
4689641122269520640	4759	2.43	1.12	6.84	-0.71	6.00	0.54	1.46	0.00	F-42112	072.D-0777(A)
4689641190988963456	4632	2.13	1.41	6.76	-0.79	5.89	0.51	1.39	0.01	R717	088.D-0026(A)
4689641190988972288	4766	2.44	1.30	6.81	-0.74	6.18	0.75	1.51	0.08	F-43415	072.D-0777(A)
4689641465868395648	4599	2.06	1.40	6.79	-0.76	5.60	0.19	1.48	0.07	R214	088.D-0026(A)
4689641775105775488	4788	2.40	1.18	6.84	-0.71	6.17	0.71	1.55	0.09	24553	073.D-0211(A)
4689641878184846464	4790	2.43	1.23	6.75	-0.80	5.80	0.43	1.35	-0.02	26713	073.D-0211(A)
4689641946904328576	4770	2.35	1.24	6.82	-0.73	5.94	0.50	1.42	-0.02	24533	073.D-0211(A)
4689641946904350720	4761	2.33	1.21	6.84	-0.71	6.07	0.61	1.45	-0.01	24463	073.D-0211(A)
			1.37	6.84	-0.71	5.99	0.53	1.31	-0.15	F-24463	072.D-0777(A)
4689641976960762240	4549	1.77	1.63	6.88	-0.67	5.55	0.05	1.42	-0.08	B-26147	072.D-0777(A)
4689641981263971584	4808	2.44	1.13	6.81	-0.74	6.02	0.59	1.41	-0.02	25770	073.D-0211(A)
4689641981263993344	4801	2.46	1.09	6.89	-0.66	5.83	0.32	1.50	-0.01	F-25674	072.D-0777(A)
4689642049983451776	4882	2.68	1.13	6.82	-0.73	5.85	0.41	1.41	-0.03	F-26218	072.D-0777(A)
4689642251832561280	4573	1.98	1.49	6.78	-0.77	5.73	0.33	1.42	0.02	R279	088.D-0026(A)
4689642286190119680	4395	1.63	1.62	6.75	-0.80	5.84	0.47	1.41	0.04	R247	088.D-0026(A)
4689642286220954112	4878	2.51	1.22	6.81	-0.74	6.18	0.75	1.48	0.05	F-29048	072.D-0777(A)

Continued on next page

Table F.1 – *Continued from previous page*

GAIA EDR3 ID	$T_{\rm eff}$ K	$\log g$	$\xi_{\rm micro}$ km s^{-1}	A(Fe)	[Fe/H]	A(Na)	[Na/Fe]	A(Ba)	[Ba/Fe]	ID	Obs. program
4689642290501499904	4241	1.36	1.55	6.81	-0.74	5.95	0.52	1.44	0.01	B-29146	072.D-0777(A)
			1.55	6.82	-0.73	5.91	0.47	1.54	0.10	R256	088.D-0026(A)
4689642324861105920	4822	2.47	1.21	6.74	-0.81	6.04	0.68	1.43	0.07	30949	073.D-0211(A)
4689642324861157504	4808	2.47	1.14	6.85	-0.70	6.01	0.54	1.54	0.07	30104	073.D-0211(A)
			1.11	6.99	-0.56	6.08	0.47	1.56	-0.05	F-30104	072.D-0777(A)
4689642389271520512	4755	2.35	1.24	6.82	-0.73	5.90	0.46	1.42	-0.02	F-42188	072.D-0777(A)
4689642423637641984	4786	2.44	1.21	6.76	-0.79	5.69	0.31	1.51	0.13	F-31519	072.D-0777(A)
4689642427940223360	4840	2.58	1.21	6.88	-0.67	6.02	0.52	1.35	-0.15	F-31871	072.D-0777(A)
4689642496660354048	4303	1.37	1.79	6.78	-0.77	5.72	0.32	1.34	-0.06	23879	073.D-0211(A)
4689642629818274176	4797	2.44	1.17	6.77	-0.78	5.98	0.59	1.31	-0.08	27499	073.D-0211(A)
4689642702818392960	4803	2.43	1.30	6.77	-0.78	5.96	0.57	1.29	-0.10	29886	073.D-0211(A)
4689642737171879936	4563	2.00	1.37	6.69	-0.86	5.57	0.26	1.30	-0.01	29490	073.D-0211(A)
			1.45	6.75	-0.80	5.55	0.18	1.29	-0.08	R231	088.D-0026(A)
4689642737178089472	4764	2.50	1.16	6.82	-0.73	5.67	0.23	1.39	-0.05	F-30311	072.D-0777(A)
4689642840257564032	4757	2.49	1.11	6.83	-0.72	5.62	0.17	1.48	0.03	F-27938	072.D-0777(A)
4689643115127053184	4499	1.86	1.46	6.78	-0.77	5.66	0.26	1.30	-0.10	F-31510	072.D-0777(A)
4689643145185459072	4635	2.10	1.45	6.87	-0.68	5.99	0.50	1.25	-0.24	R281	088.D-0026(A)
4689643145217009792	4799	2.47	1.22	6.84	-0.71	5.86	0.40	1.44	-0.02	F-31758	072.D-0777(A)
4689643218214134016	4649	2.12	1.38	6.86	-0.69	5.96	0.48	1.41	-0.07	R310	088.D-0026(A)
4689643351342005888	4417	1.71	1.51	6.73	-0.82	5.58	0.23	1.40	0.05	R266	088.D-0026(A)
4689643390013939968	4775	2.44	1.20	6.81	-0.74	5.91	0.48	1.43	0.00	33009	073.D-0211(A)
4689643591868752896	4808	2.45	1.21	6.79	-0.76	5.82	0.41	1.42	0.01	40718	073.D-0211(A)
4689643630522760960	4215	1.30	1.52	6.89	-0.66	5.95	0.44	1.57	0.06	B-41654	072.D-0777(A)
4689643660581944192	4301	1.47	1.48	6.92	-0.63	5.92	0.38	1.48	-0.06	B-41429	072.D-0777(A)
			1.62	6.82	-0.73	5.99	0.55	1.30	-0.14	R392	088.D-0026(A)
4689643729302626688	4489	1.84	1.28	6.81	-0.74	5.57	0.14	1.57	0.14	R613	088.D-0026(A)
4689643733610139648	4430	1.69	1.47	6.79	-0.76	6.13	0.72	1.44	0.03	42866	073.D-0211(A)
			1.55	6.80	-0.75	6.07	0.65	1.40	-0.02	B-42866	072.D-0777(A)
			1.50	6.78	-0.77	6.10	0.70	1.50	0.10	R656	088.D-0026(A)
4689643733610187392	4806	2.46	1.15	6.88	-0.67	5.98	0.48	1.50	0.00	F-41820	072.D-0777(A)
4689643767969828352	4457	1.75	1.49	6.78	-0.77	6.07	0.67	1.43	0.03	43852	073.D-0211(A)
			1.54	6.85	-0.70	6.10	0.63	1.54	0.07	B-43852	072.D-0777(A)
			1.45	6.82	-0.73	6.12	0.68	1.67	0.23	R704	088.D-0026(A)
4689643905408839424	4545	1.90	1.38	6.79	-0.76	5.95	0.54	1.40	-0.01	43632	073.D-0211(A)
			1.54	6.78	-0.77	5.94	0.54	1.18	-0.22	F-43632	072.D-0777(A)
			1.37	6.80	-0.75	5.92	0.50	1.41	-0.01	R512	088.D-0026(A)
4689643905408840320	4426	1.68	1.51	6.81	-0.74	6.01	0.58	1.38	-0.05	43889	073.D-0211(A)
			1.54	6.84	-0.71	6.04	0.58	1.43	-0.03	B-43889	072.D-0777(A)
			1.52	6.82	-0.73	5.98	0.54	1.41	-0.03	R450	088.D-0026(A)
4689644592602980608	4243	1.29	1.78	6.73	-0.82	5.56	0.21	1.43	0.08	B-4047	072.D-0777(A)
4689644730042488192	4545	2.01	1.34	6.80	-0.75	5.68	0.26	1.30	-0.12	1389	073.D-0211(A)
			1.44	6.76	-0.79	5.60	0.22	1.22	-0.16	F-1389	072.D-0777(A)
4689645107999550720	4288	1.50	1.56	6.77	-0.78	5.69	0.30	1.47	0.08	B-3449	072.D-0777(A)
			1.52	6.80	-0.75	5.70	0.28	1.33	-0.09	R563	088.D-0026(A)
4689645245438479360	4515	1.77	1.66	6.78	-0.77	5.67	0.27	1.41	0.01	B-3769	072.D-0777(A)
4689645795196398208	4586	2.03	1.36	6.70	-0.85	5.63	0.31	1.50	0.18	R777	088.D-0026(A)
4689645928342350976	4420	1.78	1.54	6.80	-0.75	5.82	0.40	1.33	-0.09	B-16667	072.D-0777(A)
			1.40	6.82	-0.73	5.89	0.45	1.63	0.19	R790	088.D-0026(A)
4689646001354810368	4554	2.00	1.50	6.81	-0.74	6.07	0.64	1.59	0.16	R788	088.D-0026(A)
4689646070074296960	4694	2.26	1.28	6.80	-0.75	5.79	0.37	1.35	-0.07	16597	073.D-0211(A)
			1.22	6.80	-0.75	5.95	0.53	1.66	0.24	R778	088.D-0026(A)
4689830508836705664	4217	1.32	1.61	6.73	-0.82	5.63	0.28	1.56	0.21	R213	088.D-0026(A)
4689830616214384256	4806	2.49	1.30	6.82	-0.73	6.12	0.68	1.45	0.01	F-31646	072.D-0777(A)
4689830684933831552	4620	2.17	1.37	6.78	-0.77	5.72	0.32	1.30	-0.10	R228	088.D-0026(A)
4689830753653279104	4669	2.16	1.34	6.78	-0.77	5.82	0.42	1.42	0.02	F-121	072.D-0777(A)
4689831165970072448	4486	1.77	1.65	6.79	-0.76	5.97	0.56	1.30	-0.11	R264	088.D-0026(A)
4689831264750937344	4237	1.32	1.87	6.82	-0.73	5.74	0.30	1.45	0.01	R283	088.D-0026(A)
4689831853164838784	4783	2.40	1.27	6.81	-0.74	5.98	0.55	1.33	-0.10	F-2861	072.D-0777(A)
4689832712158218880	4498	1.80	1.60	6.77	-0.78	6.02	0.63	1.21	-0.18	R390	088.D-0026(A)

G. Typical errors in the measured Fe, Na, and Sr abundances

Table G.1. Typical errors in the measured Fe, Na, and Sr abundances.

Element	$T_{\rm eff}$ K	Star ID	$\sigma(T_{\rm eff})$ dex	$\sigma(\log g)$ dex	$\sigma(\xi_{\rm micro})$ dex	σ(cont) dex	σ(fit) dex	$\sigma_{\rm i}$(total) dex
Fe I	4057	s17657	0.03	0.02	0.14	0.09	0.02	0.17
	4358	20885	0.03	0.02	0.12	0.09	0.03	0.16
Na I	4057	s17657	0.06	0.01	0.06	0.03	0.03	0.10
	4358	20885	0.06	0.01	0.04	0.03	0.04	0.09
Sr I	4057	s17657	0.06	0.00	0.00	0.01	0.09	0.11
	4358	20885	0.05	0.00	0.00	0.02	0.10	0.11

H. Abundances of Fe, Na, and Sr determined in the sample of 31 RGB stars in 47 Tuc

Table H.1. Abundances of Fe, Na, and Sr determined in the sample of 31 RGB stars in 47 Tuc.

Gaia Source ID	ID	$T_{\rm eff}$ K	$\log g$	$\xi_{\rm micro}$ km s^{-1}	A(Fe)	[Fe/H]	A(Na)	[Na/Fe]	A(Sr)	[Sr/Fe]
4689640950470780288	00251029-7158280	4133	1.18	1.64	6.75	−0.80	5.85	0.48	2.33	0.26
4689640774370214528	00242489-7159320	4235	1.32	1.55	6.77	−0.78	5.88	0.49	2.17	0.08
4689624762723599488	00234278-7211310	4343	1.37	1.99	6.79	−0.76	5.95	0.54	2.27	0.16
4689642256141727872	00232279-7201038	3982	0.85	1.85	6.81	−0.74	5.81	0.38	2.27	0.14
4689637407107299840	00224044-7208548	4114	1.09	1.58	6.75	−0.80	5.86	0.49	2.27	0.20
4689643935459451776	00235438-7158355	4143	1.10	1.79	6.82	−0.73	5.84	0.40	2.29	0.15
4689625999695578496	00241344-7211263	4118	1.11	1.73	6.67	−0.88	5.94	0.65	2.23	0.24
4689644730042501760	1062	3962	0.87	1.50	6.77	−0.78	5.80	0.41	2.26	0.17
4689651086596023040	4794	4071	1.15	1.46	6.72	−0.83	5.66	0.32	2.07	0.03
4689651151009833728	5265	3948	0.91	1.60	6.74	−0.81	5.85	0.49	2.20	0.14
4689652117388263296	5968	3959	0.93	1.45	6.71	−0.84	5.54	0.21	2.15	0.12
4689625724796264192	6798	4109	1.14	1.46	6.73	−0.82	5.63	0.28	2.19	0.14
4689626240193985280	10237	4289	1.34	1.75	6.63	−0.92	5.47	0.22	2.11	0.16
4689614970198135296	13396	4245	1.34	1.44	6.67	−0.88	5.57	0.28	2.25	0.26
4689638918944031616	20885	4358	1.41	1.76	6.69	−0.86	5.64	0.33	2.29	0.28
4689642599739335040	27678	3958	0.87	1.56	6.76	−0.79	5.87	0.49	2.19	0.11
4689642256141727872	28956	3982	0.85	1.86	6.77	−0.78	5.75	0.36	2.18	0.09
4689830508836705664	29861	4217	1.32	1.54	6.66	−0.89	5.59	0.31	2.09	0.11
4689640602571354496	38916	4173	1.22	1.41	6.80	−0.75	5.84	0.42	2.18	0.06
4689643630531051392	40394	3951	0.82	1.69	6.57	−0.98	5.73	0.54	2.30	0.41
4689623049035687040	s5270	4111	1.12	1.67	6.68	−0.87	5.99	0.69	2.30	0.30
4689625690444642560	s12272	4198	1.25	1.56	6.76	−0.79	5.93	0.55	2.34	0.26
4689626652510887168	s13795	4262	1.34	1.77	6.70	−0.85	5.56	0.24	2.15	0.13
4689638403539699584	s14583	4319	1.52	1.54	6.75	−0.80	5.79	0.42	2.33	0.26
4689626893029604096	s17657	4057	1.04	1.55	6.79	−0.76	6.03	0.62	2.32	0.21
4689638678425880576	s18623	4323	1.47	1.43	6.84	−0.71	5.95	0.49	2.27	0.11
4689638678425891712	s20002	4285	1.39	1.54	6.78	−0.77	5.87	0.47	2.31	0.21
4689639473003821440	s23821	4403	1.46	1.43	6.69	−0.86	5.82	0.51	2.31	0.30
4689639782230993664	s34847	4145	1.20	1.55	6.70	−0.85	5.65	0.33	2.28	0.26
4689640430772703232	s36828	4193	1.33	1.51	6.72	−0.83	5.73	0.39	2.27	0.23
4689643630522760960	s41654	4215	1.30	1.52	6.83	−0.72	5.97	0.52	2.30	0.15

Santrauka

Įžanga

Kamuolinių spiečių žvaigždės pasižymi specifine chemine sudėtimi, kuri nėra būdinga panašaus metalingumo lauko žvaigždėms. Sunkiųjų cheminių elementų (sunkesnių nei Si) gausos beveik visuose žinomuose spiečiuose yra vienodos tarp to spiečiaus žvaigždžių (Gratton et al. 2004), tačiau lengvųjų cheminių elementų gausos (nuo Li iki Si) skirtingose žvaigždėse gali skirtis iki 10 kartų (Carretta et al. 2009b). Galaktikos kamuolinių spiečių žvaigždėms taip pat būdingos koreliacijos arba antikorelicijos tarp skirtingų cheminių elementų, pvz., Na–O, Mg–Al antikoreliacijos (Carretta et al. 2009b), ar Li–Na koreliacija (Bonifacio et al. 2007). Apie trečdalio žvaigždžių esančių kamuoliniuose spiečiuose cheminė sudėtis yra panaši į tokio paties metalingumo lauko žvaigždžių cheminę sudėtį (Carretta et al. 2009b), tuo tarpu likusiai daliai žvaigždžių yra būdinga gerokai didesnė arba mažesnė lengvųjų cheminių elementų gausa (N, O, Na, Mag, Al, Si; pr. pvz. Bastian & Lardo 2018). Šie cheminiai elementai žvaigždėse yra gaminami protonų pagavos proceso (p-proceso) reakcijų metu, pavyzdžiui: ^{22}Ne(p,γ)^{23}Na ar ^{25}Mg(p,γ)^{26}Al. Šios reakcijos vyksta tik esant labai aukštai temperatūrai ($\geq 20{\times}10^6$ ir $\geq 70{\times}10^6$ K Ne–Na ir Mg–Al reakcijoms atitinkamai; Charbonnel 2016). Kadangi praturtinimas lengvaisiais elementais aptinkamas žvaigždėse, kurių centrinėse dalyse temperatūra yra gerokai mažesnė, kamuoliniuose spiečiuose turėjo egzistuoti kita žvaigždžių populiacija, kuri šiuos elementus susintetino ir jais praturtino dalį spiečių žvaigždžių. Tokios žvaigždės turėjo būti daug masyvesnės (tam, kad jose vyktų minėtos reakcijos), nei dabartinės kamuolinių spiečių žvaigždės. Todėl manoma, jog kamuoliniuose spiečiuose egzistavo tam tikra dalis pirmosios kartos, dabar jau mirusių, žvaigždžių (mažos masės pirmos populiacijos žvaigždės spiečiuose vis dar egzistuoja), kurios šiuos elementus susintetino ir jais praturtintą medžiagą išmetė į tarpžvaigždinę spiečiaus terpę, kur susiformavo lengvaisiais cheminiais elementais praturtintos antrosios kartos žvaigždės.

Greičiausiai ne tik antrosios kartos žvaigždžių paviršius (atmosfera) yra tokios savitos cheminės sudėties, tačiau ir visa žvaigždė, nes priešingu atveju, po pirmosios drumsties atmosferos cheminė sudėtis turėtų pasikeisti. Tai prieštarauja tyrimų rezultatams, kadangi C–N sąsaja yra aptinkama tiek pagrindinės sekos tiek ir RGB viršūnės žvaigždėse (Bastian & Lardo 2018). Taip pat, Na–O ir Mg–Al gausų sąryšiai nekinta priklausomai nuo žvaigždės evoliucijos stadijos, pavyzdžiui, 47 Tuc spiečiuje šie sąryšiai yra aptinkami tiek pagrindinės, tiek ir RGB sekos žvaigždėse (Milone et al. 2012).

Taigi, panaudojant iš stebėjimų nustatytas lengvųjų cheminių elementų gausas Galaktikos kamuolinių spiečių žvaigždėse, bei žinant kokiose žvaigždėse vyksta reikiamos nukleosintezės reakcijos, galima identifikuoti tas pirmosios kartos žvaigždes, kurios nulėmė dabar stebimas lengvųjų cheminių elementų gausų sąsajas. Tokios žvaigždės turi sintetinti lengvuosius cheminius elementus nesintetindamos sunkiųjų, kadangi geležies sklaida kamuolinių spiečių žvaigždėse dažniausiai nesiekia 0,05 dex (Carretta et al. 2009a), kai tuo tarpu lengvųjų cheminių elementų gausų sklaida gali viršyti ir 1,00 dex (Charbonnel 2016). Manoma, jog tokios pirmosios kartos žvaigždės-teršėjos galėjo būti asimptotinės milžinių sekos žvaigždės (angl. AGB – *asymptotic giant branch*;

Ventura & D'Antona 2011), greitai besisukančios masyvios žvaigždės (angl. FRMS – *fast rotating massive stars*; Norris 2004), masyvios dvinarės (de Mink et al. 2009).

Ankstyva AGB žvaigždžių karta gali praturtinti tarpžvaigždinę terpę žvaigždinių vėjų išmetama medžiaga. Vidutinės masės AGB žvaigždės dažnai laikomos vienomis iš pagrindinių aplinkinės tarpžvaigždinės erdvės praturtintojų. Tokios AGB žvaigždės, kurių masė viršija $\sim 4 - 5\,M_{\odot}$, turi konvekcinius apvalkalus, kurių apačia gali pasiekti regionus, kuriuose vyksta He sintezė. Tokiu būdu į šiuos regionus yra atnešama daugiau H, dėl ko pakyla jų temperatūra. Ji gali siekti 10^8 K, o tokios temperatūros pakanka, kad pradėtų vykti CNO, Ne–Na, Mg–Al reakcijos (Gratton et al. 2019). Šių reakcijų cheminiai produktai (Na, Mg, Al) dėl konvekcijos pasiekia žvaigždės paviršių ir tuomet žvaigždės vėjo yra išmetami į tarpžvaigždinę spiečiaus terpę. Tuomet iš šios, praturtintos tarpžvaigždinės medžiagos, susiformuoja antroji, turinti kitokią cheminę sudėtį, žvaigždžių karta (Villanova & Geisler 2011; D'Antona et al. 2016).

Greitai besisukančios pagrindinės sekos žvaigždės, FRMS, taip pat gali praturtinti tarpžvaigždinę spiečiaus terpę savo susintetinta medžiaga. Šios žvaigždės yra didelės masės (15–25 $M_{\odot}$) pagrindinės sekos žvaigždės, kurių centre yra pasiekiama reikiama temperatūra, kad vyktų anksčiau minėtos p-proceso cheminės reakcijos. Žvaigždės sukimosi sukeltas maišymasis iškelia susintetintus cheminius elementus į paviršių, kur tuomet dėl ekvatorinio vėjo ši medžiaga patenka į tarpžvaigždinę spiečiaus terpę (Krause et al. 2013).

Dauguma iškeltų hipotezių neblogai paaiškina didžiąją dalį cheminių ir fotometrinių anomalijų, tačiau visoms joms yra būdinga "masės biudžeto problema", kitaip tariant, norint turėti tokį antros kartos žvaigždžių kiekį koks yra stebimas dabar, pirmoji žvaigždžių karta turėjo būti daug kartų masyvesnė nei yra stebima dabar (Gratton et al. 2004). Egzistuoja ir kitos problemos, taigi, reikalingi tolimesni ir detalesni tyrimai norint suprasti kaip vyko ankstyvoji kamuolinių žvaigždžių spiečių evoliucija.

Kita vertus, siekiant identifikuoti pirmosios kartos žvaigždes-teršėjas, matyt reikėtų nagrinėti ne tik lengvuosius, bet ir sunkiuosius cheminius elementus. Pastaraisiais metais pasirodė kelių autorių darbai, kuriuose teigiama, jog kai kurių spiečių antrosios kartos žvaigždės gali būti praturtintos lėtojo neutronų pagavos proceso (angl. *slow neutron capture, s-process*) metu sintetinamais elementais (Fernández-Trincado et al. 2021; 2022). Nors šiuos elementus gali sintetinti tiek AGB, tiek FRMS žvaigždės, s-proceso elementų kiekiai, sintetinami skirtinguose objektuose, yra skirtingi, todėl tiriant jų gausas būtų galima tikėtis tiksliau identifikuoti galimas žvaigždes-teršėjas

Neutronų pagavos metu vyksta du skirtingi procesai, neutronų pagava ir beta skilimas. Neutronų pagavos reakcija yra vadinama lėtąja kuomet beta skilimo reakcijos sparta yra didesnė nei neutronų pagavos reakcijos sparta. Žvaigždėse vykstančios reakcijos, kurių metu išlaisvinami neutronai, yra dvi: ^{22}Ne(α,n)^{25}Mg (silpnasis s-proceso komponentas) ir ^{13}C(α,n)^{16}O (pagrindinis s-proceso komponentas). Reakcija, kuri dominuos konkretaus tipo žvaigždėje, priklauso nuo žvaigždės temperatūros, kurią lemia žvaigždės masė ir jos raidos etapas. Svarbiausia yra tai, jog nuo dominuojančios neutronų gamybos reakcijos priklauso kokie sunkieji cheminiai elementai bus sintetinami konkrečioje žvaigždėje. Žvaigždėse, kurių masė yra $M < 4\,M_{\odot}$ (AGB žvaigždės) domin-

uoja pagrindinis s-proceso komponentas ir pagrindiniai pagaminami sunkieji cheminiai elementai yra Ba, La ir Pb. Žvaigždėse, kurių masė yra $M > 4\ M_{\odot}$ (AGB, FRMS žvaigždės) dominuoja silpnasis s-proceso komponentas ir jose pagrindiniai pagaminami sunkieji cheminiai elementai yra Cu, Rb ar Zr (žr., pvz., Shingles et al. 2014).

Taigi, tiriant s-proceso cheminius elementus galima bandyti atsakyti į klausimą kokie objektai galėjo praturtinti (ar nuskurdinti) antros kartos žvaigždes lengvaisiais bei s-proceso metu sintetinamais cheminiais elementais. Lėtojo neutronų pagavos proceso metu susintetinamų cheminių elementų gausos skirtingų kartų spiečių žvaigždėse iki šiol sistemingai nebuvo tiriamos. Pavyzdžiui, viename iš geriausiai ištirtų Galaktikos kamuoliniame spiečiuje 47 Tuc cirkonio bei stroncio gausos iki šiol buvo nustatytos vos keliolikai žvaigždžių. Toks žvaigždžių kiekis yra nepakankamas, kad būtų galima patikimai nustatyti ar egzistuoja statistiškai reikšmingos šių elementų gausos sąsajos su kitais lengvaisiais cheminiais elementais, pvz, natriu. Siekiant užpildyti šią spragą, disertacijoje buvo atliktas išsamus cirkonio, stroncio bei bario tyrimas Galaktikos kamuolinio spiečiaus 47 Tuc žvaigždėse, siekiant atsakyti į klausimą ar egzistuoja šių elementų gausų skirtumai skirtingose šio spiečiaus žvaigždžių populiacijose ir jei taip, nustatyti kokios žvaigždės-teršėjos galėjo lemti šiuos skirtumus.

Tyrimo tikslas

Nustatyti Na, Sr, Zr ir Ba gausas Galaktikos kamuolinio žvaigždžių spiečiaus 47 Tuc raudonosios milžinių sekos žvaigždžių atmosferose ir ištirti galimus sąryšius tarp skirtingų šio spiečiaus žvaigždžių cheminių bei kinematinių savybių.

Uždaviniai

- Naudojant 1D hidrostatinius žvaigždžių atmosferų modelius kartu su 1D LTE/NLTE spektrų sintezės bei ekvivalentinių pločių metodais, nustatyti Na, Sr ir Zr cheminių elementų gausas Galaktikos kamuolinio spiečiaus 47 Tuc raudonosios milžinių sekos žvaigždžių atmosferose.
- Apskaičiuoti 1D NLTE gausos pataisas Na cheminiam elementui ir ištirti NLTE efektų įtaką Na I spektro linijų formavimuisi tiriamų raudonosios milžinių sekos žvaigždžių atmosferose.
- Ištirti galimas sąsajas tarp Na, Sr, Zr ir Ba gausų tiriamose 47 Tuc raudonosios milžinių sekos žvaigždėse ir taip pat atlikti sąsajų tarp šių elementų gausų bei žvaigždžių kinematinių savybių analizę.

Rezultatai ir ginamieji teiginiai

1. Nustatytos 1D LTE Sr ir Zr gausos Galaktikos kamuolinio spiečiaus 47 Tuc raudonosios milžinių sekos žvaigždžių atmosferose. Vidutinės tirtų žvaigždžių gausų vertės yra $\langle[\mathrm{Sr/Fe}]\rangle = 0{,}18 \pm 0{,}08$ dex (31 žvaigždė), $\langle[\mathrm{Zr/Fe}]\rangle = 0{,}35 \pm 0{,}09$ dex (237 žvaigždės).
2. Nustatyta 1D NLTE Na gausa 261 raudonosios milžinių sekos žvaigždžių Galaktikos kamuolinio spiečiaus 47 Tuc atmosferoje. Vidutinė tirtų žvaigždžių gausos vertė yra $\langle[\mathrm{Na/Fe}]\rangle = 0{,}41 \pm 0{,}16$ dex.
3. Apskaičiuotos 1D NLTE gausų pataisos Na I $\lambda = 615{,}4225$ nm ir Na I $\lambda = 616{,}0747$ nm linijoms yra intervaluose nuo –0,19 iki –0,07 dex ir nuo –0,27 iki –0,08 dex atitinkamai.
4. Panaudojant Ba gausos matavimus 261 47 Tuc RGB žvaigždžių imtyje buvo nustatyta, kad antros populiacijos žvaigždės šiame spiečiuje nėra praturtintos Ba.
5. Nustatyta statistiškai reikšminga priklausomybė tarp [Zr/Fe] ir [Na/Fe] gausų santykių bei tarp [Zr/Fe] gausų santykio ir žvaigždžių atstumo iki spiečiaus centro.

Mokslinis naujumas

- Atlikta Zr gausų analizė didžiausioje iki šiol Galaktikos kamuolinio spiečiaus 47 Tuc žvaigždžių imtyje. Pirmą kartą nustatyta statistiškai reikšminga priklausomybė tarp Zr ir Na gausų bei priklausomybė tarp Zr gausų ir žvaigždžių atstumo iki spiečiaus centro.
- Pirmą kartą nustatyta Sr gausa raudonosios milžinių sekos žvaigždėse esančiose Galaktikos kamuoliniame spiečiuje 47 Tuc. Nustatyta silpna priklausomybė tarp Sr ir Na gausų.
- Pirmą kartą kamuoliniame spiečiuje nustatyta priklausomybė tarp lengvojo s-proceso elemento Zr ir lengvojo elemento Na, bei priklausomybė tarp Zr gausų ir žvaigždžių atstumo iki spiečiaus centro. Pirmą kartą kamuoliniame spiečiuje nustatyta priklausomybė tarp lengvojo s-proceso elemento Sr ir lengvojo elemento Na gausų.

Autoriaus indėlis

Autorius atliko visų tirtų Galaktikos kamuolinio žvaigždžių spiečiaus 47 Tuc žvaigždžių spektrų redukavimą ir suskaičiavo 1D hidrostatinius žvaigždžių atmosferų modelius, taip pat nustatė žvaigždžių mikroturbulencijos greičius pusei tirtų žvaigždžių. Autorius nustatė cirkonio linijų ekvivalentinius pločius tirtose žvaigždėse, šie ekvivalentiniai pločiai vėliau buvo panaudoti nustatyti cirkonio gausoms kamuoliniame spiečiuje 47 Tuc. Autorius atliko 1D NLTE spektrų sintezę ir nustatė 1D NLTE Na gausas raudonosios milžinių sekos žvaigždžių atmosferose kamuoliniame spiečiuje 47 Tuc, atliko 1D LTE spektrų sintezę ir nustatė Sr gausas tirtose raudonosios milžinių sekos žvaigždėse kamuoliniame spiečiuje 47 Tuc. Autorius taip pat atliko 1D LTE spektrų sintezę ir nustatė Zr gausas panaudojant Zr II spektro linijas raudonosios milžinių sekos žvaigždžių atmosferose. Autorius nustatė geležies gausas tirtose Galaktikos kamuolinio spiečiaus 47 Tuc žvaigždėse ir nustatė radialinius bei erdvinius greičius tirtoms žvaigždėms. Disertantas su bendraautoriais atliko statistinę ir mokslinę analizę duomenų gautų atlikus Sr ir Zr analizę, įskaitant galimų priklausomybių tarp skirtingų cheminių elementų gausų (Na, Sr, Zr) analizę ir taip pat tarp šių elementų gausų bei tirtų žvaigždžių kinematinių savybių tyrimą. Autorius taip pat atliko analizę ir palyginimą tarp nustatytų s-proceso elementų gausų ir teorinių nukleosintezės modelių prognozių 47 Tuc spiečiuje.

1. Cheminių elementų gausos žvaigždžių atmosferose analizės metodai

Disertacijoje buvo naudojami archyviniai raudonosios milžinių sekos Galaktikos kamuoliniame spiečiuje 47 Tuc spektrų duomenys. Žvaigždžių spektrai buvo gauti `GIRAFFE` ir `UVES` spektrografais, kurie veikia kartu su VLT-UT2 (angl. *Very Large Telescope*) teleskopu esančiu Cerro Paranal observatorijoje Čilėje. Abu spektrografai yra šviesolaidiniai ir daugiaobjektiniai, su UVES galima stebėti apie dešimt, o su `GIRAFFE` daugiau nei šimtą objektų vienu metu. Cheminių elementų gausų stebėtų žvaigždžių atmosferose nustatymui buvo naudojami 1D hidrostatiniai `ATLAS9` atmosferos modeliai, tiriamų žvaigždžių sintetiniai spektrai suskaičiuoti su `SYNTHE` (1D LTE) bei `MULTI` (1D NLTE) programine įranga.

Spektroskopinių stebėjimų duomenys

Darbe tirtų cheminių elementų Fe, Na, Zr, Ba gausos buvo nustatytos panaudojant archyvinius VLT/GIRAFFE redukuotus spektrus, kurie buvo gauti vykdant šias programas: 073.D-0211(A) (E. Carretta), 088.D-0026(A) (I. McDonald), 072.D-0777(A) (A. Lèbre). VLT/UVES spektrai, naudoti nustatant Fe, Na, Mg, Sr gausas, buvo gauti vykdant šias programas: 073.D-0211(A) (E. Carretta), 088.D-0026(A) (I. McDonald), 072.D-0777(A) (A. Lèbre), 084.B-0810(A), 086.B-0237(A) (PI: Sbordone).

VLT/GIRAFFE stebėjimai buvo atlikti spektrografo Medusa konfiguracijoje (128 optinės skaidulos, iš kurių 15 skirta dangaus fono stebėjimams), $\sim$ 612 – 697 nm bangos ilgio intervale, HR13, HR14A ir HR15 gardelėse. Spektrų skyra yra tarp $R\sim$21350 – 26400, spektrų signalo triukšmo santykis yra S/N $\approx$ 100. Tyrimo metu naudoti VLT/UVES spektrai buvo gauti 472 – 683 nm bangos ilgių intervale, jų skyra yrarp $R\sim$48000 – 107200, signalo triukšmo santykis S/N $\approx$ 160. Naudototų spektrų normavimas ir kontinuumo nustatymas buvo atliktas panaudojant IRAF[1] (angl. *Image Reduction and Analysis Facility*) paketo programą *splot*.

Tirtų žvaigždžių atmosferų parametrai

Žvaigždžių efektinės temperatūros buvo nustatytos panaudojant Bergbusch & Stetson (2009) fotometrinius stebėjimus ir $T_{\rm eff}$ – $(V - I)$ kalibraciją iš Ramírez & Meléndez (2005). Žvaigždžių paviršiaus gravitacijos pagreičiai, $\log g$, buvo nustatyti panaudojant žvaigždės efektinės temperatūros ir gravitacijos pagreičio sąryšį:

$$\log g = 4{,}44 + 4\log(T_{\rm eff}/T_{\rm eff}^{\odot}) + 0{,}4(4{,}75 - L) + \log(M/M_{\odot}), \qquad \text{(H.1)}$$

čia $T_{\rm eff}$ – šiame darbe nustatyta žvaigždės temperatūra, $T_{\rm eff}^{\odot} = 5777$ K – Saulės efektinė temperatūra, L ir M yra tirtų žvaigždžių šviesis ir masė. Šviesiai ir masės įvertinti panaudojant Yonsei-Yale (Y^2) izochronas[2] ir laikant, kad tirtų

[1] http://iraf.noao.edu/

[2] `http://www.astro.yale.edu/demarque/yyiso.html`.

žvaigždžių masė vienoda ir lygi $M = 0{,}89 M_{\odot}$. Izochronos buvo suskaičiuotos panaudojant Z = 0,004 metalingumo vertę ir $[\alpha/\mathrm{Fe}] = +0{,}3$ α-elementų praturtinimo vertę.

Žvaigždžių metalingumas nustatytas panaudojant 17 – 28 Fe I linijas esančias 612,79 – 691,67 nm bangos ilgių diapazone, šių linijų sužadinimo potencialas yra 2,18 – 4,61 eV intervale. Mikroturbulencijos greičių vertės tirtoms žvaigždėms nustatytos kartu su Fe gausomis, keičiant mikroturbulencijos greičio, ξ_{micro}, vertę tol, kol išnyksta geležies gausos priklausomybė nuo ekvivalentinio pločio. Šiuo atveju buvo atmestos stiprios linijos, kurių ekvivalentinis plotis > 15 pm, kadangi jos yra mažiau jautrios ξ_{micro} pokyčiams.

Tirtų žvaigždžių atmosferų modeliai

Darbe tirtų žvaigždžių 1D LTE atmosferų modeliai buvo suskaičiuoti taikant `ATLAS9` programų paketą. Šių modelių skaičiavimams reikalingi trys pagrindiniai žvaigždžių parametrai: efektinė temperatūra, gravitacijos pagreičio logaritmas ir metalingumas. `ATLAS9` atmosferos modelis yra padalintas į 72 sluoksnius, kuriuose vidutinis Rosseland'o neskaidrumas, τ_{Ross}, kinta nuo $\log \tau_{\mathrm{Ross}} = -6{,}875$ atmosferos išorėje iki $\log \tau_{\mathrm{Ross}} = +2{,}00$ atmosferos viduje. Konvekcija įskaitoma parametrizuotu būdu, taikant maišymosi ilgio teoriją (angl. *mixing length theory*; Böhm-Vitense 1958). Esminė šios teorijos prielaida – konvekcinis burbulas žvaigždės atmosferoje pakilęs į viršų tam tikrą atstumą l susilieja su aplinka, tokiu būdu jai atiduodamas savo turimą energiją. Šis atstumas yra apibrėžiamas taip: $l = \alpha_{\mathrm{MLT}} H_{\mathrm{p}}$, čia H_{p} yra slėgio stulpelio aukštis, o α_{MLT} – maišymosi ilgio parametras, kuris kinta intervale tarp 1 ir 2, o konvekcijos efektyvumas yra tuo didesnis, kuo šis parametras mažesnis.

Kadangi 47 Tuc spiečiaus žvaigždės, kaip ir visų kitų kamuolinių spiečių žvaigždės, yra praturtintos α-elementais (C, O, Ne, Mg, Si, S, Ar, Ca, Ti) per +0,4 dex (Carretta et al. 2004), skaičiuojant atmosferos modelius buvo naudojamos +0,4 dex α-elementais praturtintos neskaidrumų pasiskirstymo funkcijos[3] (Castelli & Kurucz 2003). Saulės atmosferos cheminių elementų gausa paimta iš Grevesse & Sauval (1998) darbo.

Sintetinių spektrų skaičiavimas

1D LTE cheminių elementų gausos nustatymui buvo naudojamas `SYNTHE` programų paketas (Kurucz & Furenlid 1979; Sbordone et al. 2004). Šis programų rinkinys skirtas teorinių žvaigždžių spektrų skaičiavimui, panaudojant 1D hidrostatinius žvaigždžių atmosferos modelius `ATLAS9`.

1D NLTE cheminių elementų gausų nustatymui buvo naudotas `MULTI` programų paketas, kuris pritaikytas darbui su 1D hidrostatiniais `ATLAS9` žvaigždžių atmosferų modeliais. Atliekant šį tyrimą buvo naudojami keli skirtingi atomų

[3]ODF – angl. *opacity distribution function*. Šios funkcijos naudojamos aprašant neskaidrumus žvaigždžių atmosferų modeliuose. Naudojant ODF, visas spektras suskirstomas į mažesnius intervalus, kuriuose monochromatiniai absorbcijos koeficientai (suma visų atomų ir molekulių linijų, prisidedančių prie bendro monochromatinio absorbcijos koeficiento tam tikrame siaurame dažnių intervale, neskaidrumų) ties keliais bangų ilgiais aproksimuojami glotnia funkcija, kuri ir yra vadinama ODF.

modeliai: Na atomo modelį (Korotin et al. 1999) sudaro 20 Na I lygmenų ir pagrindinis Na II lygmuo, iš viso atsižvelgiama į tarp 46 lygmenų vykstančius spindulinius šuolius (angl. *radiative transitions*). Ba atomo modelį sudaro 31 Ba I, 101 Ba II lygmuo bei pagrindinis Ba III lygmuo, atliekant atomo lygmenų užpildų (angl. *level population numbers*) skaičiavimus atsižvelgiama į 91 tarp lygmenų vykstantį šuolį. Išsamus šio atomo modelio aprašas bei testų rezultatai pateikiami Andrievsky et al. (2009) darbe.

2. Zr gausa Galaktikos kamuolinio spiečiaus 47 Tuc žvaigždžių atmosferose

Kamuolinis spiečius NGC 104, arba kitaip 47 Tuc, yra vienas masyviausių mūsų Galaktikos kamuolinių spiečių ($7 \times 10^5\, M_\odot$, Marks & Kroupa 2010). Anksčiau, remiantis pagrindinės ir horizontaliosios sekų morfologija, šis spiečius buvo laikomas tipiniu paprastosios žvaigždžių populiacijos, kurios žvaigždės yra vienodo amžiaus ir cheminės sudėties, pavyzdžiu, tačiau pastaruoju metu buvo atlikta daug tyrimų, kurių rezultatai parodė, kad tai nėra tiesa. Tyrimų rezultatai atskleidė, jog šiame spiečiuje egzistuoja kelios žvaigždžių populiacijos, kurios skiriasi lengvųjų cheminių elementų gausomis (pvz. He, O, Na; D'Orazi et al. 2010; Milone et al. 2012). Hablo kosminio teleskopo stebėjimų archyvo analizė atskleidė, kad šio spiečiaus spalvos-ryškio diagramoje submilžinių seka yra padalinta į dvi skirtingas sekas (Anderson et al. 2009). Vėliau Milone et al. (2012) parodė, jog ne tik submilžinių, bet ir pagrindinė šio spiečiaus seka yra padalinta į kelias sekas, kurios tarpusavyje skiriasi helio gausa.

Šio spiečiaus žvaigždės taip pat turi įdomių kinematinių savybių. Richer et al. (2013) atrado egzistuojančią mėlyniausių pagrindinės sekos žvaigždžių savųjų greičių anizotropiją radialine kryptimi. Šios žvaigždės yra sukoncentruotos spiečiaus centre ir identifikuotos kaip antrosios kartos žvaigždės, tuo tarpu pirmosios kartos žvaigždžių tangentiniai ir radialiniai greičiai yra izotropiški. Kučinskas et al. (2014) nustatė, jog pirmosios kartos žvaigždės pasižymi didesnėmis absoliutaus radialinio greičio vertėmis nei antrosios kartos žvaigždės ir aptiko kai kurių lengvųjų cheminių elementų, tokių kaip ličio, deguonies, natrio gausos sąsajas su radialiniu žvaigždžių atstumu nuo spiečiaus centro. Šie rezultatai leidžia manyti, jog 47 Tuc dar nėra pilnai relaksavęs, todėl jame galima tikėtis stebėti ne tik elementų gausų skirtumus, bet ir kinematinius skirtumus tarp skirtingoms populiacijoms priklausančių žvaigždžių.

Na ir Zr gausų tyrimo metodai

Darbe tirtų raudonosios milžinių sekos žvaigždžių Na ir Zr gausos buvo nustatytos panaudojant 237 žvaigždžių archyvinius VLT/GIRAFFE spektrus. Na 1D NLTE gausos buvo nustatytos taikant sintetinių spektrų metodą, pritaikant `MULTI` programinę įrangą kartu su `ATLAS9` atmosferų modeliais. Analizėje panaudotos dvi Na I linijos, kurių centriniai bangos ilgiai yra ties 615,4225 ir 616,0747 nm. Sintetiniai natrio linijų profiliai buvo suskaičiuoti su `MULTI` programine įranga ir tuomet papildomai išplėsti atlikus sąsuką su Voigt profiliu,

1 lentelė. Pearson'o, Spearman'o ir Kendall'o koreliacijų koeficientai ir atitinkamos p-reikšmės [Zr/Fe]–[Na/Fe] ir gausos–atstumo plokštumose.

	Pearson'o		Spearman'o		Kendall'o	
	r	p	ρ	p	τ	p
[Zr/Fe] − [Na/Fe]	0,41	$< 10^{-10}$	0,41	$< 10^{-10}$	0,29	$< 10^{-10}$
[Na/Fe] − r/r_h	−0,26	5×10^{-5}	−0,28	2×10^{-5}	−0,19	2×10^{-5}
[Zr/Fe] − r/r_h	−0,24	1×10^{-4}	−0,22	5×10^{-4}	−0,15	6×10^{-4}

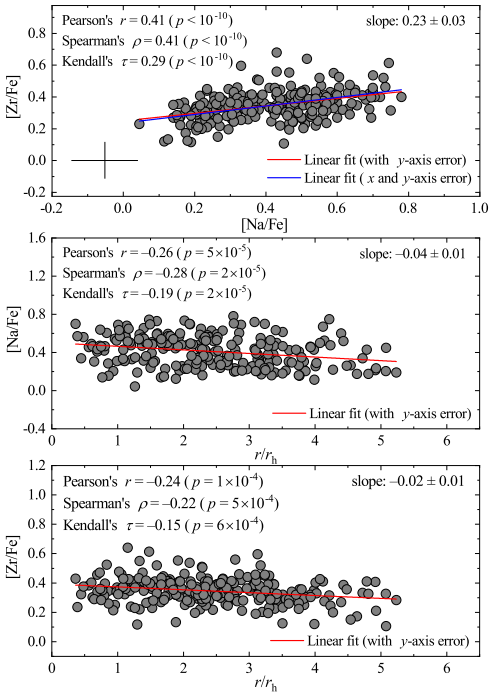

1 pav. [Zr/Fe] gausos santykiai 237 RGB žvaigždėse kamuoliniame spiečiuje 47 Tuc. Viršutinis grafikas: [Zr/Fe] ir [Na/Fe] gausų santykiai. Vidurinis ir apatinis grafikai, atitinkamai: [Zr/Fe] ir [Na/Fe] gausų santykių priklausomybė nuo radialinio atstumo iki spiečiaus centro, $r/r_{\rm h}$. Ištisinės linijos grafikuose priderintos panaudojant visus matavimus. Grafikuose taip pat pateiktos koreliacijos koeficientų vertės, tiesės polinkio vertės ir Student'o t-testo tikimybės p-vertės, suskaičiuotos panaudojant Pearson'o koreliacijos koeficientą.

kad būtų įskaičiuota instrumentinio bei makroturbulencijos greičio įtaka linijų profiliams. Tyrimo metu naudotos individualios makroturbulencijos greičio vertės kiekvienai žvaigždei, kurios, kartu su Na gausa, nustatytos iteratyviai derinant sintetinio spektro linijos profilį prie tos pačios spektro linijos profilio stebėtame žvaigždės spektre.

Zr gausos buvo nustatytos su `WIDTH9` programine įranga pritaikius ekvivalentinių pločių metodą. Analizėje buvo panaudotos trys Zr I linijos, kurių centriniai bangos ilgiai yra ties 612,7475, 613,4585 ir 614,3252 nm. Linijų ekvivalentiniai pločiai nustatyti priderinant Gauso profilį prie stebėtos Zr linijos profilio su `IRAF` programinės įrangos *splot* programa. Kaip ir Na atveju, kiekvienai žvaigždei buvo naudotos individualios mikroturbulencijos greičio vertės. Zr gausos analizėje nebuvo atsižvelgta į linijų hipersmulkiąją struktūrą, tačiau mūsų testų rezultatai parodė, jog šio efekto įtaka gausos įverčiams yra mažesnė nei 0,02 dex ir gausų matavimų rezultatams reikšmingos įtakos neturi.

Darbe nustatyta vidutinė 1D NLTE Na gausa yra $\langle[\mathrm{Na/Fe}]\rangle = 0{,}41 \pm 0{,}16$ (skaičius po $\pm$ ženklo nurodo standartinį nuokrypį nuo gausos vidurkio). Na gausa taip pat turi didelę sklaidą: $0{,}05 \leq [\mathrm{Na/Fe}] \leq 0{,}78$. Šios vertės gerai sutampa su ankstesnių darbų rezultatais: $\Delta[\mathrm{Na/Fe}] = 0{,}76$ ir $\langle[\mathrm{Na/Fe}]\rangle = 0{,}47 \pm 0{,}15$ (Carretta et al. 2009b, 147 RGB žvaigždės), $\Delta[\mathrm{Na/Fe}] = 0{,}56$ ir $\langle[\mathrm{Na/Fe}]\rangle = 0{,}36 \pm 0{,}18$ (Wang et al. 2017, 27 RGB žvaigždės).

Vidutinė šiame darbe nustatyta 1D LTE Zr gausa yra $\langle[\mathrm{Zr/Fe}]\rangle = 0{,}35 \pm 0{,}09$. Zr gausos sklaida yra panaši kaip ir Na atveju: $0{,}11 \leq [\mathrm{Zr/Fe}] \leq 0{,}68$. Šios vertės neblogai sutampa su Thygesen et al. (2014) tyrimo rezultatais šiame spiečiuje: $\langle[\mathrm{Zr/Fe}]\rangle = 0{,}41 \pm 0{,}19$ (13 RGB žvaigždžių). Šiek tiek didesnis gausos skirtumas atsiranda lyginant su Wylie et al. 2006 rezultatais (vidurkis 7 RGB/AGB žvaigždėse), $\langle[\mathrm{Zr/Fe}]\rangle = 0{,}69 \pm 0{,}15$.

Zr ir Na gausų 237 RGB žvaigždėse analizės rezultatai parodė, jog šiame spiečiuje egzistuoja silpna priklausomybė tarp šių elementų gausų, [Zr/Fe] ir [Na/Fe], santykių (1 pav., viršutinis grafikas). Siekiant įvertinti ar ši priklausomybė yra statistiškai reikšminga, laikytasi nulinės hipotezės, jog Pearson'o ir neparametriniai Spearman'o ir Kendall'o koreliacijos koeficientai (r, ρ, and τ,

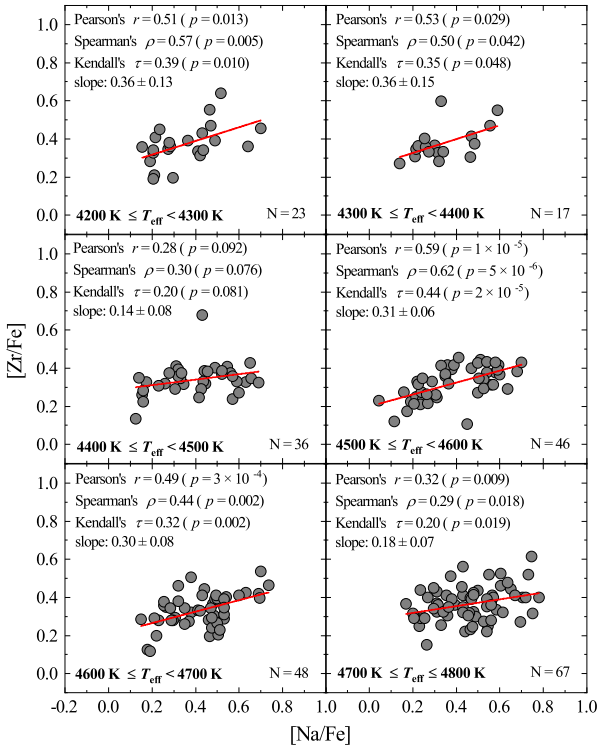

2 pav. [Zr/Fe] – [Na/Fe] grafikai tiriamų žvaigždžių imčiai, padalintai į – mažesnes, $\Delta T_{\mathrm{eff}} = 100\,\mathrm{K}$ intervalus apimančias imtis (N yra žvaigždžių skaičius kiekvienoje iš mažesnių imčių). Kiekviename grafike yra pateikti atitinkamos imties koreliacijos koeficientai ir p-vertės.

atitinkamai) yra lygūs nuliui, tai reikštų, kad [Zr/Fe] ir [Na/Fe] gausų santykiai nekoreliuoja. Šios analizės rezultatai parodė, kad nors ir gautos koreliacijos koeficientų vertės yra nedidelės, tikimybės gauti tokias vertes atsitiktinai yra labai mažos, ką galima matyti iš gautų p-verčių (1 lentelė).

Papildomai, visa tirtų žvaigždžių imtis buvo padalinta į $\Delta T_{\rm eff} = 100\,{\rm K}$ dydžio mažesnes imtis, kurias panaudojant buvo sudaryti nauji [Zr/Fe] – [Na/Fe] grafikai. Visose mažesnėse imtyse, išskyrus vieną ($4400 \leq T_{\rm eff} < 4500\,{\rm K}$) statistiškai reikšminga priklausomybė (su p-vertėmis $< 0{,}05$) tarp [Zr/Fe] ir [Na/Fe] gausų santykių išliko (2 pav.).

Mūsų analizės rezultatai taip pat rodo silpnos, bet statistiškai reikšmingos sąsajos tarp Zr gausos ir radialinio atstumo iki spiečiaus centro, [Zr/Fe] – $r/r_{\rm h}$, egzistavimą (1 pav., vidurinis grafikas), čia $r_{\rm h}$ yra 47 Tuc pusės šviesio spindulys ($r_{\rm h} = 174''$, Trager et al. 1993). Šis rezultatas rodo, jog žvaigždės su didžiausiais [Na/Fe] ir [Zr/Fe] gausų santykiais telkiasi arčiau spiečiaus centro, o tai sutampa su ankstesnių tyrimų rezultatais (pvz., Bastian & Lardo 2018). Šiame tyrime gautos p-vertės yra pateiktos 1 lentelėje.

3. Ba gausa Galaktikos kamuolinio spiečiaus 47 Tuc žvaigždžių atmosferose

Bario gausa iki šiol buvo tirta įvairiuose Galaktikos kamuoliniuose spiečiuose, tame tarp ir 47 Tuc, tačiau kol kas tik pastarajame buvo galimai nustatyta [Ba/Fe] ir [Na/O] koreliacija (Gratton et al. 2013). Nors šių autorių nustatyta priklausomybė buvo statistiškai reikšminga, tačiau, autorių teigimu, dėl nedidelės [Ba/Fe] gausos santykio sklaidos ir taip pat nustatytos priklausomybės tarp [Na/O] gausų santykio ir žvaigždžių efektinės temperatūros jų rezultatas turėtų būti patikrintas kitų nepriklausomų tyrimų. Kaip jau buvo minėta 1 skyriuje, viena iš pagrindinių s-proceso elementų tyrimų kamuoliniuose spiečiuose problemų yra ta, kad šiems tyrimams atlikti buvo naudojamos mažos žvaigždžių imtys (pvz., Thygesen et al. 2014 atliktame s-proceso elementų tyrime 47 Tuc spiečiuje buvo panaudota <15 žvaigždžių). Dėl šių priežasčių bei siekdami gauti daugiau informacijos apie galimus s-proceso elementų gausų skirtumus tarp pirmos ir antros populiacijos žvaigždžių, mes ištyrėme 1P–2P Ba gausos skirtumus 261 RGB žvaigždžių imtyje kamuoliniame spiečiuje 47 Tuc, šio tyrimo rezultatai aprašyti žemiau.

Na ir Ba gausų tyrimo metodai

Mūsų tirtų raudonosios milžinių sekos žvaigždžių Na ir Ba gausos buvo nustatytos panaudojant 261 žvaigždžių archyvinius VLT/GIRAFFE spektrus. Didžioji dalis žvaigždžių (228 bendros žvaigždės) yra tos pačios, kurioms buvo nustatytos Zr gausos, papildomai, Na ir Ba gausos buvo nustatytos dar 33 žvaigždėms. Tiek Na tiek ir Ba 1D NLTE gausos buvo gautos panaudojant sintetinių spektrų metodą su `MULTI` programine įranga bei `ATLAS9` atmosferų modeliais. Analizėje buvo panaudotos dvi Na I linijos, kurių centriniai bangos ilgiai yra ties 615,4225 ir 616,0747 nm ir dvi Ba II linijos, kurių centriniai bangos ilgiai yra ties 614,1730 ir 649,6910 nm. Sintetiniai Na ir Ba linijų profiliai buvo suskaičiuoti su `MULTI` programine įranga ir tuomet papildomai išplėsti atlikus sąsuką su Voigt profiliu, siekiant įskaičiuoti instrumentinio bei makroturbulencijos greičio įtaka linijų profiliams. Kiekvienai žvaigždei buvo naudotos individualios mikroturbulencijos greičio vertės. Tiek Na, tiek Ba gausos ir makroturbulencijos greičio vertės galiausiai buvo nustatytos iteratyviai derinant sintetinio spektro linijos profilį prie tos pačios linijos spektro profilio stebėtame žvaigždės spektre.

Na ir Ba gausų tyrimo rezultatai

Kadangi Na gausai įvertinti buvo naudoti 228 žvaigždžių spektrai, kurie buvo naudoti ir nustatant Na gausą Zr analizėje (žr. 2 skyrių), vidutinis [Na/Fe] gausų santykis nesiskiria nuo Zr analizėje gauto rezultato. Vidutinė šiame darbe nustatyta 1D NLTE Ba gausa yra $\langle[\mathrm{Ba/Fe}]\rangle = -0{,}01 \pm 0{,}06$, o vidutinė 1D NLTE Ba gausos pataisa yra apie –0,10 dex. Ši vidutinė Ba gausos vertė gerai sutampa su kitų autorių nustatytomis Ba gausomis šiame kamuoliniame spiečiuje. Viename ankstesnių darbų, James et al. (2004) tyrė Ba gausas posūkio taško ir sub-milžinių sekos žvaigždėse 47 Tuc spiečiuje, vidutinė šiame darbe

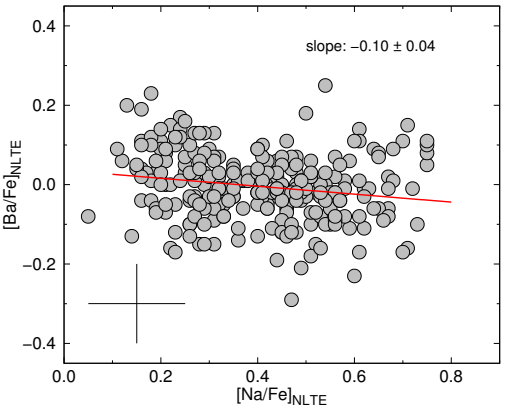

3 pav. [Ba/Fe] gausų santykiai nustatyti 261 RGB žvaigždėse esančiose 47 Tuc spiečiuje ir pavaizduoti nuo jų [Na/Fe] gausų santykių. Tipinės gausos paklaidos vertės yra parodytos pliuso simboliu apatiniame kairiajame kampe. Geriausiai prie visų taškų deranti tiesė yra pavaizduota raudona linija.

nustatyta Ba LTE gausa 8 sub-milžinėse buvo [Ba/Fe] = +0,35, ir [Ba/Fe] = +0,22 trijose posūkio taško žvaigždėse. D'Orazi et al. (2010) darbe buvo tirtos 110 RGB žvaigždės, autorių nustatyta vidutinė 1D LTE Ba gausa buvo $\langle$[Ba/Fe]$\rangle$ = −0,15 ± 0,06; įskaičius –0,10 dex Ba NLTE gausų pataisą, šis rezultatas gerai dera su mūsų nustatyta vidutine Ba 1D NLTE gausa. Didesnis skirtumas atsiranda lyginant su vidutine Ba 1D NLTE gausa nustatyta Thygesen et al. (2014) darbe, kur autoriai gavo $\langle$[Ba/Fe]$\rangle$ = 0,28 ± 0,07 (13 RGB žvaigždžių). Šį skirtumą galima paaiškinti tuo, kad Thygesen et al. (2014) darbe mikroturbulencijos greičių ir gravitacijos pagreičių vertės yra atitinkamai 0,33 km s^{-1} ir 0,30 dex didesnės nei gautos mūsų darbe (6 bendrų žvaigždžių mūsų ir Thygesen et al. 2014 imtyse palyginimo rezultatas). Naudojant Thygesen et al. (2014) nustatytus mikroturbulencijos greičius bei gravitacijos pagreičius, mūsų darbe gautos Ba gausos padidėtų per 0,20 dex ir taptų daug panašesnės į Thygesen et al. (2014) darbe gautas Ba gausas.

Darbe 261 RGB žvaigždėse nustatyti [Ba/Fe] gausų santykiai rodo silpną, tačiau statistiškai reikšmingą sąsają su [Na/Fe] gausų santykiais (3 pav.), kur Pearson'o koreliacijos koeficientas yra lygus $r_{\rm P} = -0{,}18$. Priėmus nulinę hipotezę, jog sąsajos tarp abiejų gausų santykių nėra, atliekant Student'o testą gauta tikimybė yra lygi $p_{\rm P} = 2{,}9 \times 10^{-3}$, kad šią $r_{\rm P}$ vertę galima gauti atsitiktinai. Tokį rezultatą yra sudėtinga paaiškinti pasitelkus šiuolaikinius nukleosintezės modelius, kadangi žinoma, jog Ba gali būti sintetinamas mažos arba vidutinės masės AGB žvaigždėse pagrindinio s-proceso metu, arba greitai besisukančiose masyviose žvaigždėse He degimo jų centre fazėje. Kita vertus, mūsų gauta antikoreliacija rodo, kad turėjo egzistuoti kažkoks mechanizmas, dėl kurio Ba buvo naikinamas antros populiacijos žvaigždėse, vietoje to, kad būtų sintetinamas, kaip pvz., Na. Padalinus visą tirtų žvaigždžių imtį į $\Delta T_{\rm eff}$ = 100 K dydžio intervalus, ši statistiškai reikšminga priklausomybė tarp [Ba/Fe] ir [Na/Fe] gausų santykių išlieka tik viename $4600 \leq T_{\rm eff} < 4700$ K intervale

2 lentelė. [Ba/Fe] – [Na/Fe] gausų santykių koreliacijos koeficientai pilnoje 261 RGB žvaigždžių imtyje ir $\Delta T_{\rm eff} = 100$ K intervaluose.

Pearson'o		Spearman'o		Kendall'o	
r	p	ρ	p	τ	p
Pilna imtis, N = 261					
−0,18	3×10^{-3}	−0,20	1×10^{-3}	−0,14	7×10^{-4}
$4200 \leq T_{\rm eff} < 4300$, N = 23					
−0,11	0,61	−0,09	0,68	−0,06	0,68
$4300 \leq T_{\rm eff} < 4400$, N = 15					
−0,15	0,60	−0,17	0,54	−0,16	0,42
$4400 \leq T_{\rm eff} < 4500$, N = 35					
−0,38	0,02	−0,34	0,05	−0,24	0,04
$4500 \leq T_{\rm eff} < 4600$, N = 42					
−0,15	0,35	−0,15	0,32	−0,11	0,31
$4600 \leq T_{\rm eff} < 4700$, N = 48					
−0,41	4×10^{-3}	−0,41	3×10^{-3}	−0,28	5×10^{-3}
$4700 \leq T_{\rm eff} < 4800$, N = 66					
−0,11	0,39	−0,16	0,20	−0,12	0,15
$4800 \leq T_{\rm eff} < 4900$, N = 32					
0,15	0,42	0,04	0,83	0,03	0,84

ir galbūt kiek silpnesnė priklausomybė vis dar matoma $4400 \leq T_{\rm eff} < 4500$ K intervale (2 lentelė). Labiausiai tikėtina, kad ši priklausomybė atsiranda dėl kelių žvaigždžių, esančių $4600 \leq T_{\rm eff} < 4700$ K intervale, kurios atsitiktinai turi didesnes Ba gausas. Ši priklausomybė negali būti paaiškinta, pvz., blogesne spektrų kokybe, kadangi aukštesne $T_{\rm eff}$ pasižyminčiose ir kartu mažiau ryškiose žvaigždėse šios priklausomybės nėra. Taip pat, nėra jokio astrofizikinio paaiškinimo, kodėl tokia priklausomybė turėtų egzistuoti tik tokiame siaurame $T_{\rm eff}$ intervale. D'Orazi et al. (2010) darbe, kur autoriai ištyrė 110 RGB žvaigždžių tame pačiame 47 Tuc spiečiuje, priklausomybės tarp Ba ir lengvųjų cheminių elementų gausų taip pat nebuvo nustatytos.

Taigi, Ba gausos analizė 1P ir 2P žvaigždėse kamuoliniame spiečiuje 47 Tuc rodo, jog antrosios populiacijos žvaigždės nebuvo papildomai praturtintos Ba. Šie bei ankstesni, D'Orazi et al. (2010) darbe gauti, rezultatai nesutampa su Gratton et al. (2013) rezultatais, kur autoriai aptiko statistiškai reikšmingą priklausomybę tarp Ba–Na gausų išanalizavę 114 horizontaliosios sekos žvaigždžių esančių 47 Tuc. Pastarųjų autorių teigimu, [Na/O] gausų santykis priklauso nuo efektinės temperatūros horizontaliosios sekos žvaigždėse ir tai gali dalinai (ar net pilnai) paaiškinti Gratton et al. (2013) nustatytą silpną Ba–Na priklausomybę.

Nustatyta šiame darbe vidutinė 261 RGB žvaigždės Ba gausa 47 Tuc spiečiuje, $\langle [{\rm Ba/Fe}]_{\rm 1D\ NLTE} \rangle = -0{,}01 \pm 0{,}06$, gerai dera su Ba gausa panašaus metalingumo kamuoliniuose spiečiuose bei Galaktikos lauko žvaigždėse (4 pav.).

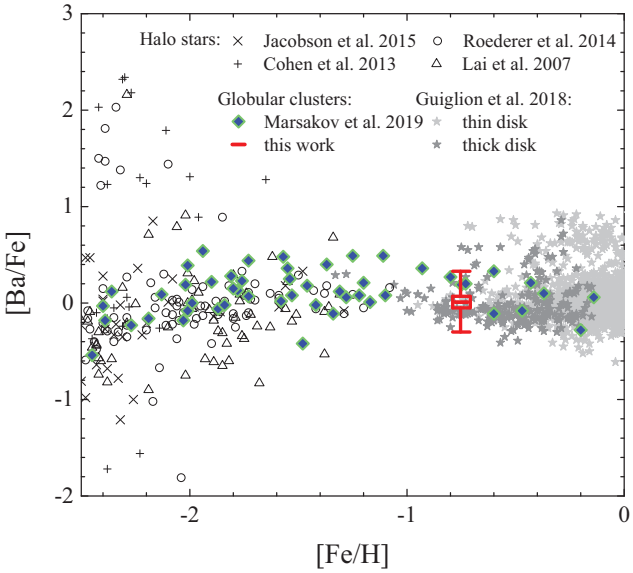

4 pav. Bario gausa Galaktikos kamuoliniuose spiečiuose (Marsakov et al. 2019 kompiliacija), Galaktikos lauko žvaigždėse (plonojo ir storojo disko žvaigždės: Guiglion et al. 2018 ir Galaktikos halo žvaigždės: Lai et al. 2007; Cohen et al. 2013; Roederer et al. 2014; Jacobson et al. 2015). Vidutinis [Ba/Fe] gausų santykis kamuoliniame 47 Tuc spiečiuje pažymėtas raudonu simboliu, kur 25 ir 75 procentiliai ir vidutinės vertės yra parodytos horizontaliomis linijomis, o vertikalių linijų galai nurodo maksimalią ir minimalią gausų vertę tirtose žvaigždėse.

Nustatyta Ba gausa turi nedidelę sklaidą, $\pm 0{,}06$ dex, kuri pilnai paaiškinama Ba gausų nustatymo paklaidomis, $\sigma_{\mathrm{A(Ba)}} \approx 0{,}12$ dex. Apibendrinus abu šiuos faktus, labai tikėtina, jog 47 Tuc spiečiuje nustatyta Ba gausa atspindi pirminio proto-debesies, iš kurio susiformavo šis spiečius, Ba gausą ir spiečiaus evoliucijos metu Ba gausa daugiau nekito.

Laikant, jog antroji populiacija buvo papildomai praturtinta Zr (žr. 2 skyrių), tačiau nebuvo papildomai praturtinta Ba, galima daryti išvadą, kad šiame spiečiuje žvaigždės-teršėjos sintetino tik tam tikrus s-proceso elementus. Nukleosintezės, vykstančios mažos ir vidutinės masės AGB žvaigždėse, modelių prognozės rodo, kad Zr ir Ba gali būti gaminamas pakankamai dideliais kiekiais, tačiau abu šie elementai turėtų būti gaminami kartu (žr., pvz., Cristallo et al. 2015). Abu šie elementai gali būti sintetinami ir masyviose, greitai besisukančiose žvaigždėse, tačiau ir šiuo atveju, abu elementai turėtų būti sintetinami kartu (Limongi & Chieffi 2018).

4. Sr gausa Galaktikos kamuolinio spiečiaus 47 Tuc žvaigždžių atmosferose

Šiame darbe buvo atlikta 237 RGB žvaigždžių Galaktikos kamuoliniame spiečiuje 47 Tuc analizė, kurios metu buvo nustatyti s-proceso elemento Zr gausos skirtumai šio spiečiaus 1P ir 2P žvaigždėse. Naudinga ištirti, ar ir kitų s-proceso elementų iš 'pirmojo s-proceso piko' (pvz., Rb, Sr, Y), susidariusių panašiomis sąlygomis kaip Zr, gausos taip pat koreliuoja su lengvųjų cheminių elementų gausomis, kaip tai yra Zr atveju. Be to, kadangi skirtingi teršėjai sintetina s-proceso elementus skirtingais kiekiais, šių elementų, pavyzdžiui, [Sr/Zr], gausų santykių palyginimas su AGB ir greitai besisukančių masyvių žvaigždžių modelių prognozėmis, galėtų suteikti daugiau informacijos apie galimus teršėjų tipus ir jų mases.

Iki šiol vieninteliame Sr gausos tyrime 47 Tuc žvaigždėse buvo naudojama labai maža imtis: aštuonios SGB ir trys TO žvaigždės (James et al. 2004). Šis tyrimas neatskleidė nei reikšmingos Sr gausos sklaidos, nei sąsajų su lengvųjų elementų gausomis. Tikėtina, jog šį rezultatą lėmė maža tirtų žvaigždžių imtis, ypač atsižvelgiant į labai mažą s-proceso elementų gausų sklaidą ir/ar silpnas sąsajas, kurios yra aptinkamos kamuolinių spiečių žvaigždėse (žr., pvz., 2 skyrių ar Fernández-Trincado et al. 2021; 2022). Mūsų atliktas Sr gausos tyrimas turėjo dvigubą tikslą: (a) nustatyti Sr gausas didesnėje žvaigždžių imtyje ir (b) įvertinti galimą 1P–2P gausų skirtumą ir/ar Sr ir lengvųjų cheminių elementų sąsajų egzistavimą 47 Tuc.

Na ir Sr gausų tyrimo metodika

Darbe tirtų raudonosios milžinių sekos žvaigždžių Na ir Sr gausos buvo gautos panaudojant 31 žvaigždės archyvinius VLT/UVES spektrus. Na 1D NLTE gausos buvo gautos panaudojant tas pačias dvi Na I linijas ir tą pačią metodiką, kuri buvo naudota Zr gausos analizėje (žr. 2 skyrių).

Sr 1D LTE gausos buvo nustatytos taikant sintetinių spektrų metodą. Sintetiniai linijų profiliai buvo suskaičiuoti naudojant `SYNTHE` programinę įrangą kartu su `ATLAS9` atmosferų modeliais. Analizėje buvo panaudota viena Sr I linija, kurios centrinis bangos ilgis yra ties 650,4165 nm. Tai – vienintelė Sr gausos nustatymui tinkama linija, matoma analizuotuose spektruose (kitų archyvinių `UVES` ar `GIRAFFE` spektrų, kuriuose būtų matomos Sr linijos, nėra). Kadangi analizuota Sr I linija susilieja su dalimi šalia esančios stipresnės V I linijos (centrinis bangos ilgis ties 650,3991 nm), nustatant Sr gausą buvo keičiama ir V gausa, tam, jog sintetinį spektrą būtų galima geriau priderinti prie stebėto žvaigždės spektro. Siekiant atsižvelgti į instrumentinio profilio bei makroturbulencijos greičio įtaką spektro linijų profiliams, suskaičiuoti sintetiniai spektrai buvo išplėsti atlikus sąsuką su Gauso profiliu. Atliekant sintetinių spektrų skaičiavimus buvo naudojamos individualios mikroturbulencijos greičių vertės kiekvienai žvaigždei. Makroturbulencijos greičio vertės buvo nustatytos iteratyviai derinant sintetinio spektro linijos profilį prie tos pačios spektro linijos profilio stebėtame žvaigždės spektre.

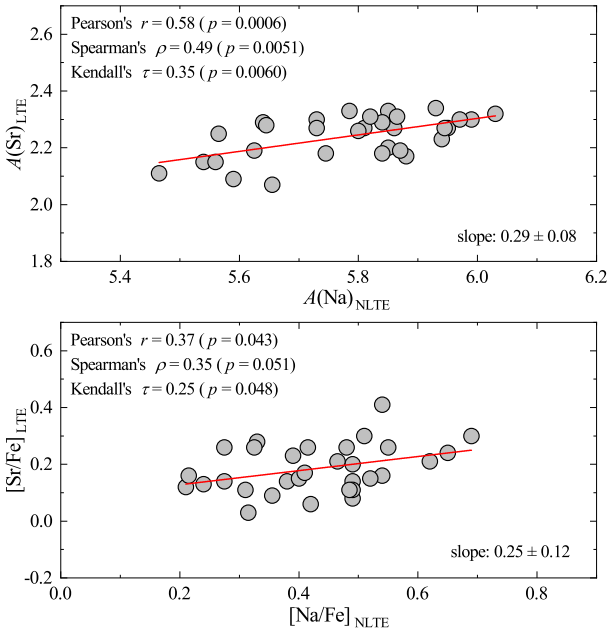

5 pav. Sr gausos, A(Sr), ir [Sr/Fe] gausų santykių tirtose žvaigždėse priklausomybė nuo Na gausos, A(Na), ir [Na/Fe] gausų santykių atitinkamai.

Na ir Sr gausos 47 Tuc žvaigždėse

Darbe nustatyta vidutinė 1D NLTE Na gausa, gauta panaudojant 31 RGB žvaigždės `UVES` spektrus, yra $\langle$[Na/Fe]$\rangle = 0{,}43 \pm 0{,}12$ (skaičius po $\pm$ ženklo nurodo standartinį nuokrypį nuo gausos vidurkio). Šis rezultatas gerai dera su Na gausa, nustatyta šiame darbe analizuojant 237 RGB žvaigždžių `GIRAFFE` spektrus (žr. 2 ir 3 skyrius): $\langle$[Na/Fe]$\rangle = 0{,}41 \pm 0{,}16$. Šie rezultatai taip pat gerai dera su kitų autorių darbų rezultatais: Δ[Na/Fe] = 0,76 ir $\langle$[Na/Fe]$\rangle = 0{,}47 \pm 0{,}15$ (Carretta et al. 2009b, 147 RGB žvaigždės), Δ[Na/Fe] = 0,56 ir $\langle$[Na/Fe]$\rangle = 0{,}36 \pm 0{,}18$ (Wang et al. 2017, 27 RGB žvaigždės).

Vidutinė šiame darbe nustatyta 1D LTE Sr gausa yra $\langle$[Sr/Fe]$\rangle = 0{,}18 \pm 0{,}08$. Vienintelis kitas ankstesnis darbas, kuriame buvo tiriama Sr gausa 47 Tuc spiečiaus žvaigždėse, yra James et al. (2004), kuriame buvo tirtos aštuonios SGB ir trys TO žvaigždės. Šių autorių nustatytos Sr gausos, atitinkamai yra $[\mathrm{Sr/Fe}]_{\mathrm{SGB}} = 0{,}36 \pm 0{,}16$ ir $[\mathrm{Sr/Fe}]_{\mathrm{TO}} = 0{,}28 \pm 0{,}14$. Skirtumas tarp Sr gausų nustatytų James et al. (2004) ir mūsų darbe gali atsirasti todėl, kad James et al. (2004) darbe buvo naudotos dvi jonizuoto Sr linijos, kurių centriniai bangų ilgiai yra ties 407,771 ir 421,552 nm, taip pat ir dėl skirtingai priderinto spektro kontinuumo lygio.

Mūsų analizės rezultatai atskleidė galimas silpnas sąsajas tarp (a) Sr ir Na gausų, ir (b) [Sr/Fe] ir [Na/Fe] gausų santykių (5 pav.). Priimant nulinę hipotezę, kad nėra Sr–Na koreliacijos, Pearson'o parametrinis bei Spearman'o ir Kendall'o neparametriniai testai rodo, kad tikimybė, p, gauti atitinkamus koreliacijos koeficientus, r, mūsų duomenų rinkinyje yra $p < 0{,}05$ (5 pav.). Tai gali reikšti, kad 47 Tuc 2P žvaigždės yra šiek tiek praturtintos Sr.

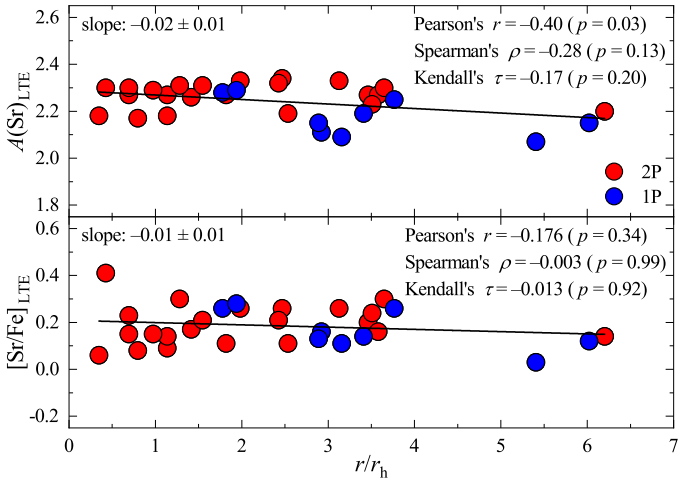

6 pav. Stroncio gausos priklausomybė nuo atstumo iki spiečiaus 47 Tuc centro. Mėlyni taškai – 1P žvaigždės ($[\mathrm{Na/Fe}] = [[\mathrm{Na/Fe}]_{\min}, [\mathrm{Na/Fe}]_{\min} + 0{,}3]$); raudoni taškai – 2P žvaigždės (turinčios didesnę Na gausą nei 1P žvaigždės). $[\mathrm{Na/Fe}]_{\min}$ vertė nustatyta šiame darbe

Kita vertus, statistinės analizės testo rezultatas nepatvirtina Sr–r/r_{h} antikoreliacijos (žr. pav. 6; čia, r yra projekcinis atstumas nuo spiečiaus centro iki tam tikros žvaigždės, o $r_{\mathrm{h}} = 174''$ yra 47 Tuc pusės šviesio spindulys, paimtas iš Trager et al. 1993). Nors šiame darbe jau buvo nustatyta Na–r/r_{h} antikoreliacija (2 skyrius), žvaigždžių imties, kuri buvo naudota Sr gausų analizei, atveju tokia antikoreliacija nėra stebima (7 pav.). Gali būti, kad šiuo atveju naudota RGB žvaigždžių imtis yra tiesiog per maža, kad būtų galima patikimai nustatyti galimą Sr–r/r_{h} antikoreliaciją.

Kita vertus, mūsų analizės rezultatai rodo, kad žvaigždės, turinčios daugiau Na, yra labiau susikoncentravusios spiečiaus centre. Tiek vizuali jų pasiskirstymo nuo atstumo iki spiečiaus centro, r/r_{h}, analizė (žr. 6 pav.), tiek Kolmogorovo-Smirnovo (K-S) testo rezultatai analizuojant kumuliatyvius 1P ir 2P žvaigždžių skirstinius atžvilgiu r/r_{h} (žr. pav. 8) rodo, kad Na praturtinta populiacija iš tikrųjų yra labiau susikoncentravusi arčiau spiečiaus centro. Tikimybė, pagal K-S testą, jog kumuliatyvus pasiskirstymas Na praturtintų ir įprastą Na gausą turinčių žvaigždžių yra vienodas, yra $p = 0{,}052$. Kita vertus, Na–r/r_{h} plokštumoje statistiškai patikimos priklausomybės nerasta ($p > 0{,}33$), greičiausiai todėl, jog žvaigždžių imtis yra per maža.

Gauti Sr rezultatai rodo, kad teršėjai, kurie praturtino 2P žvaigždes lengvaisiais elementais, taip pat galėjo sintetinti ir s-proceso elementus Sr ir Zr. Kita vertus, tai reikėtų patvirtinti atlikus išsamesnę Sr gausos analizę didesnėje žvaigždžių imtyje, taip pat ir kitų s-proceso elementų, kurie priklauso tam pačiam (pirmajam) s-proceso pikui, ypač Y ir Rb, analizę šiame ir kituose Galaktikos kamuoliniuose spiečiuose.

Iki šiol atliktų sunkesnių s-proceso elementų gausų analizės rezultatai Galaktikos kamuoliniuose spiečiuose nėra vienareikšmiai. Savo tyrime, apėmusiame santykinai nedidelę 13 RGB žvaigždžių imtį 47 Tuc, Thygesen et al.

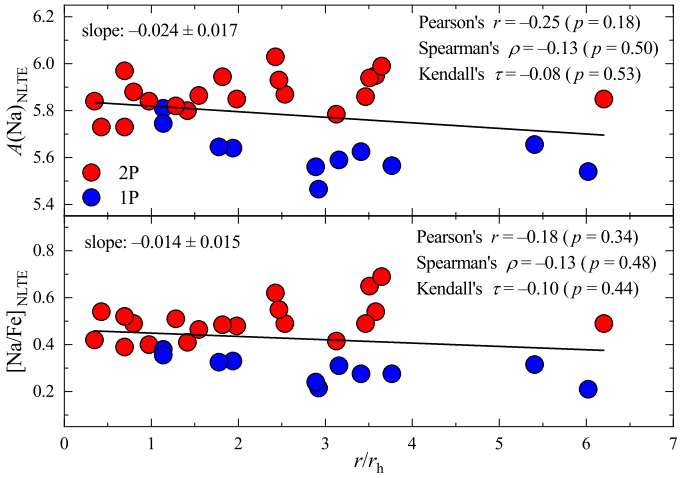

7 pav. Natrio gausos priklausomybė nuo atstumo iki spiečiaus 47 Tuc centro. Mėlyni taškai – 1P žvaigždės ($[\mathrm{Na/Fe}] = [[\mathrm{Na/Fe}]_{\mathrm{min}}, [\mathrm{Na/Fe}]_{\mathrm{min}} + 0{,}3]$); raudoni taškai – 2P žvaigždės (turinčios didesnę Na gausą nei 1P žvaigždės). $[\mathrm{Na/Fe}]_{\mathrm{min}}$ vertė nustatyta šiame darbe

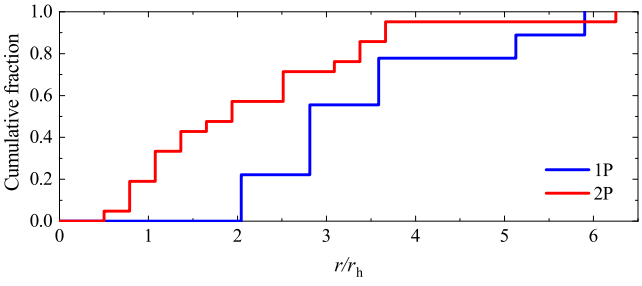

8 pav. Kumuliatyvi žvaigždžių skaičiaus pasiskirstymo funkcija abiejose žvaigždžių kartose pavaizduota nuo atstumo iki spiečiaus centro. K-S testo rezultatas rodo, jog tikimybė, kad 1P ir 2P žvaigždžių grupės būtų paimtos iš tos pačios imties yra $p = 0{,}052$.

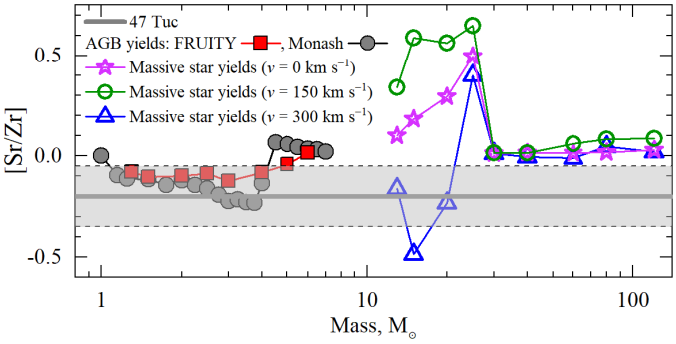

9 pav. [Sr/Zr] gausų santykio priklausomybė nuo žvaigždės masės. Teoriniai AGB modeliai: FRUITY (Cristallo et al. 2015) ir Monash (Karakas et al. 2018). Masyvių žvaigždžių modeliai: Limongi & Chieffi (2018). Horizontali pilka linija: [Sr/Zr] gausų santykis 47 Tuc nustatytas šiame darbe. Šviesiai pilka juosta: standartinis nuokrypis atsirandantis dėl natūralios žvaigždžių Sr ir Zr gausų variacijos.

(2014) nerado jokių Ba ar La gausos sąsajų su Na. Atlikus 123 šio spiečiaus RGB žvaigždžių analizę, Cordero et al. (2014) neaptiko La–Na sąsajos. Mūsų atliktoje Ba gausos analizėje 261 RGB žvaigždėje 47 Tuc mes taip pat neradome jokios sąsajos tarp Ba ir Na gausų (žr. 3 skyrių). Nors Ba ir La priklauso antrajam s-proceso pikui, AGB ir FRMS žvaigždžių modelių prognozės rodo, kad Ba ir La turėtų būti sintetinami kartu su pirmojo s-proceso piko elementais (žr., pvz., Carretta et al. 2009b; Limongi & Chieffi 2018). Kita vertus, savo neseniai atliktuose 47 Tuc ir keleto kitų Galaktikos kamuolinių spiečių tyrimuose, Fernández-Trincado et al. (2021; 2022) aptiko Ce–N ir Ce–Al koreliacijas. Faktą, kad nėra stebimas 1P–2P Ba–La gausų skirtumas, sunku suderinti su galima Ce–N sąsaja, nes Ba, La ir Ce priklauso tam pačiam antrajam s-proceso pikui ir todėl jų visų gausos vienodai turėtų arba koreliuoti su lengvųjų elementų gausomis arba būti tokios pačios abiejose populiacijose.

Vidutinio Sr ir Zr gausų santykio, [Sr/Zr], 47 Tuc palyginimas su teorinėmis s-proceso nukleosintezės prognozėmis AGB ir masyviose žvaigždėse rodo, kad abu elementai galėjo būti susintetinami arba AGB žvaigždėse, arba didelės masės ($M = 10 - 25\,M_{\odot}$) greitai besisukančiose ($v_{\rm rot} = 200 - 300\,{\rm km\,s^{-1}}$) žvaigždėse (9 pav.). Taigi, siekiant geriau identifikuoti galimus kamuolinių spiečių cheminės raidos scenarijus, reikalinga išsamesnė s-proceso elementų gausų analizė didesnėse žvaigždžių imtyse skirtinguose kamuoliniuose spiečiuose.

Pagrindiniai rezultatai ir išvados

Šiame darbe buvo tirtos galimos sąsajos tarp cheminių ir kinematinių RGB žvaigždžių, esančių Galaktikos kamuoliniame spiečiuje 47 Tuc, savybių. Tyrimo metu nustatytos 1D NLTE Na bei 1D LTE Sr ir Zr gausos, RGB žvaigždžių atmosferose, šiam tikslui naudojant aukštos raiškos spektrus, kurie buvo gauti naudojant `VLT/GIRAFFE` ir `VLT/UVES` spektrografus, veikiančius Europos pietinėje observatorijoje.

Šiame darbe tirtų žvaigždžių atmosferų modeliai buvo suskaičiuoti `ATLAS9` programine įranga. Na ir Ba gausos nustatymui, buvo atlikta 1D NLTE spektro linijų sintezė naudojant `MULTI` paketą, tuo tarpu Sr 1D LTE linijų sintezė buvo atlikta naudojant `SYNTHE` paketą. Zr gausos buvo nustatytos ekvivalentinių pločių metodu, gausų nustatymui buvo panaudotas `WIDTH9` programų paketas. Šiame darbe taip pat buvo naudoti `CO`^{5}`BOLD` programų paketu suskaičiuoti 3D hidrodinaminiai atmosferų modeliai, kurie kartu su 1D hidrostatiniais `LHD` atmosferos modeliais buvo panaudoti konvekcijos įtakos spektro linijų formavimuisi įvertinimui.

Darbe nustatytos vidutinės gausos RGB žvaigždėms 47 Tuc: $\langle[\mathrm{Na/Fe}]_{\mathrm{NLTE}}\rangle = 0{,}41 \pm 0{,}16$ (261 žvaigždė), $\langle[\mathrm{Sr/Fe}]_{\mathrm{LTE}}\rangle = 0{,}18 \pm 0{,}08$ (31 žvaigždė), $\langle[\mathrm{Zr/Fe}]_{\mathrm{LTE}}\rangle = 0{,}35 \pm 0{,}09$ (237 žvaigždės), $\langle[\mathrm{Ba/Fe}]_{\mathrm{NLTE}}\rangle = -0{,}01 \pm 0{,}06$ (261 žvaigždė), čia paklaidos reiškia standartinį nuokrypį atsirandantį dėl natūralios žvaigždžių gausų variacijos.

Tyrimo metu gautos Zr gausos pasižymi nedidele sklaida, egzistuoja silpna statistiškai reikšminga priklausomybė $[\mathrm{Zr/Fe}] - [\mathrm{Na/Fe}]$ plokštumoje ($p < 0{,}002$). Taip pat aptiktas statistiškai reikšmingas Zr gausos vidurkių skirtumas tarp 1P ir 2P žvaigždžių, kur 2P žvaigždėms būdinga $\Delta[\mathrm{Zr/Fe}]_{\mathrm{2P-1P}} \approx 0.06$ dex didesnė Zr gausa. Be to, šiame darbe atliktų gausų analizės rezultatai rodo statistiškai reikšmingą antikoreliaciją tarp Zr gausos ir atstumo iki spiečiaus centro, $[\mathrm{Zr/Fe}] - r/r_{\mathrm{h}}$ ($p = 0{,}0001$). Kita vertus, panašu, jog statistiškai reikšmingos priklausomybės tarp žvaigždžių erdvinių greičių dispersijų ir Zr gausų nėra.

Ba gausų analizė neatskleidė jokių statistiškai reikšmingų sąsajų $[\mathrm{Ba/Fe}] - [\mathrm{Na/Fe}]$ ar $[\mathrm{Ba/Fe}] - r/r_{\mathrm{h}}$ plokštumose. Tiek 1P, tiek 2P žvaigždės, 47 Tuc spiečiuje turi tokią pačią Ba gausą, todėl tikėtina, kad ankstyvuose šio kamuolinio spiečiaus evoliucijos etapuose žvaigždės teršėjos papildomai Ba nesintetino. Ba gausos 47 Tuc spiečiuje gerai sutampa su kitų spiečių, Galaktikos disko ir halo žvaigždžių, turinčių panašų metalingumą, gausomis.

Sr gausų analizės rezultatai rodo galimas silpnas sąsajas tarp Sr ir Na gausų ir tarp [Sr/Fe] ir [Na/Fe] gausų santykių ($p < 0{,}05$). Vis dėlto, statistiniai testai nepatvirtino priklausomybės $[\mathrm{Sr/Fe}] - r/r_{\mathrm{h}}$ plokštumoje egzistavimo.

Konvekcijos poveikis Sr I spektro linijai, naudotai šiame darbe, yra minimalus, tą rodo nedidelė 3D–1D LTE gausos pataisa, kuri neviršija 0,05 dex. Be to, šios pataisos priklausomybė nuo žvaigždžių atmosferos parametrų, pavyzdžiui, T_{eff}, yra labai silpna.

Tyrimo metu nustatytos Zr–Na ir Sr–Na gausų priklausomybės gali reikšti, kad objektai, kurie praturtino (ar nuskurdino) 2P žvaigždes lengvaisiais elementais, turėjo sintetinti ir lengvuosius s-proceso elementus.

Kita vertus, šio tyrimo metu atliktos Ba gausos analizės rezultatai atskleidė, jog žvaigždės teršėjos Ba papildomai nesintetino, kadangi tiek 1P, tiek 2P

žvaigždės turi tą pačią Ba gausą. Laikant, kad 2P buvo praturtinta Zr ir Sr, bet ne Ba, yra tikėtina, kad tik tam tikri s-proceso elementai buvo sintetinami žvaigždžių teršėjų, kurios praturtino 2P žvaigždes Na ir pakeitė kitų lengvųjų elementų, tokių kaip Li, N ar O, gausas, kaip buvo nustatyta ankstesniuose tyrimuose (žr., pvz., Bastian & Lardo 2018). Teoriniai mažos ir vidutinės masės AGB žvaigždžių nukleosintezės modelių rezultatai rodo, kad Zr ir Ba gali būti gaminami reikšmingais kiekiais, tačiau jie abu turėtų būti sintetinami kartu (Cristallo et al. 2015). Panašiai, dideli kiekiai Zr ir Ba galėtų būti pagaminti FRMS žvaigždėse, tačiau abu elementai turėtų būti sintetinami kartu (Limongi & Chieffi 2018).

Siekiant nustatyti, kurios žvaigždės teršėjos praturtino 2P žvaigždes savo susintetinta medžiaga galima tirti cheminių elementų gausų tarpusavio santykius. Šiam tikslui reikėtų pasirinkti tokius elementus, kurie būtų gaminami skirtingų tipų žvaigždėse ir skirtinguose žvaigždžių masių intervaluose. [La/Rb], [Pb/Zr] ar [Pb/*hs*] s-proceso elementų santykiai šiuo atveju galėtų būti ypač informatyvūs (*hs* – sunkieji s-proceso elementai, pavyzdžiui, Ba, La ar Ce). Rb yra daugiausia sintetinamas AGB žvaigždėse siaurame masių diapazone, $\sim 4 - 5\,M_{\odot}$, tuo tarpu masyvios žvaigždės šio elemento pagamina nedaug. Pb taip pat, ypač didesnio metalingumo ($>$ [Fe/H] = –1,5) žvaigždėse, daugiausia yra sintetinamas AGB žvaigždėse, o ne masyviose žvaigždėse. Didelis [Pb/hs] gausų santykis reikštų, jog s-proceso elementai daugiausiai buvo sintetinami AGB žvaigždėse. Vis dėlto, Pb gausas nustatyti žvaigždėse, ypač Galaktikos kamuoliniuose spiečiuose, gali būti sudėtinga, kadangi Pb linijos yra silpnos ir tam gali prireikti aukštos kokybės spektrų.

Taip pat, būtų naudinga nustatyti Sr ir Zr gausas didesniame žvaigždžių skaičiuje įvairiuose Galaktikos kamuoliniuose spiečiuose, siekiant nustatyti ar Sr–Na ar Zr–Na priklausomybės egzistuoja kitur, kadangi 47 Tuc gali būti išimtinis atvejis. Ba gausų nustatymas kituose kamuoliniuose spiečiuose, ypač tuose, kurių parametrai skiriasi nuo 47 Tuc (amžius, masė ar metalingumas) ir kuriuose yra aptinkamos lengvųjų elementų sąsajos su Al ir Si, taip pat gali būti naudingas.

Apibendrinant, paaiškinti stebimas gausų sąsajas Galaktikos kamuoliniuose spiečiuose pasitelkus tik vieną žvaigždžių teršėjų tipą yra sudėtinga; labai tikėtina, kad buvo aktyvūs keli skirtingi teršėjų tipai, kurie veikė vienu metu. Išsamūs gausų tyrimai, apimantys didesnį kiekį skirtingų cheminių elementų ir didesnes žvaigždžių imtis, padėtų tiriant kelių populiacijų Galaktikos kamuoliniuose spiečiuose prigimties problemą. Be to, reikalingi ir tikslesni žvaigždžių nukleosintezės modeliai, kadangi jų prognozės yra labai svarbios norint teisingai interpretuoti kamuoliniuose spiečiuose esančių žvaigždžių gausas ir jų tarpusavio sąsajas.

ACKNOWLEDGEMENTS

I would like to express my sincere gratitude to my supervisor, Arūnas Kučinskas, for his invaluable guidance, constant support, and endless patience. I am also grateful to V. Dobrovolskas, J. Klevas, D. Prakapavičius, A. Černiauskas, V. Vansevičius, D. Narbutis, K. Zubovas, J. Sperauskas, J. Sūdžius, D. Semionov, G. Tautvaišienė, and many others who helped me deepen my knowledge and shaped my growth as a scientist.

Special thanks go to M. Čeponis, R. Naujalis, A. Leščinskaitė, K. Lyvens, A. Sabulis, with whom I embarked on the path of astronomy and shared many wonderful moments studying the stars.

Finally, I would like to thank my family and friends for their unwavering support throughout this journey, as well as all those who may never read this work but nonetheless contributed to its completion.

LIST OF PUBLICATIONS

Publications on the Thesis topic in the Clarivate Analytics WoS journals:

[1] V. Dobrovolskas, **E. Kolomiecas**, A. Kučinskas, J. Klevas, S. Korotin, 2021, *Abundance of barium in the atmospheres of red giants in the Galactic globular cluster NGC 104 (47 Tuc)*, Astronomy and Astrophysics, **656**, A67.

[2] **E. Kolomiecas**, V. Dobrovolskas, A. Kučinskas, P. Bonifacio, S. Korotin, 2022, *Abundance of zirconium in the globular cluster 47 Tucanae: a possible Zr—Na correlation?*, Astronomy and Astrophysics, **660**, A46.

[3] **E. Kolomiecas**, A. Kučinskas, J. Klevas, V. Dobrovolskas, 2024, *Abundance of strontium in the Galactic globular cluster 47 Tuc*, Astronomy and Astrophysics, **682**, A126.

Conference presentations

[1] **E. Kolomiecas**, V. Dobrovolskas, A. Kučinskas, *Abundance of zirconium in the atmospheres of red giants in Galactic globular cluster 47 Tuc*, Star Clusters: from the Milky Way to the Early Universe, Bologna, Italy, 2019 (poster presentation).

[2] **E. Kolomiecas**, A. Kučinskas, V. Dobrovolskas, *Abundance of zirconium in the Galactic globular cluster 47 Tuc*, 43rd Lithuanian National Physics Conference, Kaunas, Lithuania, 2019 (oral presentation).

[3] **E. Kolomiecas**, V. Dobrovolskas A. Kučinskas, *Abundance of zirconium in the red giants of Galactic globular cluster 47 Tuc*, Cool Stars 20.5 - virtually cool, 2021 (virtual conference, poster presentation).

[4] **E. Kolomiecas**, V. Dobrovolskas A. Kučinskas, *Abundance of zirconium in the atmospheres of red giants in Galactic globular cluster 47 Tuc*, 64th conference of Open Readings, 2021 (virtual conference, poster presentation).

[5] **E. Kolomiecas**, *Abundances of Sr and Zr in the atmospheres of red giants in Galactic globular cluster 47 Tuc*, ChETEC-INFRA SNAQ, 2022 (virtual conference, oral presentation).

Vilnius University Press
Saulėtekio al. 9, III rūmai, LT-10222 Vilnius
e-mail: info@leidykla.vu.lt, www.leidykla.vu.lt
Print run copies 15